Université de Valenciennes et du Hainaut-Cambrésis

Thèse de doctorat

Pour obtenir le grade de Docteur de l'Université de

VALENCIENNES ET DU HAINAUT-CAMBRESIS

Discipline, spécialité selon la liste des spécialités pour lesquelles l'Ecole Doctorale est accréditée :
Mécanique

Présentée et soutenue par Emilie LUC.

Le 20/12/2013, à Valenciennes

Ecole doctorale :
Sciences Pour l'Ingénieur (SPI)

Equipe de recherche, Laboratoire :
Laboratoire de Thermique, Ecoulement, Mécanique, Mise en Production (TEMPO)

Mécanisme d'initiation du collage lors du laminage à chaud des aciers inoxydables ferritiques stabilisés

JURY

Président du jury
- Montmitonnet, Pierre. Directeur de Recherches. CEMEF UMR CNRS 7635. Mines ParisTech.

Rapporteurs
- Favergeon, Jérôme. Professeur. Laboratoire Roberval UMR 7337. Université de Technologie de Compiègne.
- Kubiak, Krzysztof. Maître de conférences HDR. School of Engineering. University of Liverpool.

Directeur de thèse
- Dubar, Mirentxu. Professeur. TEMPO Lab. EA 4542, Université de Valenciennes et du Hainaut Cambrésis.

Co-directeur de thèse :
- Dubois, André. Professeur. TEMPO Lab. EA 4542. Université de Valenciennes et du Hainaut Cambrésis.

Membre invité
- Damasse, Jean-Michel. Directeur du Centre de Recherche. APERAM.

Thèse de Doctorat
de l'Université de Valenciennes et du Hainaut-Cambrésis,

Discipline : MECANIQUE numéro d'ordre : 13-42

Ecole doctorale : Sciences Pour l'Ingénieur (SPI)

Equipe de recherche, Laboratoire :
Laboratoire de Thermique, Énergétique, Mécanique et Matériaux, Procédés de mise en forme, Production (TEMPO, EA4542)

Présentée et soutenue par **Emilie LUC**, le 20 décembre 2013, à Valenciennes

Initiation of sticking phenomenon in hot rolling of ferritic stainless steels

JURY
Président de jury

- **Montmitonnet, Pierre**. Directeur de Recherches. CEMEF UMR CNRS 7635. Mines ParisTech

Rapporteurs

- **Favergeon, Jérôme**. Professeur. Laboratoire Roberval UMR 7337. Université de Technologie de Compiègne
- **Kubiak, Krzysztof**. Dr, Lecturer, HDR. School of Engineering. University of Liverpool.

Directeur de thèse *et co-directeur de thèse*

- **Dubar, Mirentxu**. Professeur. TEMPO Lab. EA 4542. Université de Valenciennes et du Hainaut Cambrésis.
- **Dubois, André**. Professeur. TEMPO Lab. EA 4542. Université de Valenciennes et du Hainaut Cambrésis.

Membre Invité

- **Damasse, Jean-Michel**. Directeur du Centre de Recherche. APERAM.

Acknowledgments

I would like first to thank Mr Jean-Michel Damasse and Prof. Laurent Dubar for advising me and encouraging me in the realization of this PhD. I also want to thank them for believing in me and supporting me at each stage of this exciting project.

My gratitude also goes to Prof. Mirentxu Dubar and Prof. André Dubois, respectively director and co-director of this thesis, who supported, advised and supervised me throughout the course of this wonderful adventure.

I would also like to thank the members of the jury, Prof. Pierre Montmitonnet , President of this jury, Prof. Krzysztof Kubiak and Prof. Jerome Favergeon , reviewers, for accepting and taking their valuable time for reading and interesting in this study.

Finally, many thanks to Prof. Jerome Favergeon, Yves Wouters, Ivan Guillot and Bernard Baroux for their advices during long periods of interrogation I crossed.

My gratitude is also addressed to Prof. Maxence Bigerelle that has been always able to communicate his enthusiasm and resignation to the renew challenges that the thesis exercise may involve, as well as the valuable contribution of Mr. Raphael Deltombe, Arnaud Dessis, Jesse Schiffler, Antoine Thépenier, Didier Vil and Celine Thibaut without whom this work would not have been possible.

Finally, I wanted to acknowledge the cooperation and constant encouragement of the hot strip mill team of Châtelet who guided me, find the necessary materials for different studies, and allow me to advance in the understanding of sticking phenomenon. A big thank to Mr. Frédéric Mazurier, Yves Delpature, Didier Lemaire, Pierre Aubry and Pierre Pagnoule who contributed to this work thanks to their technical expertise, openness and willingness.

To Elliott,
To my parents and my brother.

Content

Acknowledgments 3
Introduction 9
CHAPTER 1 - FERRITIC STAINLESS STEELS 13
A/ Metallurgical description of ferritic stainless steels 13
B/ Production process of ferritic stainless steels 20
C/ High temperature oxidation of ferritic stainless steels 31
D/ Sticking defects on ferritic stainless steels 40
E/ Discussion on sticking phenomenon 52
CHAPTER 2 - ROLL ROUGHNESS EVOLUTION 53
A/ Working roll change strategy: 53
B/ Replicas on working roll: protocol and analysis 56
C/ Observation of replicas topography 64
D/Characteristic dimensions of HSS scratches 72
E/ Conclusion on scratches as nucleation sites of sticking 88
CHAPTER 3 - REALISATION OF A HOT ROLLING PILOT DEDICATED TO STICKING PHENOMENON 91
A/ Strategy to study friction according to industrial conditions of contact 92
B/ “Windows” of Process mechanical parameters 93
C/ Design of the hot rolling simulator 101
D/ Pilot validation 107
E/ Conclusion 109
CHAPTER 4 - OBSERVATION OF FERRITIC STAINLESS STEELS OXYDE LAYER 111
A/ Thermo-mechanical behaviour of strip specimens 111
B/ Scale layer fracture of ferritic stainless steels during rolling 115
C/ Observation of roll specimens 125
D/ Conclusion on roll scratches as initiation sites for sticking phenomenon 135
Conclusion and outlooks 137
References 141
APPENDIX 1 – HSS microstructure – Size of precipitates 147
APPENDIX 2 – ROUGHNESS PARAMETERS 148

Introduction

The development of stainless steel on a large scale occurred in the 1970's with the deployment of household appliances (such as washing machines, cutting tools…) resulting in an increase of austenitic stainless steel production in Europe. For many years, the use of stainless steel was essentially based on the use of one major grade: the 304 (also called 18-10 or Fe-18Cr-10Ni) which is still dedicated to all applications related to food industry.

A second step in stainless steel production increase occurred in the 1990's with the deployment of exhaust lines made of ferritic stainless steel. Ferritic stainless steel being selected due to their high corrosion resistance up to high temperatures (900°C) and high mechanical resistance (creep, and minimization of exhaust line weight). Compared with austenitic stainless steel, the major difference of ferritic stainless steel is that they don't contain Nickel, so, compared to the austenitic stainless steel, ferritic stainless steel prices are not impacted by the high volatility of Nickel price on the stock exchange. Therefore the use of ferritic grade combines not only technical advantages but also an economic one which is essential for car manufacturers.

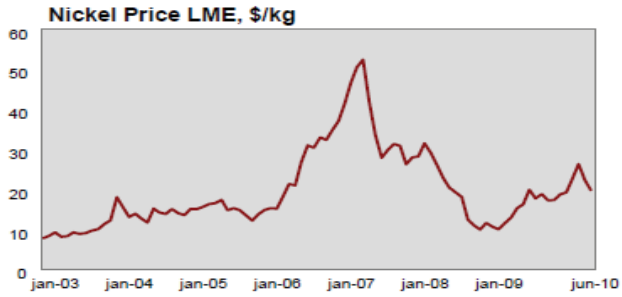

Source : INSG, LME, WorldBank, USGS, Laplace Conseil analysis

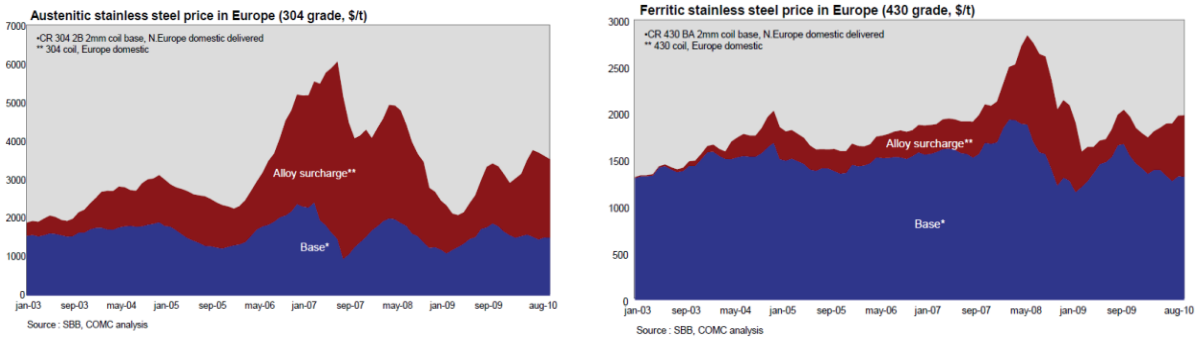

Figures 1, 2 and 3: Evolution of Ni price, and price of austenitic and ferritic stainless steels

The evolution of engines (new fuels, new engine technologies …) induces a modification in combustion parameters and the major modification results in an increase in exhaust gas temperature. As a result, we need to design new grades with higher corrosion and creep resistance. The design of a new grade is made by changing the rate of definite chemical elements known for their impact on corrosion and mechanical resistance.



Fig. 4: Examples of ferritic stainless steel applications [ISSF1]

Firstly, Chromium is known for increasing drastically the corrosion resistance. It is used in ferritic stainless steel, at a corresponding rate from 11 to 22 %wt. Molybdenum added to Chromium confers also a higher corrosion resistance.

The stabilizing elements such as Titanium or Niobium are used for two reasons:

- Added to steel which contains Carbon and Chromium, they prevent from chromium carbides formation (responsible for intergranular corrosion).
- They increase the creep resistance at high temperature by forming precipitates reducing the grain boundaries displacement.

The design of such new grades induces new challenges in their production. In cold phases, as well as in hot phases of the production, these high alloyed steels have different behavior compared to the standard ferritic grade (430 – Fe-18Cr).

In the production of hot rolled flat products, we are confronted to new defects only occurring on the grades containing more than 17% Chromium which dramatically affects the surface quality. This defect leads to a constellation of incrusted particles on the sheet surface that cannot be removed in the cold phase production.

The presence of this defect will induce two major problems during the working life of the product:

- The product cannot be used on high surface quality market (with high esthetic requirements).
- The product will corrode preferentially on the incrusted particle area leading to a decrease in the product life.

This defect affects variably the different grades, but for some grades, 100% of the coils produced are concerned with and it results in limiting the development of the whole range of high alloyed ferritic stainless steel on other metallurgical defects representing an annual stake of around 1.5 million Euros.

The aim of this work is to understand the conditions leading to the initiation of sticking phenomenon, in order to define the industrial set of parameters that will be used to suppress the defect, especially on products dedicated to high surface quality standards.

The incrusted particles are formed in the finishing mill of the hot strip mill line and are due to a sticking phenomenon influenced by process parameters such as temperature, type of antagonists, reduction that were already examined in past studies and resumed in the first chapter.

Some past studies highlight that roll surface is the key parameter explaining the initiation of this sticking phenomenon. We decided to investigate the roll roughness evolution in order to check if roll grinding or/and wear could be improved to suppress the sticking phenomenon. Roll study will be performed in chapter 2.

Nevertheless, impact of rolling parameters has to be known and adjusted in order to fix industrial line configuration, which is not always very easy because of the mechanical, metallurgical and cost constraints. Moreover, most of these parameters are interdependent (reduction, rolling speed and temperature) on the industrial line and to find the optimal set of parameters has to be determined using a pilot that allow us to test the effect of these parameters separately. That is why we had to design a rolling pilot able to reproduce the finishing mill contact conditions, which is presented in chapter 3.

Finally, a design of experiments will be carried out. The effect of temperature and reduction ratio will be evaluated on friction coefficient and oxide morphology evolution. It will help us to check the role of roll surface and also note the importance of oxide layer behavior. The main interest of this study is that the design of the rolling pilot will allow to use specimens directly extracted from industrial surface and so to be close to the industrial conditions, compared to conventional disc-on-disc tribometers.

CHAPTER 1 - FERRITIC STAINLESS STEELS

This chapter deals with the presentation of the context of the study. Ferritic stainless steels are first presented with the influence of each additional element, such as chromium, titanium and niobium, on the formation of precipitates. On a second part, the hot rolling process is described highlighting the main process parameters such as temperature, nature of antagonists and reduction ratio.
On a third part, the oxide scales formed on the industrial strips are observed and analyzed, showing an interesting presence of specific oxides, different from the ones mentioned in literature.
Finally, sticking defects are described and the last research works on the initiation of the sticking phenomenon are presented.

A/ Metallurgical description of ferritic stainless steels

1 – Matrix microstructure and phase transformation

A ferritic stainless steel contains at least 10,5% Cr and a low content of Carbon (<0,02%).
Ferritic stainless steels have a ferritic matrix (centred cubic type structure) from room temperature up to its fusion temperature (α phase).

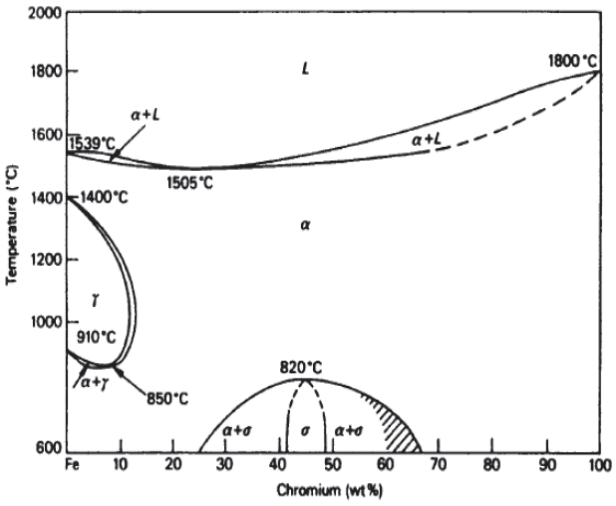

Fig. 5: Fe-Cr phase diagram [LAI09]

On the Fe-Cr phase diagram on the left (Fig. 5), we notice that between 13% and 25% Cr, the grade has a monophased ferritic structure from room temperature up to fusion domain. If the Cr content is below 13%, austenite (γ phase) appears at high temperature. When the Cr content is higher than 25%, the σ phase appears at low temperature (below 800°C). This phase has a fragile behaviour that can be very detrimental for the product despite the precipitation kinetic is low.
On grades with more than 3,5% Mo and 17% Cr (Fe36Cr12Mo10), Chi (χ) phase may also appear under 980°C.

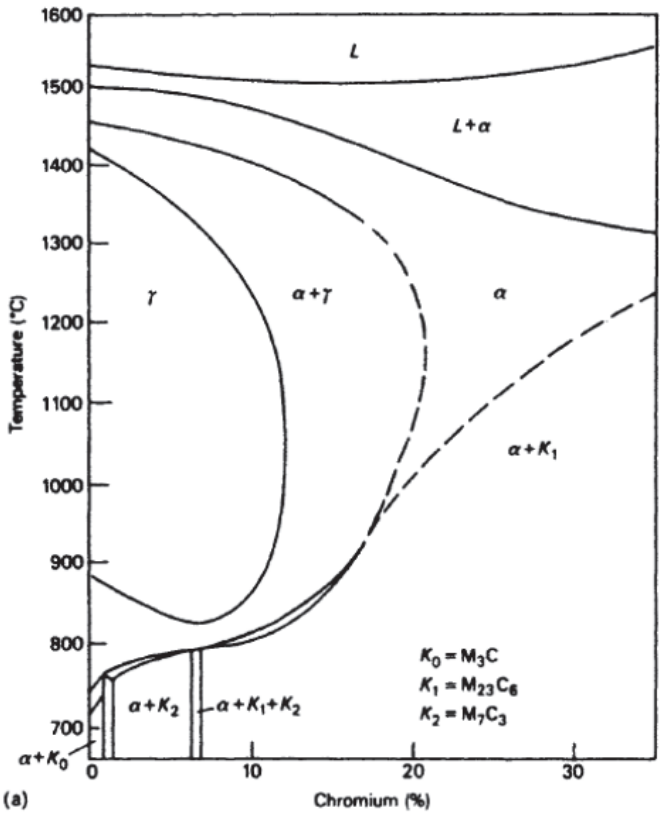

Fig. 6: Effect of 0,05% C on Fe-Cr phase diagram [LAI09]

Presence of interstitial elements such as C and N has two main consequences:

- C and N are gammagene elements that are increasing the gamma domain and also the α + γ domain with higher Cr content (Fig. 6).
For instance, the reference ferritic grade (AISI 430) which is composed at 16% of Cr and (C+N) about 0,08 % has 30% austenite at high temperature.

- C and N have a low solubility in ferrite phase. It induces the formation of $(Cr,Fe)_{23}C_6$ type carbides and Cr_2N nitrides at temperatures below 900°C. The formation of these chromium carbides occurs at grain boundaries and induces chromium depletion around the carbides. As a result, the formation of these chromium carbides is at the origin of a sensitized area where intergranular corrosion becomes possible when the steel is exposed to a corrosive environment.

2 – Precipitation and stabilisation

In order to avoid this sensitization phenomenon, we use stabilizing elements by forming nitrides and carbides that are more stable than chromium carbides and nitrides.
On the graph below (Fig. 7), we can list many elements that are more stable than chromium carbides and nitrides.

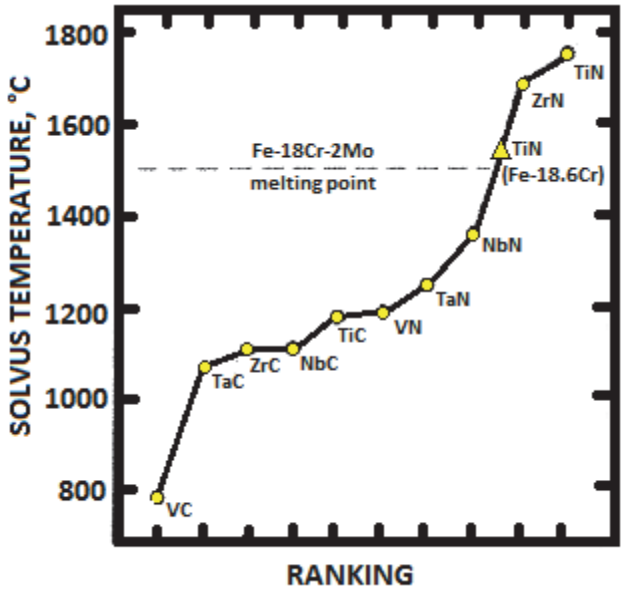

Fig. 7: Solvus in Fe of MX composites in grade Fe-18Cr-2Mo [GAT87]

Ta is not used because this element is rare and expensive.
V is rarely used because of its slow diffusion kinetic. As a result, Zr, Ti and Nb are essentially used as stabilizing elements in ferritic stainless steels.
These elements are associated to C and N to form carbides, nitrides, and carbo-nitrides, faster than Chromium carbides (to prevent intergranular corrosion). Excessive Nb (in solid solution) can react with Fe and form Laves phases (Fe_2Nb and Fe_2Nb_3), reducing creep phenomenon, useful in exhaust applications. [MIT11]
Ti and Zr can also be associated to P and S to form intermetallic phases. [LAI09]

2.1 - Ti stabiliser:

The minimal content of Ti in a 17% Cr (+ <1% Mo) ferritic stainless steel is defined by the Strauss test evaluating the intergranular corrosion resistance at various (C+N) content. The condition revealed by the test is that we have a good corrosion resistance when:

$$Ti > 0{,}15 + 4(C+N) \qquad \{1\}$$

In practical case, the grades are defined with a higher content of Ti than the Ti content predicted by equation 1 in order to be sure to completely stabilise the product.
As a result, we define the excess of Ti (in solid solution) using the following formula:

$$\Delta Ti = Ti - (48/12)C - (48/14)N \approx Ti - 4(C+N) \qquad \{2\}$$

(Where 48, 12 and 14 are the respective atomic masses of Ti, C and N)

For the AISI 409 grade, which contains only around 11% Cr, another formula is used: $Ti > 6(C+N)$. {3}
Adjunction of Ti leads to the formation of different types of precipitates: Titanium nitrides, Titanium carbides, and Titanium sulphides mainly.

211 - Titanium Nitrides (TiN):

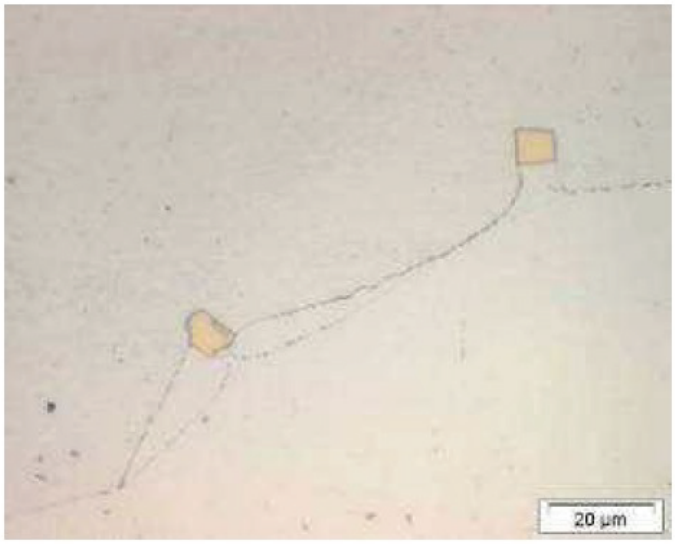

Fig. 8: TiN precipitates at the grain boundaries of a 409 grade [LAI09]

They precipitate at the liquid state and finish precipitating in the solid state.

Precipitation formulas [CHA84] :

$$Ti + N \rightarrow TiN$$

- in liquid steel:

$\log_{10}(Ti)(N) - 0{,}474(Ti) - 1{,}8(N) - 0{,}025(Cr) = -19800/T + 7{,}78$ {4}

- in ferrite :

$\log_{10}(Ti)(N) - 1{,}354(Ti) - 36{,}01(N) - 0\ {,}0094(Cr) = -17611/T + 5{,}18$ {5}

TiN generally have a big size (> 1µm) and are angulous (cubic form; cubic centred face structure) and appears generally in yellow on micrographic observations. (Fig. 8)
TiN is stable (not modified) during the hot rolling process.
The spatial repartition is uniform and they are generally surrounded by TiC (and TiS). They germinate on oxides. The presence of these precipitates induces a limitation on the grain growth at high temperature on grains bigger than 100 µm by blocking the grain boundaries (Fig. 8). As a result, they can be at the origin of structure defects (slow down of recrystallization), also major surface defects and advance wear in contacts.

212 - Titanium carbides (TiC):

TiC precipitates around 1100°C with a maximal speed at 1000°C. Precipitation is extremely fast (in few seconds). These precipitates are soluble between 1050°C and 1200°C. Nevertheless, the totality of TiC formed during the slab casting is not completely solubilised during slab reheating on hot rolling process. These precipitates can be observed easily at several steps on product surface and can induce surface defects as reflectance heterogeneities.

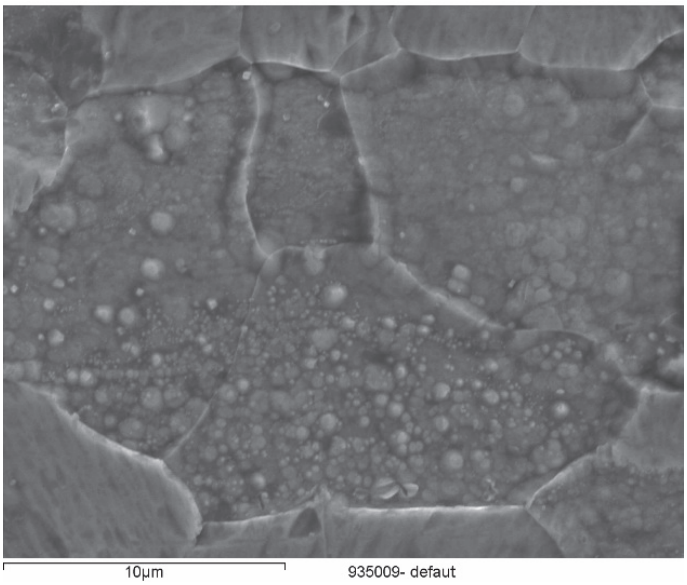

Fig. 9: TiS on annealed and pickled product surface of a AISI433 grade [HER09]

Precipitation formula on 15 – 25% Cr alloys [CHE84]:

$$Ti + C \rightarrow TiC$$

$$\log_{10}(Ti)(C) = -9000/T + 3,7 \quad \{6\}$$

The size of these precipitates is from a few 100 nm to a few µm and they are located in the grains and on grain boundaries (Fig. 9). The shape of these precipitates is globular, sometimes elongated.

213 - Titanium sulfides (TiS, Ti2S) and carbo-sulfides (Ti4C2S2) :

They start precipitating at the end of solidification process in the S and Ti enriched areas. As for TiN, they are not modified during the hot rolling step. Such precipitates are more stable than MnS or Cr_xS_y that can induce the sensitization phenomenon.

214 - Titanium Phosphides (FeTiP) :

They start precipitate between 600°C and 900°C, with a maximal kinetic around 800°C. The precipitation occurs at the beginning on grain boundaries and later, in the grains. The size is around a few 100 nm up to a few µm. The shape looks like shells or globules at the grain boundaries, in the grains or attached to other precipitates (such as TiC).

22 - NB STABILIZER :

For 17% Cr grades stabilised with Nb, the stabilisation formula is [BAR80]:

$$Nb > 0{,}20 + 5(C+N) \qquad \{7\}$$

If the grade contains C and/or N, Niobium carbonitrides Nb(C,N) are formed. It implies that the corresponding formula is:

$$Nb > A + 7(C+N) \qquad \{8\}$$

$$\text{with } A \approx 0{,}1$$

$$\Delta Nb = Nb - 93/12C - 93/14N \approx Nb\text{-}7(C+N) \qquad \{9\}$$

221- Niobium carbonitrides - Nb(C,N):

Carbonitrides start precipitate at 1150°C with a maximal kinetic at 1050°C. The precipitation kinetic is around a few seconds, which means a quench is not sufficient to prevent precipitates forming. The solubilisation starts between 1025°C for ΔNb=0,1% and 1100°C for ΔNb=0,4%. The Nb(C,N) stoechiometry is not constant, so, there is no reliable data on the solubility product. The shape of these precipitates are like coarse sticks; the corresponding length is about a few microns on black coils.

222 - Intermetallic phases FexNby and precipitates Fe3Nb3X type (X=C, N or O):

The solubility of Nb in the ferrite phase is smaller than those of Ti. As a result, the excess (ΔNb) will precipitate on two ways:
- a Lave phase Fe_2Nb (hexagonal structure)
- an undefined phase which can be an intermetallic Fe_2Nb_3 or a Fe_3Nb3X typ with X for N, C or O. (cubic structure)

These phases precipitate around 950°C with a slow kinetic (around one hour) – therefore during the cooling of the black coil after the hot strip mill. They will not participate to our study.

23 - THE SPECIAL CASE OF BI-STABILISED GRADE: 441 GRADE [SEL10]

The AISI 441 grade is a bi-stabilised grade which means that the grade is stabilised by Nb and also Ti. The origin of this grade was the result of an addition of Nb on a Titanium stabilised grade in order to increase the creep resistance on exhaust lines (by intergranular precipitation of Fe_2Nb)

The bi-stabilisation is a way to decrease the TiN size (to prevent from metallurgic and surface defects) but keeping the benefits on the sensitization phenomenon. Precipitation starts by the formation of TiN, which are suppressing the Nitrogen which is in the solid solution. Then, NbC start precipitating and Ti can be included in them (depending on the residual quantity of Ti which didn't precipitate in TiN). Finally, at lower temperatures, Laves phase (Fe_2Nb) appears.

The main differences with the (Ti) monostabilised grades are that:
- Nb(C,N) is replaced by NbC,
- there is no Fe_2Nb_3 or Fe_3Nb_3X type phase.

Two cases need to be examined:

1- There is not enough Ti to catch N totally: $Ti \leq 4N$:

$$\Delta Ti = 0 \text{ and } \Delta Nb \approx Nb + 7/4\ Ti - 7(C+N) \rightarrow \quad Nb + 7/4\ Ti > 0{,}1\% + 7(C+N) \qquad \{10\}$$

2- There is enough Ti to catch all N content and the half of the C content: $Ti > 4N + 2C$:

$$\begin{cases} \Delta Ti \approx Ti-4N-2C \\ \Delta Nb \approx Nb-3{,}5C \end{cases} \qquad \{11\}$$

The rest of C will be precipitated into Niobium Carbides.

3 – Conclusion

The AISI 441 is a very particular grade in terms of precipitation because the density of precipitates is quite high compared to other conventional ferritic stainless steel alloys. Moreover, these precipitates are mainly composed of NbC and TiN. TiN are particularly hard and angulous particles mainly responsible for abnormal wear in contacts. The role of NbC in tribological issues was not clearly exposed in bibliography. (Fig.10)
This study, based on sticking phenomenon, will be performed on this grade because, it was confirmed by hot rolling plants that this grade is the most sensitive to sticking phenomenon.

AISI	C	Si	Mn	P max.	S max.	N	Cr	Cu	Mo	Nb	Ni	Ti
441	< 0,03	< 1,0	< 1,0	0,040	0,015	-	17,5 - 18,5	-	-	0,3 - 1,0	-	0,10 - 0,60

Fig. 10: AISI441 Chemical composition (% mass.)

B/ Production process of ferritic stainless steels

1 – From the melting shop to the hot rolling

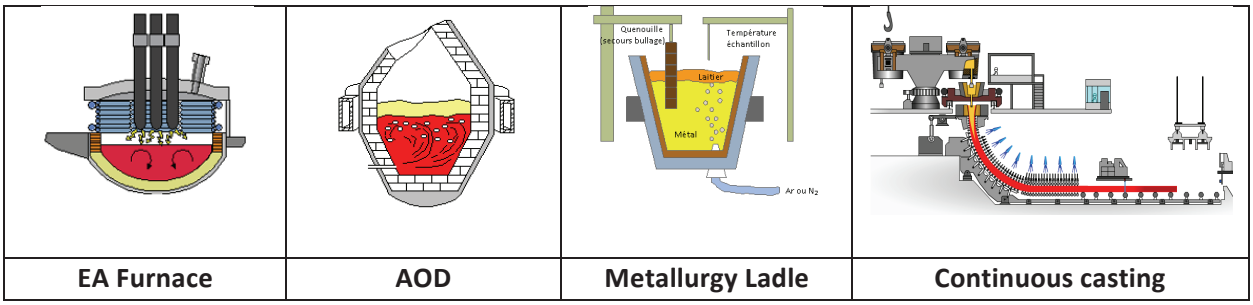

EA Furnace	AOD	Metallurgy Ladle	Continuous casting

Fig. 11: Melting shop scheme [APE00]

To produce stainless steel, scraps and ferroalloys are melted in an electric arc furnace (we don't use coke plant nor blast furnace). (Fig.11) When the metal is in the liquid state, it is transferred to a converter (AOD or VOD) where alloying elements are introduced to adjust the chemical composition and on which argon and oxygen are blown in order to decrease C and S contents and form the slag.
Then, the metal is transferred to the metallurgy ladle where the exact composition is determined by adding the final rate of alloying elements and the casting temperature is reached.
Finally, the metal is transferred to the continuous casting machine where liquid metal is solidified into a parallelepipedic slab having a width of 2 meters, a thickness of 200 mm, and a length of 18 m. Each slab is around 25 tons in weight. The slab cools slowly in the air and can enter cold in the hot strip mill or at up to 400°C.

2 – General description of the hot rolling mill

The hot strip mill line of APERAM Europe (also located in Châtelet) rolls the whole production of this company. The production is essentially composed of stainless steel : austenitic, ferritic, martensitic and duplex, but the line also rolls high alloyed special steels such as Invar®, and all Imphy alloys (Superimphy®, Phytime®, Durimphy®…). Currently, no carbon steels are processed on this line.

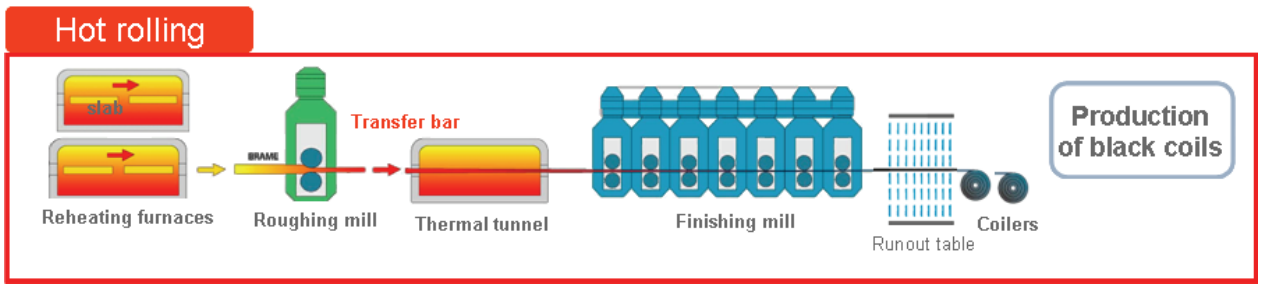

Fig. 12: Hot rolling mill scheme [APE00]

The line (Fig. 12) is composed of:

- 3 reheating walking beam furnaces which reheat the ferritic slabs from either ambient temperature or from 150°C up to 1200°C in 3 hours. The production capacity of each furnace is around 300 t/h. Both furnaces run on natural gaz.
- An hydraulic descaling box is used to descale all slabs at 140bars water pressure.
- A reversible roughing mill composed of one vertical stand (edgers) able to master the slab width and one horizontal and reversible stand which decreases the slab thickness from 200 mm to 40 mm at 1100°C. The vertical stand is equipped with a 1775 kW engine and the horizontal stand is motored by two 5800 kW engines. The maximal rolling force is around 5000 tons.
- A 60 m thermal tunnel made of 15 active panels (natural gas burners + refractories) which help to limit the thermal loss of the transfer bar before entering in the finishing mill.
- A crop shear that cuts the tail and the end (extremities) of the strip in order to be able to weld the strips between them in the cold lines.
- A seven stand tandem mill which reduces the transfer bar from 40 mm to 3 mm on average at 1000°C and 7m/s. The total power is about 63 000 kW and the maximal rolling force is around 4000 tons.
- A 80m run-out table on which the coil can be quenched by water up to very low temperature (<600°C). The maximal flow rate is around 10 680 m^3/h. On ferritic grades, quenching (by water) is not used.
- 2 down coiler which coil alternatively the strips rolled by the finishing mill.

3 - Description of the finishing mill:



Fig. 13: Châtelet finishing mill

The technology of hot rolling mill (Fig. 13) is quarto which means that each stand is composed of two working cylinders that are in direct contact with the product and two backup rolls that are used to support severe stresses by reducing deflection. The roughing mill is reversible stand and the finishing mill is a seven stands tandem: it means that the strip is trapped in the seven stands at the same time. The product is rolled only once using seven successive reductions.

At the entry, the strip is around 40 mm thick and at the exit, the strip is around 3 mm thick. The reduction in thickness results in an increase of strip speed (by conservation of metal flow rate) that can reach up to 10 m/s. The horizontal stand is maintained in position by hydraulic screws and allows an accurate control of strip thickness as well as fast adaptation of rolling forces repartition between the stands. The only temperature measurement of the strip is made at the exit of the finishing mill to know the rolling temperature. All other temperatures are calculated by the automate (supervision) that is physic and statistics based. As a result, the initial setup of the finishing mill is only based on the transfer bar temperature (operated on the roughing mill) and the statistical base of the supervision. Sometimes, a gap in temperature can be noticed between the forecasts and the rolling temperature, therefore, in order to prevent the first stand from damages, the Automatic Gauge Control (AGC) adapts the reduction schedule to avoid reaching the maximal rolling force on each stands. That is the reason why there is no conventional rolling pass schedule on tandem finishing mills.

To maintain the tension of the strip between the different stands and absorb the flow rate variations, motorized arm loopers (Fig. 14) keep the strip constant tension between each stands. This results in a tension and back tension on the intermediate stands.

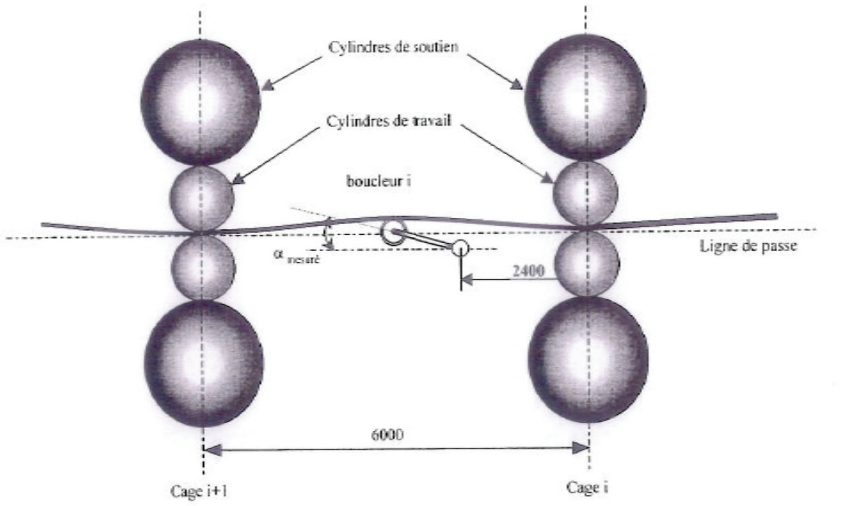

Fig. 14: Looper between stands N and N+1

4 – Working rolls:

There are two types of working rolls used in the finishing mill:
- HSS (High Strength Steel) grade located in stands F1, F2, F3, F4.
- ICDP (Indefinite Chilled Double Pour) grade which is a cast iron cylinder located in stands F5, F6 and F7.

The global quantity of working rolls available on the hot strip mill for stainless steel production represents 73 HSS type rolls and 57 ICDP type rolls delivered by different suppliers. The life of a working roll in one stand is around 1,5 year. A new cylinder is firstly dedicated to F2 stand, then with the gradual reduction of its radius (with wear and grinding) is used in F1, F3, and F4.

Upon receipt, the working rolls are accompanied by a certificate which indicates the main technical characteristics such as chemical composition of the external shell of the roll, the hardness depending on

the width, and the main dimensions of the cylinder (initial diameter, dimensions of necks and barrel) , and the total weight. No specific data per roll on microstructure are given to steel producers.

Nevertheless, some detailed studies are available on HSS and ICDP grades and we will focus on the study of HSS grade in next paragraph.

41 – COMPONENTS OF A WORKING ROLL

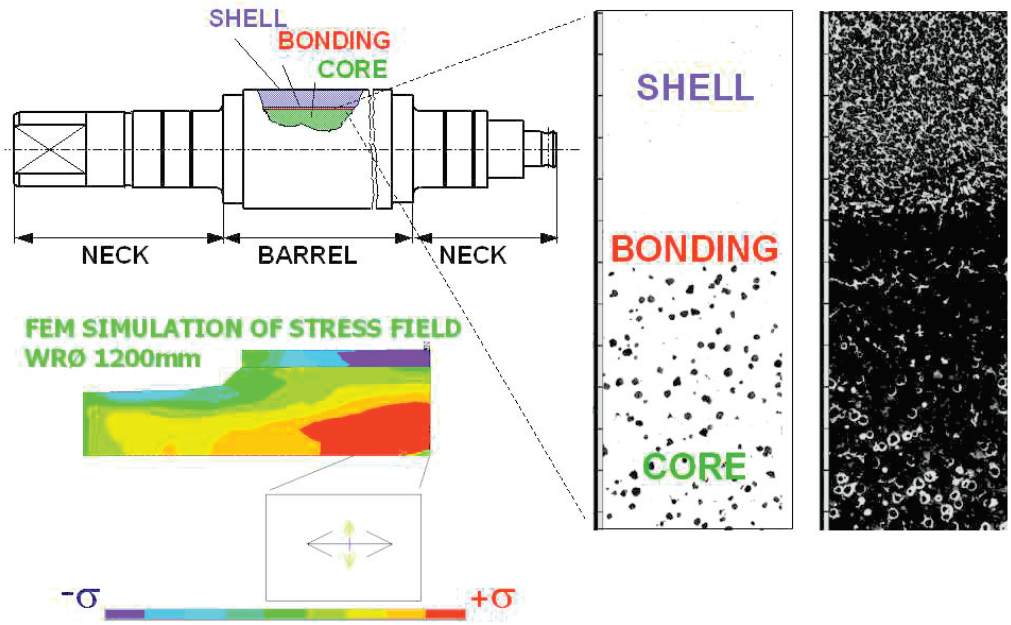

Fig. 15: Components of a working roll [ZIE07]

A working roll is composed of two parts (Fig. 15):

- The core of the roll and the extremities of the cylinder. The extremities of the roll will be machined in the form of pins that will be attached to rings and chocks to be mounted on the frame of the stand. The core of the roll provides the mechanical integrity of the device under high loads. The core must have a high strength but also a high resistance to fatigue. It is usually made of cast iron.

- The shell of the roll is the external part of the cylinder and corresponds to the wear area that will be in contact with the product and will be ground at the end of each production schedule. The shell gives the surface characteristics of the product (quality) and is subject to strong constraints: a high thermal fatigue, local high mechanical stresses, high levels of friction associated with the passage of the product, regular mechanical shocks due to the passage of the ends of bands or processing damages (strip tearing).

The shell of the rolls is composed of a matrix which nature is different depending on the grades produced on the mill, and carbides with various composition, sizes and positions in the matrix. The mechanical properties and hardness of these components contribute to the mechanical strength and wear behaviour of the working roll.

The matrix imposes the general mechanical properties (strength, hardness, resilience) of the cylinder and plays a key role in the ability to retain the hardest carbides. The grain size of the matrix has an influence on the distribution of the carbides and on mechanical properties.
Carbides impose the wear resistance and the surface quality of rolled products.

42 - CHEMICAL COMPOSITION AND MECHANICAL RESISTANCE OF THE SHELL

Depending on suppliers, the chemical composition of rolls may vary significantly even for a precise type of roll. Data sheets and certificates supplied with the cylinders do not collect sufficient information to guess the microstructure of the shell. This is why a chemical analysis performed by the steel producer is needed to gather information that allow comparing them and helping suppliers and steel producers to understand the link between the quality of the product surface, the wear resistance and the nature of the roll. However, chemical analysis of cylinders is a destructive process that is not allowed.

Different data and chemical compositions indicated on data sheets and measured on roll samples after a roll break are reported in Tab 1 and 2.

Tab. 1. HSS working roll composition used by APERAM

Elément Repère	C ppm	Mn %	P %	S ppm	Si %	Ni %	Cr %	Cu %	Mo %	Nb %	V %	Ti %	Co %	Sn %	N ppm
Cylindre HSS issue LAC	19000	0.93	0.041	150	0.65	1.54	4.38	0.13	5.38	0.032	5.17	0.006	0.015	0.005	530

Tab. 2. ICDP working roll composition used by APERAM

Elément Repère	C ppm	Mn %	P %	S ppm	Si %	Ni %	Cr %	Cu %	Mo %	Nb %	V %	Ti %	Co %	Sn %	N ppm
cylindre ICDP	30000	0.90	0.023	24	0.76	4.28	1.90	0.14	0.31	0.14	0.12	0.005	0.014	0.011	120

HSS (High Strength Steel) rolls are used as working rolls in the roughing mill and the finishing mill first stands. HSS rolls have different compositions depending on the roll use: whether the cylinder is for roughing or finishing. The content of elements that will generate carbides (Mo, V, W) is more important on HSS than on the other grades and their content varies depending on the roll, which is a consequence of carbides growth. The HSS cylinders have 5% Cr against 2% for ICDP rolls.

The ICDP (Indefinite Chill Double Pour) cylinders have high levels of C and Ni.
In most cases, the matrix of the shell is a martensitic structure. This structure allows achieving high strength values. The overall hardness indicated on the HSS type roll is HV 750 [WOO99].

Local matrix hardness of HSS is generally lower than hardness of the overall shell (25 points higher) because the overall hardness takes into account the presence of carbides at the surface which hardnesses are very important (see next paragraph). However, the overall hardness of the shell follows the same trend as the evolution of the matrix hardness: the hardness of the matrix is directly related to its Carbon content, which is given by the following equation (%wt):

$$\%C_{matrix} = \%C_{moyen} - \left(0{,}06\%Cr + 0{,}033\%W + 0{,}06\%Mo + 0{,}2\%V\right) \quad \{12\}$$

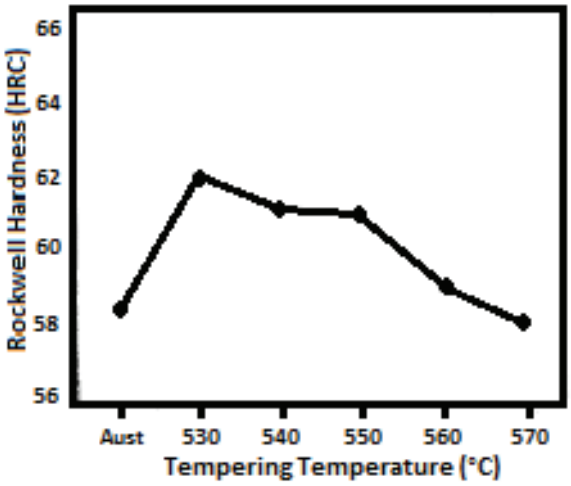

Fig. 16: Evolution of the shell hardness with annealing temperature [KAN01]

At constant chemical composition, hardness of HSS may vary depending on the tempering temperature of the roll performed at the end of its manufacturing process. Hardness evolution (Fig. 16) has an extremum at a specific temperature which depends on the chemical composition, and hardness decreases beyond this temperature. So, adjusting the annealing of the roll is a way to adjust its hardness to comply with the specifications of the customer. However, HSS rolls are very fragile. Materials with high hardness are also products with low resilience.

Brutal impact during rolling may seriously damage the rolls by initiating cracks at the interface of the shell and the core of the roll. The rolling speeds are increasing over the stands of the finishing mill, so the probability of shocks is maximal in the lasts stands. In addition, because cracks are initiated at the shell-core interface, the ruin of the cylinder is not instantaneous and can occur after several rollings before emerging to the surface and becoming visible.
It is thus difficult to predict a roll change before the explosion of the shell. This phenomenon does not exist on cast iron rolls, where crack initiation is mostly on the surface (of the shell), allowing a change of rolls earlier, after a fast surface control.

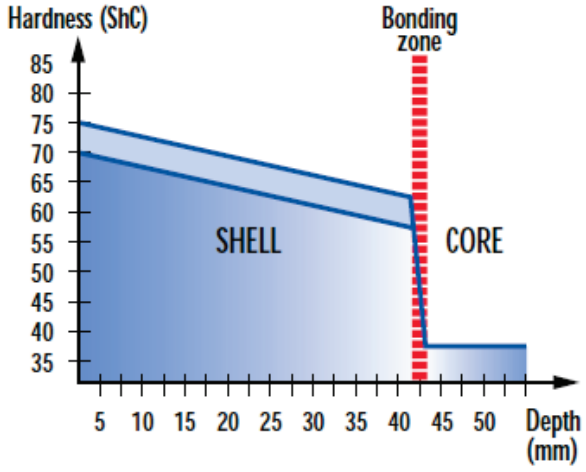

Fig. 17: Evolution of the shell hardness with the radius [MAR13]

It implies the use of ICDP rolls for two (austenitic) to three (ferritic) last stands of the finishing train. ICDP rolls have a mixed martensite / bainite matrix and their specificity is that the chemical composition of the shell varies with the radius. The smaller the radius is, the higher the free carbon content will be (graphite). So, the amount of carbides tends to decrease (Fig. 17). This leads to a decrease in hardness shell with cylinder wear. The decrease of roll hardness leads to a rapid wear and a regular roll change during production schedule. The main consequence is a reduction in productivity and additional cost of consumables.

There is no drop in hardness with decreasing radius on HSS nor Hi-Cr.

Tab. 3. Summary of mechanical properties of different types of cylinders [MAR12]

	ICDP	**HSS**
Tensile strength (Mpa)	350 - 450	800 – 1000
Young modulus (Gpa)	150 - 170	210 - 220
Compressive strength (Mpa)	1800 - 2500	3200 – 3400
Bending strength (Mpa)	600 - 700	1200 - 1500
Ductility (%)	1 – 3	8 - 10

The mechanical properties of ICDP cylinders are lower than those of HiCr, themselves lower than HSS. (Tab. 3.) There are no significant difference between the mechanical characteristics of HSS dedicated to roughing and finishing. The higher the mechanical resistance is, the higher the wear resistance will be. It is therefore expected that the consumption of the roll radius on HSS will be lower than those on ICDP. This is confirmed on the hot strip mill, where we showed that HSS rolls have a service life three times longer than ICDP ones.

43 - CARBIDES: TYPE, SIZE, DISTRIBUTION IN THE MATRIX

ICDP rolls have a double precipitation: they have both graphite and coarse carbides M_3C type (such as Fe_3C (white cementite)) (at the origin of the name "Indefinite Chilled").
The proportion of graphite is between 1 and 3%wt, while the fraction of carbide is significantly greater, between 35 and 45%wt. (Fig. 18)

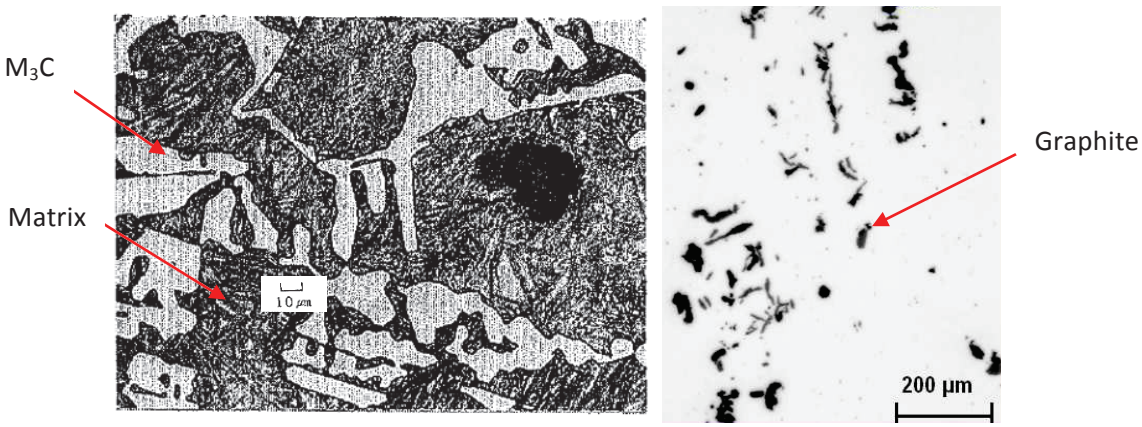

Fig. 18: Metallurgical Structure of ICDP cylinders [MAR13]

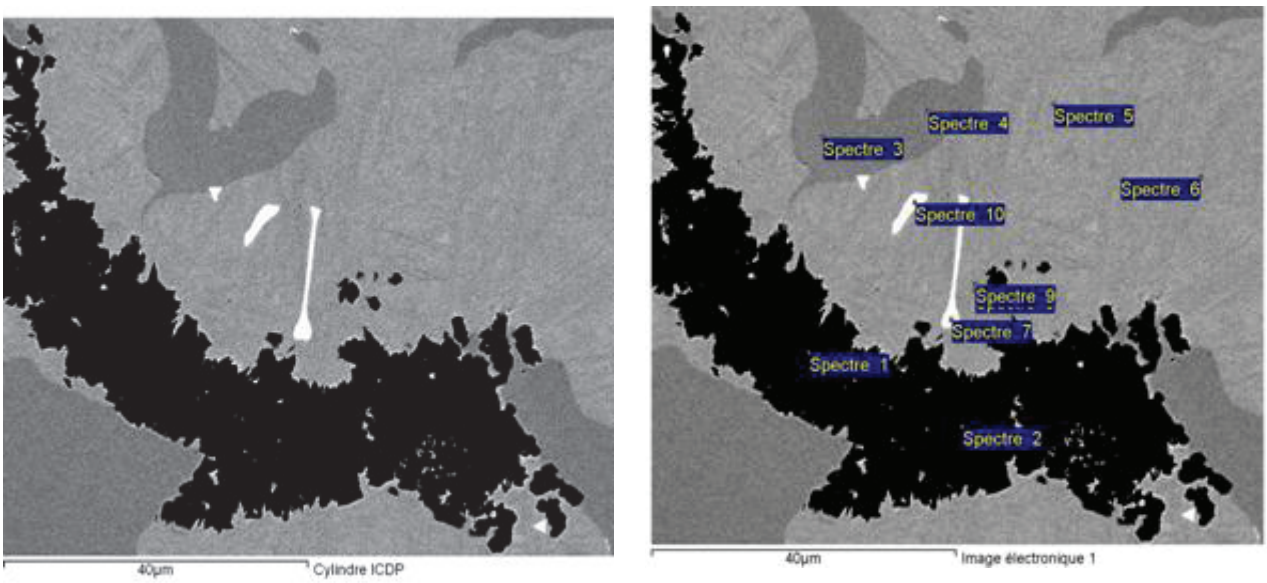

Spectrum	Si	V	Cr	Mn	Fe	Ni	Nb	Mo
Spectrum 1	3,32	0	3,7	0	85,97	0,49	0	11,35
Spectrum 2	3,72	2,68	0,72	5,8	85,74	9,16	0	0
Spectrum 3	0,02	0,44	4,1	1,19	90,91	1,6	0,05	1,69
Spectrum 5	1,16	0,06	1,16	0,94	91,08	5,15	0,06	0,4
Spectrum 10	0,07	2,81	1,01	0,14	4,38	0,33	80,34	10,91

Fig. 19: Identification of precipitates (graphite and cementite) on ICDP grade

Figure 19 represents the microstructure of ICDP rolls used by APERAM. Graphite can be easily identified as the large black particle in the middle of the picture. In the matrix, fine white particles can be also identified and are Nb carbides (spectrum 10). Their size is much reduced compared to the graphite size. There are very elongated and measures up to 15 µm. M_3C carbides are represented in dark grey (spectrum 3) and the light grey is the matrix (spectrum 5).

We analysed the surface of ICDP rolls (Fig. 20 and 21) and noticed that M_3C carbides represents around 30% of the surface which is the most present component after the matrix. Nb precipitates are very rare and represent a surface fraction inferior to 1%.
By difference, the surface fraction of graphite is computed to around 27%, so there is approximately the same surface fraction of graphite and M_3C carbides.

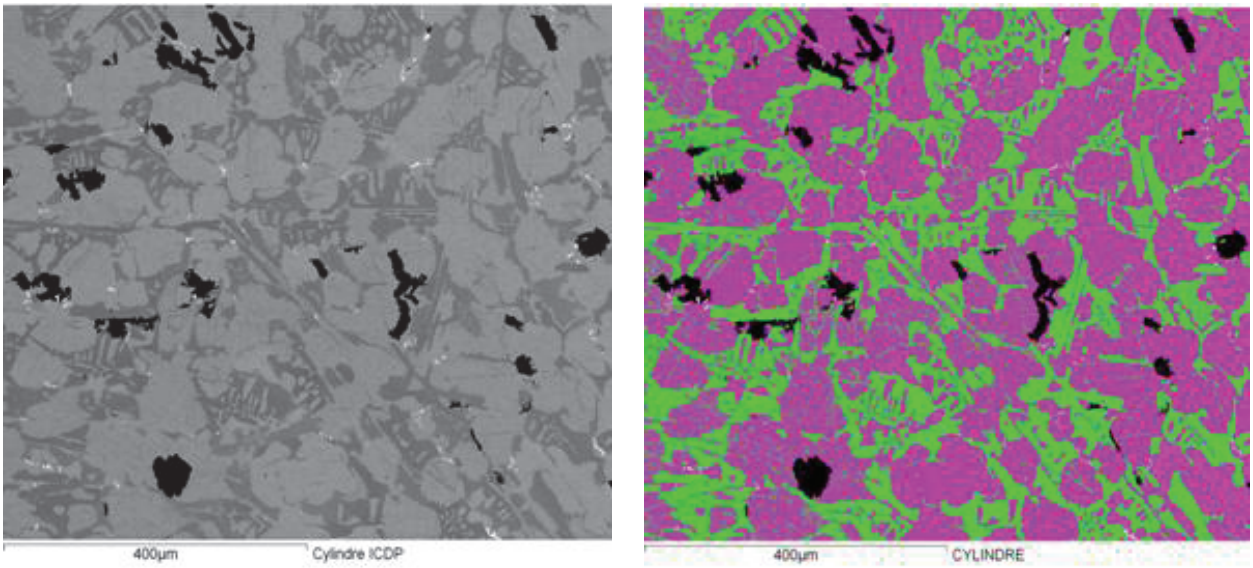

Fig. 20: Microstructure of ICDP rolls

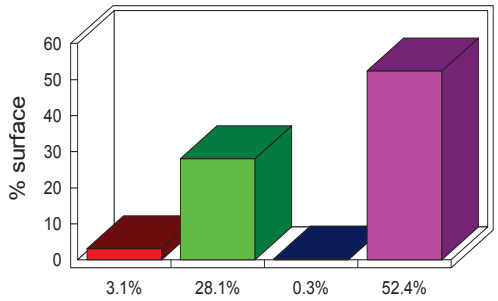

Fig. 21: Surface fraction of carbides

HSS rolls are mainly characterized by the presence of fine hard carbides, allowing on one hand to achieve higher shell hardness and on the other hand, to have higher resistance to wear and oxidation [KAN01]. (Fig. 22)

Carbides results from the addition of elements such as vanadium, molybdenum, tungsten and chromium that have a high affinity with carbon.
M_7C_3 carbides and the molybdenum-vanadium M_6C type are mainly formed along grain boundaries while vanadium carbides of MC type are distributed within the grains (in red on Fig. 22). [ZIE07, SAN92] Chromium carbides located on grain boundaries are identified in blue on Fig. 22.
M_2C carbides (due to the addition of W and Mo) may exist but are often mixed with the M_7C_3 and their fraction is so low that they are most often confused with them.
In the matrix, we can also find some very fine spheroïdal carbides of $M_{23}C_6$ type. (See Annex 1)

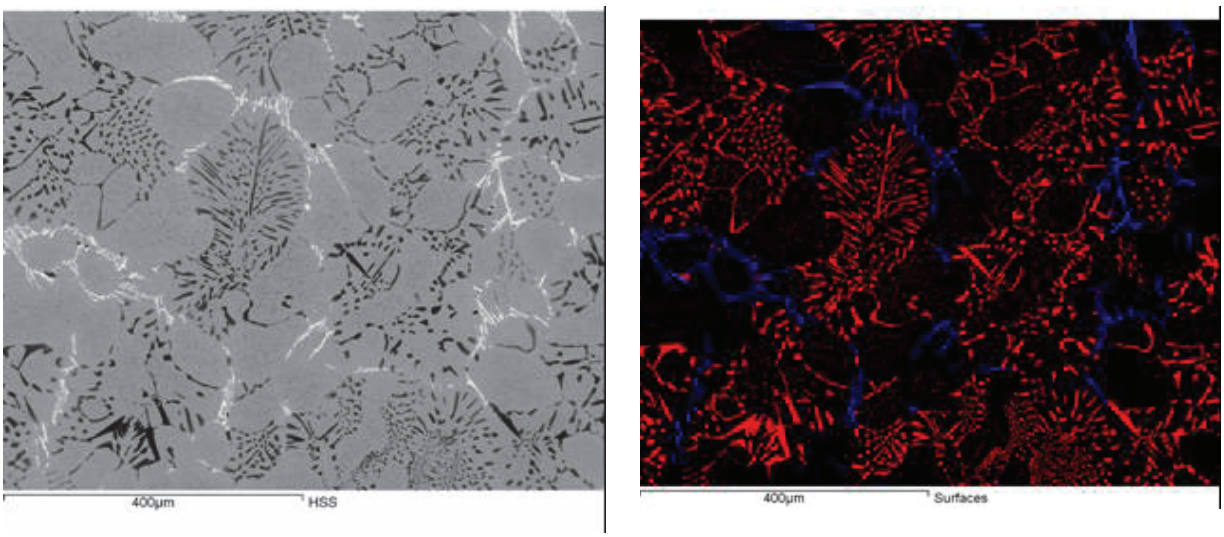

Fig. 22: Microstructure of HSS cylinder

As on ICDP grade, similar investigations were made on surface fraction of carbides for HSS rolls (Fig. 23). Vanadium carbides represent around 4 % of surface fraction. Molybdenum carbides are less present on the surface and reach up to 2,5% of the surface.

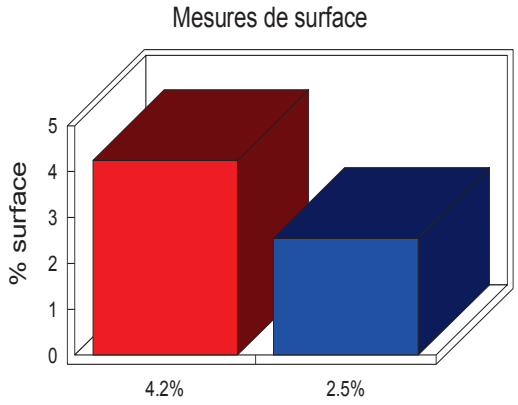

Fig. 23: Surface fraction of carbides on HSS

It was also shown that increasing Cr content (about 8-9%) induced an increase in carbide content of type M_7C_3 carbides and a decrease of MC type, without changing the total volume fraction of carbides which is around 20%. [KAN01] Previously, we saw that the carbides are involved to a lower extent to the increase in shell hardness. In the table below (Tab. 4), which summarizes the hardness values found in the literature [SAN92, KAN01], we found that the hardness of carbides is up to 3 times greater than the matrix. Thanks to their high thermo-mechanical and tribological properties, HSS rolls are the roll type the most represented in hot rolling mills.

Tab. 4. Hardness values of different types of carbides

Dureté	**MC**	**M_7C_3**	**M_6C**	**Fe_3C**
HV [SAN92]	3000	2500	2000	1300
HV [KAN01]	2740	2380		

44 - IMPACT ON THE WEAR BEHAVIOUR

On ICDP rolls, the high amount of graphite present in the roll surface induces a rapid increase in roll roughness, which can degrade the surface quality of the rolled product (Fig. 24). [ZIE09]



Fig.24: Micrographic cut of an ICDP roll after rolling [ZIE09]

The required hardness at 20°C of HSS roll is about 60 HRC. To achieve this level of hardness, tempered at about 560 ° C is required at the end of manufacturing process of the roll.
Disk-on-disk friction tests [KAN02] have shown that the higher hardness of HSS allows reducing wear. (Fig. 25) To a lower extent, the decrease in the Cr content induces a higher wear resistance of HSS rolls. (Fig. 26)

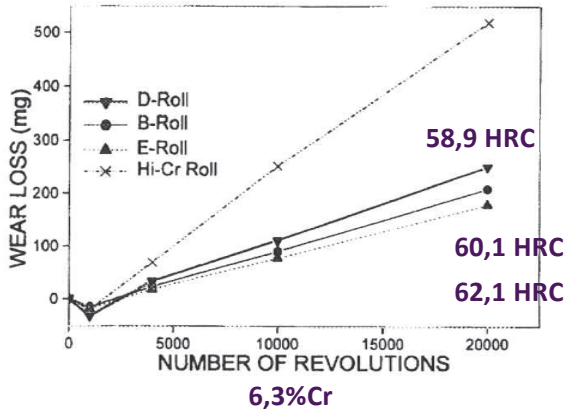

Fig. 25: Effect of hardness on wear resistance [KAN02]

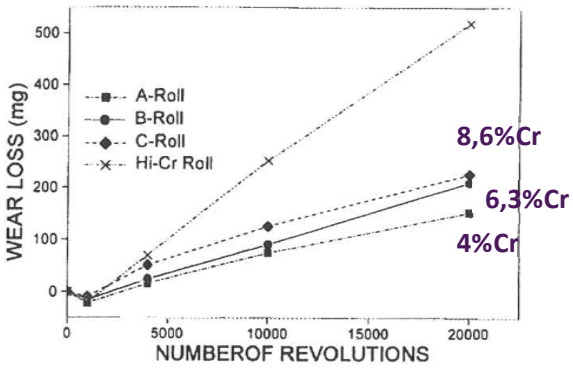

Fig. 26: Effect of Cr content on wear resistance [KAN02]

It was noted that a too high amount of vanadium leads to a higher density of intergranular carbides which induces an increase in surface roughness due to wear of roll matrix [KAN02]. However, the hardness of MC carbides is slightly lower, which limits the wear of matrix and thus postpones the increase of roll surface roughness. Ziehenberger and al. [ZIE07] showed that the wear resistance of HSS roll is up to 3-4 times greater than that of a cast iron cylinder High Chrome, because the volume fraction of carbides is more important in the HSS roll (especially MC type carbides). However, a very high wear resistance leads to a higher surface roughness because the carbides protrude over the roll surface. It increases the friction coefficient and may increase the strip roughness by roughness transfer during rolling. Nevertheless, the mechanism of roughness transfer is not very well known in hot rolling because, contrary to cold rolling, the oxide layer on the product plays the role of an interface between the roll and the product so, oxide layer could limit the roughness transfer from the roll to the cylinder. In the next paragraph, we will present in much more details the oxidation at high temperatures of ferritic stainless steels.

C/ High temperature oxidation of ferritic stainless steels

With the development of ferritic stainless steels in new markets such as solid fuel cells (SOFC) and exhaust lines dedicated to high temperature combustion engine using green fuels, most of data found in the literature concerns experiments performed at service temperature (between 600°C and 900°C for example for exhaust lines) [TOS04, BAM06, HUN07] and particular corrosive atmosphere (sulphuric acid, steam…) [FUJ 64, JIA97].

Nevertheless, few studies are dedicated to the manufacturing process or experiments performed with thermal and atmosphere conditions representing the process conditions. When manufacturing conditions were tested, it was essentially done for short time exposure and temperatures lower than 1100°C. [ISS12]

During hot rolling, scale layer is continuously modified by the process and the following step always inherits of the previous one. As a result, it is important to understand the evolution of scale all along the hot rolling. In next paragraph, a synthesis of the main results from the literature will be exposed.

1 – Different oxidation regimes in hot rolling

11 – Initial oxidation after continuous casting

When the slab comes to the reheating furnace, the surface of the product can be oxidised or ground. This initial oxidation occurs during slab cooling in the continuous casting. The oxidation conditions are not very well known: the slab is initially cooled by water jets in the secondary cooling of the casting and after some minutes in the air without any control of the air temperature or humidity.

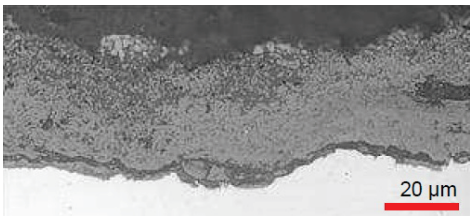

Fig. 27: Initial scale layer on AISI 445 slab [MAL09a]

The scale layer on ferritic stainless steels after the continuous casting is relatively thin, around 35 µm, and is protective. The thickness of the scale layer is relatively homogenous. (Fig. 27)

SEM examinations (Fig. 28) highlighted that there are different strata in the scale. The external part is more porous and essentially composed of iron oxides, such as Fe_3O_4. The external part is impregnated with Al, Ca, Na and Mg. These elements are at the basis of casting powder components. This powder is put in the mould to act as solid lubricant and refractory protection. A large crack close to the scale-metal interface (in blue on Fig. 28) divides the scale layer in two parts. The inner part is essentially composed of chromium containing oxides, on 5 µm deep, such as $(Fe,Cr)_2O_3$.

Finally, a very thin and incomplete edging of silica oxide (SiO_2) is located between chromium oxides and base metal. (Fig. 29) Between fayalite and mixed oxides, we can find some rare islands of Nb and Fe oxides; NbO and FeO type were found on AISI 445.

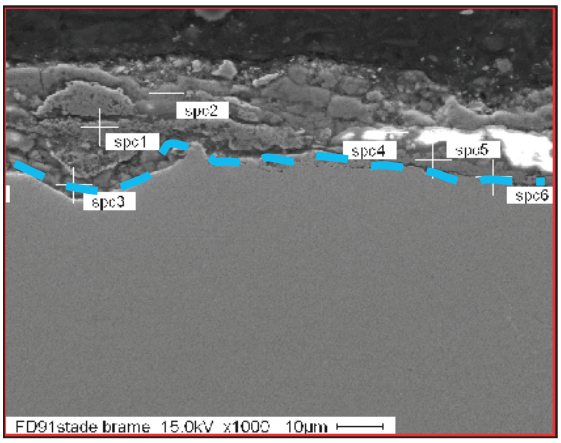

Fig. 28: Initial scale layer on AISI 444 slab [MAL09b]

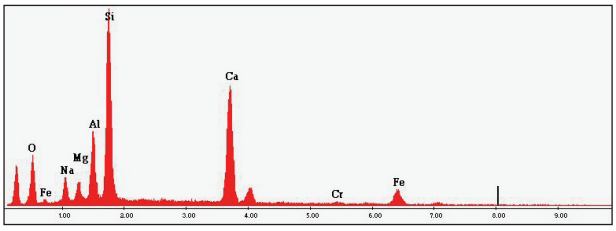

Spectra 1 – 4: Rests of casting powder (Al, Ca, Na, Mg)

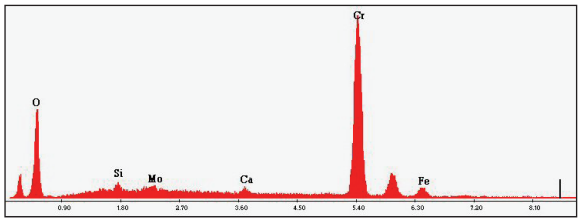

Spectrum 5: Chromium oxide

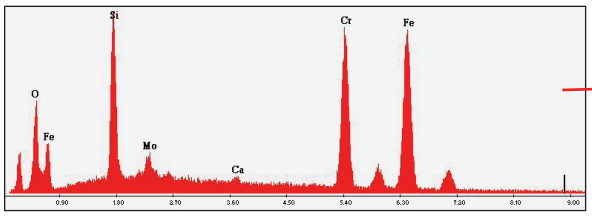

Spectrum 6: Internal oxides of silicium

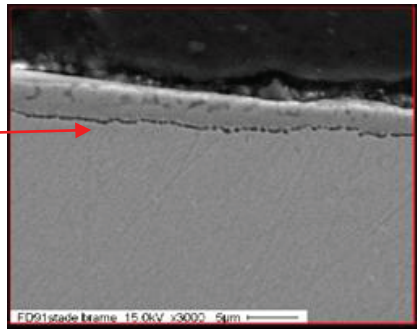

Fig. 29: AISI 444 internal oxides of Si [MAL09b]

12 – GRINDING

This scale layer can be sometimes removed by grinding. This step is a repairing manufacturing step that is used to prevent some surface defects such as laps or seams produced by inclusions or precipitates during rolling. As a result, the surface is particularly rough, but the roughness of the surface after this step is not controlled because the purpose of grinding only consists in removing a defined thickness of metal on each face of the slab (to suppress precipitates and inclusions trapped in the first millimetres of the slab during fast solidification in the mould). Only the metal thickness removed is controlled.

Some measurements of the slab roughness (Fig. 30) after grinding were performed and we found the presence of a pattern at each 2 mm and an orientation along the rolling direction contrary to the rough slab surface, which (after scale conditioning) is much more oriented along transverse direction, with a pattern around 1,5 mm.

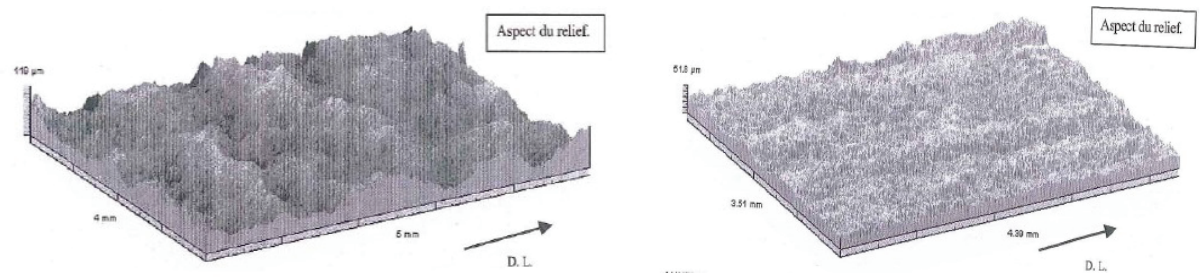

Fig. 30: Roughness of the slab, after casting on the left, and after grinding on the right.[CAL10]

13 – OXIDATION FORMED DURING THE SLAB REHEATING IN NATURAL GAS FURNACES

Reheating furnaces increases the slab temperature up to 1220°C for ferritic grades, during 150 minutes (Fig. 31) in an atmosphere imposed by natural gas combustion in the air. The air/gas ratio is around 12, corresponding to a mix of the following gazes (% vol):

% O_2 dry = 3%

% CO_2 dry = 9.5 %

% H_2O = 17 %

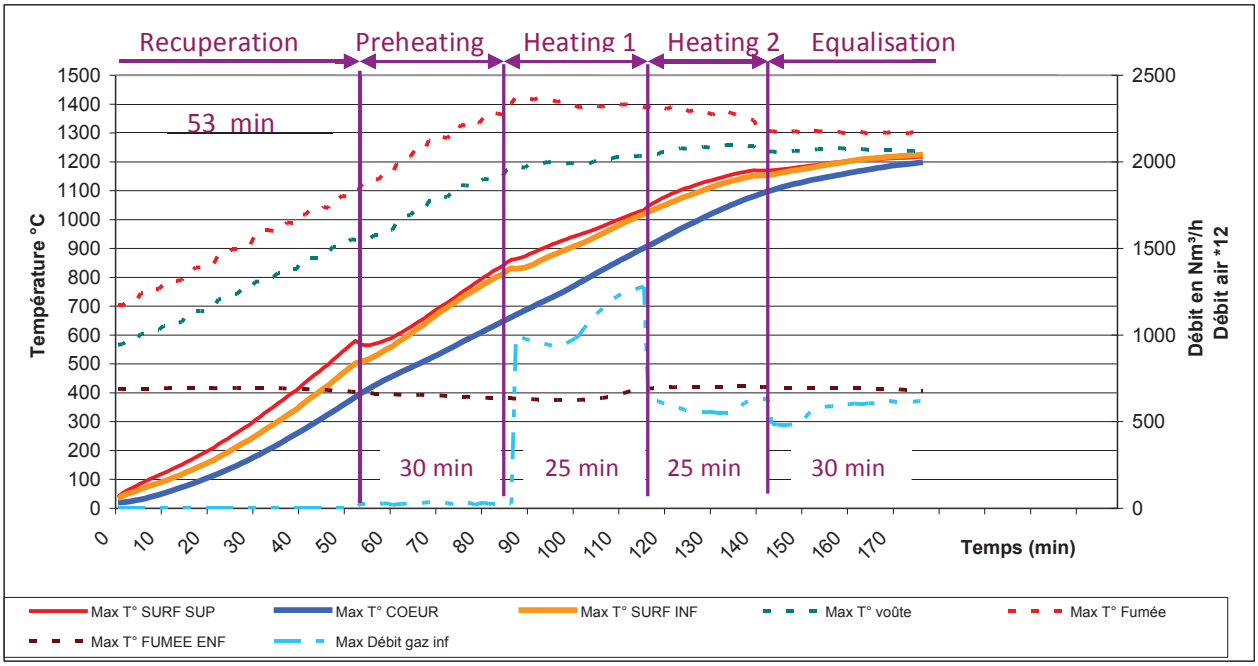

Fig. 31: Reheating profile performed in reheating furnaces on ferritic stainless steels

In order to understand the evolution of oxidation during reheating some interrupted tests were performed in a lab furnace (FASA – Fig.32) used to reproduce the exact process conditions in temperature (with thermal cycle) and the exact atmosphere.

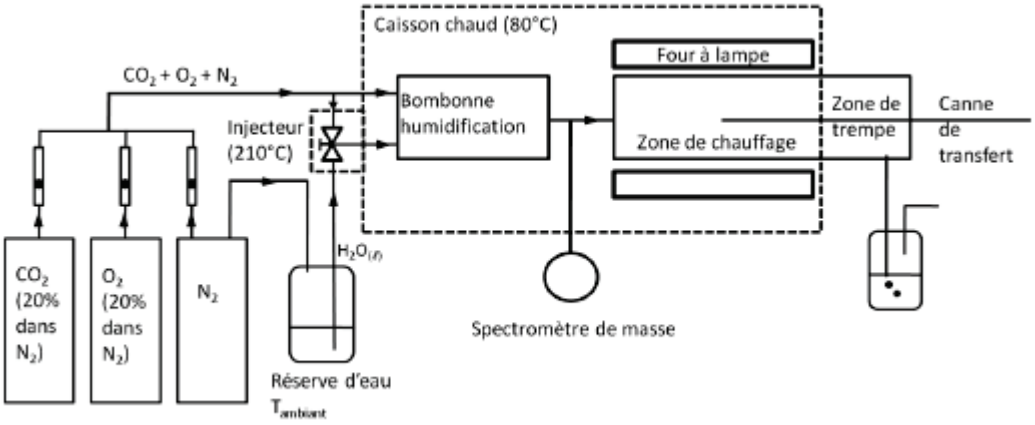

Fig. 32: FASA scheme used to perform oxidation tests representing the manufacturing process [ISS12]

Tab.5. Sample surface evolution during reheating profile execution

	Initial surface before reheating	**After 40 min – 410°C**	**After 60 min – 625°C**	**After 86 min – 850°C**	**Exit of the furnace**
With initial casting oxide	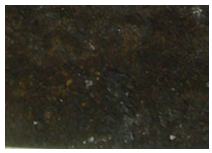	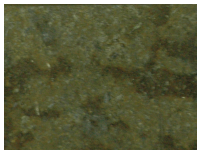			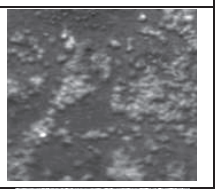
Ground		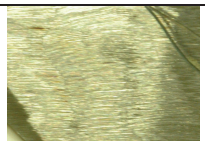	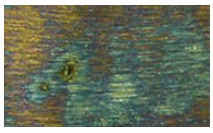		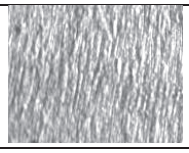

The ground sample seems to start to oxidize around 620°C, after 60 min exposure. (Tab.5) The color and therefore the oxidation is not uniform, it depends on the topography of the sample. The concave surfaces appear to be more oxidized than convex surfaces. This is due mainly to the effect of cavity induced by the roughness of surface that modify locally optical characteristics (such as emissivity) and so modify the thermal exchange flux. [HER37, DEM81] This first stage of oxidation is thinner than 1 µm at this stage on the ground sample.

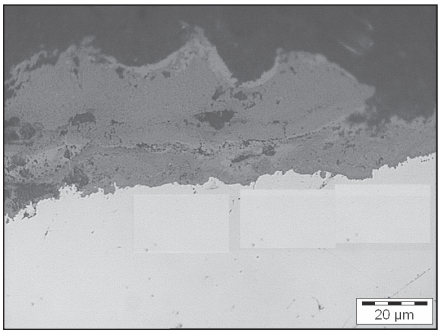

Fig. 33: Scale layer after 60 min exposure on initial rough sample [CAL09a]

No over-oxidation of the rough sample can be observed because the average thickness of scale remains the same (Fig. 33). The morphology of the metal / oxide interface is regular, as in the case of slab at the exit of the continuous casting.

After 86 min exposure (Tab.6), the oxidation can be clearly distinguished on the ground sample. The oxidation is the most visible in the bottom of the grooves. Nevertheless, it remains impossible to quantify it by conventional methods. On the ground sample, no over-oxidation was found: the scale thickness observed is even thinner than on the casting sample, because thin fragments of oxides were fractured and removed during air cooling.

Tab.6. Oxidation of AISI 445 after reheating furnace step, at the left, with initial oxide, on the right, initially ground after 86 min [CAL09a]

	With initial casting oxide	**Ground**
FASA sample	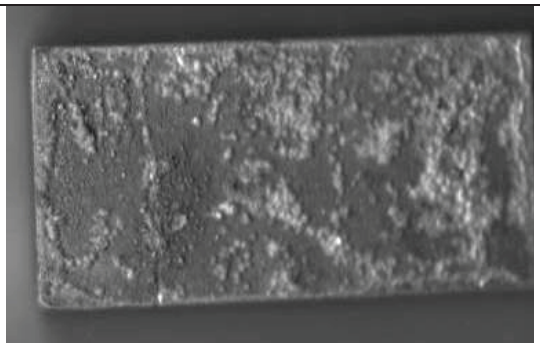	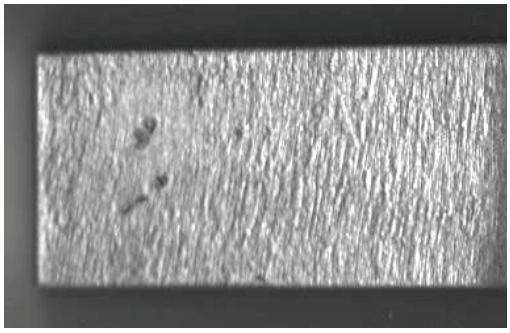
Cross section observation	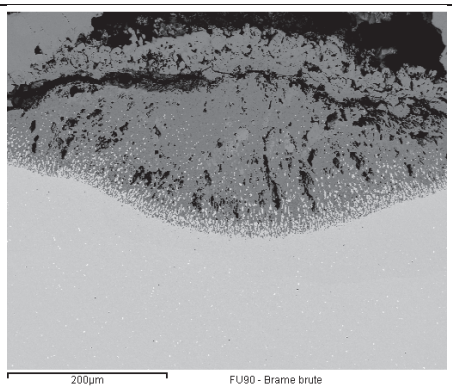	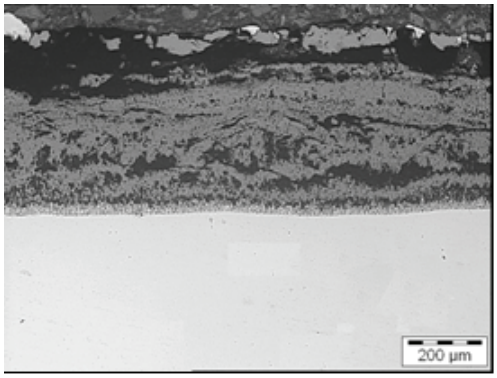

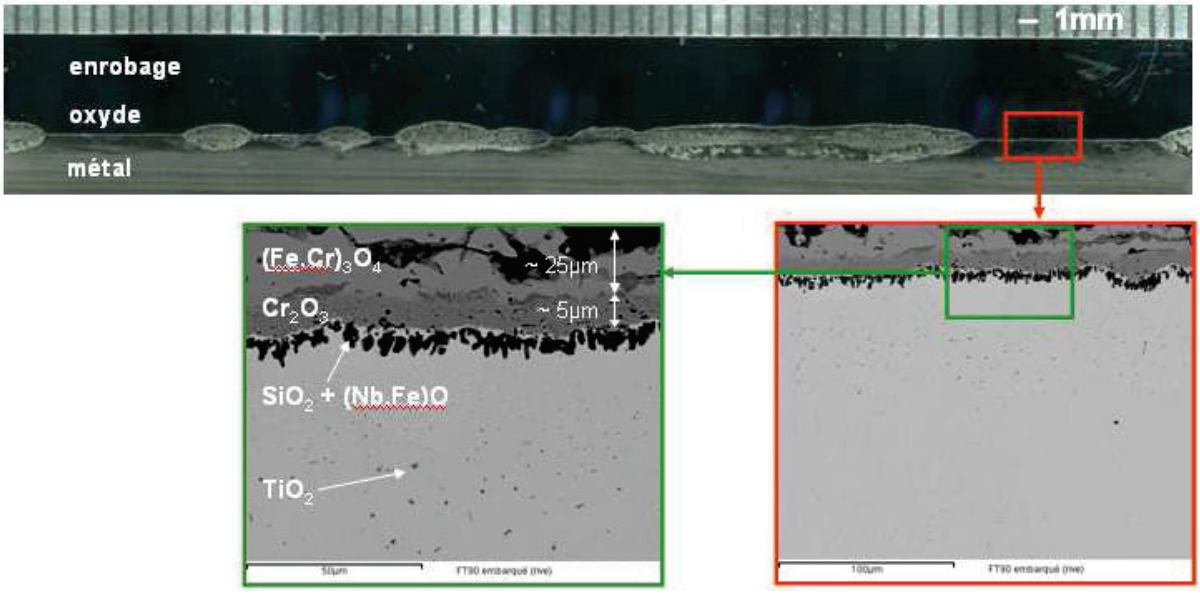

Fig. 34: composition of the thin layer between gulfs on AISI 441 [CAL09b]

We can note that there is a strong difference between casting sample and ground sample: the casting sample has an intermediate oxidation regime characterized by alternate areas of thin layer and gulfs. These gulfs are small points of oxides that can be seen on the macroscopic picture.

The thin layer between gulfs is composed on chromine (Cr_2O_3) on 5µm thickness [GON05, CAL09b]. This part of the oxide has a protective behaviour. The upper part is a mixed oxide, which composition is $(Fe,Cr)_3O_4$, over 25 µm thick. The scale-metal interface is composed of silica oxide (SiO_2) and traces of NbO. (Fig. 34)

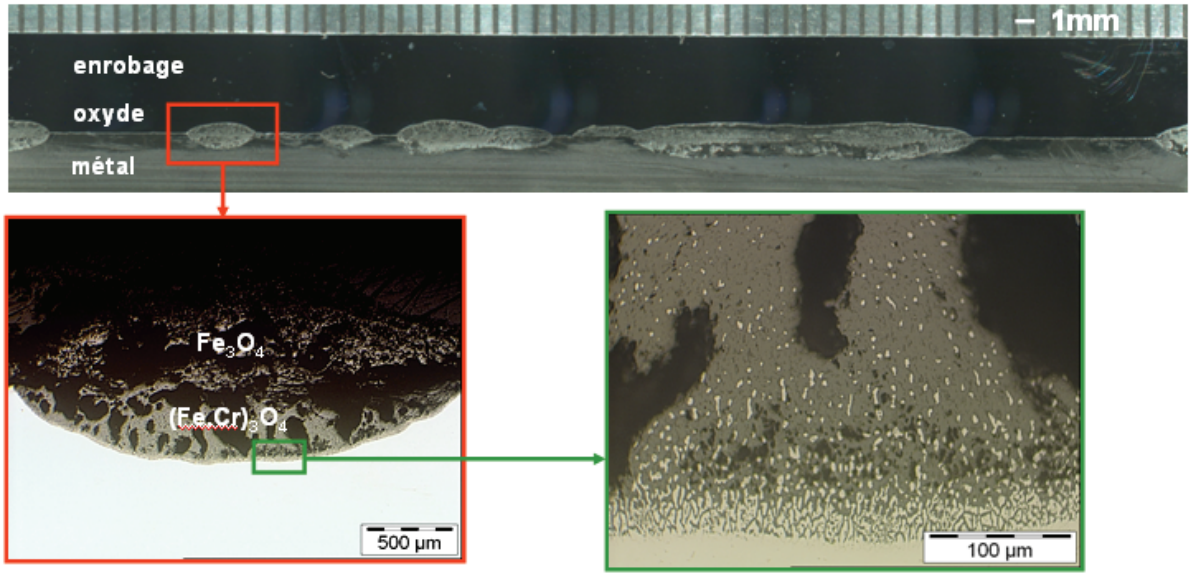

Fig. 35: Examination of oxide layer on AISI 441 [CAL09b]

The gulfs are composed of different sublayers (Fig. 35): the external part of the dome is composed of iron oxides such as Fe_2O_3, Fe_3O_4 and FeO. This dome can be easily removed during hydraulic descaling after the reheating step, because we can see a large crack through the gulf. The internal part is composed of mixed oxides such as $(Fe,Cr)_3O_4$. This part of the scale is very adherent to the metal substrate and will be not remove after hydraulic descaling. [CAL09b] The scale-metal interface is wavy and determined by chromium penetrations, linked to the selective oxidation of Cr close to the metal surface. The generation of penetrations will induce a chromium depleted area in the surface of the product (around 20 µm deep). (Tab.7)

The ground sample has a catastrophic oxidation facies characterized by a dual layer underlined with a high density of chromium-rich penetrations. The composition of this scale is similar to the composition of the gulfs, because gulfs are the initiation of catastrophic oxidation regime.
On the AISI 445, grinding has allowed to change the oxidation regime to a more advanced stage. It shows that the continuous casting scale layer plays the role of a diffusion barrier. Grinding allows this grade to get a very smooth interface (by the absence of gulfs).

Tab.7. Main dimensions on AISI 441 oxidation after reheating furnace [CAL09b]

Initial state	Oxydation regime	Dimensions	
Casting scale	Intermediary	Thin layer between gulfs	30 µm
		Gulfs	Φ = 3000 µm
			ép. = 650 µm
		Cr Penetrations	25 µm
Ground	Catastrophic	Total	120 µm
		Cr Penetrations	65 µm

The effect of hydraulic descaling is known to remove the upper part of the gulfs and the upper part containing mixed oxide on ferritic stainless steels. If the oxidation regime is catastrophic, the thick oxide is removed up to the middle of the mixed oxide layer. The average oxide layer thickness after descaling is around 30 and 50 µm.

14 – Oxidation of the transfer bar

Between the hydraulic descaling and the transfer bar state, the slab will be rolled in five successive steps in the roughing mill. There is no detailed result of the effect of roughing mill on scale layer of ferritic stainless steel. Nevertheless, some information is available for carbon steels and transfer bar can be observed. As our study will be based on AISI 441, we have examined several transfer bars of each grade.

We have measured the scale thickness and have noticed that oxide layer is very heterogeneous in thickness. Indeed, we have found an average scale layer of 35 µm, with thicker parts up to 70 µm, and thinner ones close to 20 µm.

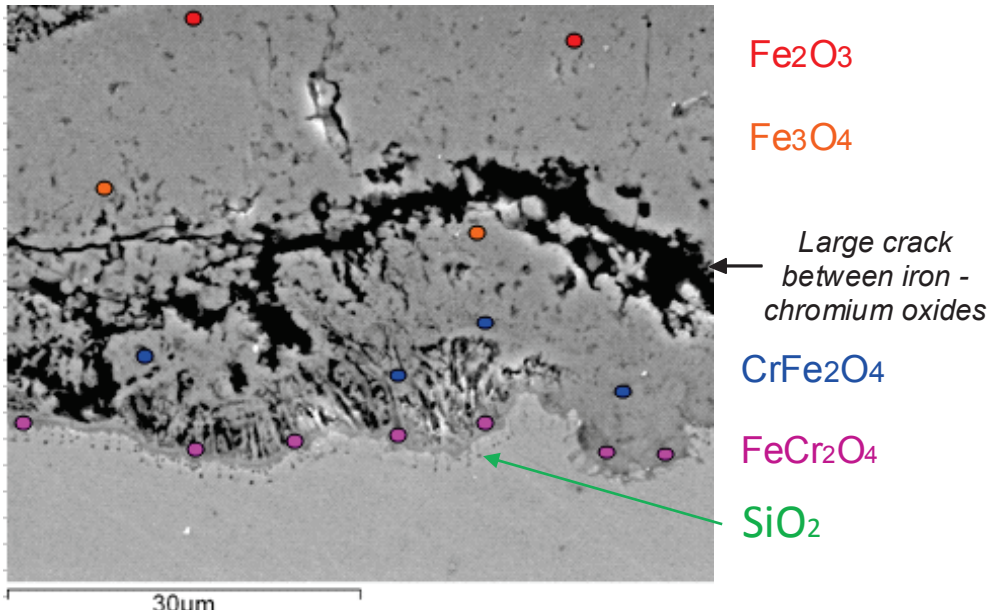

Fig. 36: Observation of oxide layer along rolling direction

The initial oxide layer is composed of 5 different sub layers (Fig. 36). The oxide is divided into two main parts separated by a large longitudinal crack that we observed all along the sample.
The two parts are porous and the external one seems to be more compact than the inner part.
This external part is composed of Fe_2O_3 at the sample surface and Fe_3O_4 close to the crack.
The inner part is very porous and contains Cr contrary to the previous part (containing only iron oxides); $CrFe_2O_4$ and $FeCr_2O_4$ were identified as main components of this inner part. These two components have a spinel structure, AB_2O_4.

The scale metal interface is characterised by a very thin stripe around 1 µm thickness, having a particular shape and essentially composed of SiO_2. This stripe is prolongated in direction to the substrate, forming like a comb. This stripe is not continuous and does not seem to be present when there is an old gulf. (Fig. 37)

To analyse this stripe in much more details, a sample was immerged into an acid solution (2g picric acid, 5ml chloridric acid, and balance by ethanol up to 100ml) in order to dissolve the metallic substrate. Using a MET grid, the observation of the surface of the scale/metal interface (oxide face) was made using EDX-SEM (Fig. 38).

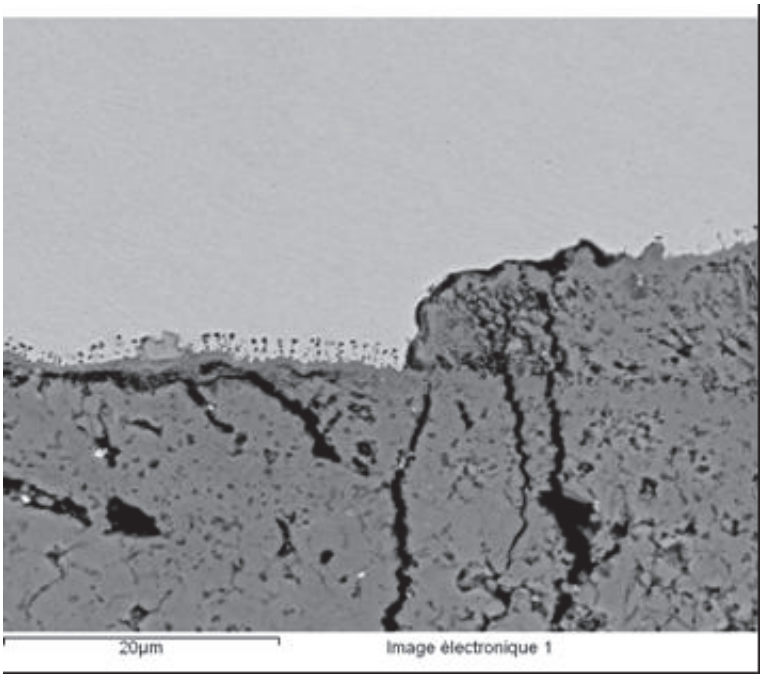

Fig. 37: Scale / metal interface – comb shape

The observations of the scale inner face reveals that the surface is very wavy and most of the surface has a spongy aspect, revealing that comb shape is a honeycomb structure made of silica oxide (Fig. 38). The spheric asperities of the surface is (partially covered by honeycomb structure) essentially composed of chromium oxides, and correspond to the gulfs already detected in the cross section observations.
Finally, small cubes can be found on the surface and are Titanium Nitrides precipitates (due to the presence of Ti in the base metal).

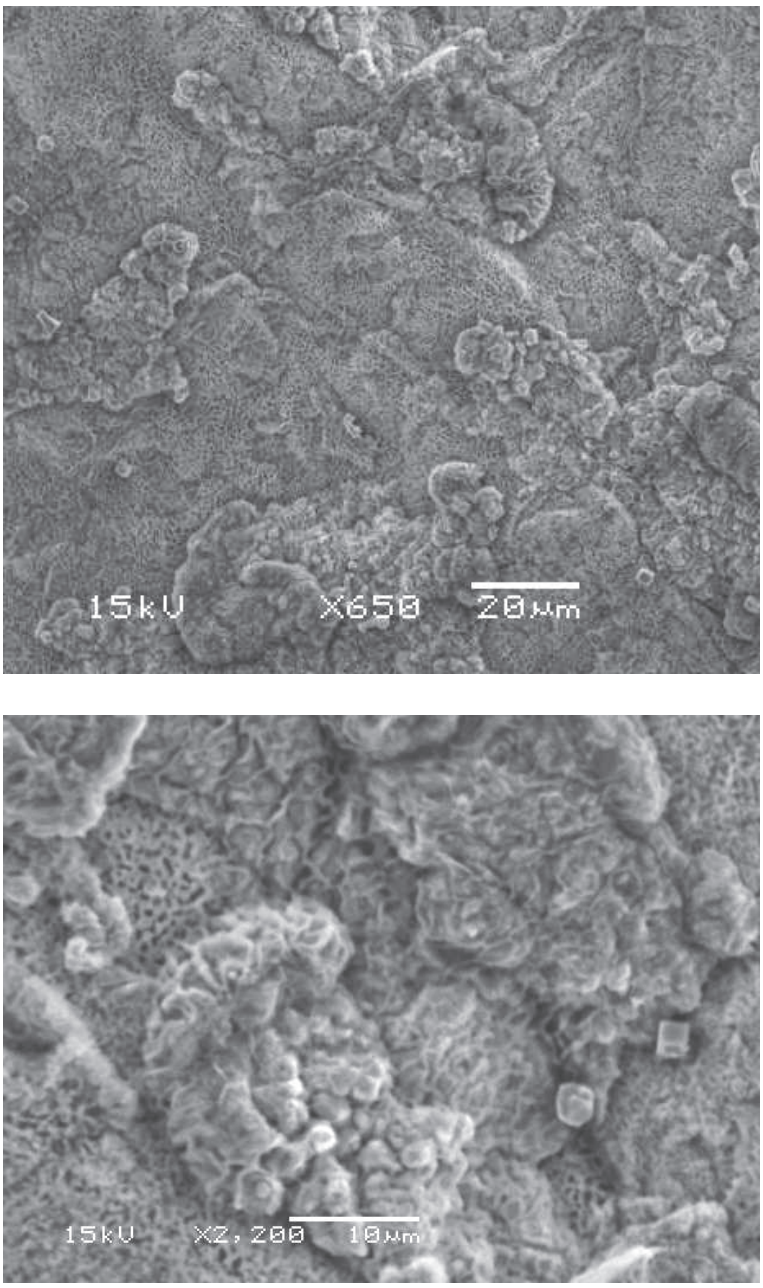

Fig. 38: Observations of the scale surface at the oxide/scale interface.

The morphology of this scale layer is very particular and very different from conventional Cr oxides such as Cr_2O_3 usually found on tribological studies performed on ferritic stainless steels [JIN08].

This particular morphology can be compared to the morphology described in J. Issartel and al. study [ISS12b], where protrusions of metal through silica oxide were observed at similar temperatures, on the same grade (441). Nevertheless, external scale layer exposed in the corresponding article is different from the external part of the oxide observed in our case.

Oxidation of ferritic stainless steels is very complex and for oxides produced during manufacturing process, there is no general modelling to understand the formation of such scales and as a result, it is also very hard to reproduce it at a lab scale.

With the evolution of new grades, the amount of alloying elements and Cr content is always increasing. It implies a constant increase of corrosion resistance.
However, the high corrosion resistance of these steels also leads to the limitation of oxidation during the hot phase processing. Actually, the oxide scales produced by several reheatings are a way to decrease the surface defects and heterogeneities, by suppressing direct contact between the strip and the working rolls.

So, the processing of high chromium ferritic stainless steels is especially risky in terms of surface quality [BOG78] because of the very thin produced oxide scale.

D/ Sticking defects on ferritic stainless steels

It's now many years that ferritic stainless steels are known to be concerned with sticking phenomena during hot rolling. They are among the most sensitive stainless steel grades as discussed by S. Lee and al. [LEE98]. Actually, stainless steel strips are sticking to the tools because of their high chemical affinity with them. We will first, describe this defect as it appears on hot rolled annealed and pickled strips (D1 ou HRAP finish). Secondly, a detailed bibliographic review of the sticking phenomenon and process parameters acting on it will be proposed. Finally, we will expose the formation mechanism of the defect proposed by W. Jin and al. [JIN00] and CY. Son and al. [SON07].

1 – Description of the sticking defect

The defect called "sticking of stainless steel" looks like small dark dots at the edges of the flat product, looking as a "salt and pepper aspect" (Fig. 39 – 40). The affected zone can cover up to 50 mm at each edges, as a result, when the product is dedicated to the high quality market, the edges have to be removed and it represents a direct decrease in production yield. Some clients require the full width of the delivered product, so when edges need to be cut off, the product has to be declassified and sold to less exigent applications towards surface quality. The defect is only observable after the first annealing and pickling, i.e step after hot rolling.

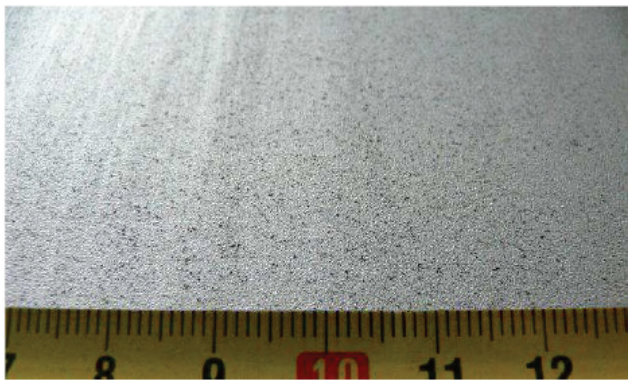

Fig. 39: Sticking defect on 441 HRAP [VIL08a]

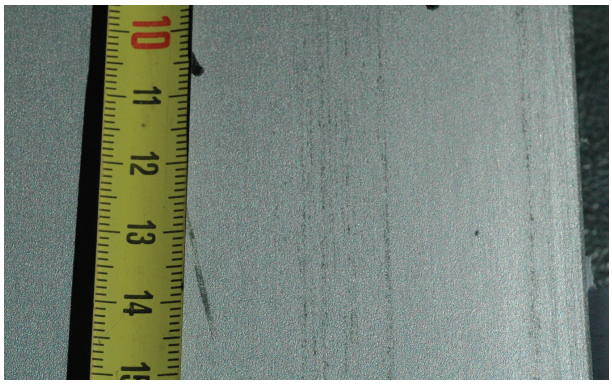

Fig. 40: Sticking on 444 HRAP [VIL08b]

We can observe two patterns: an area covered by small dots (Fig. 39) or discontinuous lines parallel to the rolling direction (Fig. 40). The fact that this defect can only be observed after the first pickling can induce errors by confusing it with under-pickling. To be sure that we are in presence of sticking, we need to perform a microscope or SEM observation in a transversal cut of the defect.

The defect (Fig. 41) is characterised by a particle incrusted in the product top surface. The average size of those particles is around 100 – 200 µm in width and is around 50 µm deep. We can observe a continuous oxide layer between the product and the particle. The particle itself is composed of a mix of oxide and metal. We can notice up to 4 or 5 layers. First, we have performed an EDS analysis and then a quantification analysis in the particle in order to identify the nature of the metal.

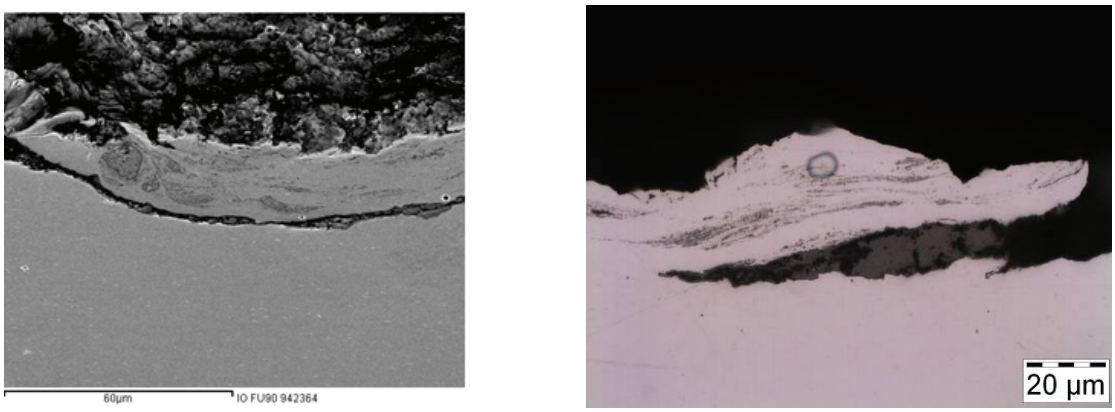

Fig. 41: SEM observations of a “sticking particle” in a cross section (AISI 445)

The EDS analysis (Fig. 42 and Tab. 8) indicates the presence of Si, Mo, and Cr which are the main components of 444 grade tested here. The quantification indicates a higher content of Oxygen in the particle which is related to the presence of oxides. The other elements such as Si, Cr, and Mo have a similar content than in the matrix. **As a result, the incrusted particle that constitutes the sticking phenomenon is a particle of mixed metal base and oxides.** We haven’t found elements coming from the roll such as V nor W. Moreover, the high content of Cr (> 15% here against 5% only in the roll grade) in the particles confirms that it could not come from the roll. **It implies that the particle is not coming from the roll matrix.** W. Jin and al. [JIN00] performed tribological trials on a two discs simulator and observed a similar defect on the antagonist representing the work roll. The defect is constituted by four metal fragments and the first one appeared on an initial defect (scratch) on the cylinder. (Fig.43) They affirm that the different layers were formed at different times during hot rolling simulation. They also performed an EDS analysis confirming that the particle comes from the stainless steel product.

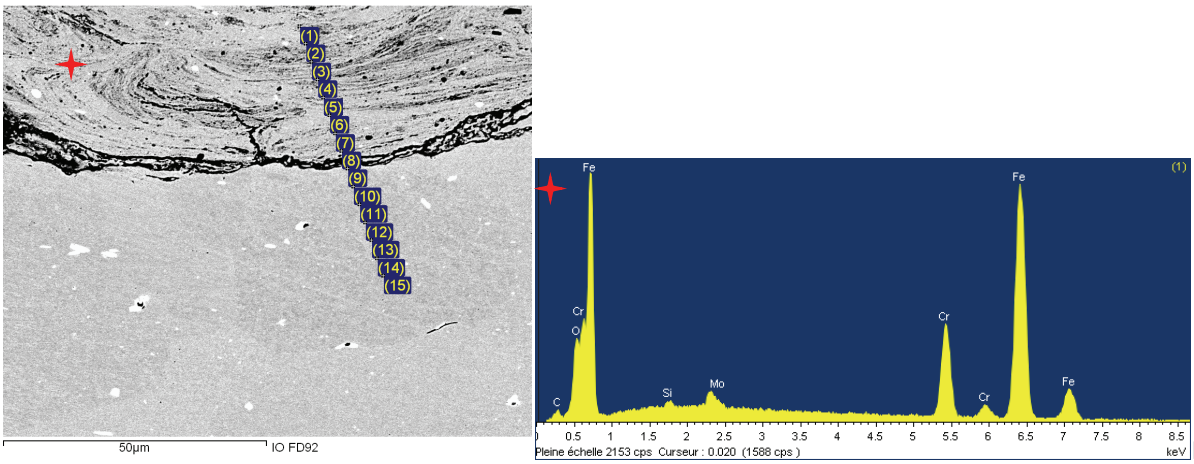

Fig. 42: EDS analysis in the metal particle

Tab.8. SEM quantification on the base metal and the particle

Spectre	O	Si	Cr	Fe	Mo
1	3,7	0,37	16,72	76,8	2,41
2	2,38	0,16	15,45	79,57	2,44
3	8,6	0,59	20,62	68,29	1,89
4	2,78	0,24	16,19	78,85	1,95
5	3,95	0,35	18,89	75,79	1,03
6	1,2	0,04	16,68	79,48	2,6
7	3,35	0,43	16,87	77,19	2,17
8	1,85	0,13	14,52	81,19	2,31
9	1,35	0,12	13,99	82,13	2,41
10	0,77	0,38	16,18	80,32	2,35
11	1,05	0,32	18,75	77,61	2,28
12	0,9	0,37	19,81	76,86	2,06
13	0,87	0,39	20,25	76,16	2,34
14	0,96	0,39	19,83	76,58	2,23

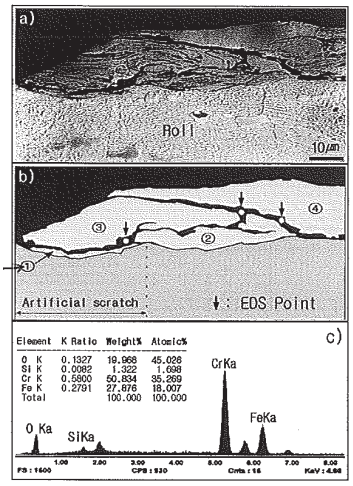

Fig. 43: Cross section of the roll
a/ particle stuck on the artificial scratch of roll
b/ schematic diagram of sticking particle
c/ EDS analysis result of scale layer in particle

2 – Main parameters having an impact on sticking phenomenon

21 – EFFECT OF THE GRADE

211 – Industrial observations

On the industrial plant, we noticed that the defect concerns only ferritic grades and especially the grades containing more than 17% Chromium. The higher the Chromium content is, the higher the sensitivity of the grade to the sticking phenomenon will be. Industrial statistics help us to classify the different grades regarding their sensitivity to this phenomenon (Fig.44)



445	441	444	436	439M	439	430	409
%Cr = 20.2	%Cr = 17.8	%Cr = 17,7	%Cr = 17.5	%Cr = 16.5	%Cr = 17.5	%Cr = 16.5	%Cr = 11.3
		%Mo = 1.85	%Mo = 1.25				
% Cu = 0.50	%Ti = 0.15	%Ti = 0.15		%Ti =0.4	%Ti = 0.35		%Ti = 0.18
%Nb = 0.42	%Nb = 0.50	%Nb = 0.27	%Nb = 0.6				

Fig. 44: Sensibility of grades on sticking phenomenon

We also noticed that grades containing Nb were more sensitive to sticking phenomenon.

212 - Austenitic/ferritic comparison:

S.Lee and al. [LEE98] were the first to explain the main differences between austenitic products and ferritic products towards sticking. In fact, austenitic and ferritic grades both stick to the rolls but the sensitivity of austenitic is very small compared to the ferritic ones.
On the graph of Fig. 45, Lee noticed that contrary to ferritic grade, the sticking of austenitic grade is a stable phenomenon (after 20 revolutions); it was interpreted by the fact that when the particles of austenitic metal are stuck to the roll they will not be transferred back to the product. That is the reason why we don't see defect on these types of grades on the industrial line.

The main behaviour difference between the two families of grades depends essentially on their high temperature properties such as hardness: the ferritic grade (here STS 430J1L) has a low hardness at high temperature (compared to austenitic one) because of martensite to austenite transformation around 900°C [LEE98] (Tab.9).

The grain size is also responsible for the ductility gap between the two families: the ferritic grain decreases at such temperatures (Fig. 46).

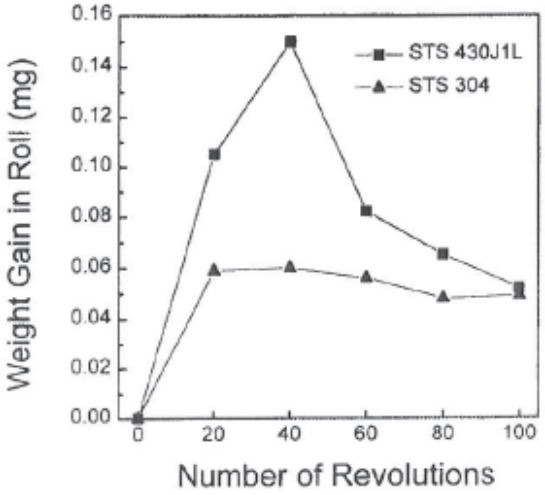

Fig. 45: Weight gain of the roll disc vs. number of revolutions on AISI 304 and STS 430J1L [LEE98]

Tab.9. Mechanical properties of the tested grades [LEE98]

	Rm 20°C	**Ductility**	**Vickers Hardness 600 – 900°C**	**Vickers Hardness 20°C**
304	262	657	65	164
430 J1L	363	601	24	171

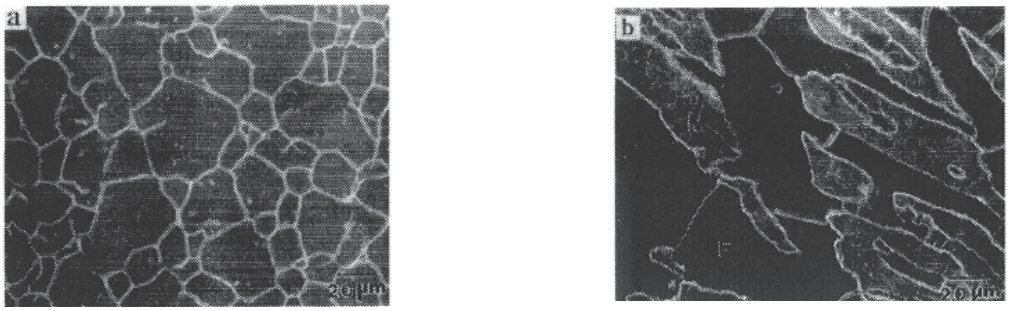

Fig. 46: SEM micrographs of 304 (a) and 430J1L (b) – M is for martensite – F is for ferrite [LEE98]

213 – Effect of alloying elements on sticking

D.J Ha and al. [HA09] showed that alloying elements act on sticking in three ways:

- Alloying elements modify the oxide layer: as already exposed early the oxide layer plays the role of an interface between the roll and the product. Testing alloys with different type and amount of precipitates helped to highlight that an addition of 0,4% Cu or 0,5% Si will decrease significantly sticking by increasing chromium oxides fraction volume.
- Alloying elements can induce precipitates formation that will increase matrix hardness: an addition of 0,02% Zr helps to decrease sticking, especially at low temperatures, by increase of hot hardness. [HA09] (Tab. 10, Fig.47)

Tab.10. Effect of 0,02% Zr add on hardness [HA09]

(wt%)	C	Mn	Cr	N
Ref. Steel	<0.015	<0.3	21.0	<0.015
Ti	Ni	Cu	Zr	Si
0.3	0.3	0.4	_	0.1

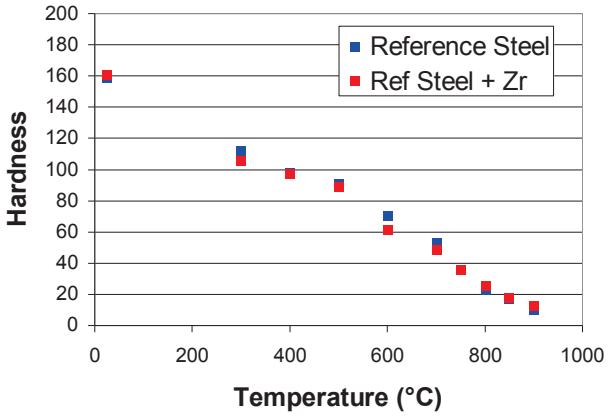

Fig.47: Evolution of hardness with a Zr add

- Alloying elements can induce precipitates formation that could play the role of third body in the contact. Aksoy and al. [AKS09] prove that grades with a Nb addition are composed of two types of carbides: $M_{23}C_6$ and NbC.

The first type of carbides, $M_{23}C_6$, is located at grain boundaries and plays the role of a third body. During rolling, such carbides will be fragmented and the wear behaviour is abrasive; this phenomenon occurs in parallel with adhesion due to the sticking phenomenon.

The second type of carbides, NbC, can be very detrimental for the contact when the carbide size is important. Indeed, when the carbide is big, the bonding between the matrix and the carbide will be low. The fragile behaviour of such carbides will also generate abrasion in the contact.

In an older study, Aksoy and al. [AKS01] already highlighted that the bigger the carbides, the lower the bonding between the carbide and the matrix. As a result, fine carbides are preferred to increase wear resistance. Additions of Mo and V are more interesting because precipitates formed are finer and spread all over the matrix (at grain boundaries and in the grains). NbC are coarse precipitates essentially located at grain boundaries; that is why Nb is particularly detrimental to sticking phenomenon reduction. Titanium addition is more interesting because it allows to form TiC which are spread all over the matrix and precipitate size is smaller than NbC.

214 - Cr content effect on the sticking:

W. Jin and al. [JIN00] observed that the higher the Cr content in the product, the more sensitive to sticking (Fig. 48). We confirm this trend by industrial observations summarised in Fig. 44. This article relates also that the AISI 409 grade is never concerned by this phenomenon (whatever the cylinder roughness). This phenomenon is explained by the fact that the higher the Cr content, the lower the oxidation rate of the product.

As a result, the scale thickness raised on the product (in same oxidising conditions) is smaller when Cr content is higher, so, the scale thickness is too low to create an interface between the product and the roll surface and so, statistically cannot prevent the sticking efficiently.

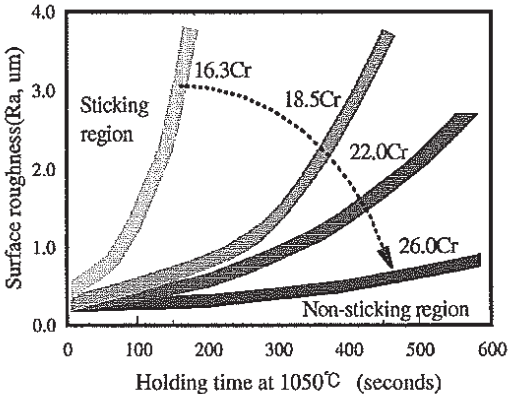

Fig. 48: Sticking sensibility with Cr content and surface roughness. [JIN00]
(HSS roll and modified ferritic grades with different Cr content)

22 – Effect of oxide layer

Oxide layer of the product plays the role of a natural barrier against direct metal contact between the hot product and the roll. As a result, having an oxide layer prevents from sticking occurrence. I. Guillot [GUI90] reported that on many plants rolling of carbon steels is performed before rolling of stainless steel in order to coat partially the rolls with product oxide, as a coating layer.

On disc-on-disc tribological tests, Jin and al. [JIN00] noticed that the presence of a 3µm scale layer is sufficient to suppress sticking. Nevertheless, on the original hot rolling process, thermal and mechanical solicitations are higher than on tribological tests.

DJ. Ha and al. [HA08b] confirmed that scale layer helps to reduce sticking phenomenon but noticed that some types of oxides are more efficient to protect the product surface. They distinguish layer type oxides from infiltrated type oxides and confirmed that the most efficient oxides are the layer type oxides that play the same role than a protective coating on the surface. As a result, internal oxidation (as already seen on the paragraph C) will not play a beneficial role in sticking, contrary to external scale layer composed of iron oxides and mixed chromium-iron oxides.

Nevertheless, with a high Cr content, ferritic stainless steels have usually thin scale layer, which can also explain the various sensitivity to sticking phenomenon. On figure 49, we confirm the observed ranking of grades in industrial plant (Fig. 44). The major results illustrated by the figure 49 are that decreasing production rate by increasing the time spent on hot rolling line (after roughing mill) will not be sufficient to create a scale layer preventing from sticking. As a result, the first industrial actuator tested to increase oxide layer thickness is rolling temperature.
Modifying rolling temperature leads to an increase in scale thickness and also chemical oxide change.

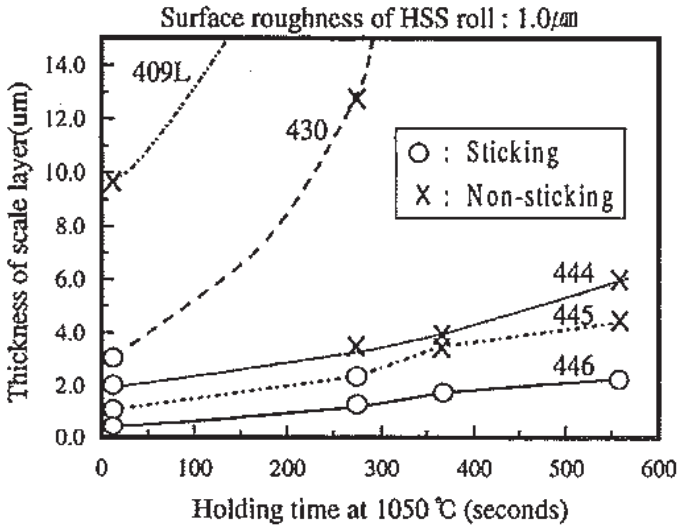

Fig. 49: Effect of scale thickness on sticking of various stainless steel grades [JIN00]

23 – Effect of temperature

On the hot rolling mill of APERAM, it was noticed that the higher the finishing mill temperature (after stand F7), the lower the sticking defect. Indeed, the preferential localisation of the defect in the edges is related to the colder areas of the strip. Temperature heterogeneities have to be reduced as much as possible and many improvements were already done: increase of rolling speed in order to reach higher rolling temperature and increase of slab temperature (limited by creep phenomenon in reheating furnace), reduction of descaling and use of thermal tunnel between the roughing and finishing mill. Despite these improvements, the defect is still present on most sensitive grades.

Jin, Choi and Lee [JIN98] performed disc-on-disc tribological tests on several grades and noticed that sticking phenomenon is important for temperatures near or below 900 ° C (Fig. 50).

This result is the optimal configuration, consequence of two contradictory trends. Rolling temperature simultaneously acts on two parameters:
- The thickness of scale created on the product.
- The product rheology.

With the increase of temperature, the increase of oxide scale thickness will decrease sticking.
With the increase of temperature, the decrease of product mechanical strength will increase sticking.
Different tests [JIN98] have shown that the ideal configuration is to determine the temperature generating high scale thickness with high product strength (Fig.51).

This study explains why ferritic steels have a worse behaviour than austenitics: mechanical strength of ferritics at high temperature is lower (than austenitic) and Cr content on ferritics is also higher.
An additional study [SON07] revealed the existence of a transition temperature on sticking phenomenon. Tribological tests were carried out at 900 ° C, 1000 ° C and 1070 ° C and confirm that a change in the tribological behaviour of the scale for temperatures around 1070 ° C on grades AISI 446 and AISI 436L [SON07, HA08a] (Fig. 52).

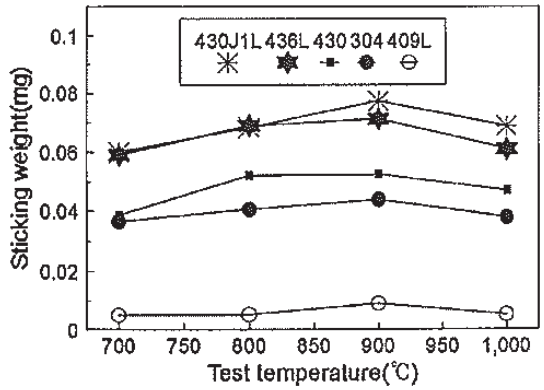

Fig. 50: Effect of temperature on sticking (HSS roll, after 20 revolutions) [JIN98]

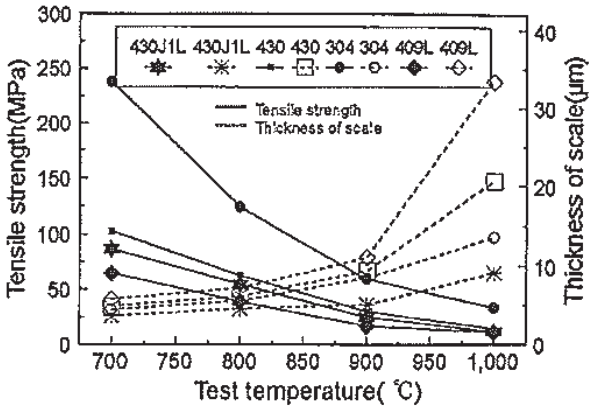

Fig. 51: Changes of tensile strength and scale thickness of stainless steels with temperatures. [JIN98]

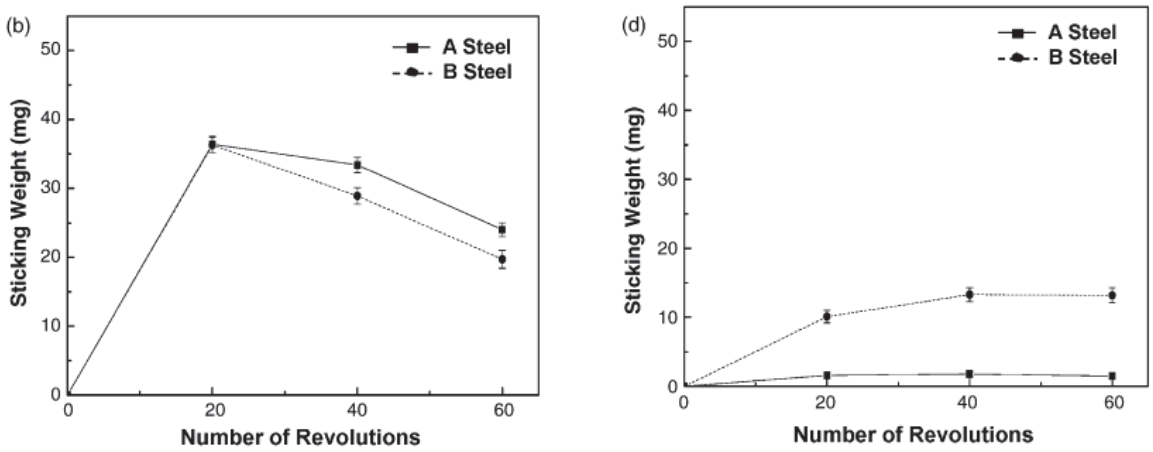

Fig. 52: Weight gain of roll specimen after 20 revolution on disc-on-disc test performed at 900°C (b) and 1070°C (d) on AISI 430J1L steel (steel A) and Cr rich - AISI 430J1L (steel B).

The study of D.J. Ha [HA08a] highlights that increase in sticking resistance at 1070°C is linked to the formation of Cr oxides on the disc (representing the hot product), forming a harder contact surface (Tab.11).

DJ. Ha and al. [HA08b] confirmed in a second study based on lab rolling tests that rolling temperature plays a significant role in modifying chemical composition of scale layer rather than scale thickness. It was confirmed by Aksoy and al. [AKS01] who explained that at low temperatures, the scale layer is essentially composed of external oxides of Fe_2O_3. This oxide helps to decrease wear. At higher temperatures, FeO is promoted and the brittle behaviour of this oxide leads to an increase in wear rate. Cr_2O_3 will also be promoted but its formation kinetic is slow. Aksoy and al. [AKS01] also confirmed the presence of FeCrO4 oxide which forms a glaze surface by debris agglomeration.

Previous paragraph explained that having an oxide layer on stainless steel is beneficial to decrease sticking. As a result, the use of descaling has to be prohibited to decrease sticking phenomenon [HA08b].

Tab.11. Increase of volume fraction of Cr oxides and surface hardness at 1070°C. [HA08a]

Steel	Vickers hardness[a] (VHN)		Volume fraction of Cr oxides (%)	
	1000 °C	1070 °C	1000 °C	1070 °C
A	352 ± 5.8	383 ± 7.2	9.1 ± 0.5	10.3 ± 0.7
B	361 ± 4.2	423 ± 8.8	6.2 ± 0.2	7.5 ± 0.7

[a] Vickers hardness was measured under a load of 5 g.

24 – Effect of roll grade and roll roughness

As explained on paragraph B/4, there are mainly 2 types of rolls used in stainless steel hot rolling process: HSS and ICDP. For flat carbon steel rolling, another grade family can be found: Hi-Cr rolls. It is the most represented grade in steel rolling; as a result, main studies are based on comparison between this grade and HSS. That was the subject of Jin's study [JIN98] that compared wear results of HSS and Hi-Cr rolls toward sticking phenomenon on disc-on-disc tribometer. Chemical and mechanical data are presented in Tab.12 and 13. On Figure 53, the evolution of sticking weight of tested roll is represented with the number of revolution. It clearly appears that during the first revolutions, the sticking rate is higher on HSS grade, corresponding to a running in period. After 10 revolutions, sticking amount on Hi-Cr roll exceeds the HSS one, whose behaviour is more stable with time.

Tab.12. Chemical composition of tested rolls [JIN98]

(wt%)

	C	Si	Mn	Ni	Cr	Mo	V
HSS	2.0	1.0	1.0	1.0	5.0	2.5	4.0
Hi-Cr	2.9	0.7	1.0	1.0	18.0	1.4	0.2

Tab.13. Microstructure and Mechanical behaviour of tested rolls [JIN98]

Properties	HSS roll	Hi-Cr roll
Microstructure	Carbide(MC + M_7C_3 + M_6C, 12%) + Martensite	Carbide(M_7C_3, 26.5%)+ Martensite
Total hardness(Hv)	702	558
Hardness of matrix(Hv)	650	450
Tensile strength (MPa)	960	850
Resistance to heat-cycled fatigue	excellent	fair
Resistance to abrasion	excellent	fair

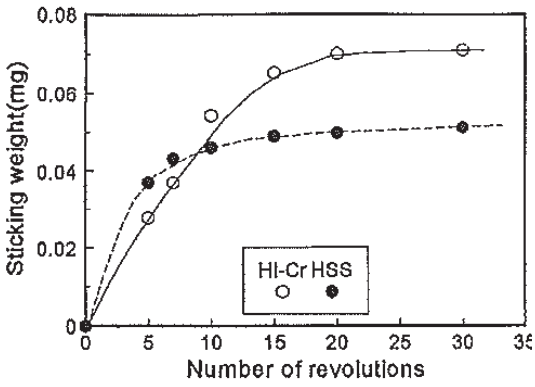

Fig. 53: Effect of roll grade on sticking phenomenon [JIN98] (product grade: AISI 430)

There are many reasons for this trend:

- Cr content of Hi-Cr roll is higher than HSS (5% Cr on HSS against 18% Cr on Hi-Cr), and it increase the chemical affinity between the product and the roll.
- Jin and al. [JIN98] found that Hi-Cr rolls have a higher number of nucleation sites. These nucleation sites are cracks formed during rolling because of a lower hardness and also a lower thermal fatigue resistance than HSS rolls.
- Roll microstructure: the volume content of carbide on HSS roll is 12% against 27% for a Hi-Cr roll and

mechanical characteristic difference between carbides and matrix is more important for Hi-Cr roll than on HSS. This is why the abrasion resistance of Hi-Cr cylinder is lower than the HSS.

I. Guillot [GUI90] compared three roll grades (ICDP, HiCr and HSS) on a disc-on-disc tribometer. The test was performed on ferritic stainless steel containing 17% Cr and 0,4% Ti, but first revolutions were performed on an XC38 carbon steel. (This study highlighted the interest of an initial oxide layer on roll surface to prevent sticking).
As on previous studies, the mass of stuck particles on the roll was measured, and the test highlighted that HSS roll had the best behaviour and Hi-Cr roll had the worst results and is completely incompatible with stabilised ferritic rolling. ICDP grade had an intermediate behaviour, closer to the HSS behaviour.
The oxidation of such grades at high temperatures (500 – 700°C) was pointed out to explain the beneficial effect of HSS, in addition to microstructural explanations.

Despite similar roll surface roughness at the beginning of trial, many cavities are generated on the Hi-Cr surface. Their more ductile matrix wears faster and carbides network (located at the grain boundaries) are found in extreme surface and tear very easily. These barefoot carbides increase roughness and are nucleation sites of sticking phenomenon [JIN00]. Figure 54 reminds the influence of roll roughness on sticking.

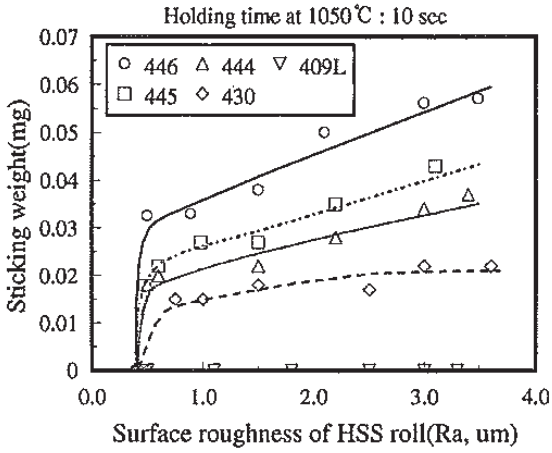

Fig. 54: Evolution of sticking with HSS roll roughness [JIN00]

25 – Sticking phenomenon mechanism proposed by W. Jin and CY. Son

W. Jin and al. [JIN00] proposed a formation mechanism related to their observation on the two disks simulator. (Fig.55)
The sticking phenomenon starts when a direct contact between the metal of the strip and the metal of the rolls occurs. The initiation of the phenomenon is explained by the presence of an initial scratch (or micro-defect) on the working rolls, that becomes an initiation site to the sticking phenomenon.
At following rotations, the first fragment acts as a new initiation zone for the second fragment sticking. The particle rises up to a critical size and is transferred back to the roll.

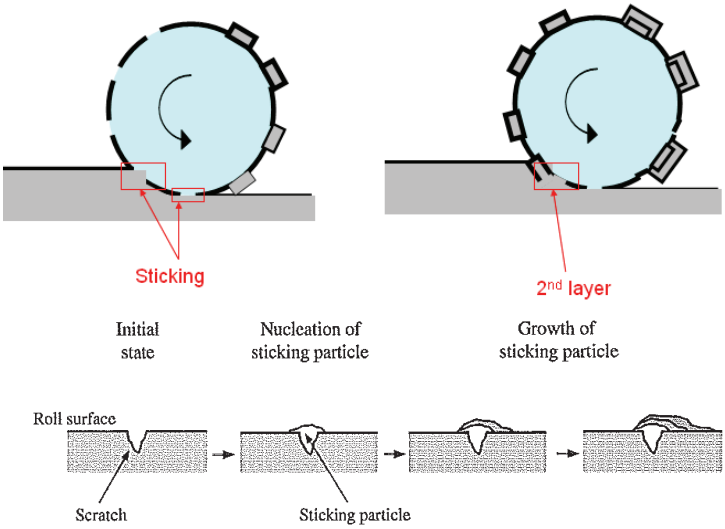

Fig. 55: Sticking mechanism [JIN00]

To prove this hypothesis, W. Jin and al. [JIN00] made artificial scratches on roll surface of 5µm deep and 30 µm wide. They put this roll onto an AISI 446 sample which has a very slow oxidation rate. The test starts on a sample deprived of oxide (before sample reheating) and Jin observed that sticking occurs immediately on scratch corresponding areas. S. Lee and al. [LEE98] were the first to observe the initiation of the sticking and the raise of the particle.

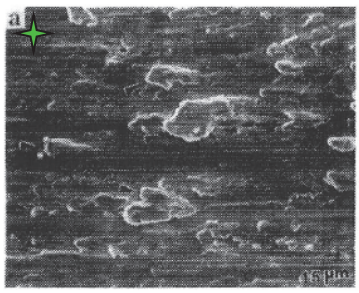

Fig. 56: Initiation of sticking on the roll antagonist [LEE98]

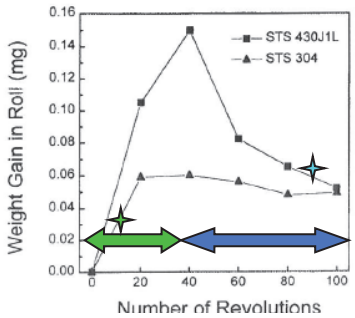

Fig. 57: Transfert from roll to product [LEE98]

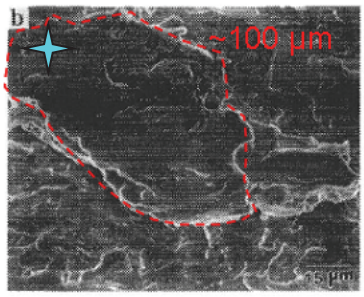

Fig. 58: Removed particle [LEE98]

The graph (Fig. 57) represents the weight gain (directly due to the stuck mass of product to the roll) on the cylinder as a function of the time for two alloys: the 304 austenitic steel which is industrially not concerned by the defect and the 430J1L, corresponding to a 430 grade with 19% Cr and 10 mill of Mo, concerned by the defect.

We noticed that both steels stick onto the roll, but the ferritic stainless steel sticks with a higher kinetic in the first rotations. The weight gain passes by a maximum value (around 40 rotations) before decreasing. This last step corresponds to the transfer of the stuck particle back to the product. At the old place of the particle, there is a cavity (Fig. 58) on the cylinder surface that can act as a nucleation site for next roll rotations (Fig. 56).

E/ Discussion on sticking phenomenon

In this chapter, the specificity of ferritic stainless steels towards sticking phenomenon was exposed. The several metallurgical details about stainless product and rolls were given. The preponderant role of carbides was detailed on both antagonists. The oxidation of the hot product was described following the different manufacturing process steps. We understand that oxide layer has a significant role on sticking. Industrial observations were confirmed by different authors that had the possibility to decorrelate the effect of temperature, oxidation, metallurgy and mechanical behaviour on sticking using lab tests (disc-on-disc tribometer described in [LIU09]). Other tests such as compressive tests [ZHA12] or rolling simulations [JIN02] also confirmed most of the results found on disc-on-disc tribometers.

Nevertheless, all of these lab studies were performed on machined samples (without the original scale layer from the process) with a defined surface roughness. Publications do not give details about surface roughness before the test (except for roll sample). However, these conditions are particularly important because sticking formation mechanism was built on the hypothesis that sticking occurs on an initiation site that could be a scratch on the roll surface. Oxides described in literature are different and generally have an easier structure and composition than on the industrial transfer bar. As a result, we are not sure that the transfer bar scale layer will have a similar tribological behaviour than on lab tests.

In the real manufacturing process, scale layer on transfer bar is around 35 µm (with thinner parts to 10 µm). So, if the roll sample was representative from industrial working rolls, the complete depth of the scratch will be in contact with oxide but not with ductile metal. To generate sufficient direct contact between roll surface and ductile fresh metal, the depth of roll scratches has to be higher than 70 µm. Nevertheless, we have no available and accurate data on roll surface roughness evolution during rolling on the different stands.

As a result, these tests cannot be used as a direct transposition of the industrial hot rolling process but only as a way to compare conditions of process between them. Next chapter will be dedicated to the roll surface roughness evolution during rolling in order to determine if there is a topographic pattern on roll surface and try to evaluate the main dimensions of such pattern.

CHAPTER 2 - ROLL ROUGHNESS EVOLUTION

In previous paragraph, we learned that sticking phenomenon is specific to ferritic stainless steel during hot rolling. Main parameters (process, product...) were listed and the roll surface was pointed out as responsible for initiation of sticking by W. Jin and al. [JIN00]. This mechanism was based on the assumption that scratches over roll surface are deeper than oxide thickness of the product. As the result, ductile metal could be extruded into the roll scratch and direct contact between hot metal and roll could occur.

Nevertheless, we don't have industrial references in order to compare the depth of roll scratches and transfer bar oxide thickness. As a result, even if most of the observations made by Jin and its team about sticking phenomenon can be validated by industrial hot rolling trials, the high frequency of the defect could never by linked directly to the roll surface state. An in-line measurement of roll surface state (roughness, wear rate...) is particularly hard to set up because of the severe environmental conditions between finishing stands. Several attempts were done and the most promising is the rollscope. But, its goal is not to define the accurate roughness evolution of roll surface during a production schedule.

More conventional scientific approaches have to be done in order to have more details on roll surface evolution. Off-line measurements performed on industrial working rolls are required. Nevertheless, working rolls are not easily accessible and accurate measurements need a specific protocol in order to insure the validity of measurements.

The goal of this protocol will be to collect several replicas of roll surface (at different positions along roll width, different roll diameters (corresponding to several rolling campaign lengths), several roll grades) and to be able to analyse them (after sorting and "cleaning" rough acquisition data from an interferometer) in order to define what are the specific dimensions of a scratch on roll surface. It will also allow us to localise the stand where scratches are the deepest. But, before the description of measurement protocol and the analysis of results, the working roll changing strategy has to be explained in order to understand choices that have been made for this study.

A/ Working roll change strategy:

The frequency of roll change varies depending on the finishing mill type, whether tandem mill or steckel technology. We will focus on the working roll change of a tandem finishing mill. Working rolls are directly connected to engine with shafts that is the reason why fast roll extraction during the production schedule is not allowed. A conventional roll change takes 10 to 15 min. As a result, it will be not possible to perform measurements during rolling.

In order to have continuous data on roll surface evolution, Centre of Research in Metallurgy (CRM) lab located in Belgium [LER10] set up a device named Rollscope whose goal is to make pictures of roll surface

at defined time interval. This system was used on roughing mill on a French plant rolling flat carbon steels. This experiment allowed defining and distinguishing 8 types of roll defects (banding, peeling, oxidation, small scratches, salt and pepper…). These industrial observations were coupled with lab rolling tests and during this lab test, sticking phenomenon was observed on roll surface.

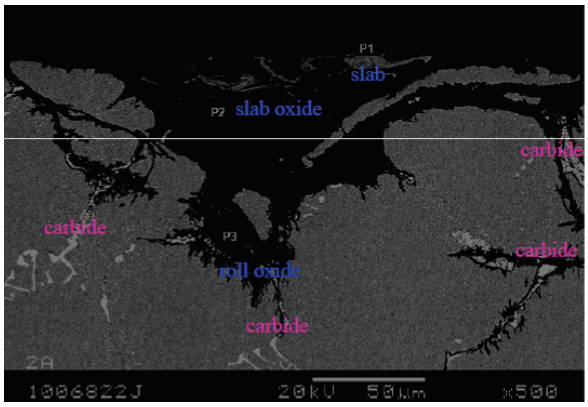

Fig. 59: Sticking on a crack caused by carbide oxidation [LER10]

Sticking occurred at the vertical of a large crack (80 µm deep and 80µm wide) caused by roll oxidation. The crack is localised at the former place of carbide, as we can see on figure 59. Nevertheless, Rollscope is still an experimental device that is more defined as a control system as Automated Surface Inspection Systems (ASIS). Moreover no numerous roughness data are available with this system, so no criterion based on surface roughness can be defined.

The working rolls of the finishing train are not all changed at the same time. Rolls of stand F1, F2, F3 and F4 are changed together and are used for two successive ferritic production schedules (without intermediary grinding). Other stands (F5, F6 and F7) are changed at each ferritic program. The two groups of rolls correspond to the grades used for ferritic rolling: 1-4 stands are equipped with HSS grade and stands 5 to 7 are equipped with ICDP grade. This strategy is based on the fact that, at the end of the first ferritic schedule, neither specific defect nor oxidation was found on roll surface. This choice was not made taking into account roll surface.

A ferritic schedule gathers between 100 and 140 slabs of various grades. The scheduling of product is made by width decreasing class and after by thickness decreasing class. AISI 430 (standard ferritic grade) and AISI 441 (figure 60) represent a global volume of 60% of the total production. Composition of a schedule is changing upon order and client demand, but some rules are defined to build up a ferritic schedule. The maximal length of a ferritic program is defined at 45 km per width category, and reduced to 30 km for limited standards (harder to produce). Roll change on stands F1 to F4 are required between two ferritic schedules if a ferritic program reaches the kilometre limit in all width category.

As a result, the large variety of configurations and industrial constraints (production rate and roll changing time, safety risks) imply that roll inspections have to be made on grinding workshop (Fig 61). After rolling, rolls are sent to grinding workshop and are placed in a cooling machine, spraying water onto roll surface in order to decrease roll temperature. After 30 minutes cooling, rolls are placed on a restricted area where safety conditions are maximal. Rolls are ready to be analyzed. As a result, roll surface is only accessible just after schedule end.

Investigations performed on roll surface will be made after the end of the first and the second ferritic program, by a non-destructive method. Replicas of roll surface will be made in order to be analyzed in TEMPO laboratory by interferometer device. Then, a huge volume of data produced by interferometer will be analyzed using an original methodology. Roughness parameters will be defined to be able to characterize the surface variations and visual analysis of replicas will be made and compared to bibliography.

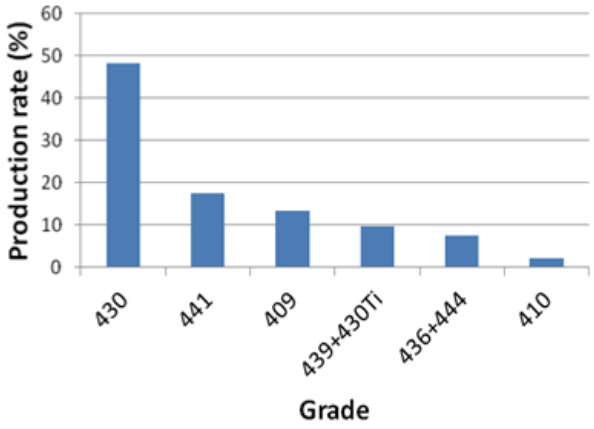

Fig. 60: Grade repartition in global production

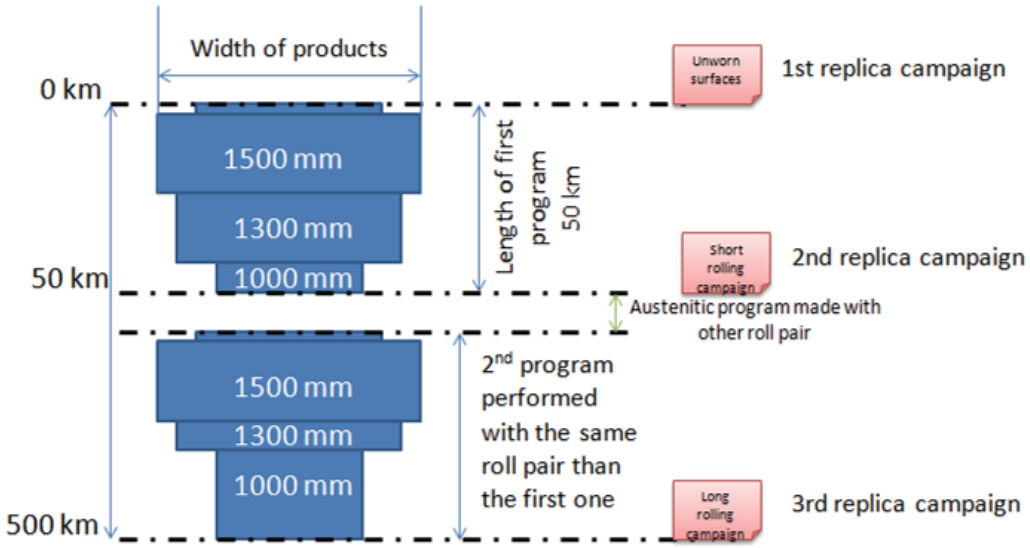

Fig. 61: Schematic representation of ferritic rolling program using two times the same roll pair.

B/ Replicas on working roll: protocol and analysis

1. Replicas on hot mill cylinder

In order to characterize the roll surface, and because of their large dimensions (from 680 mm to 760mm in diameter and 2,5 m long), some replicas onto the roll surface were performed.



Fig. 62: Replicas position on roll surface

On ferritic stainless steel production schedule, only 3 different strip widths are processed on the hot rolling mill of APERAM. Indeed, samples at 4 different chosen areas were taken as defined on the scheme in Fig. 62.

The first replica was taken in the middle of cylinder length, corresponding to the centre of the strip (of each width category), which correspond to the position C. A second sample was taken at 60 cm from the previous position in direction to the motor side, corresponding to strip width of 1300mm. A third sample was taken at 70 cm from the middle of the cylinder (strip width of 1500 mm). A last sample was taken at 1m from the middle. No ferritic strip of 2 m wide are produced, as a result, the surface taken as last sample corresponds to a non-worn part of the roll by strip rolling. Superior and inferior cylinders were analysed.

Replicas were made using the Repliset T3 resin (proposed by Struers®) after roll surface cleaning with cleaning agent and ethanol. Samples were identified by roll number, the position along cylinder length (centre, 1300 mm, 1500 mm, 2m), and strip length rolled with it, giving an idea of roll wear. The roll pairs were analyzed after 50 km and after 500 km processing.

2. Roughness measurements

The white light interferometer (NewView 7300, Zygo) is used for characterizing and quantifying surface roughness. Optical resolutions of x20 Mirau objective used are 0.71µm for x, y axes based on Sparrow criteria which take into account the lens numerical aperture and 0.01µm for z axis. Indeed, spatial sampling based on camera pixel size (0.55µm) is lower than the optical resolution. The inspected surface area is 1200 µm by 900 µm obtained by stitching 16 of each single measurement with 20% overlap. Figure 63 represents the 3D topography map corresponding to the upper third cylinder after 500 km of wear. Five surfaces are measured on each replica. As a total, one gets 70 3D surfaces to analyze (and in fact 16 times more due to stitching).

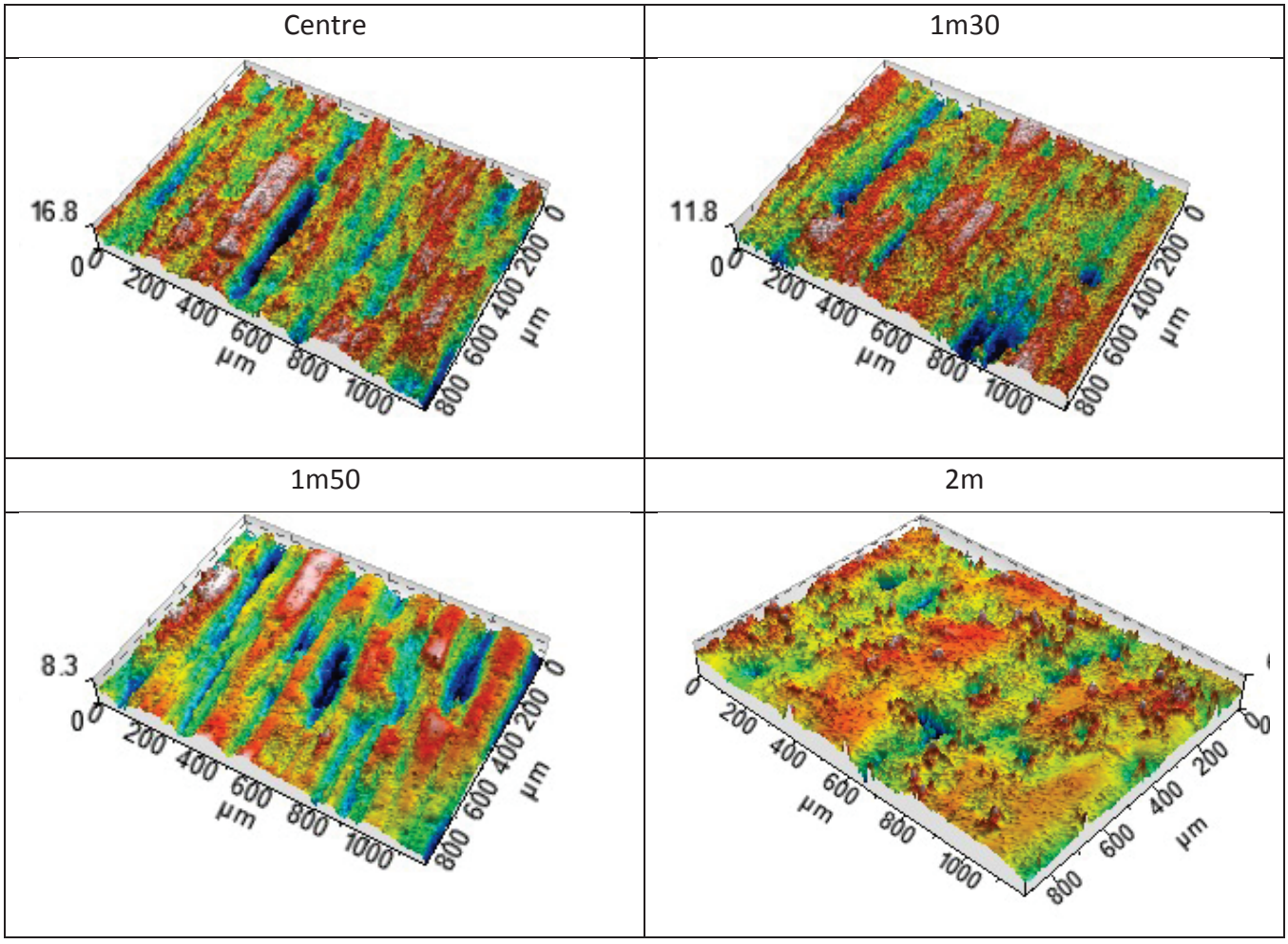

Fig. 63: Evolution of the topography along the axis cylinder in meter corresponding to the upper third cylinder after 500 km of wear.

2.1. The multi-scale decomposition

The Gaussian filter has been recommended by ISO 11562-1996 [ISO96] and ASME B46.1-1995 [ASM95] standards for determining the mean line in surface metrology. This filter was adapted in order to filter the 3D surfaces with a given cut off value [YUA00]. In this study, only the high pass filter will be presented (for the sake of simplicity, we omitted the results of pass band filter because best parameters were not

relevant in this study). Our system is used to filter all surfaces with different cut-off in order to obtain a multi-scale decomposition. The 30 consecutive steps are used in this decomposition with a cut-off varying from 2µm to 360µm. Figure 64 represents three high pass filters and three low pass filters for the surface decomposition. When the cut-off decreases, microscopic details appear on filtered surfaces.

Then 3D Roughness parameters are computed. 3D roughness parameters are defined by the following standards: ISO 25178 [ISO12] define 30 parameters, EUR 15178N [EUR93] also define 30 parameters but some are identical to those of ISO 25178 [ISO12]. Only 16 parameters are the latest ones, however S_z (maximum height of surface roughness) and S_{td} (texture direction) are calculated differently in both standards. Further, 7 3D roughness parameters related to surface flatness are defined by ISO 12781 [ISO11], and ASME B46.1 [ASM95] define 7 similar parameters as ISO 25178 standard [ISO12] (with different predefined filters) and one new parameter S_{Wt} (area waviness height). This gives a total of 56 different 3D roughness parameters, which will be considered in this study. The 3D roughness parameters (see Table of Annex 2) can be classified into the following groups: amplitude parameters, spatial parameters, hybrid parameters, functional parameters, feature parameters, other 3D parameters.

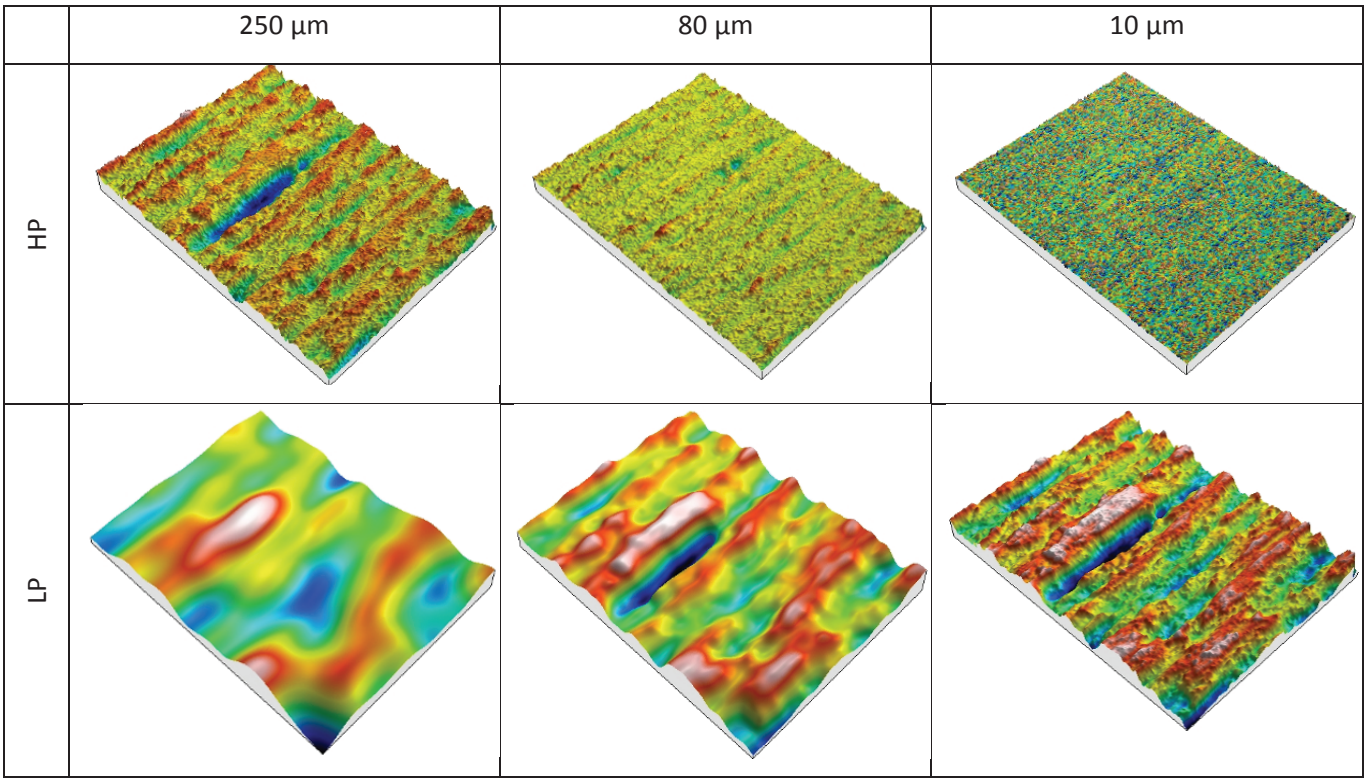

Fig. 64: Examples of multi-scale decomposition using Gaussian high pass (HP) and low pass (LP) filtering at cut off 250, 80 and 10 µm corresponding to the upper third cylinder after 500 km of wear measured at the center of the cylinder.

2.2. SELECTION OF THE REPRESENTATIVE TOPOGRAPHY

2.2.1. Principle of the Method

The aim of this work is to select the topography that is the most representative of the whole. This philosophy allows us to select only topography to visualize that will be very more comfortable to analyze process in other study. For each sample, N measures are carried out. Then different filtering cut-off are performed to reconstruct roughness and waviness of the surface leading to computation of $p_{i,\varepsilon,c,n}$ roughness parameters related to the nth surface ($i \in \{1 \ldots I\}$) computed at the filter *c* with a cut off ε. Then the mean of each roughness parameter computed from the N surfaces is evaluated leading to $\overline{p}_{i,\varepsilon,c}$ and standard deviation $\sigma_{i,\varepsilon,c}$. The indicator $q_{i,\varepsilon,c,n}$ is then proposed for the nth surface:

$$q_{i,\varepsilon,c,n} = \left(\frac{p_{i,\varepsilon,c,n} - \overline{p}_{i,\varepsilon,c}}{\sigma_{i,\varepsilon,c}} \right)^2 \quad \{13\}$$

Then the optimal surface seen by the $p_{i,\varepsilon,c}$ for the n surfaces is given by:

$$n_{opt}(i,\varepsilon,c) = n / \min_{n \in N} q_{i,\varepsilon,c,n} . \quad \{14\}$$

Then the different "best" surfaces $n_{opt}(i,\varepsilon,c)$ are counted to plot the frequency histogram that represents the number of multiscale parameters seen as better for the n surface and is noted $F_{n,opt}$.

Finally, the most representative n_{opt} surface is given by:

$$n_{opt} = n / \max_{n \in N} F_{n,opt} \quad \{15\}$$

This relation claimed that the most representative surface is closed to the mean of all surfaces characterized by all roughness parameters computed at all scales.

At the contrary, the less representative surfaces will be then given by:

$$n_w = n / \max_{n \in N} F_{n,w} \quad \{16\}$$

With

$$n_w(i,\varepsilon,c) = n / \max_{n \in N} q_{i,\varepsilon,c,n} \quad \{17\}$$

Surface n_w can be considered as irrelevant if statistically $F_{n_w,w} > F_{n,w}$, $n \in \{1 \ldots N\}, n \neq n_w$. This method allows us to find surface that are badly recorded or presents some default and must be excluded from the analyses. We will define these surfaces as irrelevant surfaces. However, to statistically prove that $F_{n_w,w} > F_{n,w}$, one have to construct an original protocol to construct the probability density function of each $F_{n,opt}$ and $F_{n,w}$. Then, we decide to use the bootstrap philosophy to construct an estimator of the probability density function.

In order to include the robustness of the relevance of roughness parameters, bootstrap is used that allows estimating the error in the computation of the coefficients of statistical modeling. For these reasons, we shall introduce a recent technique called the bootstrap which is a resampling technique [EFR85, HAL92]. The basic idea of the bootstrap is to create a new dataset by randomly sampling with replacement from the original data set and then performing the same statistical analysis as carried out on the original data set.

2.2.2. The irrelevant surfaces.

Let now investigate if from all measurements (96 series of measures), one gets a surface that can be seen as irrelevant. For that, we process to 100 bootstraps. These steps allow us to suppress some irrelevant measures and then to select the most representative one. The next step in the analysis is to calculate the mean Probability Density Function (PDF) of the F_n for all parts of the 14 cylinders. Then visually, irrelevant surface can be easily found and suppressed from the analyses. For example, a suspicious surface is found and represents Stand F2, 53 km, inferior, centre. Figure 65 represents the value of these F_n PDF for this part of measurement (histograms). The F_3 is seen higher than other F_n and can be seen as non representative or irrelevant. It can be observed that the irrelevance is very high because no overlap appears and surface 3 can be seen as different from the others and must be excluded. By analyzing images (figure 66), it can be seen that this image presents an abnormal smoothing in the bottom left part and is due to a bad replication of the surface by the elastomer.

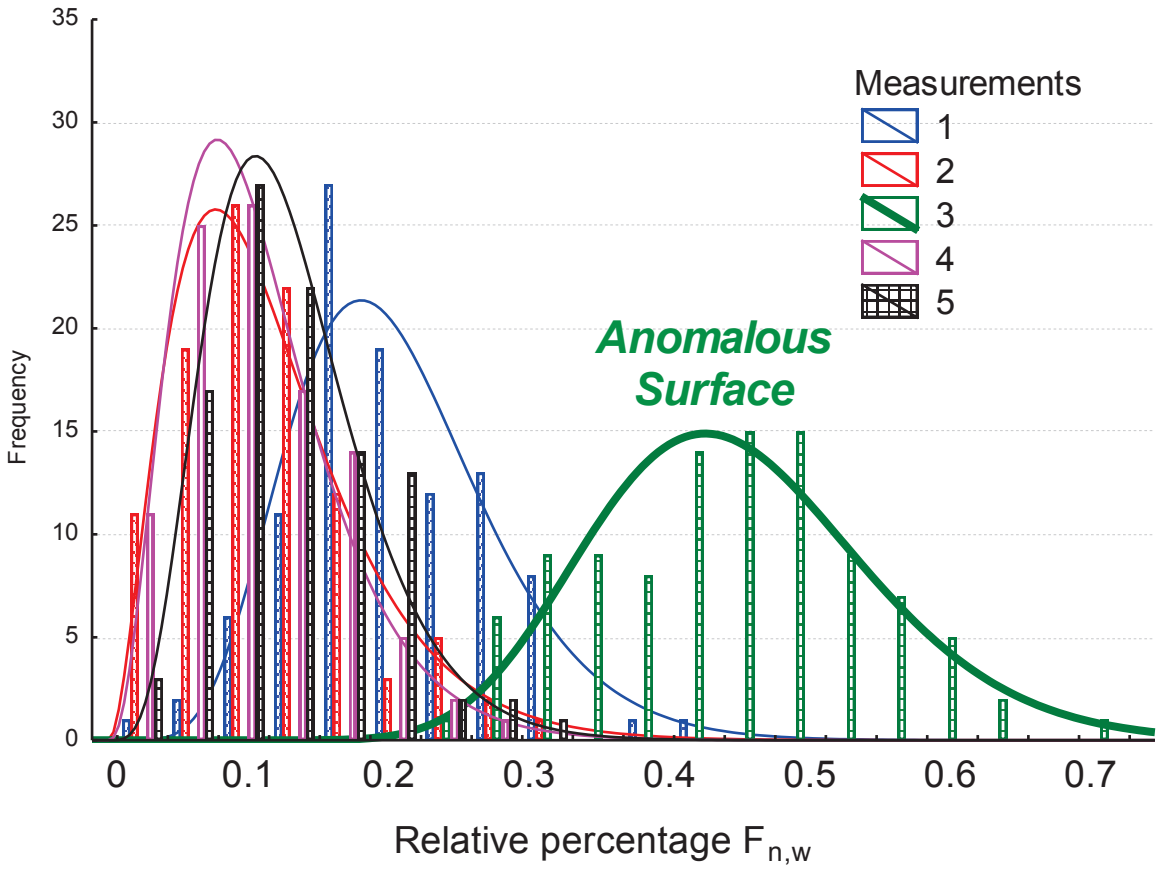

Fig. 65: Analyze of the F_n PDF for the anomalous surface corresponding to the 5 surfaces taken at of a worn cylinder Stand F2, 50 km, inferior, centre.

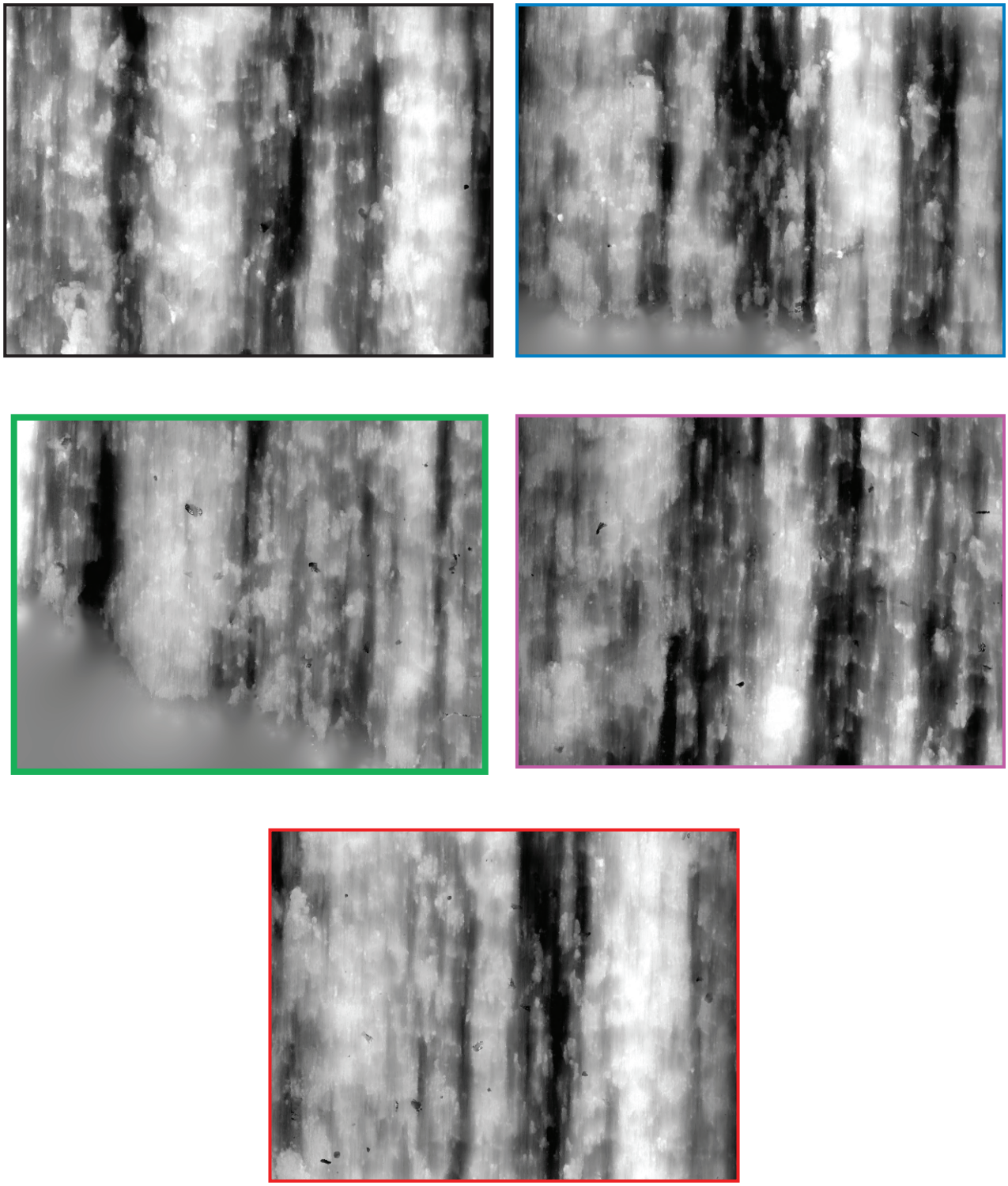

Fig. 66: Similar topographical images on the center of a worn cylinder Stand F2, 50 km, inferior, centre (the anomalous surface is in green).

2.2.3. The representative surface

Let now investigate among all measurements (96 series of measures), which one is the most relevant surface for all replicas. After suppressing the irrelevant surface, we process again to new analyses with 100 bootstraps. Next step in the analysis is to calculate the mean Probability Density Function (PDF) of the F_n for all parts of the 14 cylinders. Let now analyze an example: for Stand F2, 50 km, inferior, 2 meter (figure 68). The figure 67 represents the value of these F_n PDF for this part of measurement (histograms).

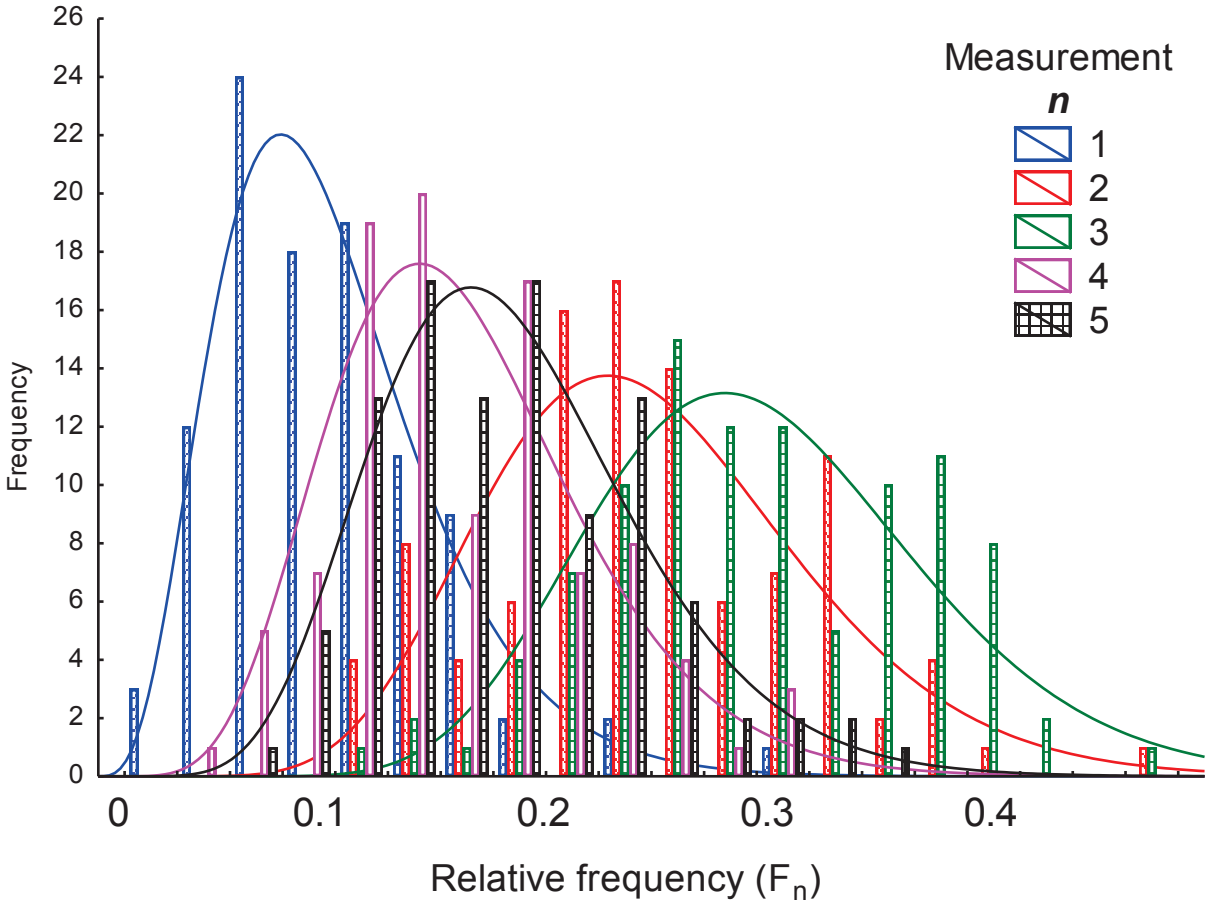

Fig. 67: Analysis of the F_n PDF for the anomalous surface corresponding to the 5 surfaces taken at of a worn cylinder stand F2, 50 km, inferior, 2 m.

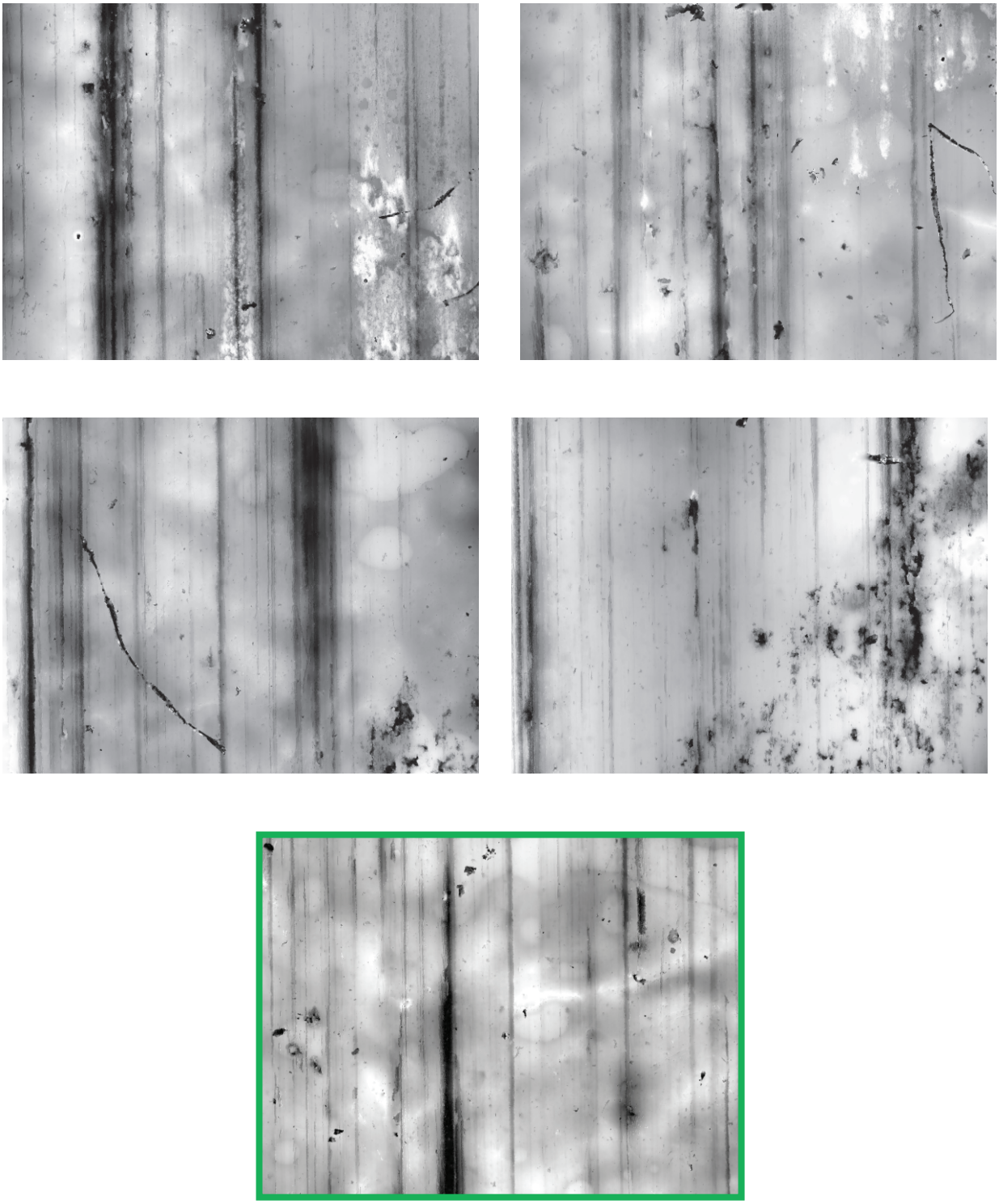

Fig. 68: Similar topographical images on the center of a worn cylinder Cage F2, 50 km, inferior, 2m (the most representative is in green).

C/ Observation of replicas topography

The method is then applied to a complex system: the wear of cylinders of a 7 stands tandem hot rolling mill. At different zones of the cylinder, replicas are done during process on all cylinders at different lateral positions. (See. Scheme of Fig. 69) Algorithm explained in previous paragraph is then applied and most representative images are selected and used to analyze topography.

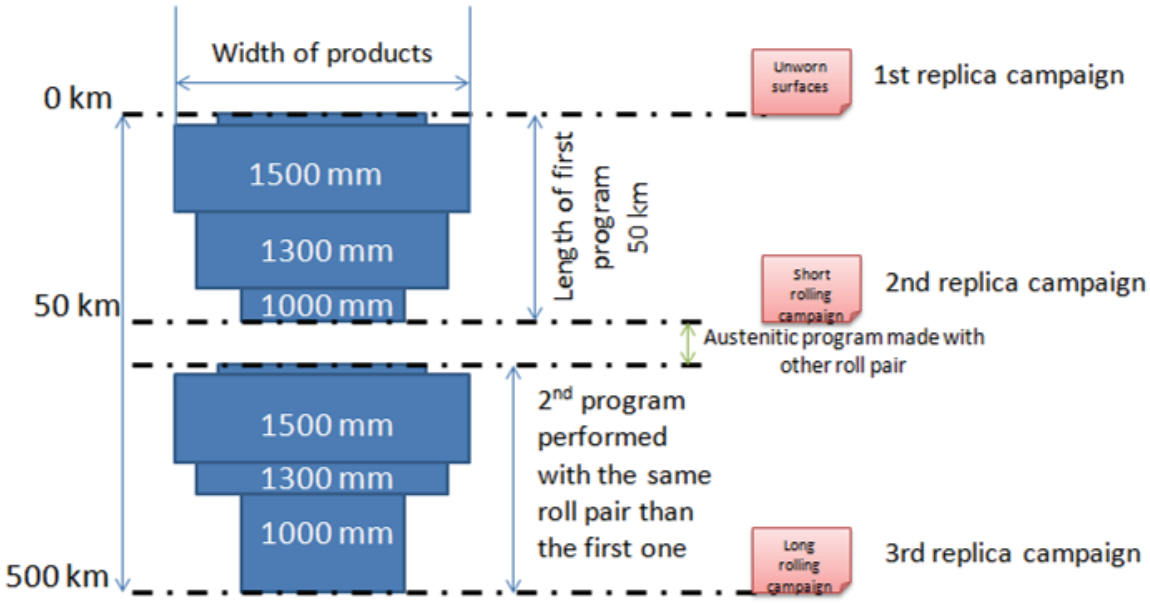

Fig. 69: Scheme of replica campaigns done in ferritic rolling schedule

The goal of this paragraph is to have a precise idea of topography evolution on different stands. We will try to understand roll wear mechanism based on topography evolution and check if geometrical pattern exists. The goal is also to characterize this pattern and to compute average dimensions in order to compare it to the artificial scratches performed by W. Jin [JIN00] and oxide layer dimensions reported in first chapter.

The effect of roll grade will be also studied thanks to a comparison between stand F4 and F5, because these two stands have similar rolling conditions (speeds, reduction ratio, temperature) and the main difference between these two stands is the roll grade (HSS on stand F4 and ICDP on stand F5).

1. Evolution of topography on each stand.

1.1 Comparison between unworn areas (0 km) and center of the roll position (worn areas: 50 km)

As already explained, all replicas taken corresponding to strip width of 2m are unworn areas of the roll, because Aperam do not roll ferritic strips of such width.

The following figure 70 and 71 gather the replica topographies of 2m position on seven stands.

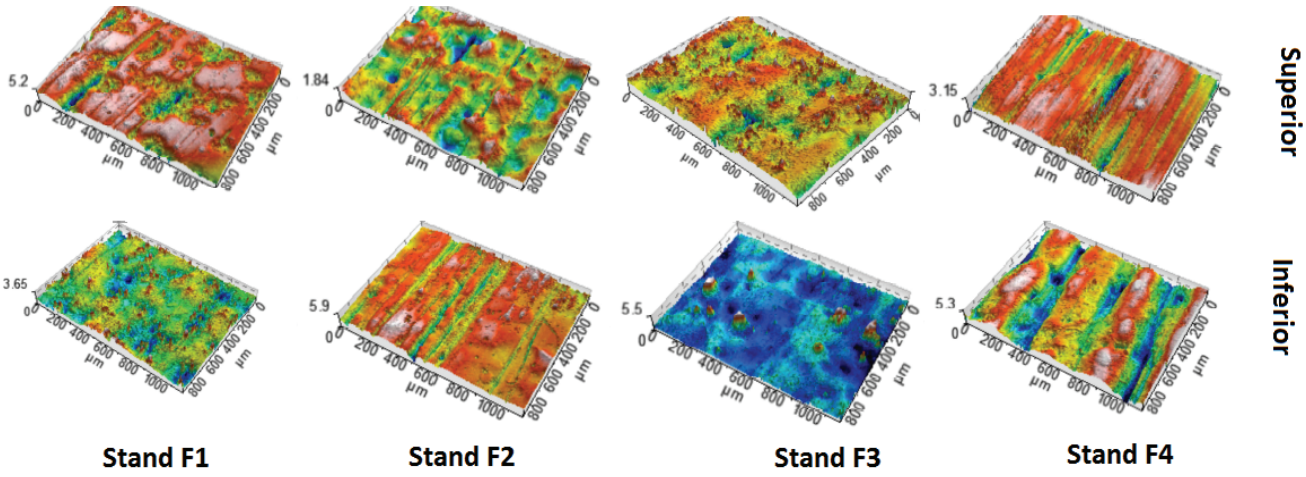

Fig. 70: Replicas of 2m position area of superior and inferior HSS cylinders from stand F1 to F4

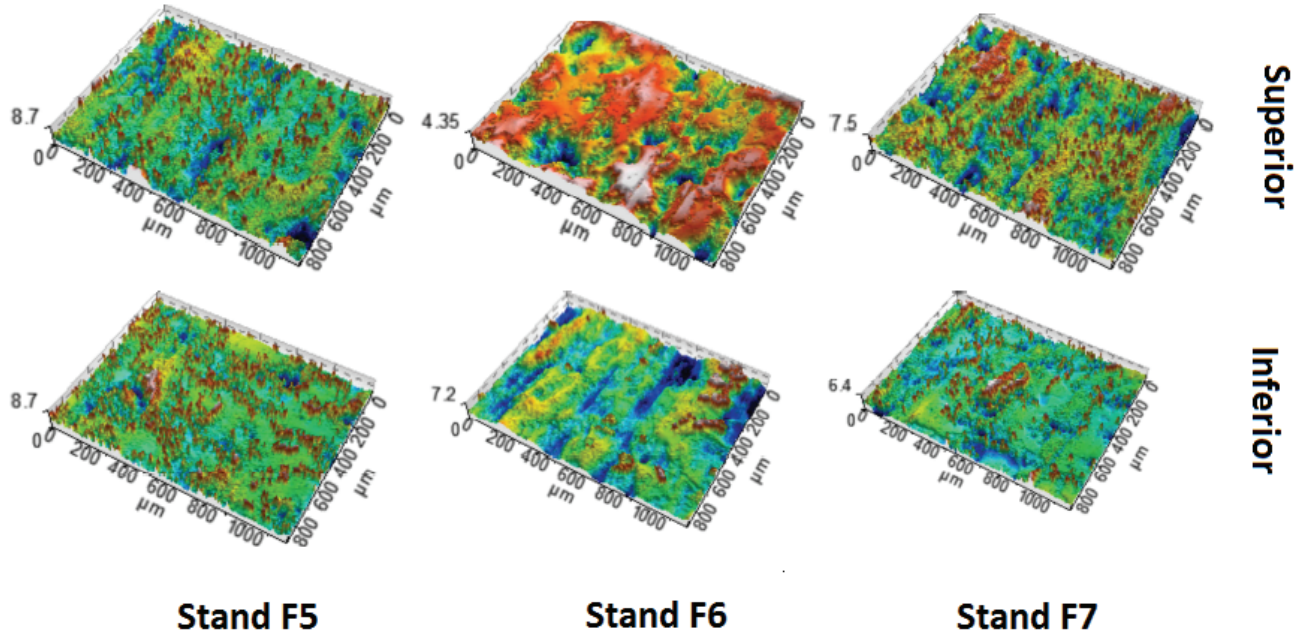

Fig. 71: Replicas of 2m position area of superior and inferior ICDP cylinders from stand F5 to F7

As the roll is fresh from grinding, all replicas of figure 70 should have approximately the same topography. This remark is also available for fig 71 (ICDP rolls). Nevertheless, Figure 70 highlights the high heterogeneity between superior and inferior HSS rolls. We can notice the presence of thin scratches especially on stand F2 and F4. These scratches are not very deep and can be assimilated to grinding scratches made during the grinding operation.

On stand F1 and F6, topography of superior and inferior cylinder is characterized by large plateau. This could be due to direct contact between working and backup rolls at roll extremities, because of their deflection during rolling.

Deepest scratches are inferior to 6 µm. The deeper scratch was identified on stand F2 and is around 6 µm depth. Other replicas seem to be more regular and no specific pattern can be easily identified. We can only notice a major difference between stands F1 to F4 and F5 to F7 which is probably linked to roll grade. ICDP rolls seem to have a topography characterized by small protuberances (brown dots).

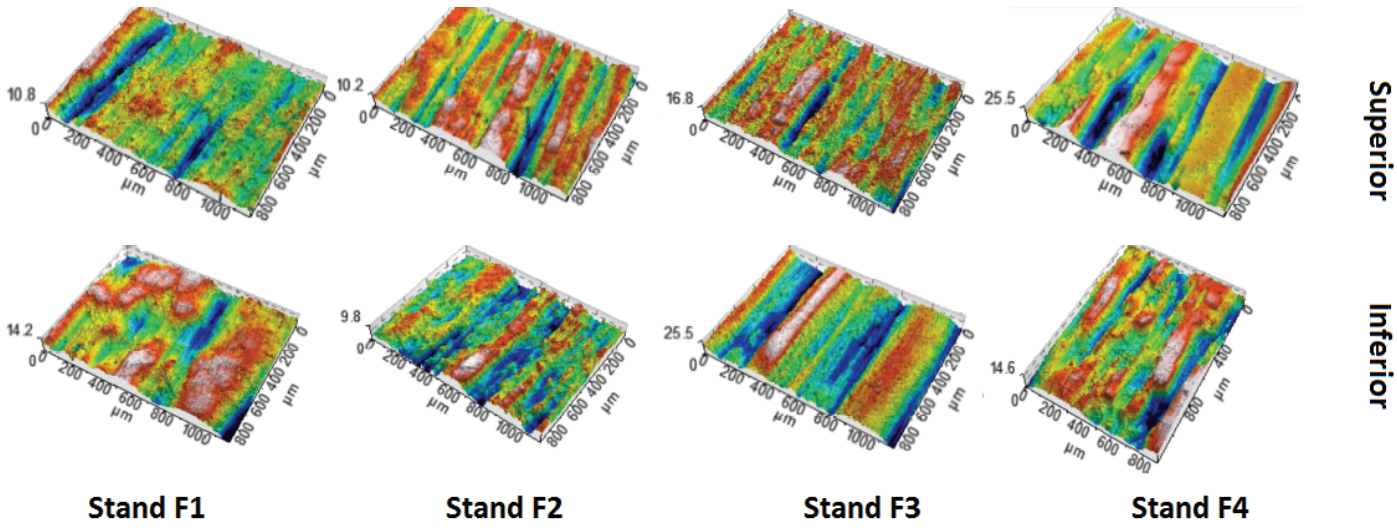

Fig. 72: Replicas of centre of superior and inferior HSS cylinders from stand F1 to F4

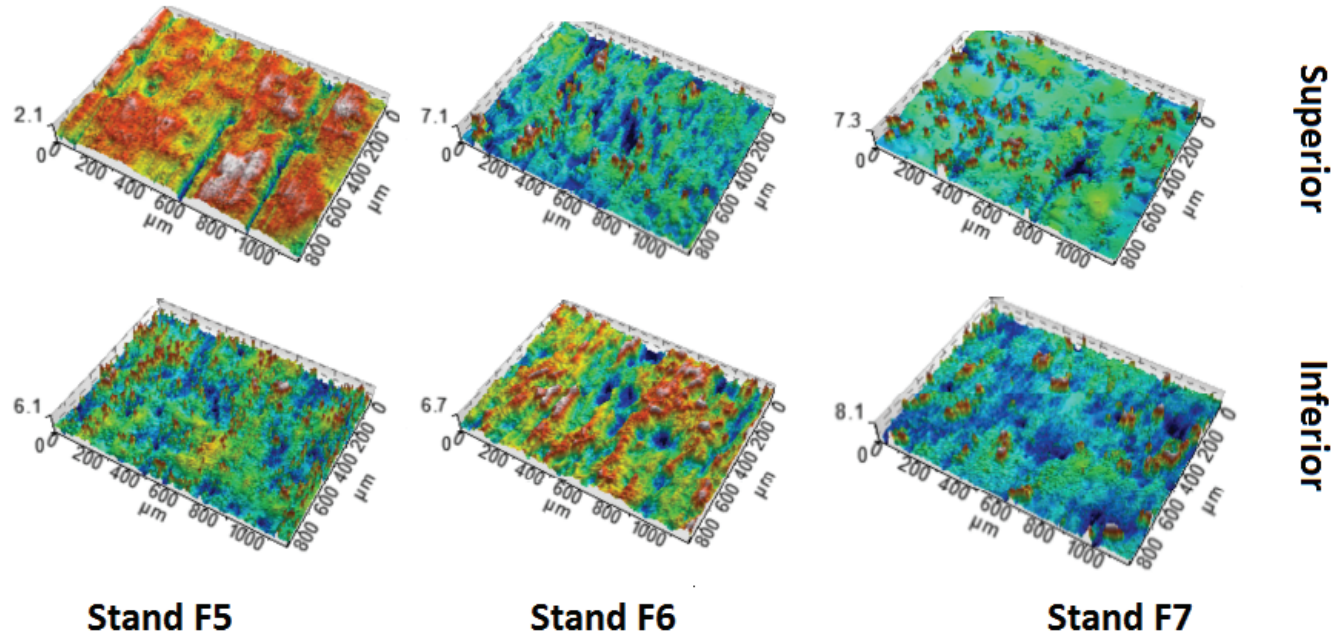

Fig. 73: Replicas of center of superior and inferior ICDP cylinders from stand F5 to F7

Contrary to Fig. 70 and 71, replicas on Fig. 72 and 73 were taken on worn surfaces. On HSS rolls, large and wide scratches can be identified (blue lines), and are assimilated to scratches induced by strip rolling. The vertical axis on roughness measurements clearly shows that these scratches are up to five times deeper that original grinding scratches (25 µm).

Deepest scratches are inferior to 26 µm and were identified on stand F3 and stand F4. These two stands are the conventional stands noticed to be the most worn in terms of radius decrease (NB: The roll shop investigates wear of roll by measuring the roll diameter decrease after successive grinding and compare it to perform statistics on supplier, type of rolling program…). It is mainly due to reduction scheme and thermal profile of the strip. In terms of rolling forces, stand F3 and F4 are the most solicited to decrease strip thickness. Depending on stands, size and density of these scratches can be very different. It will be studied in much more details on the following paragraph dedicated to scratches investigation by means of roughness parameters. Contrary to HSS rolls (Fig. 72) where scratches can be easily identified, on ICDP rolls (Fig. 73), no wide scratches can be identified. ICDP rolls are much more concerned by homogene roughness linked to carbides wrenching.

1.2. Effect of roll grade on roll surface evolution

We will focus on topography of cylinder surface on stand F4 at 50 km and 500 km (long and short rolling campaigns) according to different positions on its length, for top and bottom cylinder. (Fig. 74)

1.2.1. Example of stand F4 – HSS roll

As already explained in previous paragraph, there is no ferritic production in 2m width, as a result, on the right column of figure 74, replicas should have similar topography. Nevertheless, we can see a significant difference between superior and inferior cylinder. On the superior cylinder, we can observe very linear stripes that are representative of the grinding operation (Fig. 75). On the contrary, on the bottom cylinder that has only rolled 50 km of strip, we can observe small dots (in red). These dots (Fig. 76) seem to make round shapes on the surface whose diameter is approximately 100 µm. Grain size on HSS cylinder can be observed on appendix 1, and have a similar size, around 100 - 200 µm in diameter.

We suspect that these dots are the carbides located in grain boundaries oxidized by cylinder heating during rolling. This phenomenon was highlighted by several authors [ZHU10, ZHU11, JOO07] that pointed out that all carbides start to oxidize before the matrix and within carbides, the MC type carbides containing Vanadium is the first to be oxidized, at 550°C after 30 min in dry air. Moreover, thanks to the description of carbides oxidation made in [ZHU10], we think that red areas of figure 74 corresponding to unworn areas (4th column) correspond to a grain covered by Vanadium carbides. The blue areas could correspond to a grain containing only Chromium and Molybdenum carbides, having a slower oxidation rate.

Cooling of cylinder is made by a spraying system on cylinder pair and we know that the cooling of the inferior cylinder is less efficient (than the cooling of the superior cylinder) because of effect of gravity on water jet. The contact time between the water and the cylinder is higher on superior cylinder than on inferior one. As a result, we suspect that this difference in cooling will be sufficient to promote a small over-oxidation of cylinder surface especially on inferior cylinder.

The replica corresponding to the inferior cylinder at 2m width position after 500 km rolling looks like a worn surface and it is particularly difficult to know if this shape is due to an advanced oxidation state cumulated by irregular grinding operator or the result of heterogeneous wear having an

unknown origin. What is comforting is that the height of irregularities is about 5 µm maximum against 15 – 20 µm for worn surface. So, the topography of this replica could be due to accidental stripes.

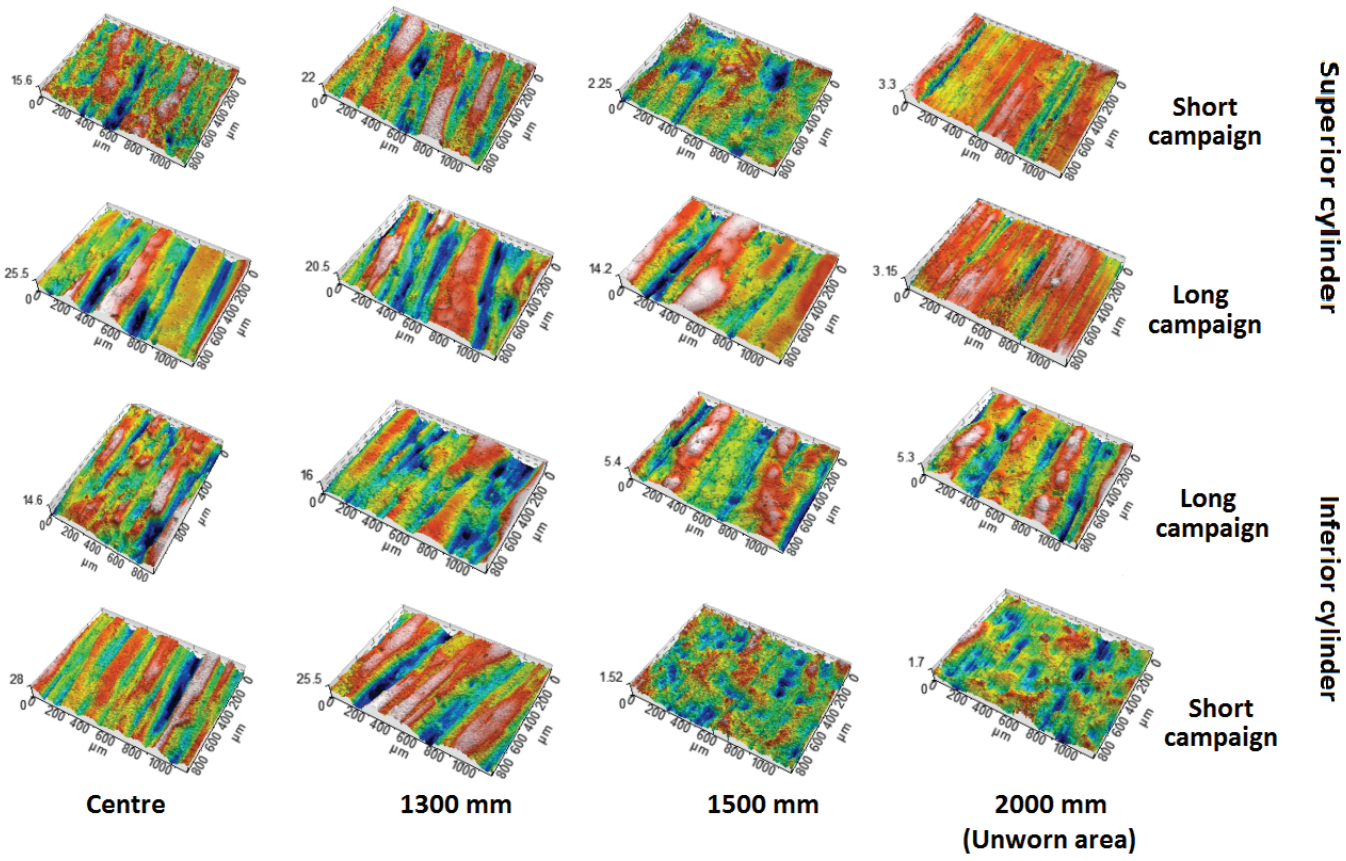

Fig. 74: Evolution of the representative topography along the axis cylinders stand F4.

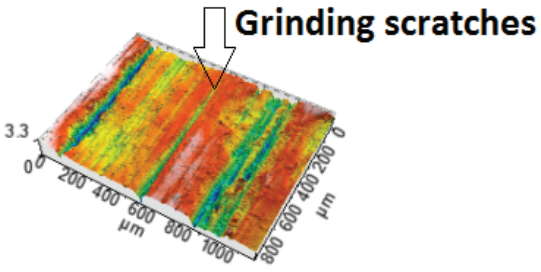

Fig. 75 : Grinding scratches

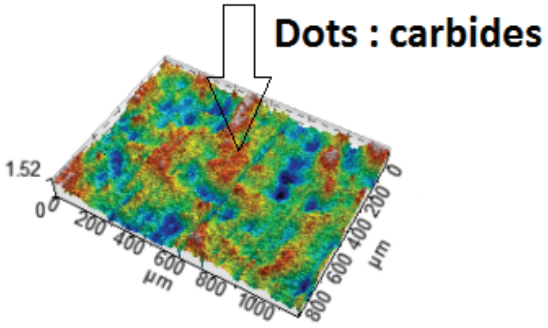

Fig. 76: Dots

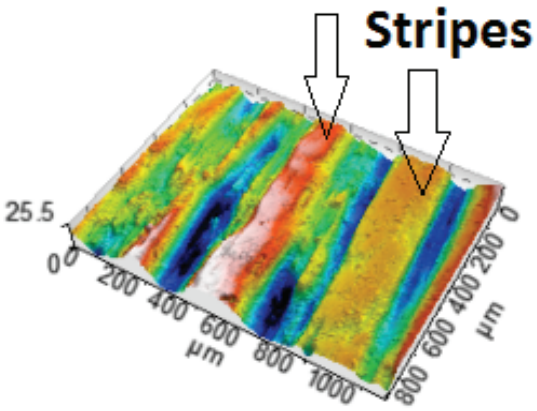

Fig. 77: Stripes

The replicas corresponding to 1,5 m strip width are quite simple to analyze. The first production schedule rolled coils up to 1300 mm width and the second one rolled up to 1550 mm coil width. As a result, we can notice that on the superior and inferior cylinder, all replicas corresponding to the short campaign (50 km) are similar to the replica corresponding to 2m width, inferior cylinder, 50 km. So, the topography corresponds to the oxidation of carbides due to thermal conduction in the cylinder. On replicas corresponding to the long campaign (500 km), large stripes (Fig.77) can be easily found on the surface. These large stripes are due to the wear induced by coil edge rolling.

The replicas corresponding to 1,3 m coil width are quite equivalent between the superior and inferior cylinder. We clearly observe a difference between the short (50 km) and the long campaign (500 km). On the short campaign, stripes seem to be larger but with a lower density, opposite to the long campaign where stripes seem to be thinner but the density of these stripes seem to be higher. It could be explained by the fact that on the short campaign, these stripes correspond to the rolling of coils edges of 1300 mm width, representing a side effect. On the long campaign, stripes due to edge rolling will be affected (partially erased?) by rolling of wider coils, so the large stripes will be eroded by the rolling of smoother surfaces.

The replicas corresponding to the middle of cylinder length, so to the middle of the coil, are more homogeneous. Thin strips are observed on replicas corresponding to the short campaign and more severe stripes (higher amplitude) are observed for the long campaign, translating a more severe wear.

1.2.2. Example of stand F5 – ICDP roll

The topography of the replicas presented in figure 78 is very different from those on figure 74. The major difference between the two stands is that the fifth stand is associated to ICDP cylinders for rolling of ferritic stainless steels.

The replicas concerning the 2m position are characterized by small (red) dots (Fig. 79) randomly spread over the cylinder surface. There is no specific geometric shape associated to the position of these dots. The density of these dots seems higher on the replicas corresponding to the long campaign (500 km). There is a difference in density between the superior and the inferior cylinder on

the short campaign. The height of these dots is around 7 to 16 µm, which is very high compared to the values found on figure 74.

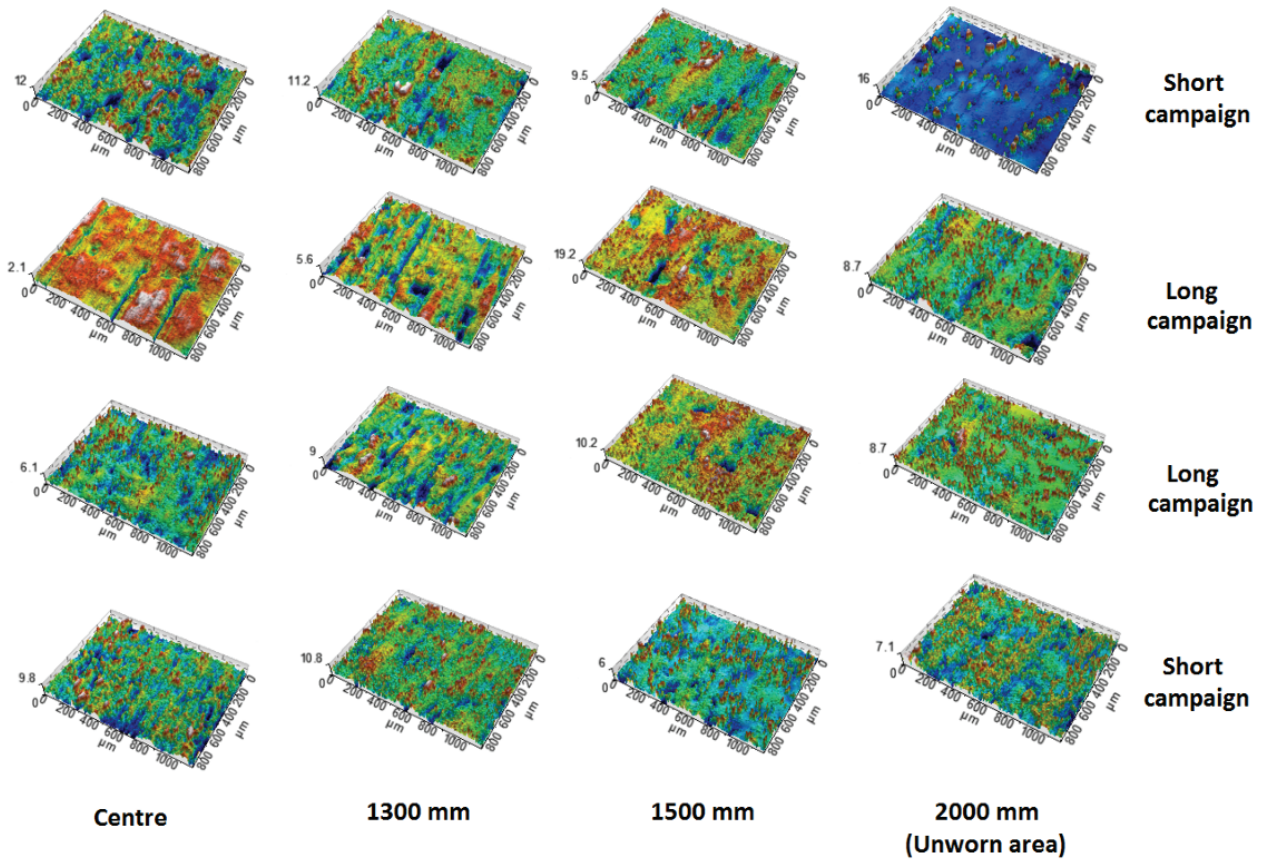

Fig. 78: Evolution of the representative topography along the axis cylinders stand F5.

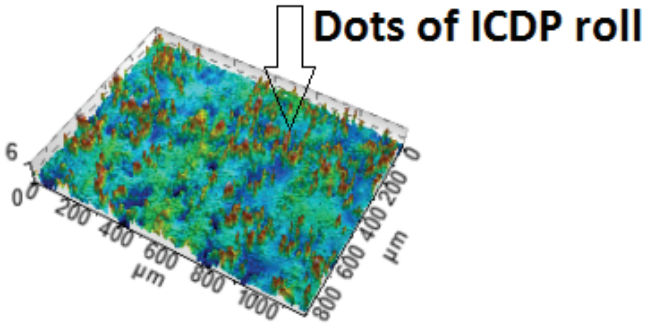

Fig.79: Dots on ICDP roll

We notice that the height of dots tends to decrease with length of coil rolled on worn areas (center, and 1,3 m width) and between the ground and worn areas : the higher the wear, the lower the height of the dots. Nevertheless, these results are opposed in terms of dots density. The maximum is reached on the replica corresponding to the center of the cylinder, the long campaign (500 km).

Based on observations made by K.H. Ziehenberger and al. [ZIE07], these dots could be due to

oxidation of carbides at cylinder surface. Indeed, with increasing wear, the amount of graphite at cylinder surface will increase, leading to an increase of cylinder roughness.

Based on micrographs of this study, we observed that the corresponding size of graphite precipitates is around 50 µm which could correspond to the size of the dots. The possible oxidation of Cementite (Fe_3C carbides) was also confirmed by H. Chaudansson and al. [CHA92] on ICDP grade at 700°C.

Another interesting remark is that the highest dot noticed on stand F5 (on the long campaign) is around 16 µm compared to 26 µm for the deepest scratch on stand F4. It shows that ICDP roll surface is less prone to have deeper irregularities than HSS one, but density of these irregularities seems to be higher on ICDP than on HSS. As a result, with these elements, it is very hard to conclude if ICDP grade will induce more easily sticking phenomenon than HSS.

If we take into account only depth of irregularities on roll surface, we could propose that HSS grade will induce higher sticking defects than ICDP grade. But, at equivalent pressure level, we know (by industrial experience and also I. Guillot [GUI90] work) that ICDP are more concerned by sticking phenomenon than HSS grade. It shows that **the height of roll surface irregularity is not the only parameter that explains the different sensitivity of roll grade towards sticking phenomenon**.

1.3. Partial conclusion based on topography

In this paragraph, we learned that rolls have heterogeneous wear even in areas of the roll that are not in contact with the stainless strip. The areas which are not in contact with rolled metal are degraded by two main phenomena: the direct contact between superior and inferior roll and surface oxidation due to thermal conduction from the strip to the roll. Oxidation phenomenon is starting on carbides and then propagates to the matrix.

This study also highlighted that topography of HSS rolls is characterized by three main patterns, revealing different wear modes. Worn areas can be characterized by two patterns: the first one is small dots that could be oxidized carbides, and large scratches. ICDP rolls have only one characteristic pattern looking like protrusions (that could be the consequence of Cementite oxidation) of 6 µm high.

If we are taking into account the mechanism proposed by W. Jin and al. [JIN00], sticking HSS is more prone to be generated close to edges of strips having a width of 1300 mm and seems to be created at the stand F3 and/or stand F4. These observations confirm the industrial knowledge and why following investigations will be performed on HSS roll.

On this basis, we could deduce that:

- HSS rolls are more prone to generate sticking than ICDP ones.
- An irregularity of 26 µm depth seems to be sufficient to generate sticking.

But, these two conclusions are not correct, because it was already demonstrated that ICDP is more susceptible to generate sticking than HSS at equivalent pressures [GUI90] and that a scratch of 26 µm is too small to penetrate an oxide layer higher than 35 µm.

Our conclusion is that maximal height of the roll surface irregularities is not the only or the main criterion that could explain the initiation (and sensitivity) of sticking phenomenon.

Nevertheless, the value of **26 µm is not the characteristic depth of HSS scratches**, because it is only the maximal distance between the lowest ordinate and the highest ordinate of the replica. Using the 3D analysis to define the depth of a scratch is not the best way. 3D analysis is an easier way to track main differences between atypical patterns. But our goal is to have a better evaluation of scratch depth, as a result, we need to perform a roughness study on 2D images and use the most appropriate roughness parameter to define what the statistical dimensions of a scratch are.

D/Characteristic dimensions of HSS scratches

The goal of this paragraph is to define the characteristic dimensions of a scratch on HSS roll. 2D roughness analysis based on previous replicas will be useful. Secondary elements will be investigated in order to understand how these scratches are forming. A similar investigation will be performed also on ICDP rolls in order to prove the origin of protrusions on roll surface. Before giving results, the methodology has been detailed according to stand F4, HSS superior roll, after 50 km rolling. The initial acquisition by interferometer is given in Fig. 80.

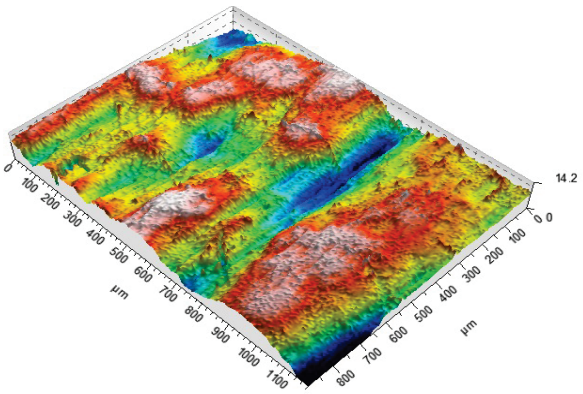

Fig. 80: Initial acquisition result by interferometry apparatus

1. Methodology used to analyze roughness

1.1. Step 1: Modify replica orientation.

NB: The 2D roughness analysis was not made based on 3D results. To perform 2D analysis we only use the acquisition of “rough” 3D files. As a result, the whole surface treatment has to be done anew.

Replicas are made manually along rolling direction. But the paper support of replicas surface cannot be positioned with a high accuracy, especially because roll surface is not flat and no physic marks are available. As a result, replicas can be lightly twisted and roughness measurements can be a source of uncertainty. A direction searching operator is used to define the main orientation of each replica and a correction on image direction will be applied (Fig. 81). The main consequence of this step is a small reduction of image resolution.

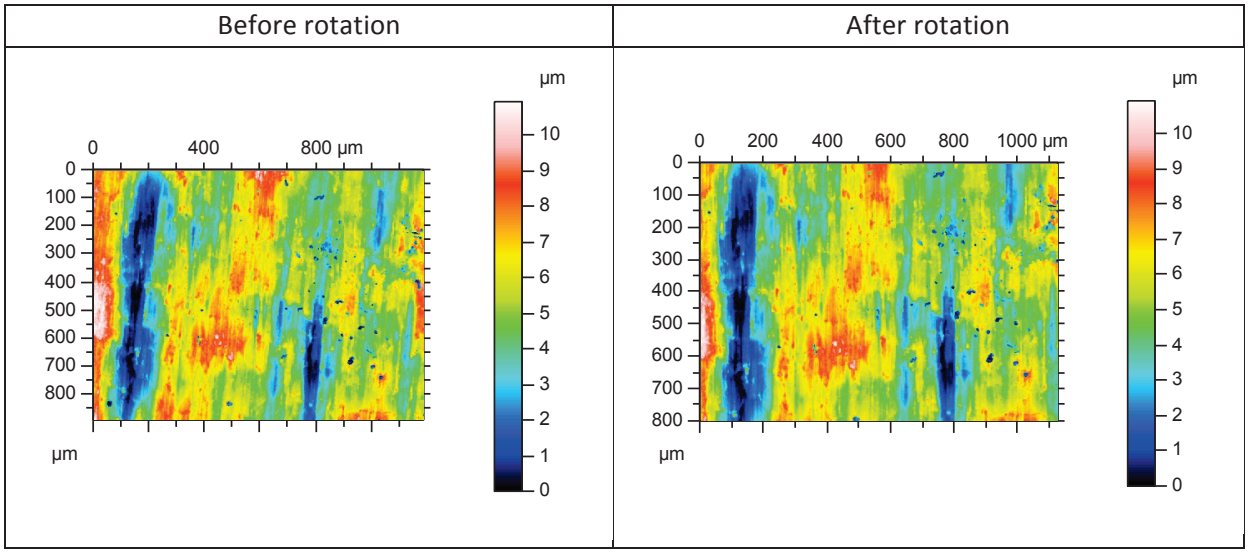

Fig. 81: Step 1 – Modification of image orientation to be parallel to rolling direction

1.2. Step 2: Filtration by double Gaussian filter

There are many solutions to filtrate roughness images but filtration leads to a decrease in roughness information, especially when filter is not adapted to the phenomenon that we need to observe.
We will test two types of filters: conventional Gaussian filter (25µm) and double Gaussian filter (25µm).

1.2.1 Conventional Gaussian filter (25µm)

Gaussian filter is a linear windowed filter. Its name is due to the fact that filter weights are calculated according to Gaussian distribution (defined by equation {18}). The highest importance is given to the central pixel and lower weights are given to close neighboring pixels.

$$G(x) = \frac{1}{\sigma\sqrt{2\pi}} e^{-\frac{(x-a)^2}{2\sigma^2}} \qquad \{18\}$$

Main drawbacks of this filter are the contrast decrease and the move of image edges.

The scratch located in the bottom left angle of the replica is due to bad execution of the replica. So it is an artefact that has to be removed to properly use the whole replica surface in order to increase the robustness of the statistic. The scratch does not disappear with the simple Gaussian filter, on high pass and low pass filter. (Fig. 82)

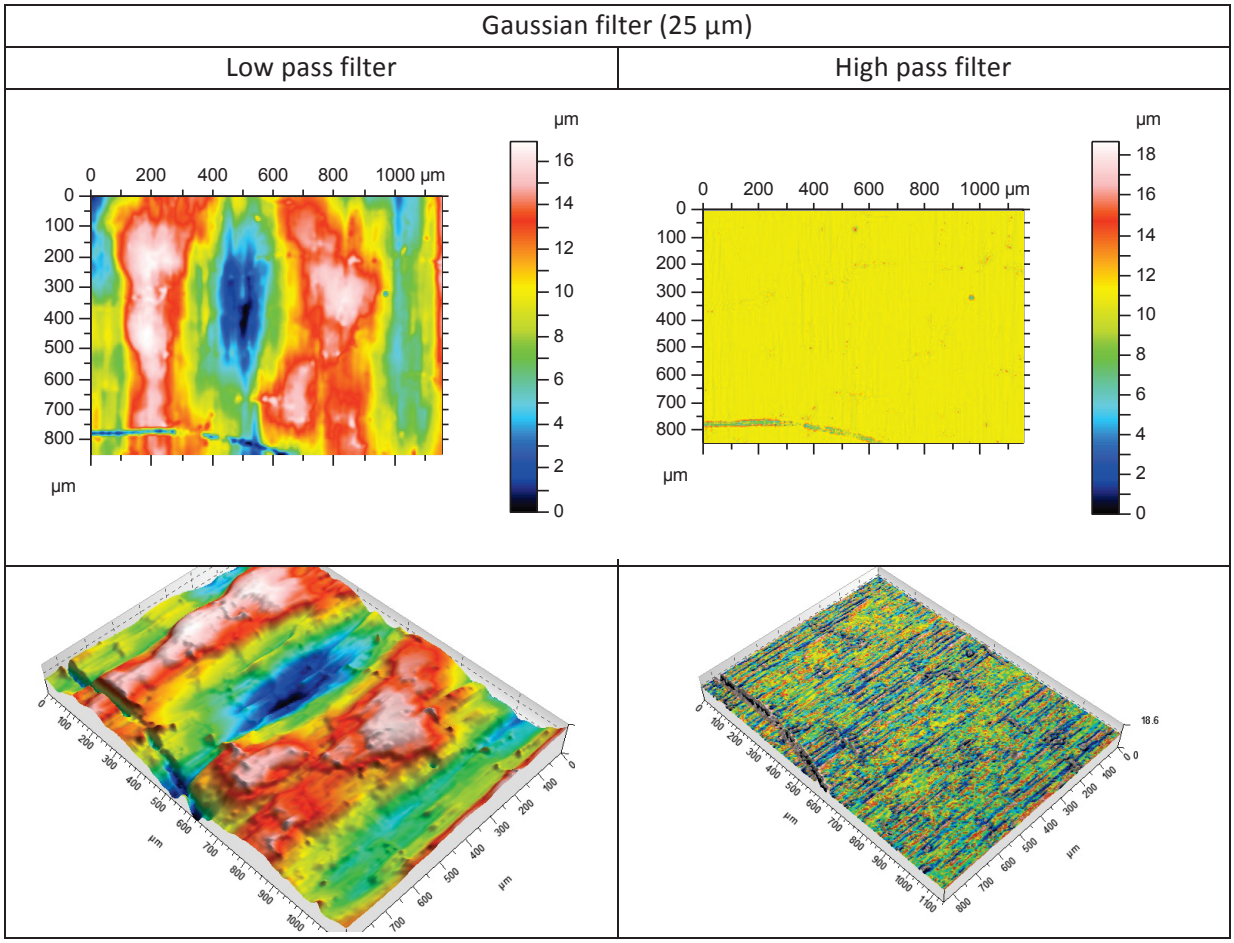

Fig. 82: Effect of simple Gaussian filter

1.2.2 Double Gaussian filter (25µm)

The filtering is done in different steps. The first one is preliminary filtering of the primary profile with the phase correction filter in accordance with ISO 11 562. All valleys lying under this mean line are removed and replaced by the mean line curve. The same filter will be used a second time on this new profile. A new profile will be determined which is the reference line. Final roughness profile will be determined by difference between the original profile and this reference line. Cut-off wavelength is generally taken equal to 0.8. (Fig. 83) [WHI13]

The scratch initially located on the bottom left of the replica is removed on the low pass filter. (Fig. 84) Plateaus are very well conserved but micro-roughness on them will be removed.
Double Gaussian filter will be definitely used for each replica.

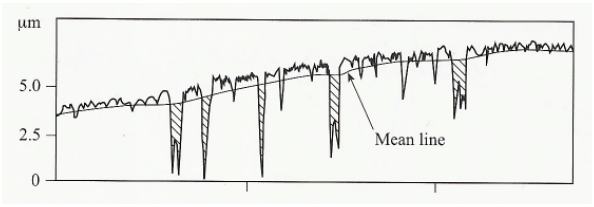

Unfiltered primary profile and 1st mean line (determined by filter ISO 11562)

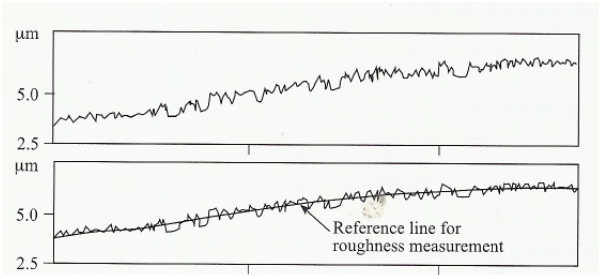

New profile after suppression of valleys

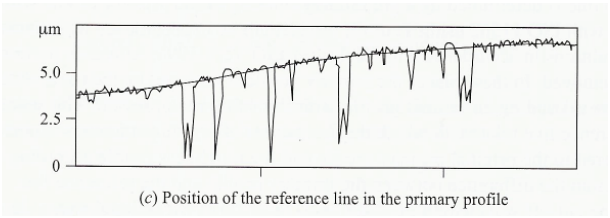

Reference line after the second Gaussian filter

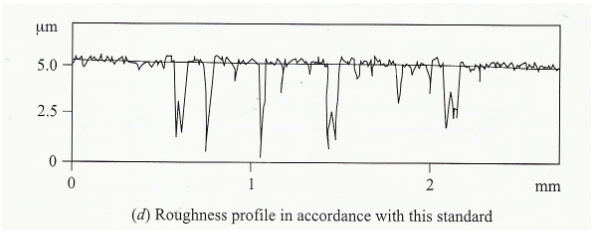

Final roughness profile

Fig. 83: Double Gaussian filter definition

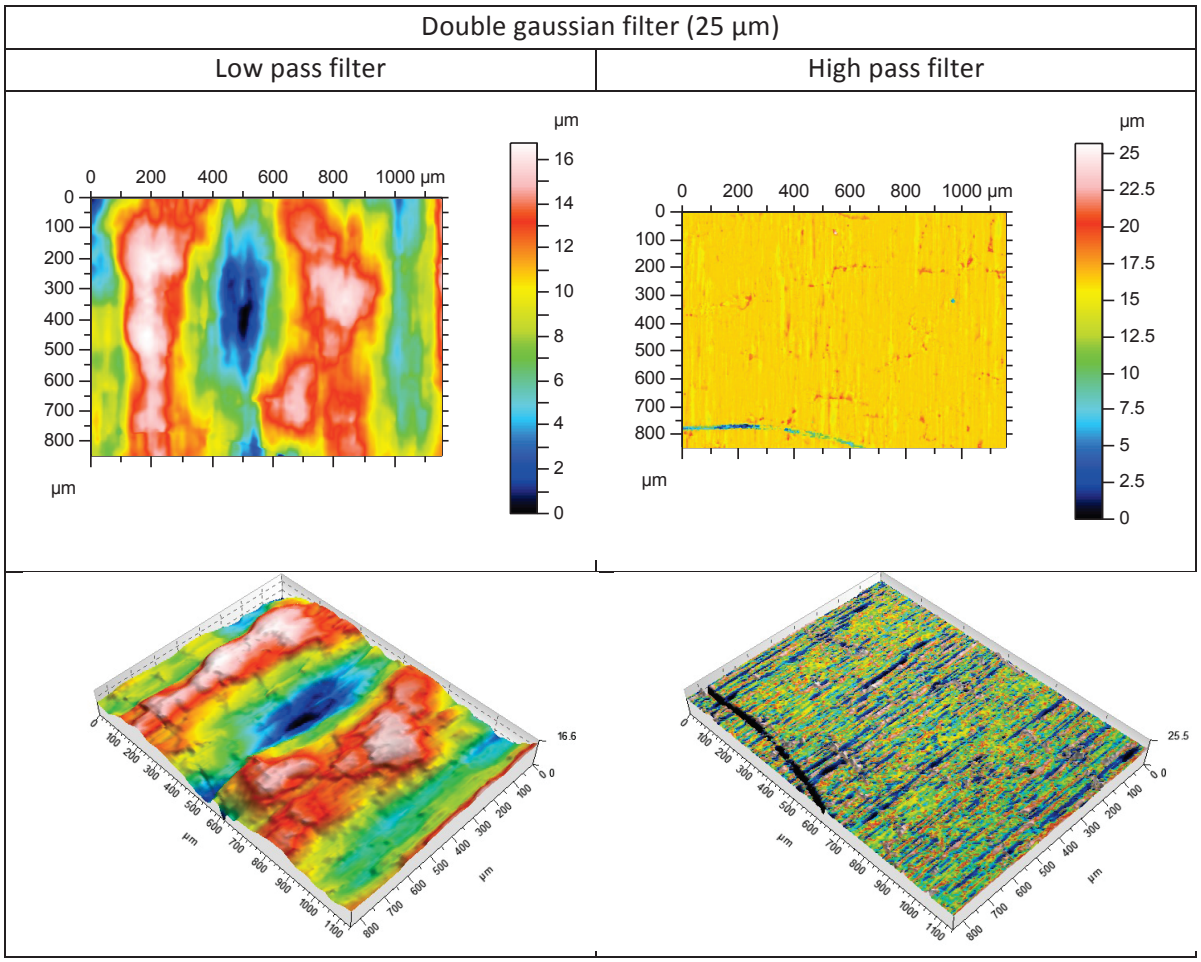

Fig. 84: Effect of double Gaussian filter

1.3. Step 3: Isolation of stripes and scratches

Our study was initiated to have much more details on scratches, found essentially on HSS rolls for stands F3 and F4. As a result, we used a technique that will help us to isolate scratches, and consequently stripes surrounding them (Fig. 85).

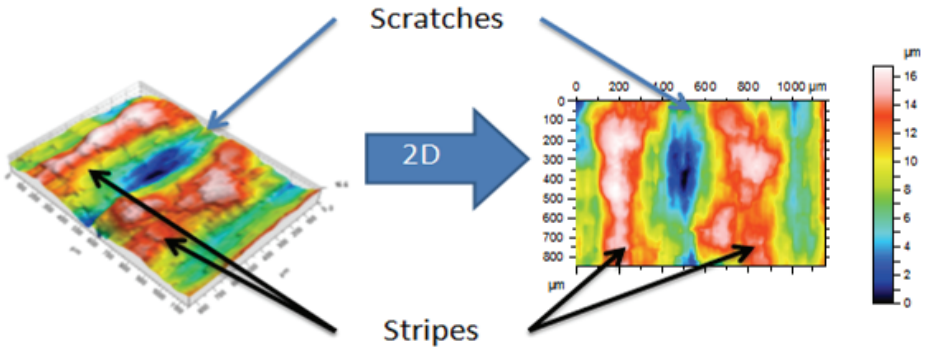

Fig.85: Definition of stripes and scratches

The filtered image is treated to become binary. An automatic program will remove small islets (inferior to 300 µm²) in the picture to have smoother contours. (Fig. 86)

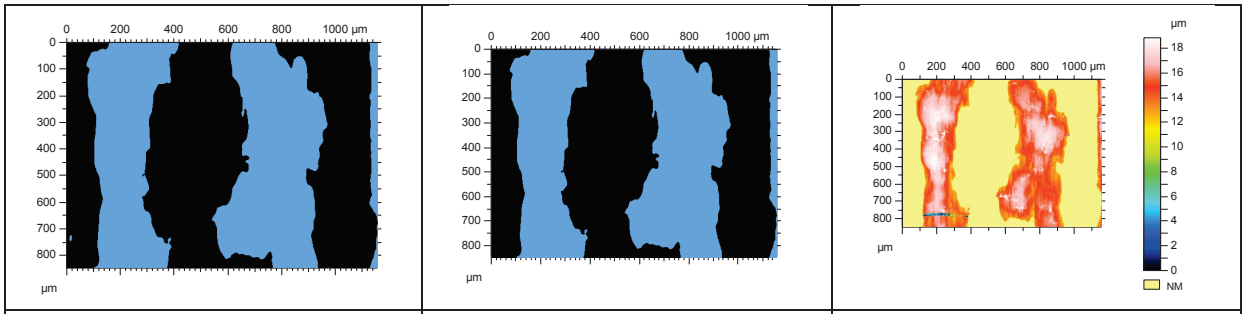

Binary image	Removal of islets	Reconstitution of image

Fig. 86: Isolation of stripes

1.4. Step 4: Statistical analysis

With the final image of step 3, some investigations are possible to find physical explanations to the studied phenomenon. Depending on the phenomenon we want to highlight, the roughness parameters that we have to take into account will change. Example of Fig. 87 is based on stripes dimensions characterization.

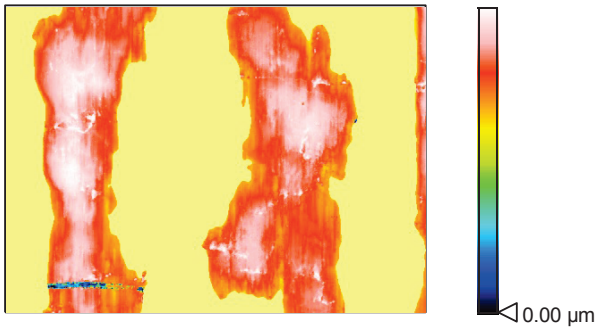

Nombre d'îlots	3
Volume moyen des îlots	0.00228 mm³
Hauteur moyenne des îlots	18.8 µm
Surface moyenne des îlots	149534 µm²
Rapport hauteur / surface	0.000126 µm/µm²

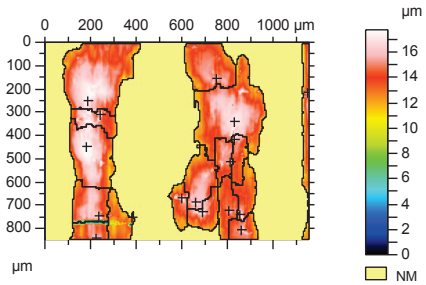

Nombre de motifs	17
Hauteur Moyenne	2.03 µm
Aire moyenne	0.0265 mm²
Volume moyen	4487 µm³
Périmètre moyen	889 µm
Moyenne des diamètres équivalents	172 µm
Moyenne des diamètres moyens	160 µm
Moyenne des diamètres min/max	111 µm / 276 µm
Moyenne des angles du diamètre min/max	14.1 µm° / -5.24°
Moyenne des facteurs de forme	0.425
Moyenne des rapports d'aspect	3.88
Circularité moyenne	0.454
Compacité moyenne	0.658
Orientation moyenne	84.3°
Rayon de sphère moyen	*****

Fig. 87: Statistical analysis available on the treated image

2. Application of the methodology

As explained earlier, before analyzing characteristic dimensions of scratches, two investigations will be done, first, to better understand how scratches are generated on roll surface, second, to check if dots of ICDP roll, are Cementite (carbides) localized on particular areas of the roll surface.

2.1. How are scratches generated on HSS roll surface?

We will compare the replica made on stand F1 (HSS inferior roll) according to the three different positions: 1300 mm, 1500 mm and 2000 mm. (Fig. 88) On 2000 mm position replica, we can notice the presence of small red dots that could be small oxidized carbides (as already seen on previous topographies). We also observe that these carbides are essentially distributed on yellow plateaus.
According to the ferritic schedule rules, the wear (reduction of roll radius) at position 1,5 m is lower than 1,3m position, because a higher number of strip kilometer will be in contact with the roll in 1300 mm width than in 1500mm width. If we observe the two replicas, we can clearly observe that on the less worn area, 5 islets can be observed for a total surface of 24 000 µm². On the most worn area (position 1500 mm), we observe only 2 islets but the total surface is around 204 000 µm². We can easily suppose that stripes come from the juxtaposition of small islets.

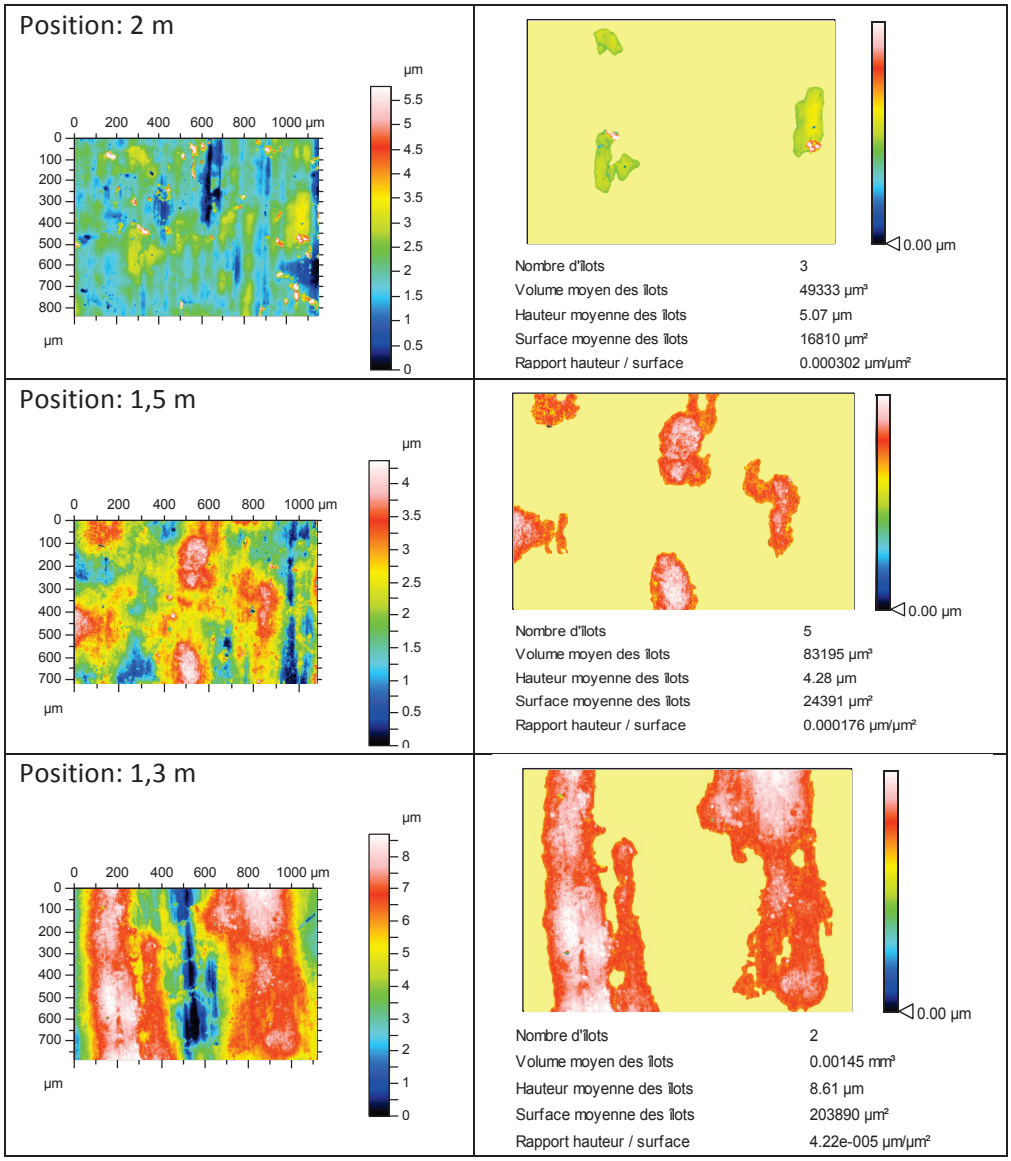

Fig. 88: Constitution of HSS stripes with wear

2.2. Localization of dots (carbides) on ICDP roll surface

We performed similar analysis on stand F5 and F7 on **unworn areas** (2m position) and we also noticed that the roughness is linked to the presence of carbides oxidation forming particular forms on roll surface. (Fig. 89) These carbides seem to be localized on plateaus and look like Fe_3C carbides (cementite) described on chapter 1. This result could be easily understood because the role of carbides is to increase global wear resistance, by increasing locally the hardness of the surface. As a result, due to rolling of strip, the roll shell matrix will be eroded (as explained in chapter 1) and it results in a global surface roughness increase because of the carbides extrusion.

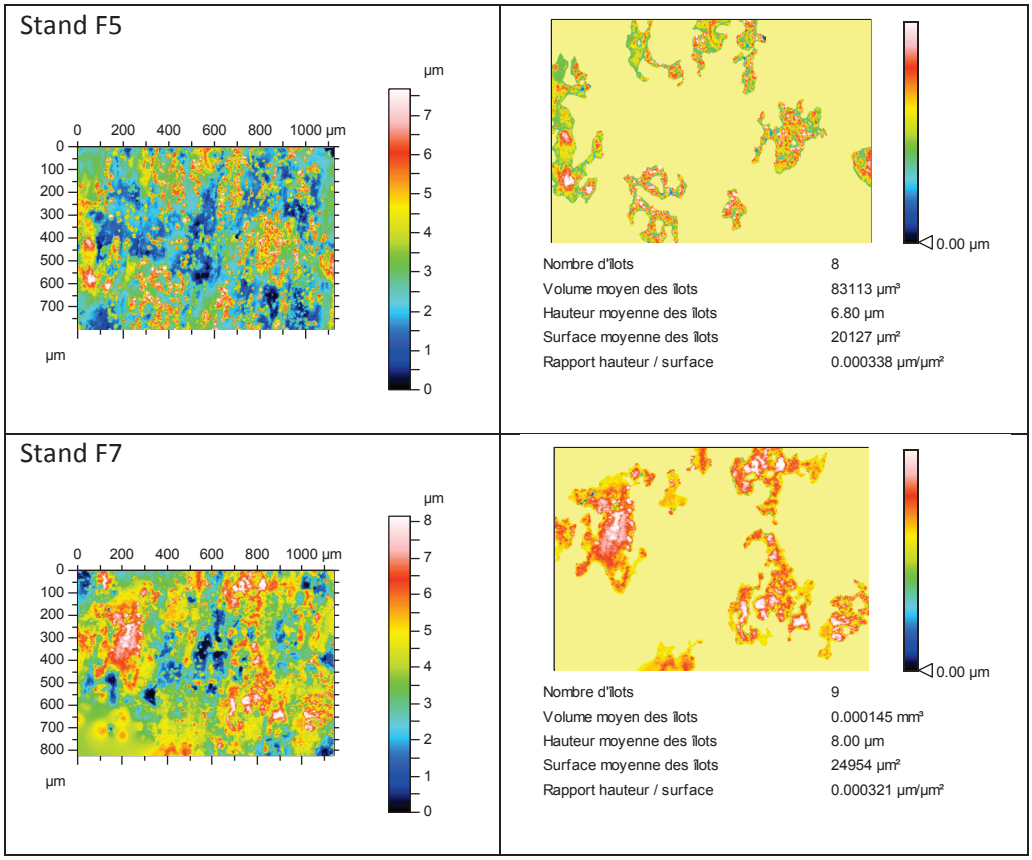

Fig. 89: Preferential position of graphite on higher plateaus for ICDP grades

An equivalent work can be done to evaluate the size, the volume and repartition of such elements after isolating them from the general roughness **on worn areas.**

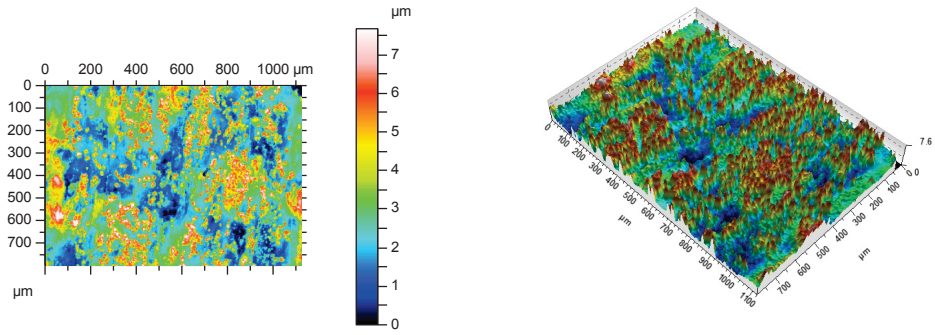

Fig. 90: Initial replica of ICDP roll surface (stand F5)

A double Gaussian filter (80 µm) was applied on it (Fig. 90) and we conserve the high pass filter described earlier. Image is transformed to a binary image and a circularity criterion was applied on the islets to remove atypical forms (circularity criterion is the most suitable criterion for Fe_3C carbides at this scale; if we had to observe them at a smaller scale, around 10 µm, circularity criterion will not be most relevant, because we saw in chapter 1 that the shape of Fe_3C is looking more like small sticks and triangles) (Fig. 91).

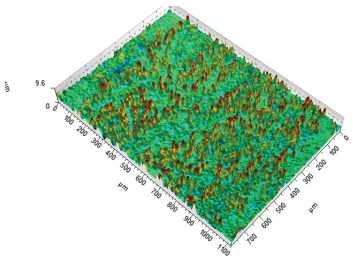	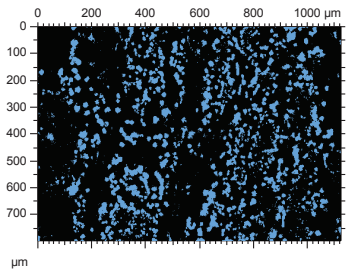	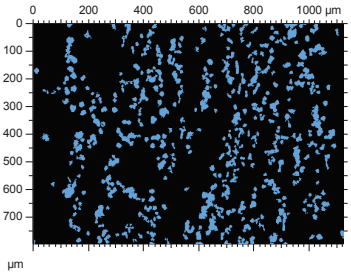
Filtered image with high pass filter	Binary image	Image after circular criterion

Fig. 91: Replica image treatment to access to size, density and volume of carbides

Extractable results (Fig. 92) allow us to find that there are 322 islets representing 120 067 µm². It represents 13,4 % of the total analyzed surface. Islets radius is around 20 µm +/-17 µm. This typical size could correspond to the graphite size described in chapter 1. The uniform repartition of them into the matrix helps to confirm this hypothesis.

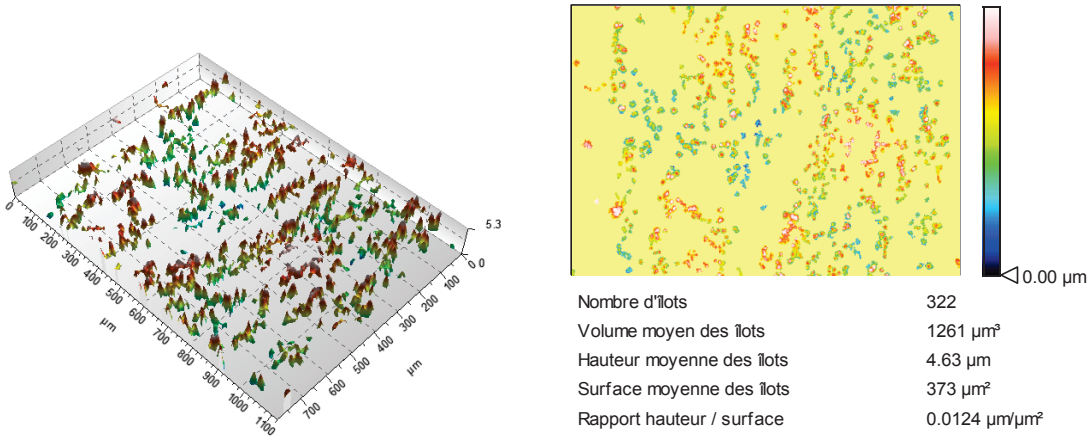

Fig. 92: Results of statistical analysis

2.3. Localization of dots (carbides) on HSS roll surface

This methodology has also been applied to other stands: HSS grade has a very different microstructure, where carbides have a very different morphology and size (Fig. 93). On the unworn area (2000 mm), carbides are randomly spread over the whole surface and no preferential localization could be determined. We do not see the typical forms we saw on ICDP. Nevertheless, on this picture, we clearly show that carbides are localized on plateau (yellow area).

On worn area, we still observe the stripes. Carbides seem to be located in the scratch and not on plateaus. Size of carbides is around 50 µm and as seen on chapter 1 (and appendix 2) these carbides could be the Molybdenum and Vanadium intragranular carbides. At this state, it is difficult to say if the localization of these carbides is due to wear that pulled them out to the scratch or if the roll was preferentially worn on areas where there was statistically a lower density of carbides, so that no more carbide could be observed on plateau.

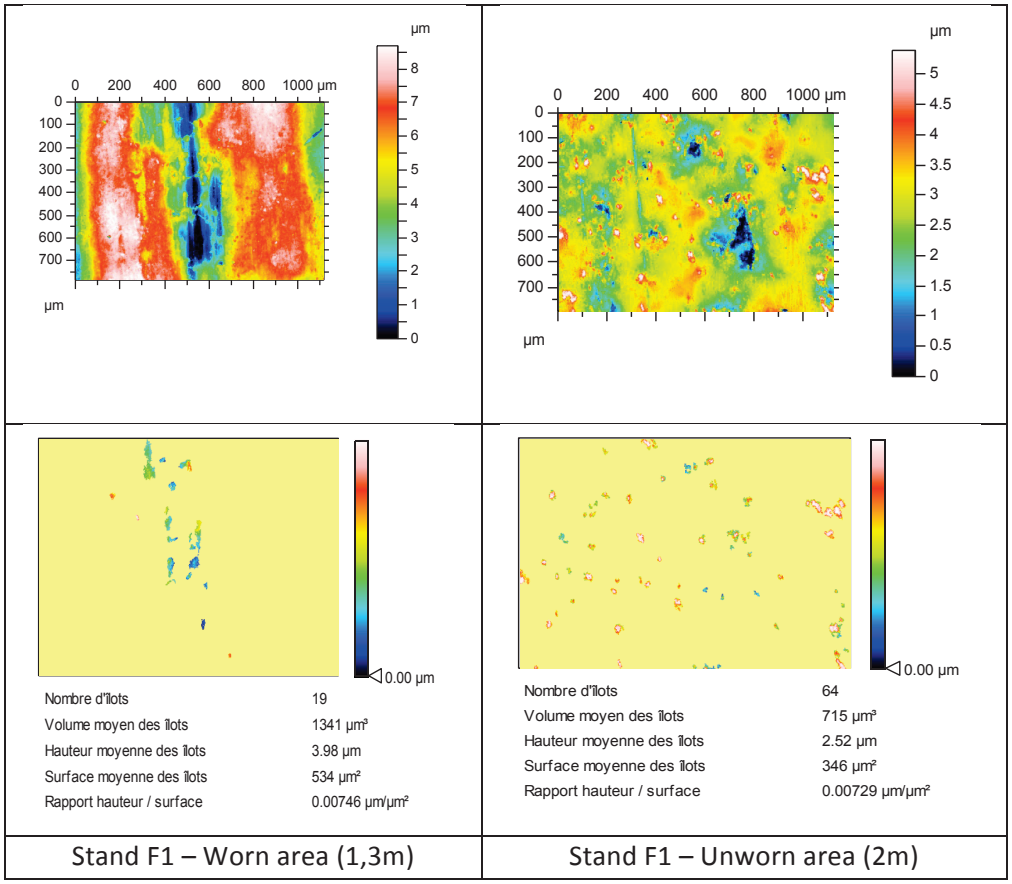

Fig. 93: HSS carbide analysis

3. Scratches analysis

3.1 Depth of scratches

As observed in previous paragraphs, we can conclude that if sticking mechanism initiates on scratches as suggested by Jin and al. [JIN00], the phenomenon has more chances to be initiated on HSS roll than on ICDP because scratches number is higher than on ICDP rolls.
In order to have more details on sticking initiation, the height of stripes (equivalent to scratches depth) is studied on each stand and for a short and long campaign, at the four positions.

Each graph (Fig. 94) corresponds to one position along the roll, and one campaign length.
H stands for the longest campaign, about 500 km and L stands for the shortest campaign, about 50 km. One point on the graph corresponds to the average information collected on 5 images per replicas on superior and inferior cylinder. So, 10 images give information for one point computation.
The abscissa of each graph corresponds to stand number.

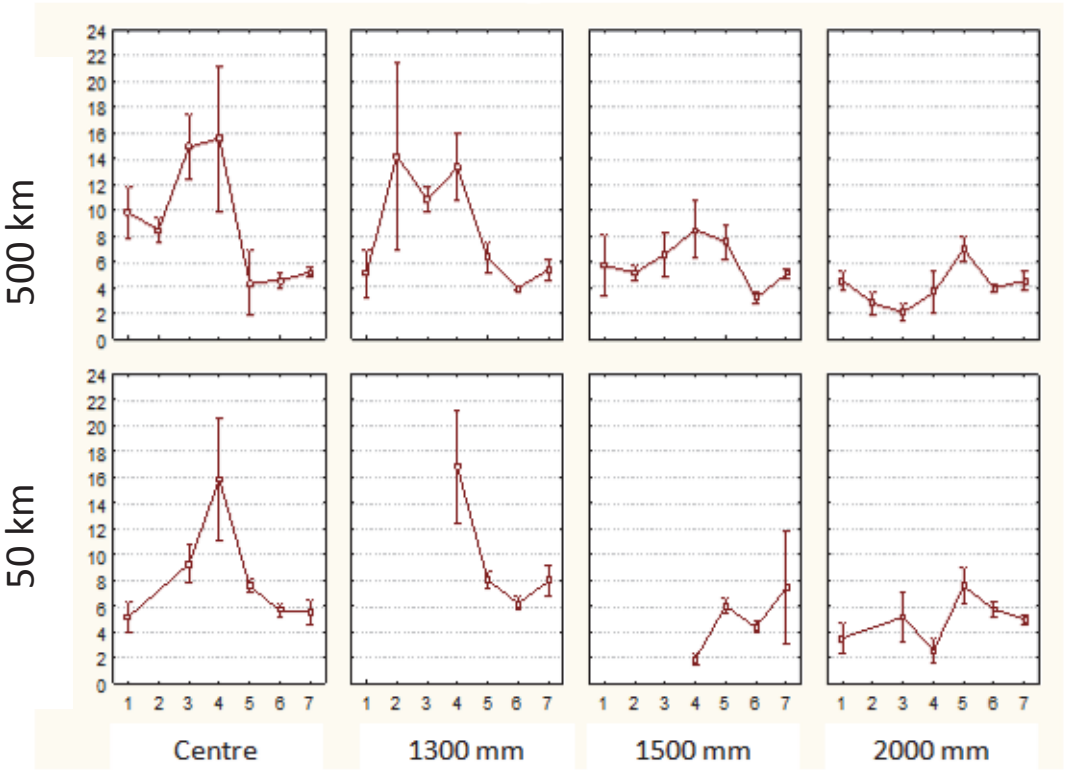

Fig. 94: Mean height of stripes per stand, per campaign length and per roll position

On Fig. 94, maximal height of islets was noticed both on long and short campaign and on the roll centre and at 1300 mm position.

Stands F4 is particularly concerned by deep scratches. The maximal depth is around 16 µm.

3.2 Characteristic dimensions of stripes on HSS rolls

In order to go further in roughness analysis, deeper investigations can be made on 2D measurements. 2D profiles along transverse direction (perpendicular to rolling direction) will be extracted from 3D images. The goal is to couple frequency and height parameters.

On replicas topographies, we can notice that on all stands, an undulation around 300 µm (period) seems to exist. The amplitude is depending on position on roll surface, on roll grade, and with presence (or not) of precipitates.
Roughness will be analysed using wavelet analysis – Coiflet 4th order.

3.2.1. Wavelet analysis [EKA05]

The continuous wavelet analysis is a continuous method, based on the use of a window that moves (can be translated) and changes of scale. This notion of scale (which replaces the notion of frequency in Fourier decomposition for example) is richer and more realistic because it includes both the notion of variable size and concept of frequency. The analysis is a space/scale analysis (or time/scale analysis) rather than space/frequency analysis (time/frequency analysis). This analysis will be conducted by adapting the analysis window to the analyzed signal fully respecting the principle of Heisenberg-Gabor. A key point is that the analysis will be done in a proportional relationship of the scale with the average frequency.

Wavelets are windows ψ(x) which expand and contract (Fig. 95), and are well localized in the spatial domain (or time) and frequency.
Starting from such a ψ(x) function which is called "mother" wavelet with a given window width, it combines the "girls" wavelet $\psi_{(a,b)}(x)$ generated by translations and scale changes (expansion or compression). This family is of the following form, where "a" is the parameter of scale or resolution, and "b" the translation parameter.

$$\psi_{a,b}(x) = \frac{1}{\sqrt{|a|}}\psi\left(\frac{x-b}{a}\right) \qquad \{19\}$$

Wavelets have a constant form but variable size, proportional to the scale parameter “a”. This means that whatever the setting, the number of oscillations of the wavelet remains the same. This parameter plays a very important role because it determines the width of the window. If a> 1, the width increases relative to the initial length of the analyzing wavelet: it is the expansion phenomenon. On contrary, if a <1, the width of the window decreases from the initial width: it is the compression phenomenon.

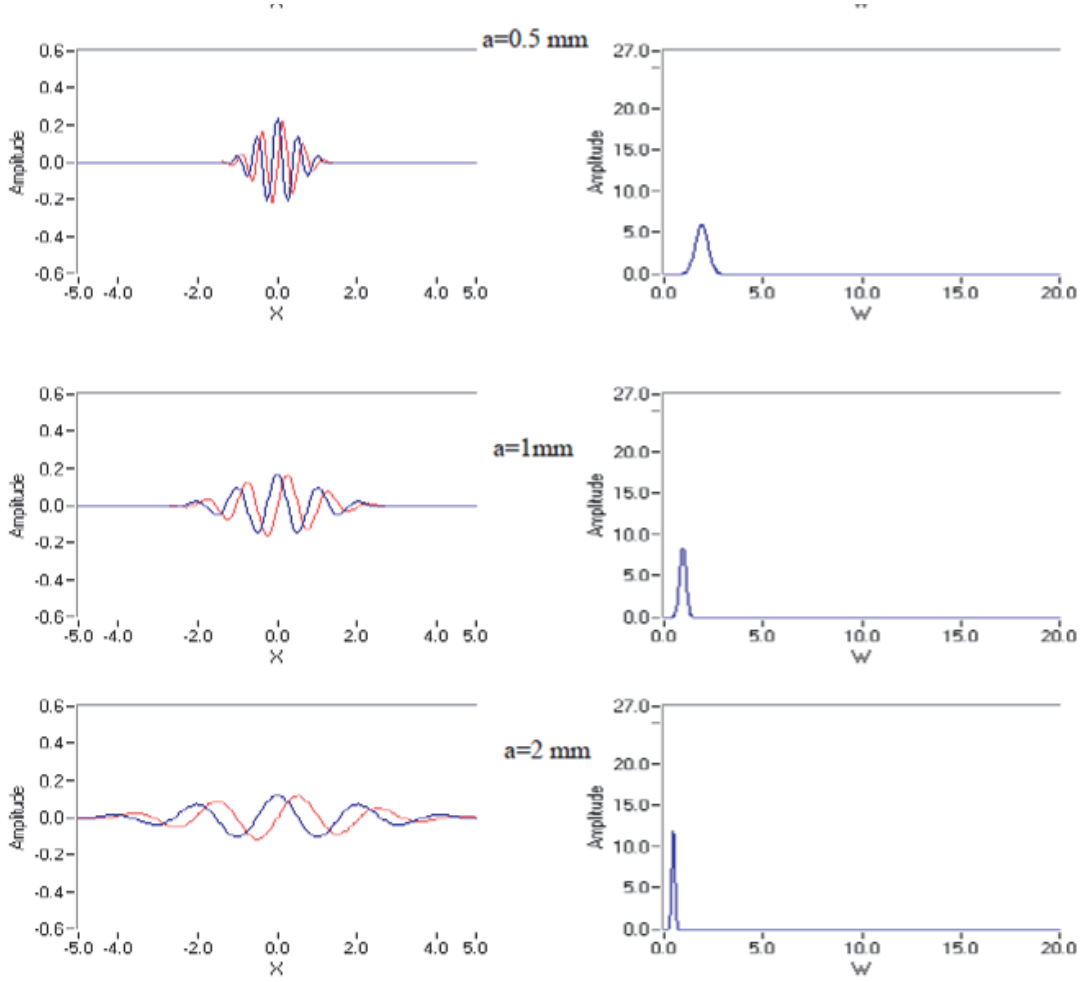

Fig. 95: Effect of scale parameter to wavelet [EKA05]

3.2.2. Characteristic dimensions of scratches

In this study, a Coiflet wavelet of the fourth order will be used [WEI97].

A wavelet is called a *generalized coiflet of order l* (denoted by $\psi_{l,ŧ}$) if for some ŧ ϵ R, the wavelet $\psi_{l,ŧ}$ and its scaling function (denoted by $Ø_{l,ŧ}$) satisfy

$$\int_{\mathbb{R}} (t-\bar{t})^p \phi_{l,\bar{t}}(t)\, dt = \delta_p \qquad \{20\}$$

$$\int_{\mathbb{R}} t^p \psi_{l,\bar{t}}(t)\, dt = 0 \qquad \{21\}$$

For p=0,1,…l-1

Figure 96 represents the effect of wavelet treatment and Figure 97 is the 2D average profile that will help us to determine the depth of scratches on all stands.

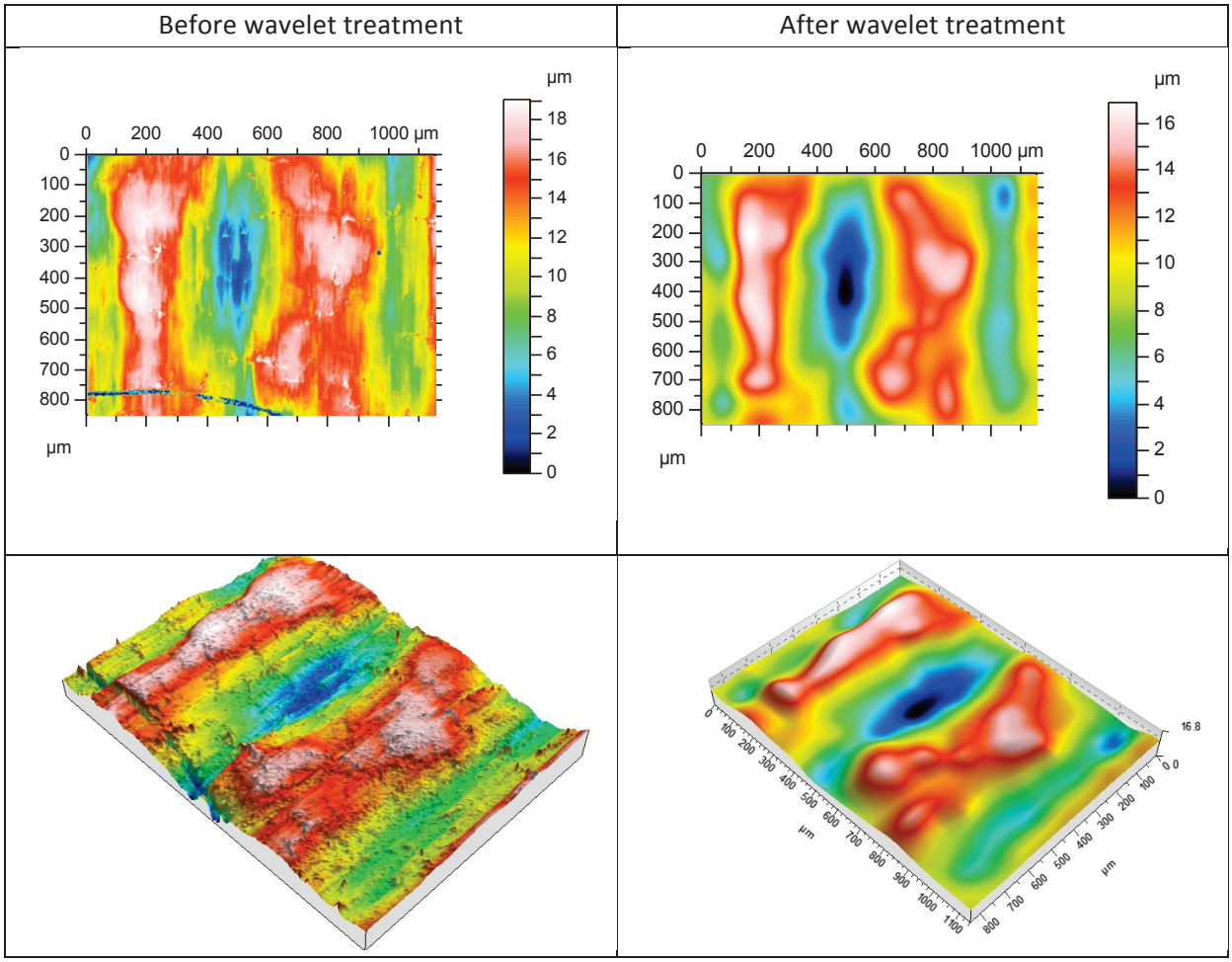

Fig. 96: Coiflet wavelet treatment on roughness parameter

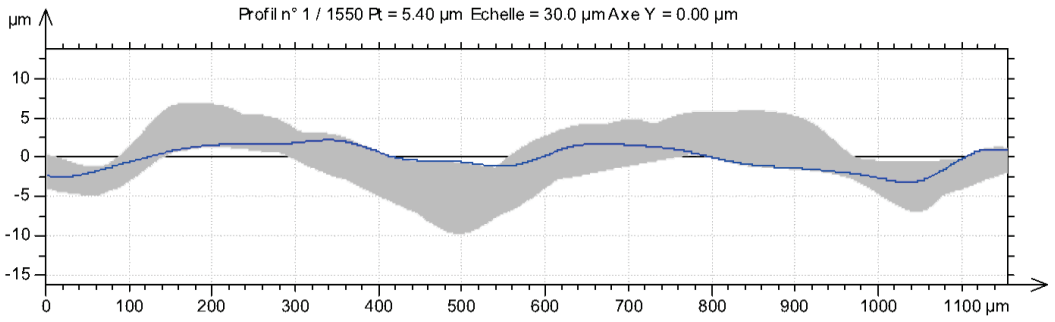

Fig. 97: 2D profile extracted along transversal direction

To describe stripes and scratches pattern three parameters are required (Fig. 98, 99):
- Pz is giving the maximal amplitude of the profile. The deepest scratch is confirmed to be of 16,2 µm. The average scratch depth is around 12 µm.

ISO 4287						
		Contexte	Mean	Std dev	Min	Max
Paramètres d'amplitude - Profil primaire						
Pp	µm		5.45	1.21	2.35	7.03
Pv	µm		6.51	1.62	3.06	9.47
Pz	µm		12.0	2.68	5.40	16.2
Pc	µm		9.96	1.95	4.85	12.4
Pt	µm		12.0	2.68	5.40	16.2
Pa	µm		2.88	0.640	1.32	3.90
Pq	µm		3.35	0.747	1.52	4.44
Psk			-0.186	0.150	-0.473	0.0532
Pku			1.99	0.303	1.62	2.76
Paramètres d'espacement - Profil primaire						
PSm	µm		495	26.1	426	518
Pdq	°		2.70	0.439	1.29	3.37
Paramètres liés au taux de portance - Profil primaire						
Pmr	%	*c = 1 µm sous le pic le plus haut*	11.5	6.48	4.96	28.9
Pdc	µm	*p = 0%, q = 50%*	5.30	1.20	2.39	6.95
Paramètres liés aux pics - Profil primaire						
PPc	1/µm	*+/-0.5 µm*	0.00172	7.58e-005	0.000865	0.00173

Fig. 98: Roughness parameters determined on 2D average profile (stand F4)

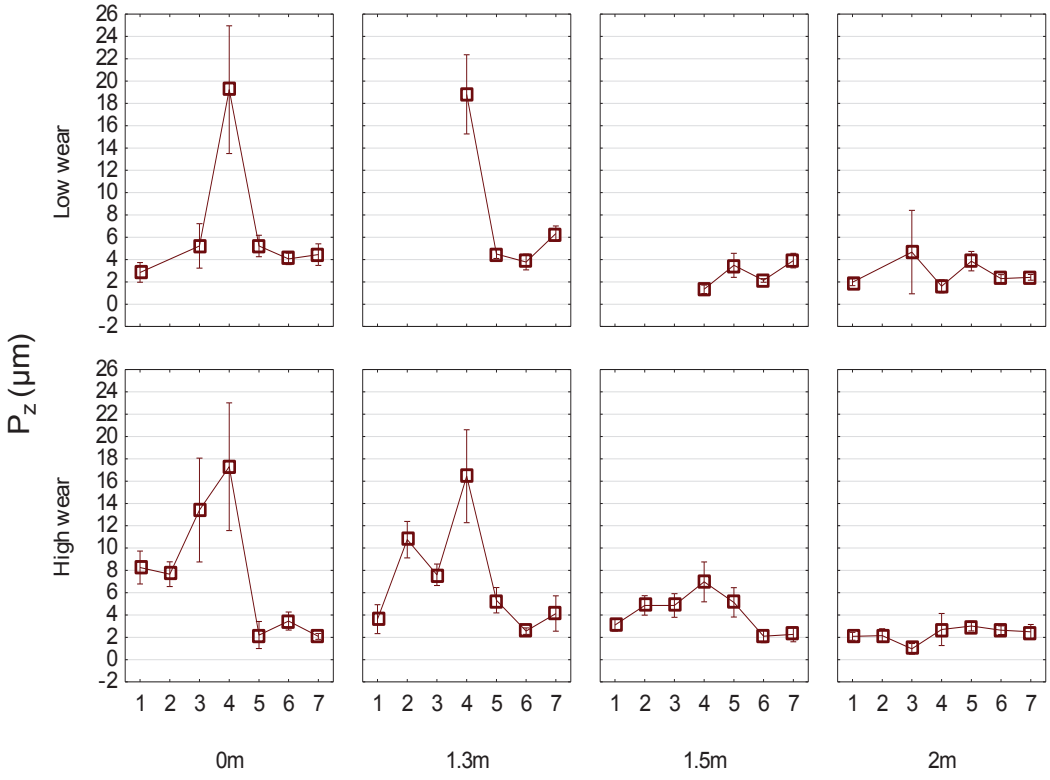

Fig. 99: Pz value depending on stand number and wear rate

Based on Fig. 87, stand F4 is identified as being the stand where the maximal amplitude of stripes is the higher, around 17 µm in the middle of the coil and 1,3m. On this graph we also clearly noticed the huge difference between positions on the one hand, 0, 1,3 and on the other hand, 1,5 and 2m. This large difference is due to the fact that no product was in contact with rolls at these positions.
The increasing value of Pz with stand number up to stand F4 could be explained by the fact that in a same campaign, roll of stand F4 do more rotations than roll of stand F3, and so on stand F2 and Stand F1, due to the increasing total reduction rate with increasing stand number.

- PSm is the average distance between two consecutive stripes. The distance is determined between the medium of the two stripes (Fig. 100, 101). The average value is around 500 µm and minimal distance is around 420 µm.

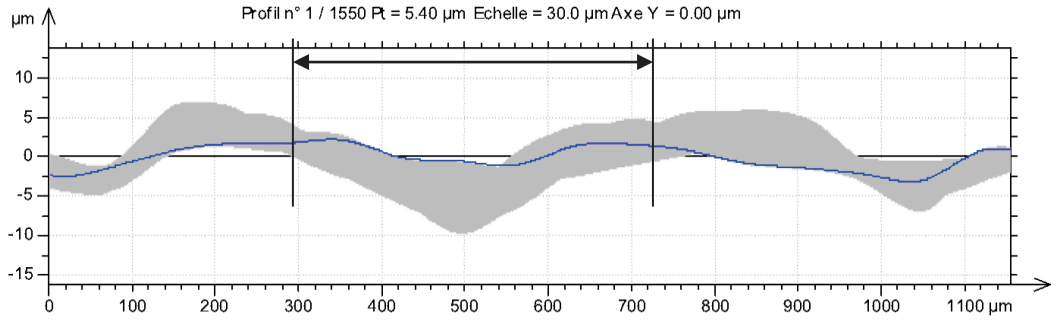

Fig. 100: Definition of PSm

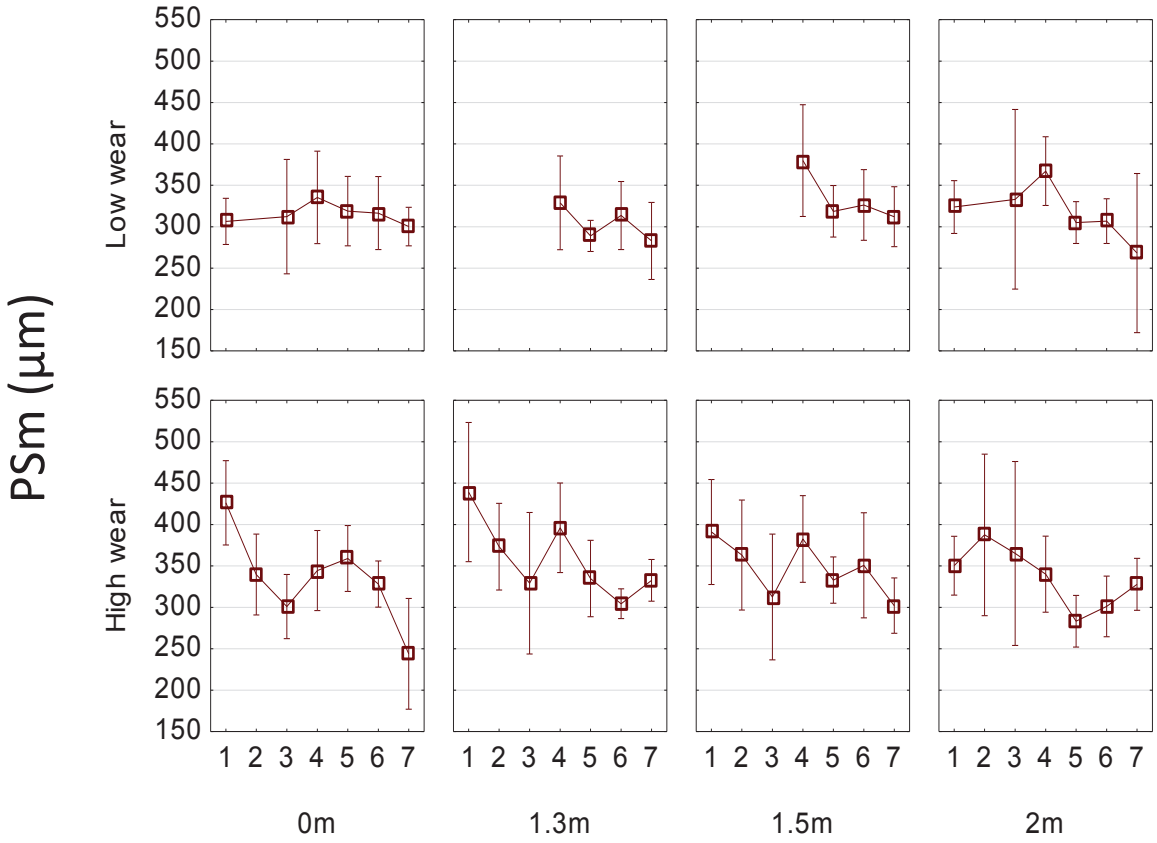

Fig. 101: PSm value depending on stand number and wear rate

The average distance between two consecutive stripes is relatively stable between stand number, around 300 and 350 µm. This value could correspond to two or three grain sizes of the roll.

- Pmr is the characteritic width of the stripes. The maximal size is around 30 µm and the average is around 10 µm.

3.2.3. Discussion on roll wear mechanism

Many studies performed on ICDP, HSS and HiCr grades on wear mechanism highlight thermal fatigue as the most probable origin for roll surface degradation [KAT92]. In APERAM hot strip mill, no thermal fatigue pattern was found on rolls. As a result, the origin of scratches cannot be linked to thermal fatigue.

Pellizzari and Liu [PEL05, LIU06] showed that initiation of roll degradation is linked to the oxidation of matrix and cracks generated in matrix/carbide interface that will lead to carbide removal (roll defect named peeling). Nevertheless, even if these mechanisms were encountered on roll grades samples after lab rolling test, no equivalent scratches were noticed as on our study.
It is likely that roll degradation has been studied by authors on the early stages, contrary to our study on which, roll is studied at the end of a complete rolling campaign. So the initiation of roll wear is not easily visible.

The existence of scratches cannot be neglected and we propose to link the size of these scratches to the grain size of the roll. The plateaus found on roll surface are the real contact area that was generated by abrasion / oxidation phenomena.

Investigations are in progress in APERAM Hot strip mill to compare rolls coming from different suppliers, having different grain size, on defect generation, and friction coefficient evolution.

E/ Conclusion on scratches as nucleation sites of sticking

In this chapter we have seen that three main patterns are representative of roll surface topography:
- on unworn areas, we can observe small grinding scratches, whose depth is lower than 6 µm.
- on worn areas, HSS rolls present large and deep scratches, whose depth is lower than 26 µm and ICDP rolls are characterized by protuberances caused by cementite oxidation and after cementite extrusion (due to matrix consumption during rolling).

We noticed that protuberances on ICDP rolls were smaller than scratches on HSS, as a result, if mechanism proposed by Jin is available, HSS rolls will be more prone to initiate sticking phenomenon. Deeper scratches were found on stand F4. Nevertheless, the 26 µm depth corresponding to the maximal amplitude of stand F4 3D topography is not characteristic of the scratch depth. In order to have a statistic value of the maximal scratch depth, a 2D analysis of roughness has to be performed on the pattern composed of 1 scratch and 2 stripes (corresponding to plateaus surrounding the scratch). In order to perform a suitable roughness analysis, a finite number

of roughness parameters have to be selected in order to a have a physical approach of the surface state.

These three parameters are:
- Pz: the maximal amplitude of the profile; maximal value is 16 µm.
- PSm: the average distance between two consecutive stripes; average value is 500 µm.
- Pmr: the characteritic width of the stripes; average value is around 10 µm.
It implies that average scratch width is around 480 µm.

This study confirms that if scratches are the corresponding initiation sites for sticking phenomenon, the transfer bar oxide layer should be smaller than 16 µm and that the defect size should be smaller than 480 µm in diameter! The observed diameter of the sticking defect is around 200µm after hot rolling – annealing – shot-blasting and etching process. As a result, the last assumption is validated by our industrial observations. Nevertheless, as presented in chapter 1, the transfer bar oxide layer is more than 40 µm thick. **As a result, when comparing entering scale layer and a degraded roll surface scratch, the hypothesis of roll scratch to be the initiation site of sticking phenomenon is not very probable.** Moreover, in I. Guillot [GUI90] PHD report, it is mentioned that Fos-sur-Mer hot strip mill was concerned by sticking when only ICDP rolls were used. If only scratches were at the origin of initiation site of sticking, no or less sticking defects would be found when using ICDP roll because there are fast no scratch over there and small dots (carbides) are too small to be considered as nucleation sites.

Nevertheless, the mechanism explains that direct contact occurs in the roll bite; as a result, contact condition in the roll bite has to be detailed in order to study this hypothesis under a new scope. Conventional tribological tests (disc-on-disc tribometers) are not adapted to such a study, because the contact conditions are not reproduced. Moreover, **the use of original antagonists with original scale layer is not possible. As a result, it has been decided to build a lab pilot using samples extracted from original transfer bar surface and original HSS roll sample.**

CHAPTER 3 - REALISATION OF A HOT ROLLING PILOT DEDICATED TO STICKING PHENOMENON

As shown in the previous chapter, the sticking material observed on the work roll derives from direct contact between the transfer bar and the rolls. This result highlights the key role of tribology on the "success" of the hot rolling process. As a consequence, a perfect knowledge of the tribological behaviour of hot rolling is required to understand the sticking occurrences in order to limit them. But it is well known that tribology, and consequently friction, implies complex phenomena and should be studied with great care in order to guaranty the reliability of the results.

Indeed, tribology depends on many variables, such as stress state, bulk yield stress, plastic strain rate, plastic strain, sliding velocities, the real contact surface (and subsequently roughness), temperatures, viscosity and other physic-chemical properties of lubricants, surface reactivity, surface oxidation, etc. The best way to study tribology and identify friction would be to operate measurements directly on the process. Unfortunately, this cannot be done, due to interaction with production line and to the extreme difficulty to equip the process with specific sensors.

As a consequence, tribological data have to be collected on friction bench. Nonetheless, in order to ensure a reliable identification of tribological data, the replication on the bench of realistic mechanical, physical and chemical parameters of the surfaces involved in the contact is required [Sch84]. It is impossible for a laboratory bench to simulate each and every "physico-chemico-mechanical" parameters acting on friction [Bay02]. Nevertheless, it is always possible to operate reliable tests by paying some attentions to the bench adjustments [Dub00].

The following chapter is related to the design of a new friction bench dedicated to hot rolling. First the strategy used in the TEMPO laboratory to simulate contact conditions and identify friction according to process reality is presented. Then the strategy is developed in order to quantify the technological constraints the friction bench will have to undergo. Finally, the design of the new friction bench is presented.

A/ Strategy to study friction according to industrial conditions of contact

The strategy to simulate and acquire accurate data on friction test is presented in fig. 102.

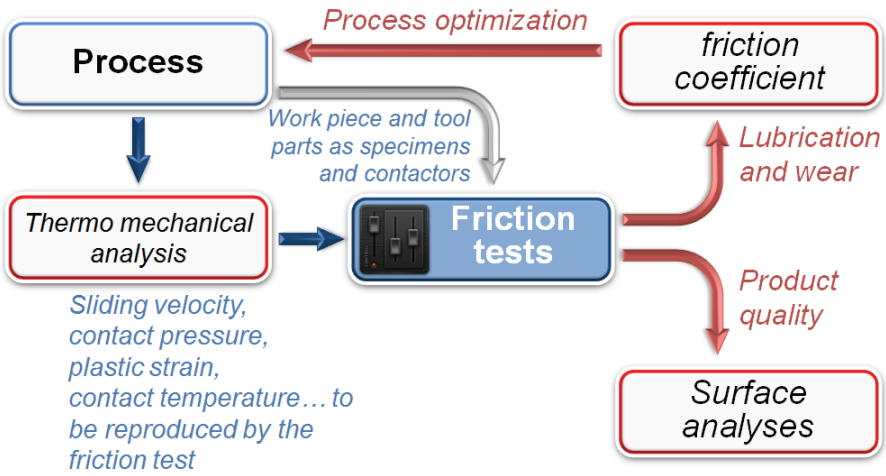

Fig 102: Strategy to perform friction tests according to industrial contact conditions [Dub00]

The methodology is centred on the friction simulator but is strongly linked to the process. First, specimens are machined from real bars, contactor are machined from real working rolls in order to reproduce the physics and chemistry of the contact. As a consequence, surfaces in contact on the simulator have the same roughness, hardness, cleanliness, surface energy than those of the process.

Second, a thermo-mechanical analysis of the process is performed in order to identify the key mechanical parameters the friction test will have to simulate.

Then, the bench is adjusted to simulate the mechanical contact condition identified on the process. An important feature in the design of a test bench is then to ensure the bench will allow adjustment with a window large enough to cover the range of mechanical data encountered on the industrial process.

Finally, tests are performed and results are analysed in order to provide information on the process. Although this last step may differ from a study to another, most of the analyses are expressed in terms of surface quality (mostly qualitative results) or in terms of friction identification (quantitative results) [Dao08]. As a consequence, a second important feature when designing a bench is that it must at least provide force measurements in two perpendicular directions, sliding speed and temperature as close as possible of the contact surface. An easy access to the contactor surface to perform SEM-EDS and profile meter analysis after the test is also required.

B/ "Windows" of Process mechanical parameters

1. Mechanical parameters

In order to design the friction bench, we have first to define the process parameters to be simulated and, second, their range of variation.

At high temperature, strain rate, contact pressure and temperature are known to have direct influence on the steel behaviour. So, reliable simulation of tribology of hot forming processes requires respecting those mechanical data, since variation of steel behaviour will affect the response of the system. In order not to be affected by process size effect, the bench has to respect some "geometric invariants" [Doh13]. So, four parameters are selected to become "invariants" (i.e. to have the same value on the process and on the test bench). The invariant parameters are:

- The mean deformation applied on the product (I_1)
- The slenderness ratio, due to the mass flow rate conservation in the roll bite (I_2)
- The mean strain rate (I_3)
- The normal pressure in the contact (I_4)

In the case of rolling, invariants I_1 can be expressed either using the thickness ratio (geometrical parameter), or using the mean plastic strain (mechanical parameter). In both cases, I_1 parameter will imply to the same technological constraint on the test bench since mean plastic strain is a function of the thickness ratio:

$$\bar{\varepsilon} = \frac{2}{\sqrt{3}} \ln\left(\frac{e_e}{e_s}\right) \quad \{22\}$$

where $\bar{\varepsilon}$ is the mean equivalent plastic strain, e_e the initial thickness of the product and e_s the final thickness.

I_1, I_2 and I_3 are then given by the following equations:

$$\begin{cases} I_1 = \dfrac{2}{\sqrt{3}} \ln\left(\dfrac{e_e}{e_s}\right) \\ I_2 = \dfrac{e_e}{d} = \dfrac{e_e}{\sqrt{Dc(e_e - e_s)}} \\ I_3 = \dot{\bar{\varepsilon}} = \dfrac{\bar{\varepsilon}}{t_0} \end{cases} \quad \{23\}$$

where:

- e_e and e_s are respectively the enter and exit thickness of the rolled bar (mm),
- Dc is the diameter of the working cylinder (mm)
- d is the contact length in the roll bite (mm)

- ω is the rotation speed of the cylinder (rad/s)
- t_0 is the contact time (time needed for a material point located on the surface to move from the entry and of exit of the roll bite):

$$t_0 = \frac{2.\sqrt{Dc(e_e - e_s)}}{\omega Dc} \quad \{24\}$$

The normal pressure invariant I_4 has to be determined by Finite Element simulations. By introducing these equations, the correct entry and exit thickness of the sample can be defined respecting the equality of invariants thereby reproducing the same phenomenon as that found on the process to be simulated.

1.1 - Values of invariants 1 to 3

Tab. 14. Finishing Mill Parameters. Industrial data related to the slab n° 93764310, grade K41, width 1307 mm.

	FORMULA	TRANSFER BAR	FINISHING MILL						
			STAND 1	STAND 2	STAND 3	STAND 4	STAND 5	STAND 6	STAND 7
Thickness (mm)	ee, es	44,12	26,8	18,16	12,83	9,36	7,22	5,95	4,99
Reduction (%)	R%	-	39,3	32,2	29,4	27,0	22,9	17,6	16,1
Force (tons)	Fn	-	1175	1049	1019	878	904	811	807
Speed (cyl) (m/s)	Vc	-	0,9	1,33	1,89	2,58	3,38	4,18	5,04
Fws %	Fws = 1 - Vc/Vs	-	7	6	6	6	5	4	2
Traction strip (kgF)	Ft	-	13383	9384	8342	9464	9337	9197	
Roll Diameter (mm)	Dc	-	755	769	727	695	686	756	718
Cedage (T/mm)	C	-	4,64	4,28	4,69	5,12	4,62	5,17	4,53
Temperature (°C)	T	1072	1056	1033	1013	993	975	957	940
Length of contact arc (mm)	L = ((Dc/2)*(Ee-Es))^0,5	-	114,4	81,5	62,2	49,1	38,3	31,0	26,3
Contact time in the roll bite (s)	T = L/Vc	-	0,13	0,06	0,03	0,02	0,01	0,01	0,01
Strain	ε = 2/3^0,5 * ln(ee/es)	-	0,58	0,45	0,40	0,36	0,30	0,22	0,20
Strain rate (/s)	ε̇ = ε/T	-	4,53	7,33	12,18	19,13	26,44	30,14	39,00

Table 14 presents the main rolling parameters on the seven stands of the Châtelet finishing mill.
The first stand of the mill is where the contact conditions are the more severe: the bar temperature is higher than 1070°C at the entry of the contact, and the reduction ratio is close to 40% (which is equivalent to an increase of plastic strain equal to 0.58). Due to conservation of volume, the rolling speed increases with the reduction ratio, and evolves from 1 to 5 m/s as the bars pass from the first to the last stand, and the mean plastic strain rate increases from 5 to 40 s^{-1}.

As a consequence, the friction bench will have to perform test at temperatures up to 1070°C and to generate equivalent plastic strain on specimens equivalent to that induced by a reduction ratio of 40%. It has to be able to reach strain rate up to 50 s^{-1}.

1.2 Invariant I4, the contact pressure

As it has been mentioned previously, the determination of the contact pressure along the roll bite has to be determined numerically. The numerical model is performed with the finite element software ABAQUS.

1.2.1. Numerical simulation of the process

Symmetry of the industrial rolling stand:

As already exposed in the first chapter, a finishing mill stand can be considered in first approximation as a horizontal symmetric system. As a result, we decided only to model the upper half of the stand, and also the half of the roll bite. Nevertheless, this symmetry is not absolutely true. There are two main differences between the top and the bottom part of the stand:

- The diameter of the bottom cylinder is always bigger than the upper cylinder. The maximal difference between the two diameters is about 0.3 mm. The use of a bigger bottom cylinder is necessary to increase the bottom parietal speed and so to induce a slightly positive curvature of the strip at the exit of the stand. It helps to ensure the introduction of the strip in the next stand at the beginning of the rolling. Nevertheless, this dissymmetry is relatively negligible compared to our phenomenon (the difference between the upper and bottom cylinders is lower than 0,05%).

- A positive curvature of the strip at the exit of the roll bite also exists during the rolling because of the looper presence.

As already exposed in Chapter 1, a looper is used to maintain the tension of the strip between each stand. The angular position of this arm determines the tension applied on the strip (at the exit of the stand N and at the entry of the stand N+1). The position of the looper is automated. An average value of 28° is measured all along the pass on the looper in the interstand 1-2 (α angle on Fig 103).

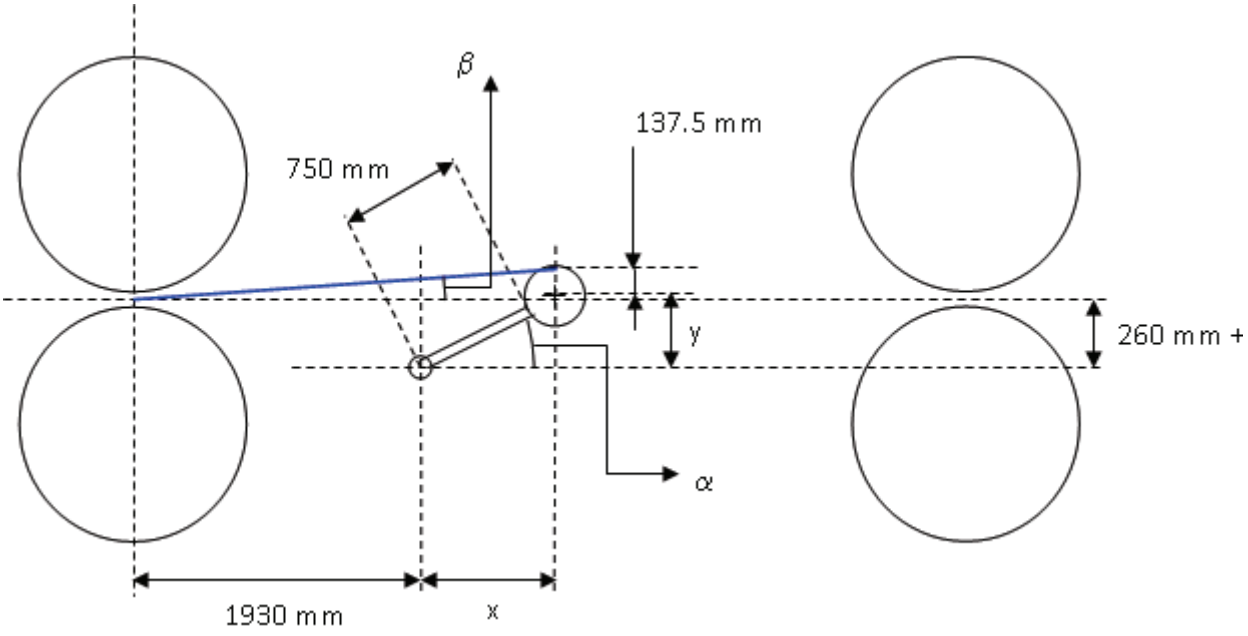

Fig. 103: Dimensions of the looper in the interstand 1 – 2.

The direct consequence of the presence of looper is that the exit part of the strip and the horizontal symmetric axis of the stand are not parallel. As a result, the tension applied on strip made an angle with the symmetric axis of the stand and the value given by the automate need to be interpreted in order to calculate the projection of this force on the line of pass (horizontal symmetric axis of the stand).

The vertical distance between the line pass and the rotational axis of the looper depends on the roll diameter. This value is about 260 mm added to a corrective parameter "a" which is adjusted with the wear of the cylinder (Tab.15)

Tab. 15. Effect of roll diameter to *a* parameter

Situation	Corresponding roll diameter	Value of "a" parameter
New roll (no initial wear)	764 mm	+25 mm
Old roll	724 mm	- 15 mm
Our current situation	755 mm	+15 mm

As a result, the vertical distance between the line pass and the rotational axis of the looper is about 275 mm. Depending on the dimensions and position of the looper on the interstand, we deduce the angle made by the strip with the horizontal axis: 5.9° (Eq. 25).

$$\alpha = 28°$$

$$x = (750 + 137.5).\cos(28) = 783.62\,mm$$

$$y = (750 + 137.5).\sin(28) = 416.65\,mm$$

$$\beta = \arctan\left(\frac{137.5 + y - 275}{1930 + x}\right) = 5.9° \quad \{25\}$$

Knowing the β angle, we can deduce the horizontal component of the traction applied on the strip. We conclude that the relative gap between the traction applied on the strip and the horizontal component is very small, around 0, 53%.

As a result, in the simulation we will use the indication given directly by the automate and we will model only half of the roll bite by considering the stand with a horizontal symmetry on the pass line.

As a conclusion, we validate the simulation of a half roll bite to be the representative of the industrial system.

We chose to model the problem in 2D because the deformation of the product in the width (transversal direction) is negligible compared to the deformation in the rolling direction (Unit section = 1m). As a result, the hypothesis of plane strain is used in the resolution of this problem.

Description of the 2D model:

The finite element mesh is composed of two parts. The first one is the cylinder (diameter: 755 mm) made with 2D discrete rigid wire. The corresponding elements are R2D2, linear rigid elements. The centre of the roll is set up as a Reference Point (RP) in the model on which we will apply the boundaries conditions.
The second part is a half transfer bar where we represent only half of the thickness (initial thickness: 22,06 mm). The transfer bar is 1 m long on the model and is constituted by CPE4 elements with 4 nodes, bilinear with a complete integration. The mesh is made up of 22 elements in the thickness of the transfer bar (each element represents approximately 1 mm²) and the mesh is structured (Fig. 104).

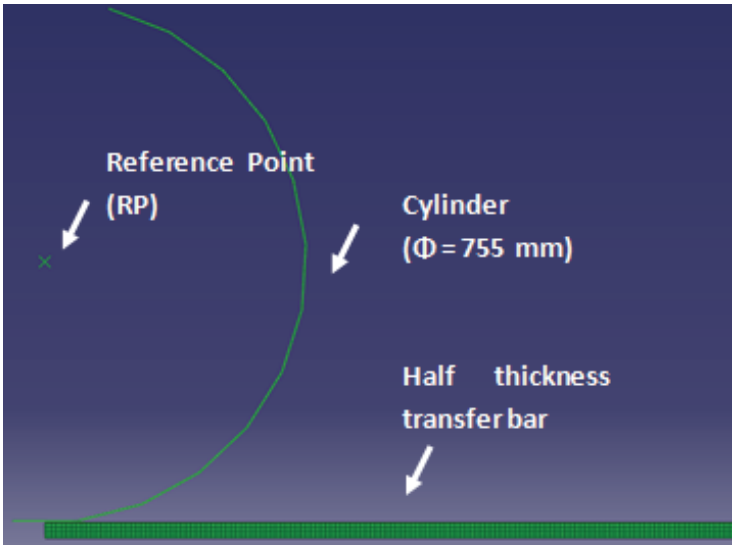

Fig. 104: Finite element mesh for the simulation of a half roll bite

Modelling of friction between the roll and the transfer bar:

The modelling of friction is made by the use of Coulomb model, defining a tangential reaction (Tangential behaviour/ Penalty/Isotropic/ μ=0,3) proportional to the normal reaction by the friction coefficient (Normal behaviour / Hard contact). The friction was set up by the way of Surface-to-surface / standard interaction. “Finite sliding” is chosen because we are in presence of a large strains problem.

Material properties:

We use the material properties of a 436 grade, which is a ferritic Nb-stabilised stainless steel grade. As we are rolling at high temperatures (above 1000°C), the grade has an elastoviscoplastic behaviour, which depends on the strain rate. We use the Sellars & Teggart law determined experimentally on this grade by Aperam lab with torsion bar tests performed on a temperature range about 700 – 1100°C and strain rates between 1 and 40 s^{-1}. The different test results helped to build a general rheological model based on Sellars & Teggart law.

$$\sigma = \alpha^{-1}.\arcsin h\left(\left(\frac{Z}{B}\right)^{1/n}\right).\sqrt{1-\exp(-f\varepsilon)}$$

with $\begin{cases} \alpha = 1/57{,}14 \\ n = 3{,}45 \\ B = 10^{14} \\ Z = \dot{\varepsilon}\exp\left(3{,}54.10^5 \,/\, 8{,}314.(T+273)\right) \\ f = 10 \end{cases}$ and T in °C and έ in s^{-1} (11)

The elastic part of rheology is defined by the Young modulus taken equal to 1550 MPa. The density at 1056°C is 7388.10^{-9} kg/mm^3. The Poisson ratio is taken equal to 0.3. [LNE10]

Calculation steps and boundary conditions:

The model needs to activate the "NL geom." option so as to take into account the friction parameters.

The step #1 corresponds to the application of the reduction on the transfer bar (static computation). The initial point the two parts are put into contact at the vertical of the centre of the roll and the upper left corner of the transfer bar. (Position of the Reference Point at the step #0: X = 0 ; Y = 22,06 +377,5 = 399,56 ; Z = 0). The first step consists in moving the roll by (-) 8,66 mm (representing the half of the reduction made in the stand #1) along the Y axis in the direction of the transfer bar. The displacement is imposed by a ramp on 1s. During this step, the roll is blocked on the X and Z axis.

The step #2 corresponds to the rolling of the transfer bar. Contrary to the "real" process, on the simulation the cylinder moves over the transfer bar, when the transfer bar is fixed. The computation is made by dynamic implicit algorithm. We impose the rotation of the roll on the RP (Z axis) with a corresponding speed of 2,384 rad/s. We impose also the translation of the cylinder along the X axis with a corresponding linear speed of 900 mm/s at RP, and we keep constant the position on the Y axis.

During this step, the roll is blocked on Y axis by the use of the option "fixed at current position" at RP point. The duration of the last step is around 0.7 s because the boundary conditions are fully applied after 0,5 s and only 0,2 s are necessary to observe stable results.

During both steps, the transfer bar is submitted to two boundary conditions:
- a symmetry along Y axis is imposed at the bottom edge : Y = Ur_x = Ur_z = 0
- a symmetry along X axis is imposed at one edge of the transfer bar.

Validation of the numerical model:

In order to check the reliability of the model, numerical results are compared to some exit parameters available on the industrial process:
- The speed of the transfer bar at the entry of the roll bite should be approximately around 0.58 m/s
- The speed at the exit of the roll bite should be around 0.96 m/s.

There are some unknown parameters that are considered as entry parameters in this simulation such as friction coefficient. In order to determine the friction coefficient, some runs have to be performed on friction coefficient tuning up to find a normal reaction on a RP (Reference Point) during rolling step of $8{,}829.10^6$ N (900 kgF).
When the correct friction coefficient is determined, we need to check the strain rate obtained during the simulation, and finally, the corresponding contact pressure.

After some runs, we determine the final following results:

$$\begin{cases} \mu = 0.28 \\ \dot{\varepsilon} = 6.s^{-1} \\ F_x = -500.kN/ul \\ F_y = -8.7\ 10^6\ N/ul \\ P = 109.25\ 10^6\ MPa/m \end{cases} \quad \{26\}$$

Vertical force is around $8{,}6.10^6$ N for 1m width (of the transfer bar). The initial value proposed in the table 14 was $11{,}5.10^6$ N for a corresponding transfer bar of 1,3m wide. As a result, these two values are in accordance.

2. Specimens and contactors materials

As mentioned in the part A of this chapter, it is important to have specimens and contactors extracted from original process to guarantee the reliability of the tests. As it will be presented in the following, the pilot will deform specimens between two rolls and will be adjusted to be representative of the first finishing mill stand. So the specimens will be extracted from the transfer bar and the rolls from real cylinders.

2.1. WORKING ROLLS

The pilot contains two cylinders extracted from genuine finishing mill working rolls. The geometry of rolls used on the pilot is cylindrical and roll radius is identified in order to respect the Invariants of the process. Both cylinders are connected to the engine with the same rotating speed ω_b. The roll grade is HSS, coming from an APERAM supplier, whose chemical composition is given in Tab. 16.

Tab. 16. Chemical composition of rolls

C ppm	Mn %	Ni %	Cr %	Mo %	V %	N ppm
19000	0.93	1.54	4.38	5.38	5.17	530

In chapter 2, we noticed that an industrial roll surface has scratches whose depth is 16 µm maximum. These scratches seems to be sufficient to generate sticking (even oxide scale layer of transfer bar is higher than 35 µm thick). W. Jin [JIN00] showed that if roll roughness is sufficiently low (below 0.5 µm in its case), there is no more sticking phenomenon initiation.

In order to check this assumption, we used initial rolls having a roughness profile described on the following figure 105.

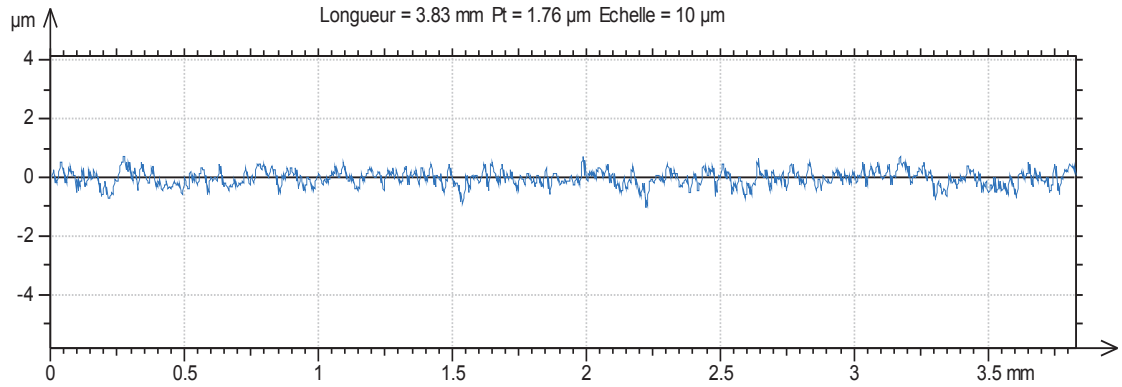

	Pilot rolls before test	Real rolls (chapter 2)
Pz	1,49 µm	17
PSm	46,7 µm	500
Pmr	28 µm	10 - 30

Fig. 105: Roll profile before rolling tests and main roughness parameters

Compared to the roll measurements performed on chapter 2, pilot roll scratches are ten times less deep and distance between stripes is also 10 times smaller. Pmr value representing the width of the stripes is similar to the industrial observations. Taking into account the oxide thickness described in first chapter, between 20 and 70 µm, the direct contact between hot ductile metal (from the specimen) cannot be in contact with the roll material. As a result, with this initial profile, no initiation of sticking phenomenon should occur during the test, according to the W. Jin mechanism [JIN00].

2.2. Specimen production

As it has been described in chapter 1, the very specific structure of 441 oxide layer (chemical composition, morphology...) could not be reproduced easily at a lab scale because the exact conditions of appearance are not precisely known. So, specimens are extracted from a transfer bar. One side of the specimens corresponds to the original surface of the bar, and presents the “industrial” scale. The opposite side is machined in order to adjust the thickness of the specimen to

the given values. The geometry of the specimens and their machining are defined so that the sliding direction on the pilot will correspond to the sliding direction on the industrial process.

A particular attention is paid during the machining in order to avoid the industrial surface to be polluted by machining lubricant.

The very specific structure of 441 oxide layer (chemical composition, morphology...) described in chapter 1 could not be reproduced easily at a lab scale because the exact conditions of appearance are not precisely known.

C/ Design of the hot rolling simulator

1. General description

The new bench has been designed in order to simulate contact condition encountered in hot rolling. The choice has been made to deform specimens between two cylinders, like a pilot mill (Fig. 106). So the hot rolling simulator is composed of three main modules:
- the engine (in green on Fig. 107), involved to generate the rotation of the cylinders,
- the inductor which allows to reheat the sample at the desired temperatures (pink in Fig. 108)
- the frame (in grey), which includes a gear box, the cylinders and the load cell.

The pilot is maintained in housing (1) in which a controlled atmosphere can be added through orifices in the box and valves during the rolling process.

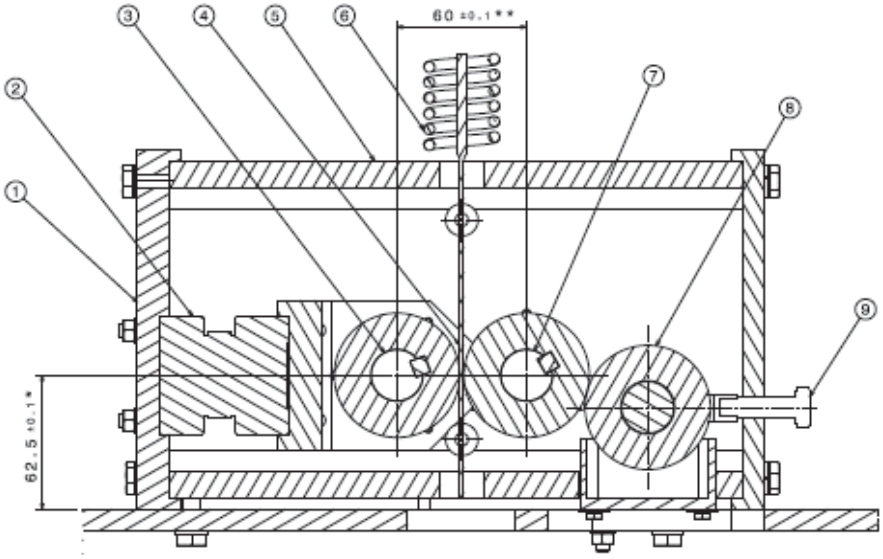

1 : Housing
2 : Force sensor
3 : Instrumented cylinder
4 : Strip sample
5 : Superior housing
6 : Inductor
7 : Motored cylinder
8 : Lubricant roll
9 : Screw

Fig. 106: Cross section view of the test bench

The pilot is composed of 2 HSS rolls mounted on a frame so that a constant 2 mm gap is kept between them. The two working rolls are mounted on an axis and are linked to a reduction gear on which we can adjust the rotational speed. One of the work rolls is instrumented by a 3D load cell which allows the measurement of the roll separation force and of the tangential force. The load cell has a maximum capacity of 30kN which allows reduction up to 50% at 900°C (Reference of the sensor is Kistler 9347C).

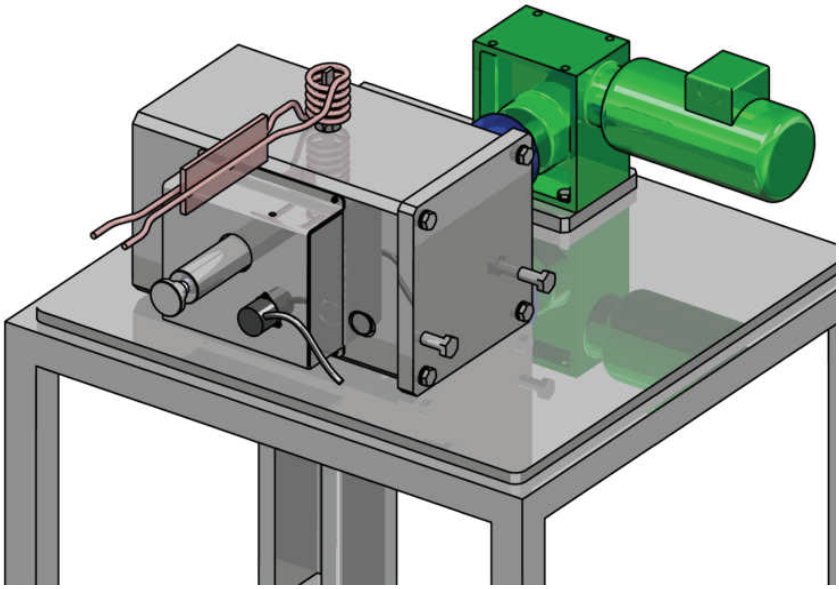

Fig. 107: General overview of the test bench

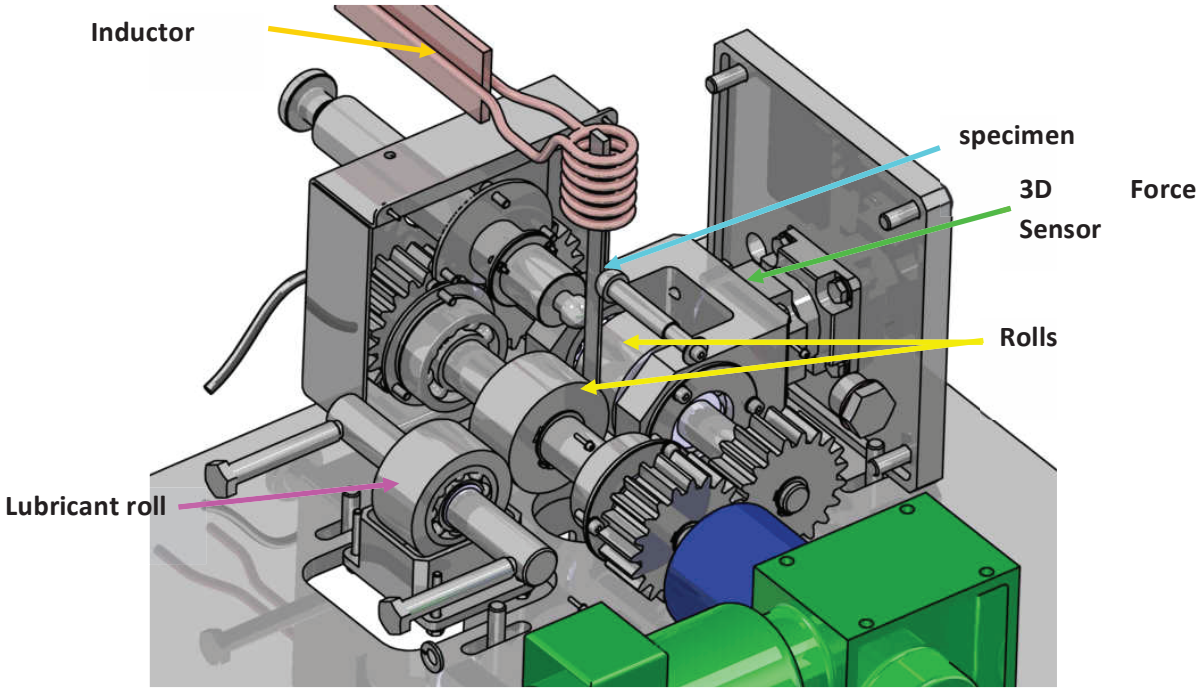

Fig. 108: Internal design of the test bench

A third roll is used to bring lubricant from a removable container to the contact zone between rolls and specimens. This roll is in contact with the working roll acting on the “industrial” surface of the specimen. The contact pressure between the lubricant roll and the working roll is adjusted by the screw n°9.

The geometry of the specimen is presented in Fig. 109 Specimens are 207 mm long but only 50 mm of the specimen are submit to plastic deformation at high temperature. The thinner part of the specimen is introduced vertically in the pilot by the hole of the superior housing (5) and plays the role of a guide, keeping the sample vertical during rolling. The thicker extremity of the specimen (where the original oxide scale is present) is reheated by induction, so the position of the sample has to be fine tuned in order to reheat the complete thick part of the sample (included the fillet).

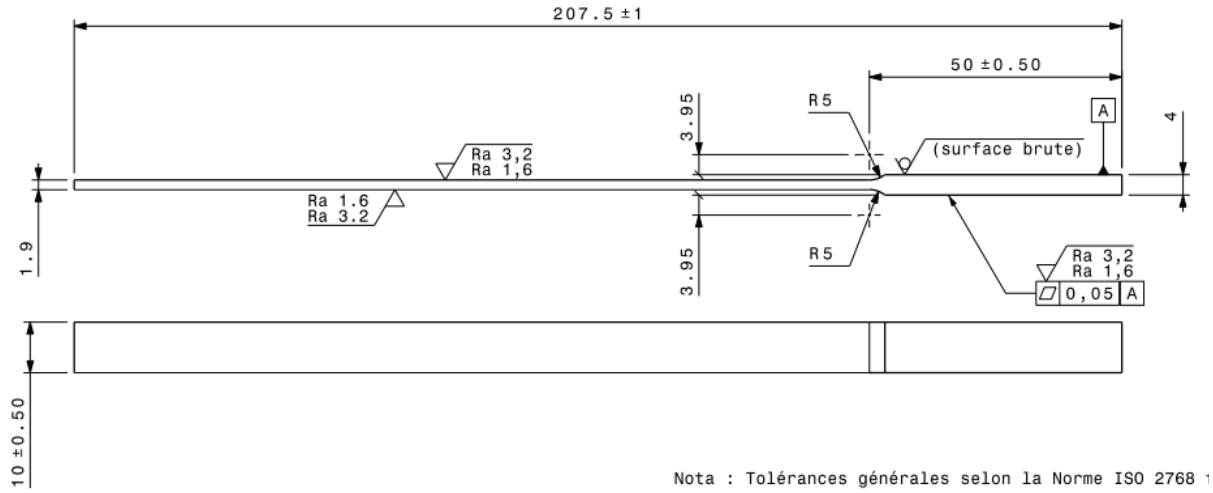

Fig. 109: Strip sample scheme

Test operates in two steps:
- the specimen is introduced in the bench frame and its thicker part is heated to the testing temperature,
- the cylinders rotation is activated and the specimen is rolled.

A bichromatic pyrometer is used to control specimen temperature at the entry of the bench. A sensor is placed above the frame to measure the exit speed of the specimen. Main test results are the forces applied on the rolls, the specimen exit speed, and the evolution of specimen and cylinder surfaces.

2. Test bench dimension and capabilities: adjustment to process invariants

According to equations 27 and to the fact that the final thickness of the specimen is imposed equal to 2 mm, we can identify the initial thickness of specimen e_e, the diameter of test bench rolls Dc and their rotational speed ω_b:

$$\begin{cases} I_1 = \dfrac{2}{\sqrt{3}} \ln\left(\dfrac{e_e}{e_s}\right) \\ I_2 = \dfrac{e_e}{d} = \dfrac{e_e}{\sqrt{Dc(e_e - e_s)}} \\ I_3 = \dot{\bar{\varepsilon}} = \dfrac{\bar{\varepsilon}}{t_0} = \dfrac{I_1}{t_0} \end{cases} \Leftrightarrow \begin{cases} e_e = e_s . \exp\left(\dfrac{\sqrt{3} I_1}{2}\right) \\ Dc = \dfrac{e_e^2}{(e_e - e_s).I_2^2} \\ \omega_b = \dfrac{I_3 \sqrt{Dc(e_e - e_s)}}{Dc.I_1} \end{cases} \quad \{27\}$$

As already mentioned, the distance between the two rolls is a fixed value of 2 mm. In order to reach several reduction ratios, we designed specimens with a thicker part on one of its extremities. The thickness of this extremity is variable and depends on the reduction ratio that we want to test (Tab. 17). The pilot is then able to simulate reduction ratios up to 40%.

Tab. 17. Different samples used to simulate the reduction rate variation

Initial sample thickness (mm)	Final sample thickness (mm)	Reduction ratio (%)
2,5 mm	2 mm	20 %
2,86 mm	2 mm	30 %
3,33 mm	2 mm	40 %

The gear box that controls the rotational speed of the cylinders allows adjustments from 0.08 to 4,6 rd/s, which correspond to strain rate ranging from 2 to 12 s^{-1}. The bench is then able to reproduce the I_3 invariant corresponding to stand 1 and 2 of the Châtelet hot strip mill. As a consequence, the gear box of the bench would have to be upgraded to enable rotational speed equal to 40 rd/s if the respect of invariant I_3 is expected when simulated contact conditions of stand 7.

A finite element computation of the pilot has been performed in order to identify the contact pressure applied on the specimens during the tests. The finite element model is defined to simulate the contact condition on the stand #1 of the Châtelet hot strip mill. The invariants are then given by:

Stand#1 data:
- e_e = 44.12 mm
- e_s = 26.8 mm
- Dc = 755 mm
- ω = 2,348 rad/s

So:

$$\begin{cases} I_1 = \dfrac{2}{\sqrt{3}} \ln\left(\dfrac{e_e}{e_s}\right) = 0.58 \\ I_2 = \dfrac{e_e}{d} = \dfrac{e_e}{\sqrt{Dc(e_e - e_s)}} = 0.38 \\ I_3 = \dot{\bar{\varepsilon}} = \dfrac{\bar{\varepsilon}}{t_0} = 4.53.s^{-1} \end{cases}$$

And consequently:

$$\begin{cases} e_e = e_s.\exp\left(\dfrac{\sqrt{3}I_1}{2}\right) = 3.3\,mm \\ Dc = \dfrac{e_e^2}{(e_e - e_s).I_2^2} = 56\,mm \\ \omega_b = \dfrac{2I_3\sqrt{Dc(e_e - e_s)}}{Dc.I_1} = 2{,}372\,rad/s \end{cases}$$

Then, the numerical model of the pilot is characterized by:

- 2D plane strain model,
- symmetry condition along the X axis,
- roll modelled as rigid body,
- plane strain elements with 4 nodes and 4 integration points,
- structured mesh with 22 elements through the thickness of the specimen (à verifier),
- Coulomb's friction coefficient equal to 0.28 (same value as for simulation of the process),
- Sellars & Teggart law to describe the thermal plastic behaviour of the stainless steel,
- specimen fixed at one of its edge,
- roll drive in rotation and translation.

The following results are obtained:

$$\begin{cases} \mu = 0{,}28 \\ \dot{\varepsilon} = 6.s^{-1} \\ F_x = -43{,}3.kN/m \\ F_y = -0{,}645.10^6\,N/m \\ P = 104{,}0.10^6\,MPa/m \end{cases} \quad \{28\}$$

This final result shows that contact pressures are similar on the test bench and on the stand #1 of the Châtelet finishing mill, with a difference lower than 5%.

3. Entry and exit parameters

3.1. Mastering of sample temperature

Before performing rolling tests, we have carried out reheating tests in order to evaluate the emissivity ratio of the strip material. The sample was initially instrumented with K-type thermocouples and this measurement is coupled with bi-chromatic pyrometer measurement. We adjust the emissivity index of the pyrometer in order to find a concordance on both equipments. The emissivity parameter has been checked and defined before each design of experiments.

During the test campaign, temperature control is made by a bi-chromatic pyrometer pointed on the sample. We tested various temperatures between 900°C and 1100°C.

Initial tests performed with thermocouples gave us the possibility to evaluate thermal losses between the reheating step and the rolling step. At a reheating temperature of 1050°C corresponds a rolling at 900°C. This thermal loss is very high and was taken into account on friction coefficient identification (Fig. 110).

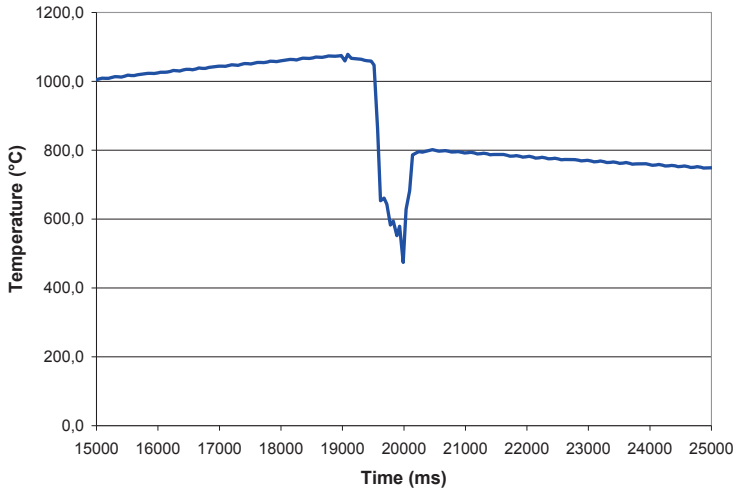

Fig. 110: Thermal losses between reheating and rolling on the pilot

3.2. SPEED CONTROL

Roll speed is monitored directly by the engine. Sample speed is different from roll speed, due to flow rate conservation. Forward slip (as defined previously) is directly deduced from roll speed and exit speed of the sample. In order to validate the forward slip value, we equipped the exit box under the pilot with an index fixed on the exit box and a camera that will film the test.
The speed is assessed on distance measurement (due to index) between three successive pictures given by the camera. This measurement is not very accurate because sample is not falling very straight and could oscillate during rolling.
Another device using two photodiodes to assess the sample exit speed was also tested but did not help to have better results. Oscillation of samples did not help to detect the position of the sample and so speed could not be computed accurately.

D/ Pilot validation

There are three points to check in order to be sure that pilot is reproducing the configuration of the first finishing mill stand.

1. Absence of scale modification during sample reheating

The effect of reheating on the sample could modify the oxide of the sample, so, to assess the possible consequences of the reheating step we will compare both sides of the sample immediately following the reheating step. Indeed, on the machined sample, no oxidation should occur. This checking should be done before all temperature test configuration. With very fast reheating speed, the re-oxidation phenomenon can be prevented. This relatively short reheating time between 10 and 18 seconds (depending on the temperature condition) induces no additional oxidation layer on the sample (Fig. 111). The superior face had a similar scale layer and presence of the four identified oxide phases were found onto the scale layer. No development of scale layer on the machined face was observed.
NB: Pink lines were manually added on the figure 102 to help distinguishing scale layer from the sample preparation resin.

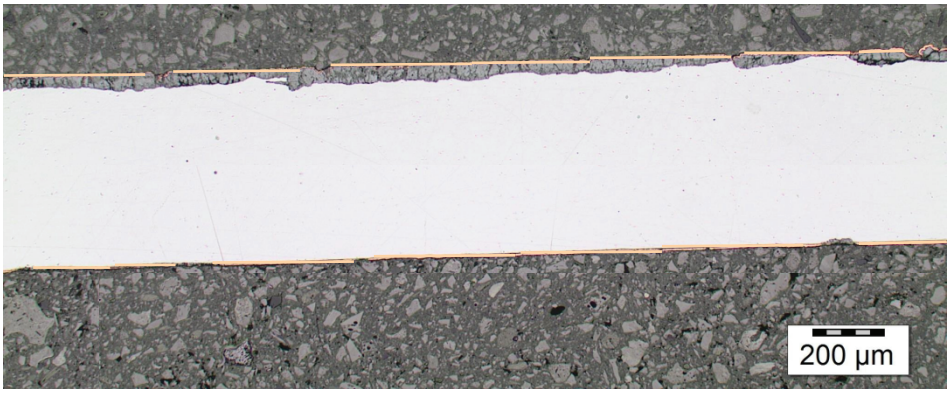

Fig. 111: No scale modification with reheating

2. Friction coefficient identification

Test results are composed of “direct results” and “non direct results”.
Direct results are the observation of specimen and roll surfaces. These observations will be performed by using microscope, SEM-EDS and 3D profilemeter. They will provide information on the evolution of the morphology of the oxide scale during the plastic deformation at high temperature.

Non direct results are mainly the determination of friction coefficient from the normal and tangential forces recorded during the tests. The identification is made by inverse method (Fig. 112). The same model as presented on pilot modelling (to check contact pressure) is used for this step. Only the half of the pilot is modelled. The roll (radius = 28 mm) is meshed with 121 R2D2 elements and the strip is meshed with CPE4 elements. The number of elements used on strip modelling depends on sample

entry thickness, and on our configuration one element represents 0.1 mm.

Friction coefficient is an entry parameter of FEM model and the normal and tangential forces are the result of the simulation. As a result, the friction coefficient put as entry parameter has to be optimized and a loop is done on its value to reach one half of the normal and tangential forces given during the test (because of the modelling of one half of the pilot).
Strain rate value is an indicator that has to be checked before validating the value of friction coefficient. This parameter has to be as close as possible to the value used in the material law.

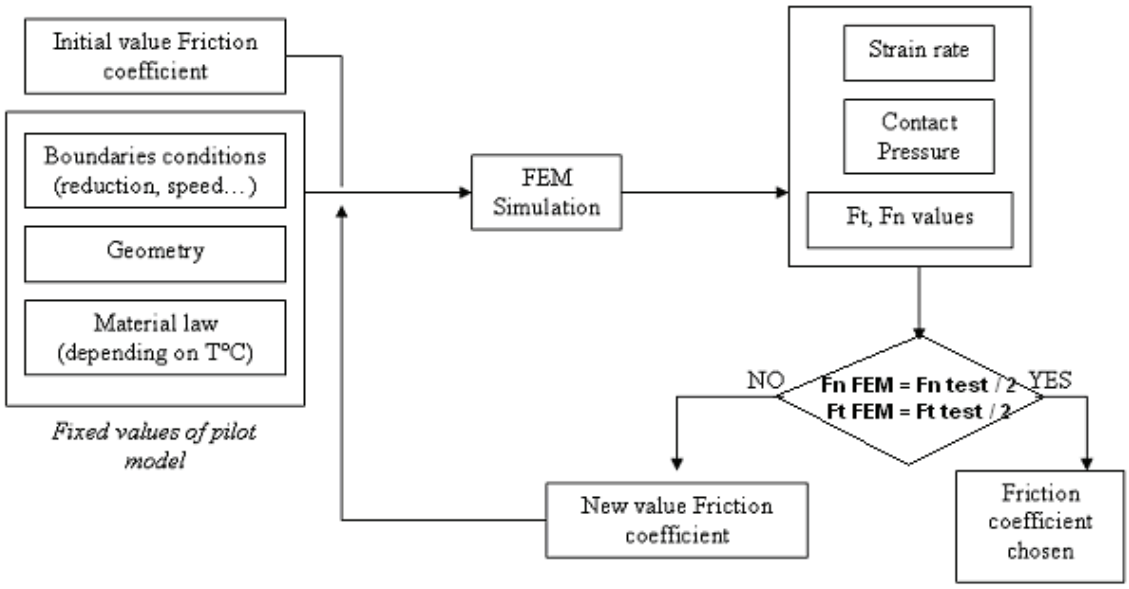

Fig. 112: Diagram of hot rolling contact condition simulation by pilot methodology

3. Thermo-mechanical response of the pilot – Validation of finishing mill configuration

In order to check reliability of the rolling pilot, some trials were performed at 1060°C and 40% of reduction in order to be as close as possible from industrial configuration described in the beginning of this chapter.
Measurements of rolling forces were made thanks to 3D force sensor and the average value of the force along rolling step was taken into account in order to compute the friction coefficient.

Normal force was around 6500 N and tangential force was around 450 N. These values imply a friction coefficient close to 0.3, which is in correlation with the computed friction coefficient as reference in the industrial configuration.

E/ Conclusion

In this chapter, a new rolling pilot was designed in order to reproduce the contact conditions of the first two stands of the hot strip mill, based on process conditions and the definition of invariants.

The main interest of this device is the use of specimens directly machined from the industrial transfer bar. As a result, the exact industrial surface is used in the test and it allows reproducing rolling conditions with a high accuracy. Using the original industrial surface implies the use of the original scale layer that is, as already seen, very particular in terms of scale composition and structure. This test will be much more specific than conventional disc-on-disc tribometers because we are now able to study the deformation of the scale, contrary to disc-on-disc tribometers were we can only test fresh oxide layer created during the reheating phase of the test.

The main results provided by this pilot are qualitative such as surface evolution (reproduction of defect, roughness modification...) of strip and roll specimens and also quantitative results such as the friction coefficient. The goal of next chapter will be to propose a design of experiments in order to study the effect of various process parameters and try to make correlations between the friction coefficient evolution and surface modifications.

CHAPTER 4 - OBSERVATION OF FERRITIC STAINLESS STEELS OXIDE LAYER

In the second chapter, it was highlighted that scratches generated on HSS working rolls are so small compared to the transfer bar oxide layer thickness that there is a low probability for roll scratches to be a nucleation site for sticking phenomenon. In order to go further with this topic, we designed a pilot to perform several tests to study the effect of rolling parameters on sticking.

The aim of this chapter will be also to examine in details the scale layer behaviour during rolling. Deformation of scale layer in the roll bite will help us to have an idea of metal/metal contact initiation.

A/ Thermo-mechanical behaviour of strip specimens

1. Design of experiments

Literature highlights the predominance of thermo-mechanical parameters of oxide layer as key parameter to understand the tribological behaviour of oxide layer. As a result, the two main rolling parameters that will be tested are rolling temperature and reduction ratio. To identify large trends, rolling temperature will ranges from 900°C up to 1100°C. Tested reduction ratios will range from 20% to 40%, corresponding to the minimal and maximal reduction ratio encountered on the finishing mill. Roll speed will be considered as a constant parameter, around 2.4 rd/s, which corresponds to the rolling speed in the first stand of the industrial mill.

In this work, no lubricant will be inserted in the device, inducing that only dry contacts will be studied because the first stands in finishing hot strip mill are not lubricated. Lubrication effect has to be evaluated in a second stage, after understanding the evolution of oxide layer in dry contact conditions. Each test condition was tested 5 times and results presented in this chapter correspond to the average of the three intermediate values.

All specimens used in this study are coming from two different transfer bars that were successively processed on hot strip mill, in the same ferritic production schedule (Number 91). The two products are coming from the same heat that is why they have the same chemical composition. First the chemical composition is presented (Tab. 18) and secondly, the main process parameters (Tab. 19).

Tab. 18. Specimens chemical composition in %wt

Grade	C	N	Cr	Cu	Mn	Mo	Nb	P	Si	Ti
AISI 441	0,015	0,02	17,55	0,09	0,32	0,01	0,40	0,03	0,59	0,14

Tab. 19. Process parameters used to produce transfer bars at the origin of specimens

Slab number	Sequence	Descaling	Transfer Bar Temperature (°C)	Stand F1 Temperature (°C)	Transfer Bar Thickness (mm)
9452 7330	114	Yes	1085	1073	34,72
9452 7190	115	Yes	1063	1050	39,47

Test conditions are summarized here below (Tab. 20).

Tab. 20. Test conditions

Rolling temperature /Reduction	950°C	1000°C	1050°C	1100°C
20%	x	x	x	x
30%	x	x	x	x
40%	x	x	x	x

The results of the tests are of various natures. First, normal and tangential forces are recorded during the test and numerical computations are involved to identify a Coulomb's friction coefficient by inverse method. Second, at the end of each test, specimens are examined by optical microscope on a longitudinal cross section. A particular attention is paid to the thickness and to the morphology of the residual oxide scale. Finally, modifications of roll surface at the end of each campaign are examined by optical microscope and SEM, both in cross-section and perpendicularly to their surface.

2. Friction coefficient evolution

Friction coefficient was computed for each test condition, gathering 12 x 5 results. On the figure 113 are presented the average value for each test condition. The standard deviation on each series of five measures is around 0.02.

2.1. Effect of reduction on friction coefficient

On a general way, friction coefficient increases with reduction ratio. At 1050°C, this trend is not completely true because, friction coefficient à 30% reduction and 40% reduction seems to be confused.

2.2 Effect of temperature on friction coefficient

At 20% reduction, the friction coefficient is quite stable with temperature. A small increase of friction coefficient is noticed on the two last temperatures: 1050°C and 1100°C.
At 30% reduction, friction coefficient tends to increase up to 1050°C and decreases at 1100°C.
At 40% of reduction, friction is quite stable but decreases slightly with temperature.

As a result, reduction ratio and temperature can have contradictory effects on friction coefficient and different phenomena could be at the origin of these trends.

A study proposed by W. Jin (Fig.114) highlighted that friction decreases with temperature, at 30% reduction, on strip and on slab. We cannot directly confirm this study at 30% reduction, but more at 40% reduction. Moreover, friction coefficient values presented by authors are quite different from those computed earlier. The main goal of this study was to point out the different behaviour of strip surface and slab surface, i.e. the specific effect of scale layer structure on friction. Using a transfer bar specimen, the scale layer structure is quite different from scale structure used by Jin and could explain the gap between the two studies.

D.J. Ha [HA08a] specified that friction increases with temperature up to 1000°C, and decrease on higher temperatures due to the creation of Cr oxides on the product surface. We will investigate oxide layer morphology and oxide layer changes in following paragraphs.

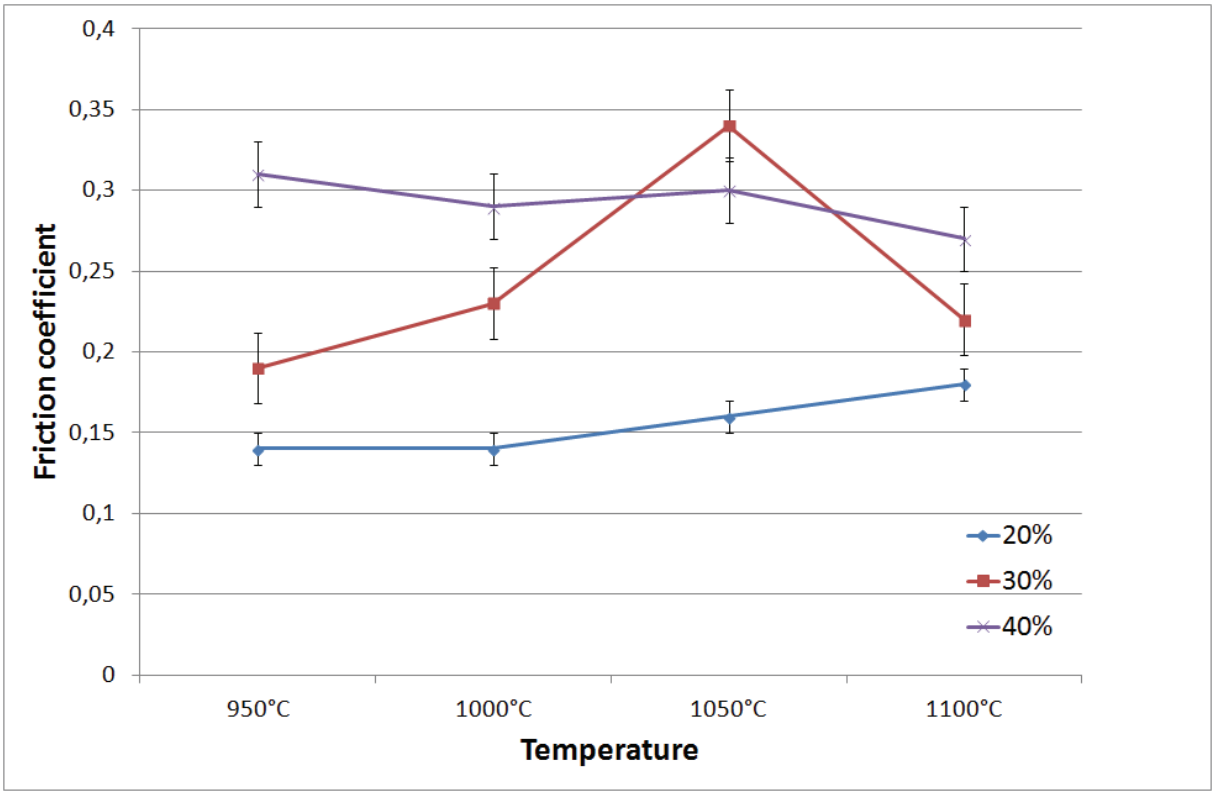

Fig. 113: Friction coefficient evolution with reduction ratio and temperature

Table 21. Value of friction coefficient computed for each test condition

Friction coefficient	20%	30%	40%
950°C	0,14	0,19	0,31
1000°C	0,14	0,23	0,29
1050°C	0,16	0,34	0,30
1100°C	0,18	0,22	0,27

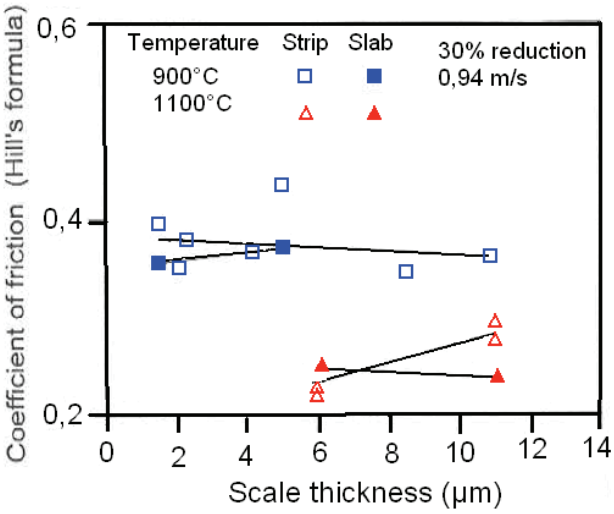

Fig. 114: Evolution of friction coefficient with temperature and scale thickness [JIN02]

2.3. Effect of scale thickness on friction coefficient

Oxide thickness was measured after rolling test (Tab. 22) and, according to Fig. 115, friction is not directly linked to oxide thickness evolution. If we analyse fig. 115 in details, at 40% of reduction or at 950°C, the thicker the oxide layer, the higher the friction coefficient, but this trend is not confirmed on lower reduction ratios, nor higher temperature. We can notice that the minimal value of scale thickness **after** rolling test is around 15 µm.

Table 22. Average oxide thickness measured on transfer bar specimens after rolling test

Average oxyde thickness (µm)	20%	30%	40%
950°C	36	43	53
1000°C	25	45	38
1050°C	40	44	45
1100°C	36	37	28

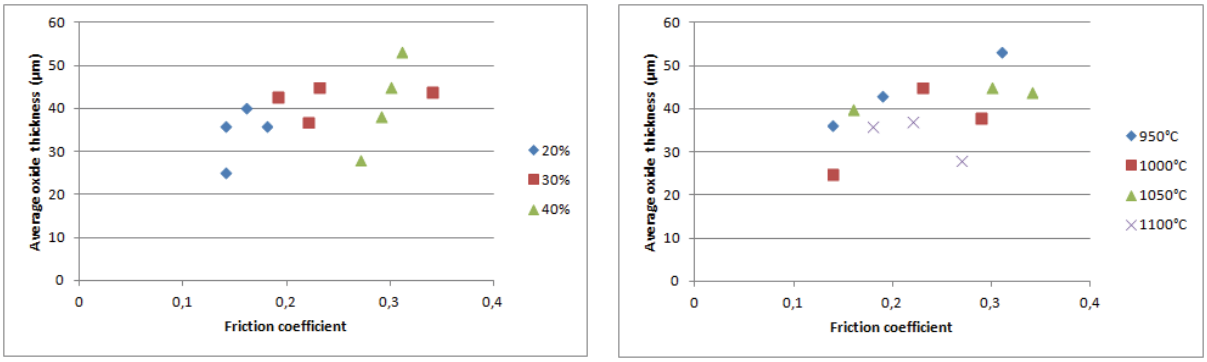

Fig. 115: Evolution of oxide thickness with friction coefficient, temperature and reduction ratio.

Jin and al. [JIN02] highlighted that scale thickness from slab or strip has no effect on friction coefficient, and we confirmed this trend. Usually, on flat carbon steels, oxide layer is known for having a lubricant behaviour, but on stainless steel this effect seems not to occur. Friction coefficient evolution at high temperature seems to be linked to another process parameter.

As oxide thickness is not the key parameter explaining friction coefficient variations, some investigations in scale layer morphology were performed in order to understand such changes.

B/ Scale layer fracture of ferritic stainless steels during rolling

In order to understand the particular evolution of friction coefficient with temperature and reduction ratio in this study, the evolution of oxide layer morphology along rolling and transversal directions is analysed and the evolution of oxide chemical structure with temperature is detailed.

1. Fracture of scale layer in the roll bite

1.1. Bibliography on ferritic scale fracture

Picqué [PIC04] noticed that scale fracture on carbon steels performed by 4 points bending tests induces cracks oriented to transverse direction. Two cracks pattern can be identified:
- equidistant cracks through the complete oxide layer thickness representing a fragile behaviour.
- oxide has a plastic behaviour and there is no through-thickness cracks. Oxide layer is delaminated and an interfacial cracks between substrate and oxide layer is present.

The distance between cracks is a measurable criterion that is linked to the strain intensity: the higher the stress, the higher crack density. For high strain values, equidistant cracks mechanism is replaced by delamination phenomenon.

Strain rate increase also increases crack density especially on oxide layer having a plastic behaviour. Strain rate influence gives an indication of the viscoplastic behaviour of the scale.

Temperature is also an influencing parameter on cracks formation. On carbon steels, Picqué [PIC04] showed that oxide behaviour changes with increasing temperature:
- between 600 and 700°C, the oxide layer has a fragile behaviour
- between 700 and 800°C, ductile deformation of the oxide is noticed
- at 1000°C, oxide is fragile again. Picqué explains that this particular behaviour could be due to phase transformation and dilatation coefficient difference between oxide and matrix.

Scale thickness variation may influence the results analysis on various temperature tests. In four point bending tests, specimens having scale thickness of 70 – 100 µm are used. Too thin scales (as industrial transfer bar specimens) cannot give reliable results, so transfer bar scales cannot be tested in such lab test.
Toscan [TOS04] compared austenitic and ferritic stainless steels in terms of scale adherence and fracture. Several tests were performed to compare final results. Inverted blister test performed on 150 µm thick strip specimens after 150 oxidation cycles (total duration of 50h) at 850°C under air. (Oxide layer was around 10 – 20 µm thick.)

Tests show that the increase of oxidation temperature leads to an increase in adherence energy. Oxidation duration has a negative influence on adherence. Initiation of cracking is observed with SEM and beneficial effect of Ti on stabilised ferritics on scale adherence is due to the formation of intergranular oxides of Ti (TiO_2) that creates a mechanical bonding between scale layer and metal substrate. Effects of temperature and duration of oxidation can be explained by scale/metal interface modification in terms of undulations and TiO_2 formation.

Three point bending tests were performed on ferritic grades (430 = Fe-18Cr, Fe-18Cr-0.2Ti, Fe-18Cr-0.4Ti, 436 = Fe-18Cr-Nb, 441 = Fe-18Cr-Ti-Nb), to compare such results with specimens closer to industrial strip thicknesses. Cyclic oxidation at 850°C and 950°C was performed during 50 and 100h in an atmosphere composed of Ar and 20% O_2.
All grades except Fe-18Cr-Nb did not present cracks so have an “elastic” behaviour. Fe-18Cr-Nb exhibits a large crack at metal/scale interface. Delamination of oxide layer of this grade proves that scaling sensitivity of this grade is higher than on other conventional stabilised and non-stabilised ferritic stainless steels.
Effect of temperature and oxidation duration were confirmed with this test but adherence energies were different from those measured by inverted blister tests, essentially because of metallographic substrate differences (grain size…).
Only Fe-18Cr-Nb could be characterized by three point bending test because no crack was found on other grades. As a result SEM traction tests on all grades were performed and allowed the comparison with the inverted blister test. Both tests (Fig. 116) highlighted that standard ferritic grade AISI 430 is the grade the most concerned by oxide scaling. Element addition, leading to the formation of inter and intra granular oxides, will generate a mechanical bonding between the scale layer and the metal. Most “efficient” addition is 0.4% Ti. Nb addition is less effective. Nevertheless, both tests give different adherence energy values that are hard to compare, and probably linked to the specimen metallurgical characteristics.

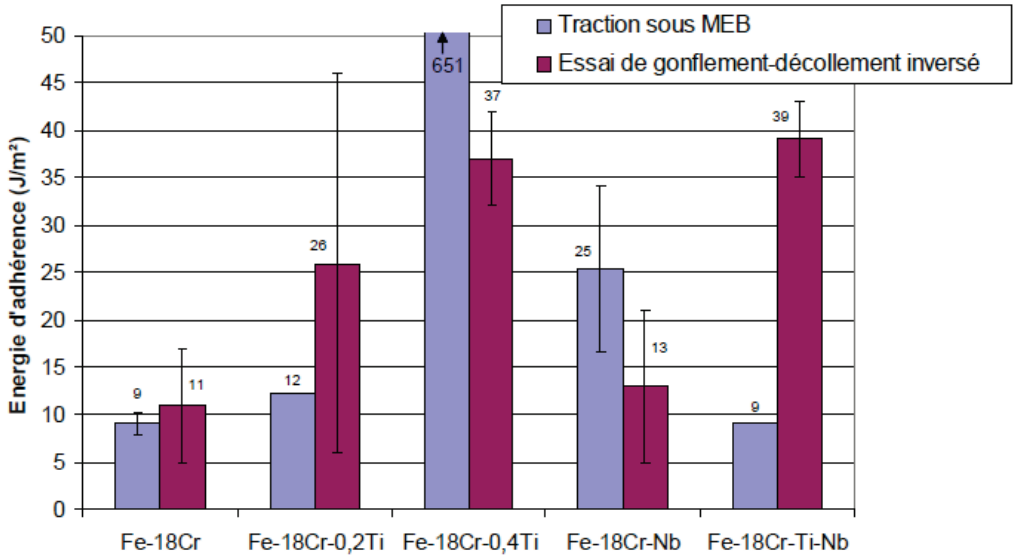

Fig. 116: Comparison of adherence energy of several ferritic grades with inverted blister test and SEM traction [TOS04]

1.2. SCALE FRACTURE AFTER ROLLING TRIALS

Specimen examinations show clearly that rolling trials induces cracking of the scale layer perpendicular to the surface and along transverse direction, representing the fragile behaviour of oxide scale during rolling (Fig. 117). The longitudinal crack between Cr-rich and Fe-rich oxides was suppressed by compression imposed during rolling trials.

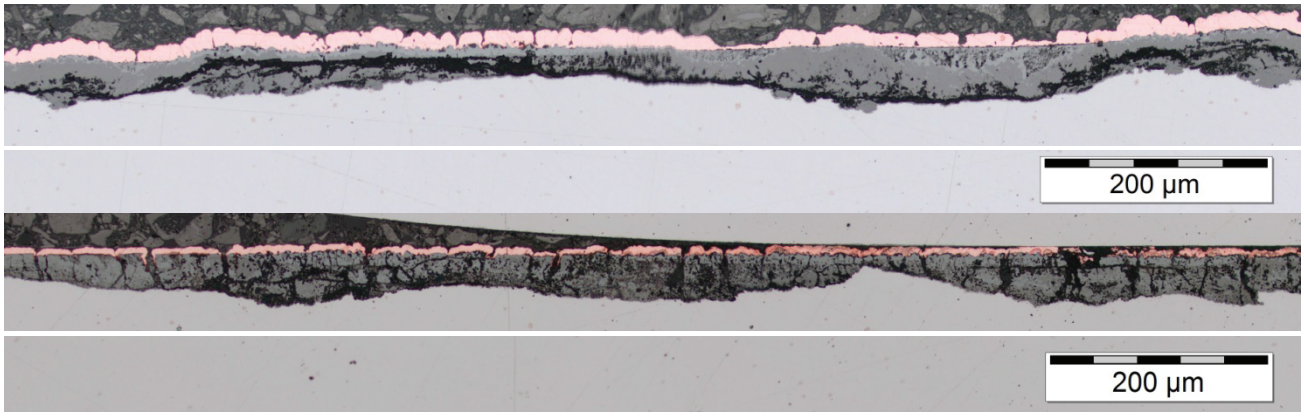

Fig. 117: Oxide layer observation along rolling direction – a) Before rolling test – b) 1000°C

The density of cracks along rolling direction was analysed at 20% reduction, on cross section (Fig. 118) (along rolling direction) and, as for friction coefficient, **an increase of cracks density is noticed with temperature**, especially for temperature higher than 1000°C. (The high number of cracks on specimen reheated at 1000°C is explained by the high amount of oxide spallation that induced measurements on a smaller distance than on other specimens.)

No correlation was found between cracks density and oxide thickness, as on B. Piqué study performed on flat carbon steels [PIC04]. The influence of reduction ratio is not as evident as

explained on bibliographic paragraph. Indeed, on tests performed at 950°C, with several reduction ratios, **no linear trend between crack density and reduction ratio was found (Fig. 119).**

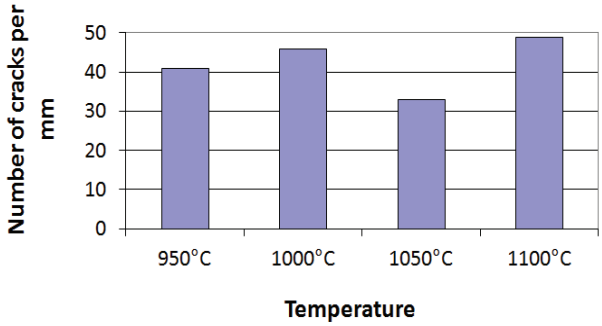

Fig. 118: Evolution of cracks density with temperature (20% reduction)

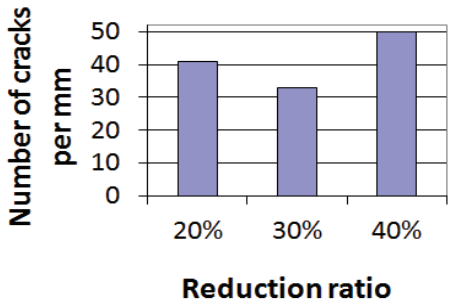

Fig. 119: Effect of reduction ratio on crack density at 950°C

Nevertheless, these results have to be used with caution because it is particularly hard to distinguish cracks generated by plastic behaviour and due to air cooling.

2. Interest of scale layer observation in transversal direction

Specimens were also observed on transversal direction (perpendicular to rolling direction). As strip specimens are narrow (1 cm), all specimens were polished three times up to mirror finish, so equivalent observed distance was around 3 cm on each specimen. (Fig. 120)

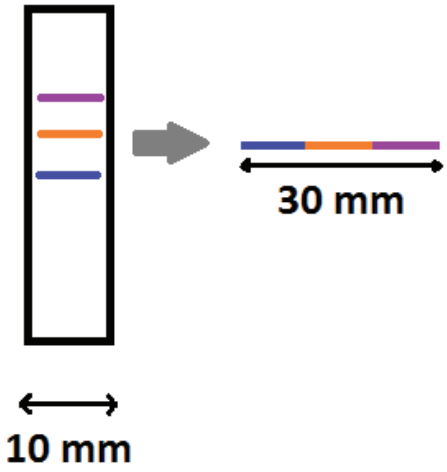

Fig. 120: Transversal cut of specimens

Presence of plateau was noticed on a high number of specimens (Fig. 121). **Plateaus are surface deprived from oxide layer and where direct contact may occur with the rolls**. Their width and their density, defined by the number of plateaus along one centimetre of specimen width, have been measured.

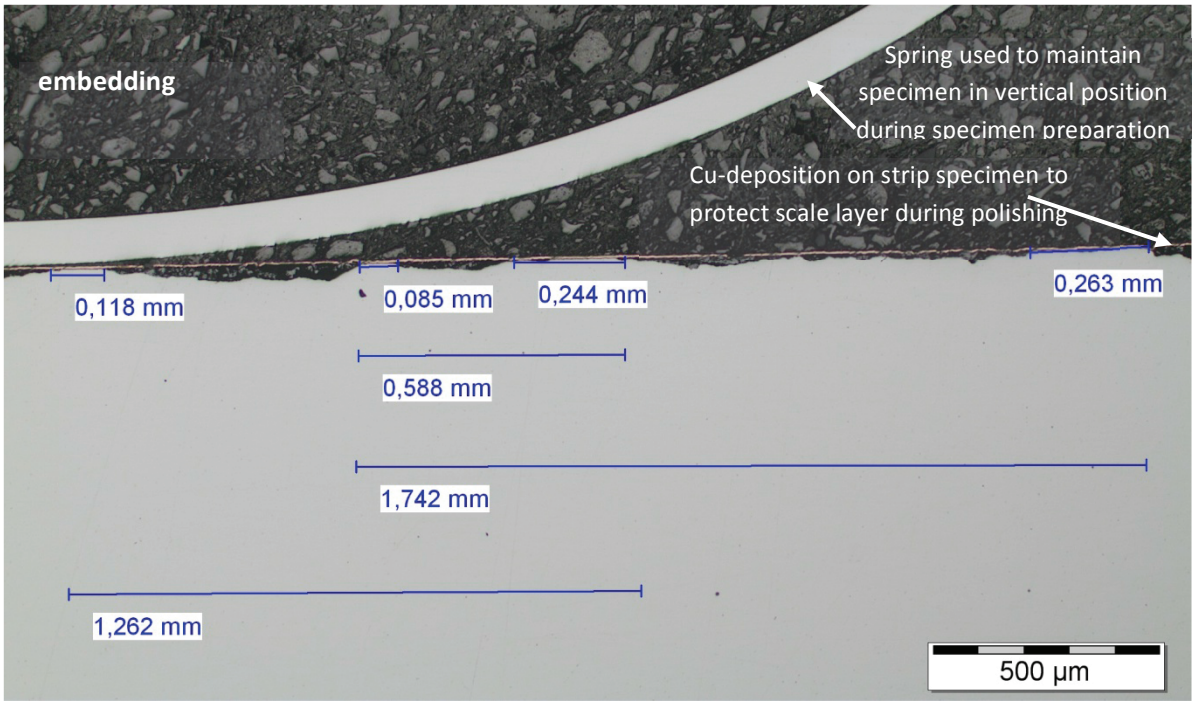

Fig. 121: Presence of plateaus on specimen observed in transversal direction

There is no typical distance between plateaus per specimen, as a result, the phenomenon seems to appear randomly.

We noticed that plateau can be isolated or grouped forming a larger contact area up to 2 mm wide. Table. 23 gathers size measurements of plateau. On specimen corresponding to test conditions 20% reduction and 950°C, after the first polishing, we saw only one plateau whose size is around 250 µm. After the second polishing, no plateau was found, and after the third polishing, two plateaus were found: the first one was 350 µm wide and the second was 340 µm wide. As a result, the total width covered by plateaus on this polished cut is about 940µm over 10 mm cross-section observed.
In this test configuration, the wider plateau was identified after polishing 3 and was 350 µm wide. Wider plateaus are highlighted in yellow per each test configuration and are summarized in table 24.

Investigations performed on different samples highlight that the minimal size of plateau **is around 50 µm** and the **maximal is around 900 µm**. The average size of plateau is **of 200 µm**. **This dimension corresponds to the average size of the sticking defect observed on industrial stainless strips**.

If we take into account only the maximal values of plateau size per each test configuration (values highlighted in yellow on Tab. 23), we can notice that the size is quite stable on tests performed at 40% reduction, whatever the temperature. At 20% of reduction, plateau size seems to be higher with increasing temperatures. At 30% reduction no trend is evident. As a result, we can suppose that formation of plateau is, firstly depending on reduction ratio, and secondly on rolling temperature.

Tab. 23. Plateau size measurements performed on strip specimens at various temperature and reduction ratios

	950°C	1000°C	1050°C	1100°C
20%				
Polishing 1	**250µm**	**200µm**	**1mm**	**No plateau**
Polishing 2	**No plateau**	**1.53mm** 130µm => **760 µm**	**650 µm** 430µm +530µm => **1.18mm**	
Polishing 3	350µm + 340µm => **940µm**	790µm + 500µm=> **1.63mm**	540µm + 920µm + 50µm => **2.39mm**	
30%				
Polishing 1	400µm + 250µm + 350µm => **1.2mm**	**100 µm** 100µm+ 81µm => **300 µm**	**150µm** **550µm** **100µm**	**250µm**
Polishing 2	670µm => **870µm** **230 µm** **110 µm** 60µm + 220µm => **560µm**	110µm + 70µm + 140µm => **610 µm** 60µm + 210µm =>**910 µm**	**100µm** **60µm**	80µm + 140µm => **640 µm** 590µm + 310µm => **1.45mm**
Polishing 3	190µm + 300µm + 100µm => **1.50mm**	**290µm** 100µm + 370µm => **760µm** **100µm** **100µm**	**100µm**	**100µm** 70µm + 80µm + 210µm + 120µm **=> 1.28mm**
40%				
Polishing 1	No trial	**370µm** **50µm**	100µm + 100µm + 100µm =>**550µm** 200µm + 70µm => **500µm**	80µm + 150µm + 350µm + 100µm => **1.1mm** 100µm + 8 µm + 250µm => **1.2mm** 80µm + 250µm + 260µm => **1.7mm**
Polishing 2		**180 µm** **20 µm** 20µm + 80µm => **360 µm** **140 µm** 20µm +100µm => **390 µm**	**320µm** **190µm** **500µm**	**130 µm** 240 µm + 190 µm => **1.06mm** 340µm + 290µm + 370µm + 520µm => **2.18mm** 50µm + 90µm + 340µm => **620µm**
Polishing 3		260µm + 300µm => **760 µm** 50µm + 280µm + 150µm + 210µm => **1.75mm** **510µm**	90 µm + 130 µm => **330µm** **1.26mm**	40µm + 220µm + 110µm => **780µm** **40µm** **320µm** **270µm** **290µm**

Tab. 24. Maximal size of plateau per test configuration

Maximal size of plateau	950°C	1000°C	1050°C	1100°C
20%	350	790	920	0
30%	670	370	550	590
40%	x	510	1260	320

A very particular point is the test corresponding to 20% reduction at 1100°C. This configuration leads to the formation of no plateau. We suspect that this result is not in good agreement with reality but we did not found any reason that could explain this particular behaviour.

The average plateau size (Fig. 25) was computed using measurements of Tab. 23. Similar trends as those observed on maximal diameter size can be found. But, the evolution of average plateau dimension is also increasing with increasing temperature at 30% of reduction.

The industrial current configuration of ferritic processing in the finishing mill is 40% reduction at 1070°C. The observed defect size is around 200 µm and it is in good accordance with the average values found on Tab. 25 who predicts an average size of defect between 280 and 200 µm.

What is interesting for industrial application is that the minimal value of sticking defect (except configuration 20% reduction at 1100°C) is found for 30% of reduction and small temperature (950°C).

Tab. 25. Average size of plateau

Size	950°C	1000°C	1050°C	1100°C
20%	313	506	588	0
30%	112	140	176	195
40%	x	171	278	202

Tab.26. Density of plateau on strip specimens

Density	950°C	1000°C	1050°C	1100°C
20%	1	2	2,3	0
30%	3,6	4,3	2	3,3
40%	x	5,3	3,6	9

The density of plateau (i.e. number of plateau computed on 1 cm of specimen width) was also deduced from Tab. 23 and results are summarised in Tab. 26. As a result, density of plateau is first depending on reduction ratio and second, depending on temperature. The lower density is obtained for 20% reduction at 1050°C

If we multiply the density of plateau by the average plateau size, we can notice that the best configuration (i.e. the smallest value) is obtained for the configuration test: 20% reduction at 950°C. Nevertheless, this configuration cannot be recommended because it results in a limitation of general reduction ratio, so it will decrease the capability of hot strip mill.

The general evolution of density of plateau seems to be correlated to friction coefficient evolution, except for 40% reduction tests, and temperatures higher than 1050°C at 30% reduction. Plateaus are the contact area between roll and specimen, as a result, the wider the contact area, the higher the friction coefficient.
Study of 40% reduction case and 1050 -1100°C at 30% reduction have to be done by investigating oxide chemical composition in more details.

If we put these results in perspective to the sticking phenomenon and suppose that these plateaus could be the initiation site of sticking phenomenon onto the strip, we deduce that these results are in contradiction with Jin and al. study [JIN98] who highlights that sticking was more intense at 900°C and lower at higher temperature thanks to the formation of an oxide layer that plays a protective interface towards sticking. Our study differs from Jin's one by the nature of specimen used to perform tribological test. Indeed, in our case, results will be very dependant from the behaviour of scale layer. In the case of disc-on-disc tests, results are influenced by the formation of a thin scale

layer during the test. It is also normal that results of the trials will be slightly different.

The developed rolling test is much more effective to study fracture and abrasion of oxide layer in a roll bite than studying the tribological effect of a developing oxide layer by dry corrosion. The main interest of this test is that it is more adapted to study the effect of reduction ratio, which is not possible with conventional two disks type.

3. Chemical composition of oxide layer after 40% reduction

In order to understand the evolution of friction coefficient on tests performed at 30% and 40% reduction, SEM examinations of the scale layer after rolling test were performed (Fig. 122). Quantitative analysis was performed at different layers observed in the scale thickness after normalising oxygen with Cr_2O_2 and Fe_2O_3.
Descriptions of different specimens (having different rolling temperature) have to be compared with the previous scale layer description of chapter 1. Description of chapter 1 was done on transfer bar specimen (before the rolling test).

First difference before and after the rolling test is that the longitudinal crack between iron rich and chromium rich oxides was suppressed, due to the compression imposed during the rolling test.

The inner part of the oxide (close to steel substrate) essentially composed of $CrFe_2O_4$ and $FeCr_2O_4$ is present in all temperature case (from 950°C to 1100°C) and are very compact.
The outer part of the oxide essentially composed of iron oxides (Fe_2O_3 and Fe_3O_4) tends to disappear on rolled specimen with increasing rolling temperature. On the oxide picture corresponding to 1100°C, the absence of comb form at scale/metal interface (see Chapter 1) is linked to the absence of Fe_3O_4 and rare presence of Fe_2O_3 in the outer part of the scale.

Iron oxide initially present at specimen surface seems to leave the specimen and play the role of a solid powder lubricant during rolling. It could explain why, at high temperatures, (and high reduction rate) friction coefficient is decreasing despite of increasing contact areas and plateaus size. Outer part of oxide layer will be transferred in the third body or onto the roll surface. We will investigate this point in next paragraph dedicated to the roll.

The silica layer is still present on all specimens (whatever the temperature). We suppose that the particular morphology of this oxide layer makes it particularly adherent to the metal substrate but will not be thick enough to prevent sticking phenomenon on whole surface of the specimen. Moreover, we already noticed that this layer is not continuous on specimen surface and seems correlated to the adherence of the outer part of scale layer.

The inner part is the most important layer to decrease sticking, because, thanks to the presence of two Cr spinels ($CrFe_2O_4$ and $FeCr_2O_4$) in this layer it helps to maintain a continuous interfacial layer between the metal substrate and the roll.

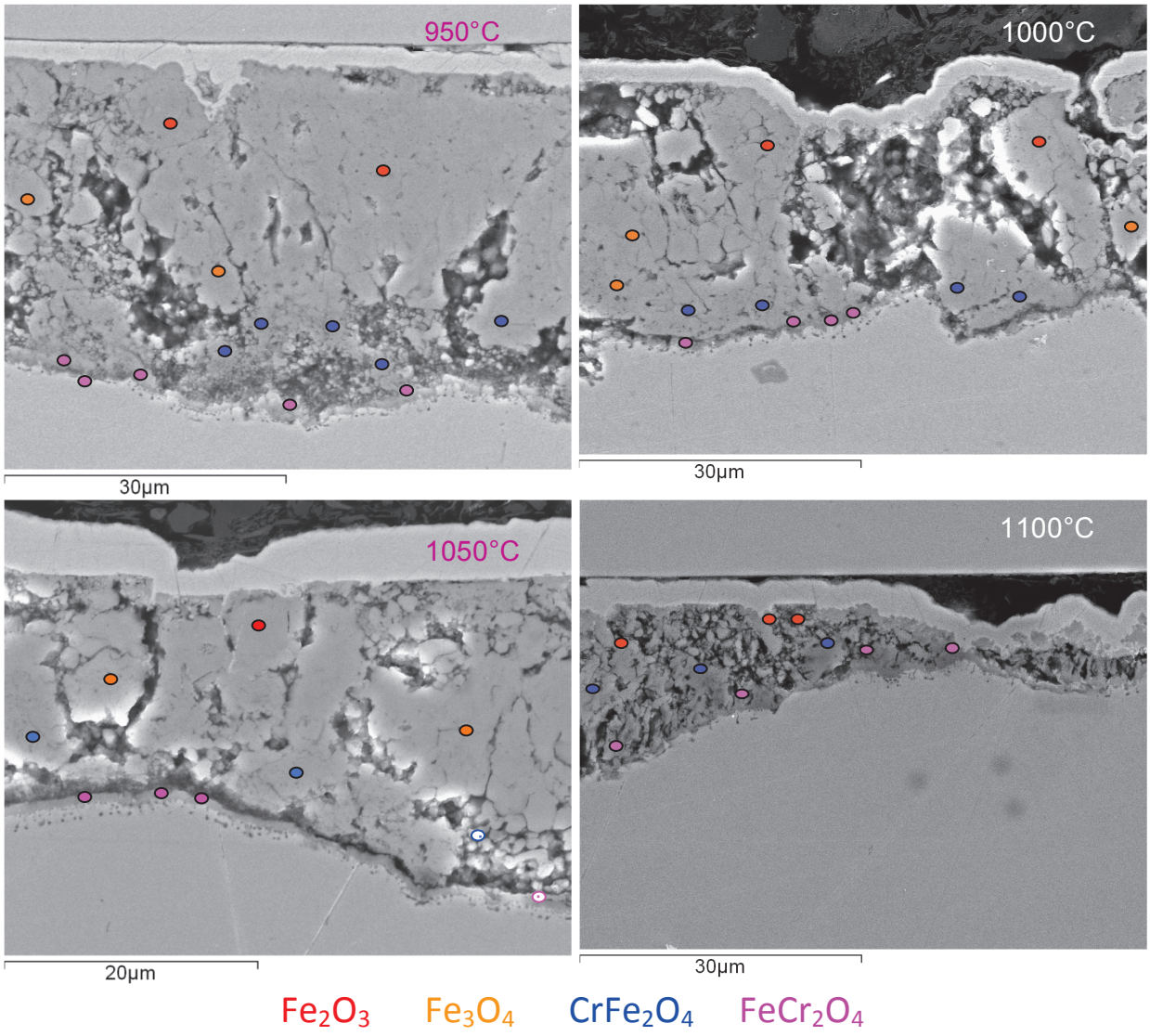

Fig. 122: Evolution of oxide layer with temperature (after 30% reduction rolling tests)

4. Conclusion of friction coefficient evolution and crack generation towards scale modification with temperature and reduction rate

Friction coefficient increases with increasing temperature at 20% reduction and decreases at temperatures higher than 1050°C for reduction rates superior to 30%. We explain this trend on our pilot by the fact that scale layer will be abraded and the outer part of the scale will be removed and play the role of a solid lubricant. Iron oxides are removed especially when silica layer is small (no comb pattern). At lower temperatures, iron oxides will only be compacted and increase of friction coefficient is only explained by the increase of surface contact between rolls and specimen (plateaus).

Bibliography shows that scale adherence increases with temperature, but it is in contradiction with the increase in plateau size (with temperature). It highlights that oxide nature acting in the contact is the first order parameter and scale adherence has a second order of importance.

Reduction ratio increase leads to an increase of friction coefficient which corresponds to higher normal pressure into the roll bite. This trend is confirmed by the increasing density and size of plateau. Nevertheless, cracks density seems not to be directly linked to plateau density and it could explained by the fact that it is hard to make the difference between cracks generated by plastic deformation and cracks made during specimen cooling in the air.

5. Formation mechanism of plateau

Formation mechanism of plateau seems to be generated in the roll bite by scale layer abrasion. Indeed, we noticed that, during rolling, scale is firstly compacted, especially the outer part, rich in iron oxides. At higher temperature, we notice that scale is abraded and the outer part is removed from the strip specimen. This phenomenon is reinforced especially when silica layer is smaller without comb pattern.

Abrasion will create plateau on strip surface, increasing surface contact area between roll and strip. Plateaus are mainly composed of oxide on their top but, as explained previously, small oxide particles are removed from plateau surface. On Fig. 123, the white part of strip surface corresponds to plateau surface. We can notice that a valley (in black) in middle of the picture is oriented in the rolling direction. We can notice small abrasion scratches are present on plateaus.

Figure 124 is a scheme illustrating the effect of rolling onto strip surface. The wavy profile of the transfer bar before rolling will generate these plateaus whose size depends on contact conditions, but also on roughness profile of the strip.

SEM observations of strip specimen surface highlight the presence of through-thickness cracks (as mentioned on previous paragraphs) (Fig. 125). The darker areas are flat surfaces constituted by compacted oxides forming like a glassy surface. Whiter areas have a granulated aspect and are composed on fragmented oxides. Fracture of scale layer is generating some islands of oxide whose equivalent diameter is approximately of 100 µm. On the second picture of Fig. 125, we can see in the bottom left corner, the spallation of an oxide island and the underlying base metal. On Fig. 124, we noticed that plateau corresponds to the higher part of strip roughness. As a result, abrasion will compress oxide in valleys and cut oxide and metal asperities on peaks. **These (old) peaks will be transformed into metal spots on strip surface that could lead to sticking initiation site with roll surface contact.**

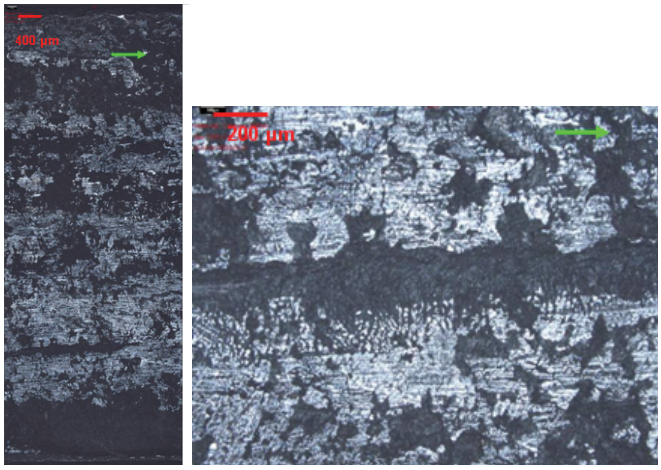

Fig. 123: Surface observation of scale layer after rolling test

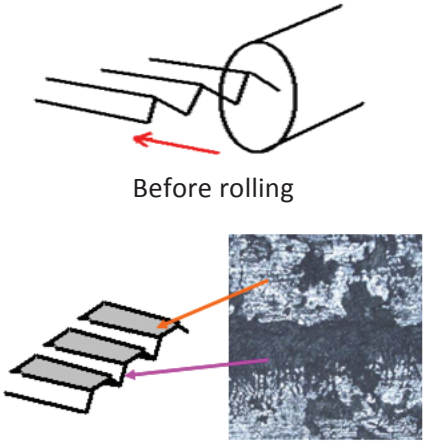

Before rolling

After rolling

Fig. 124: Formation mechanism of plateau

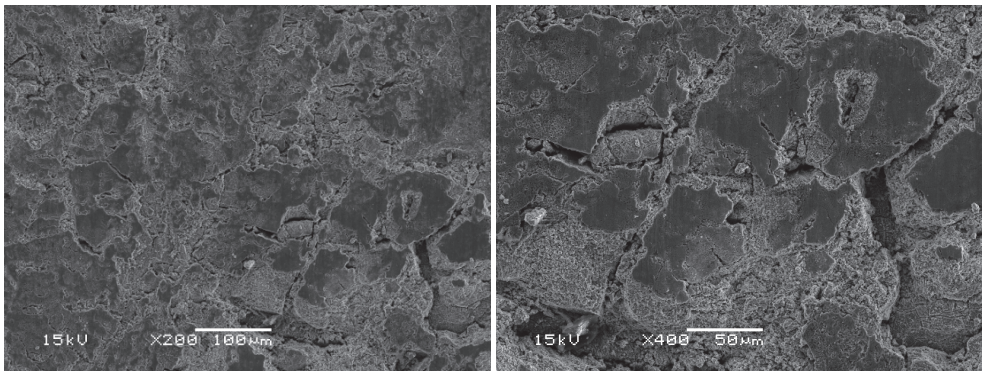

Fig. 125: SEM observation of strip specimen surface (1373K – 40% reduction)

C/ Observation of roll specimens

In order to confirm if plateau could be initiation sites for sticking phenomenon, roll specimens were examined. This paragraph is dedicated to the roll specimen investigations at the end of rolling campaign.

1. Reproduction of sticking defect onto the pilot

As mentioned in chapter 3, rolling pilot is composed of three rolls (Fig. 126). Two rolls are in direct contact with the strip specimen: the A roll, ref. 3 on Fig 27, is in contact with the machined surface of the specimens and the B roll (ref. 7) is in contact with the scale layer. The last cylinder, ref. 8, is involved to impregnate the previous cylinder with lubricant. No lubricant was used in the present study since the survey is restricted to dry contacts; however, the C cylinder is in contact with the B roll.

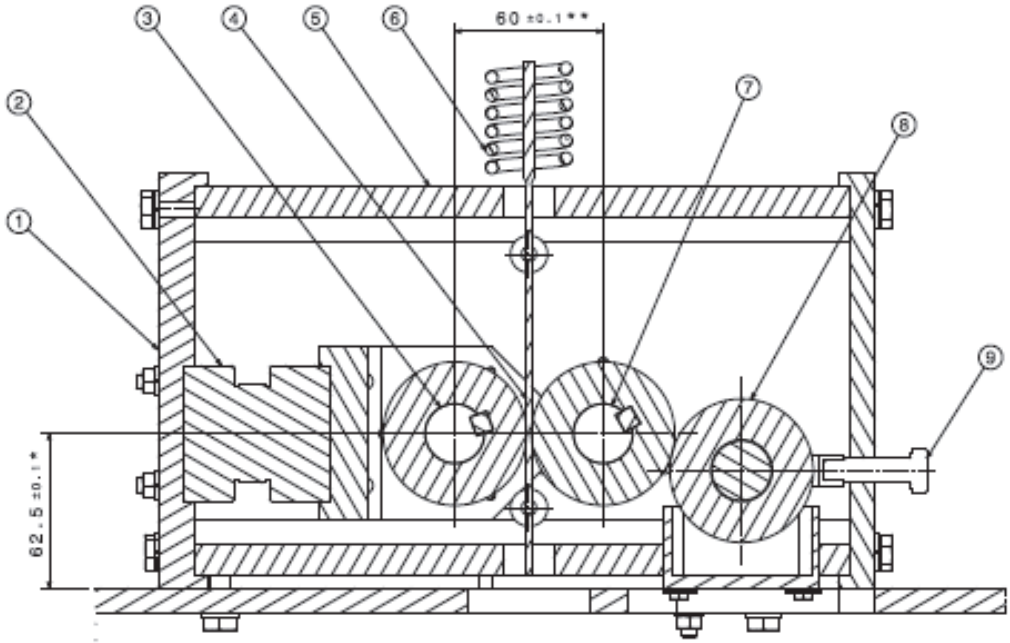

Fig. 126: Roll configuration of the rolling pilot

At the end of the rolling campaign (see Design of experiments at the beginning of this chapter), three rolls were removed from the pilot to be examined. 67 specimens were rolled, including 6 who were trapped in the roll bite.

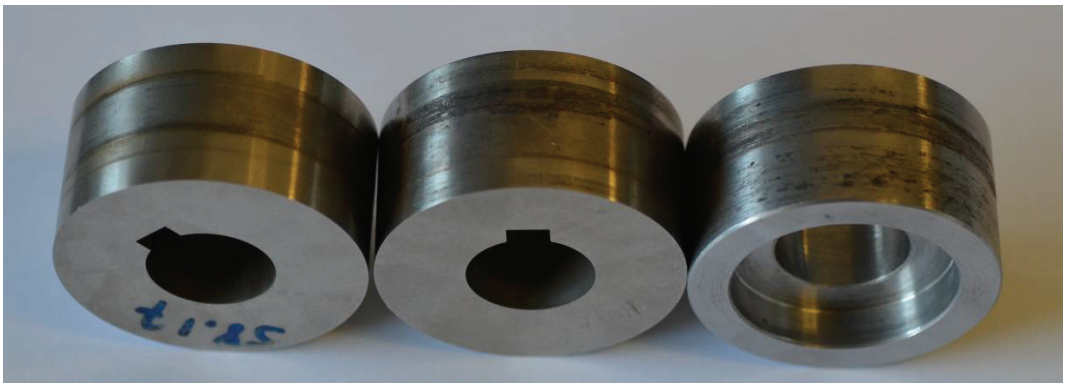

Fig. 127: Extracted rolls from rolling pilot: A roll (in contact with specimens machined side), B roll (in contact with specimens oxidized side) and C roll (in contact with B roll)

Cylinders feature are very different: the scale can be observed on cylinders that were in contact with the original scale of the specimen.

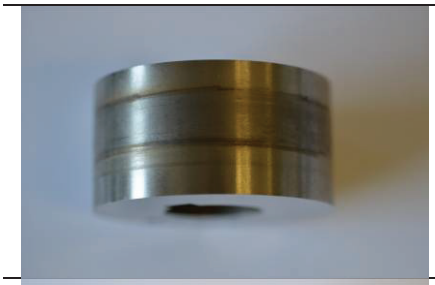	*A roll* seems to be burnt especially on two rings that correspond to the edges of the specimens. The area corresponding to the machined surface of the specimen has a matte wear feature. It is looking slightly rougher than cylinder edges, which remained identical to the initial cylinder surface (before testing).
	*B roll* (in contact with oxidized specimen surface) has an irregular wear along its generatrix. An edge seems to be more marked than the other: an oxide coating covers the specimen edge area. Wear on the half-width of the specimen is higher than on the A cylinder because it appears that a thin layer of very adherent oxide is present.
	*C roll* has two clearly distinguishable areas: a strong oxidized area which is symmetrical to that of the B roll, and a flecked area corresponding to the surface in contact with the specimen (indirectly). Initial surface aspect has a turned finish: we see machining ridges.

Fig. 128: Rolls extracted from pilot after the two first campaigns, respectively, A roll, B roll and C roll



Fig. 129. Zoom on C roll and presence of machining ridges over the surface



Fig. 130. General aspect of C roll

1.1 Roll surface before rolling test

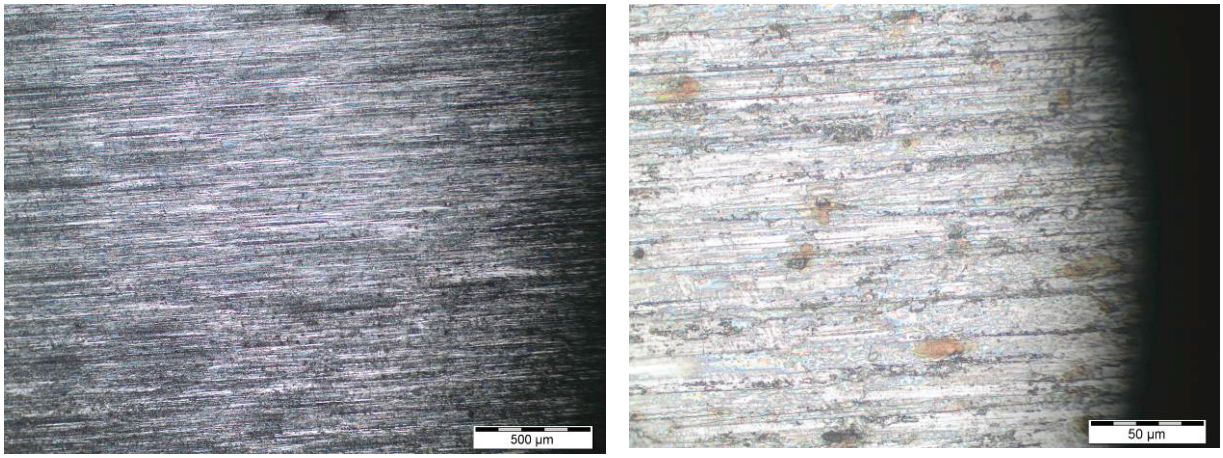

Surface of the unworn area of A roll – X 50 *Surface of the unworn area of A roll – X 500*

Fig. 131: *A roll* surface before rolling trials

Presence of (precision) grinding ridges, small cavities and uprooting (black dots on the right picture of Fig. 131) can be noticed on HSS roll surface before the test. Uprootings are probably due to carbides tearing during the passage of the wheel. Yellow traces are residues of oxidized lubricant products (coolant). The average size of uprootings is around 8 µm and it could correspond to nodular carbides of MoC or VC that are presented in Appendix 1.

1.2. A roll examination

Macroscopic observation of A roll (Fig. 132) is sufficient to distinguish some dots corresponding to particles that are looking like stuck particles on roll surface. These particles can reach up to 2 mm along rolling direction and 1 mm in transverse direction.



Fig. 132: Suspected area on A roll having stuck particles

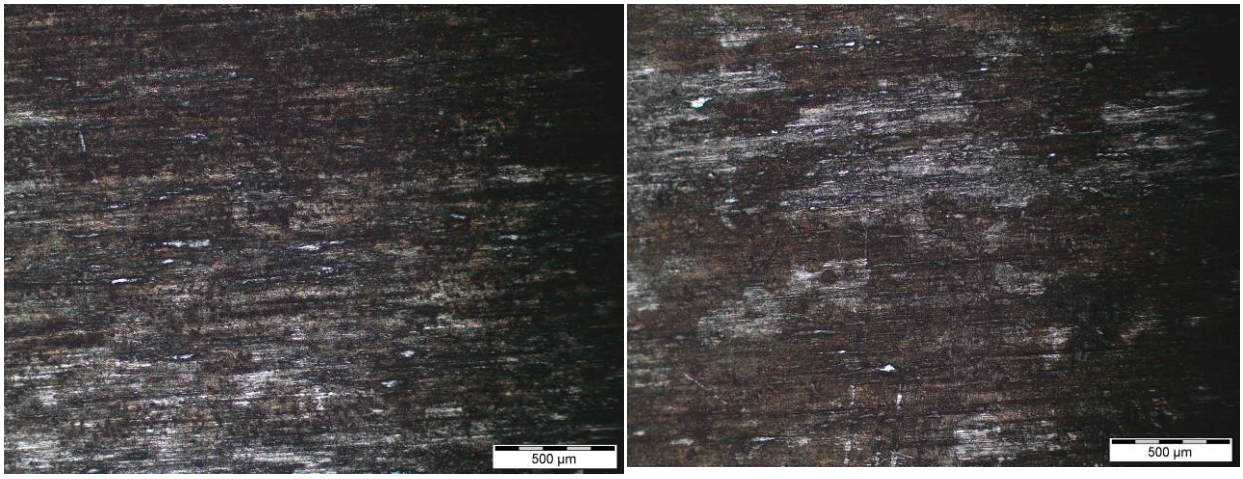

Fig. 133: Oxidized area and yellow area of A roll surface – X 50

The cylinder is covered with a thin oxide layer which is opaque in the dark zone and non-covering in the yellow area (Fig. 133). Points that are visible (in white on both pictures) are abraded metal particles onto the surface. The size of these particles is about 20 microns in diameter and 22 points were counted on an area of 2,2 mm². The approximate density is around 10 particles per mm². Grinding ridges are visible under oxide surface.

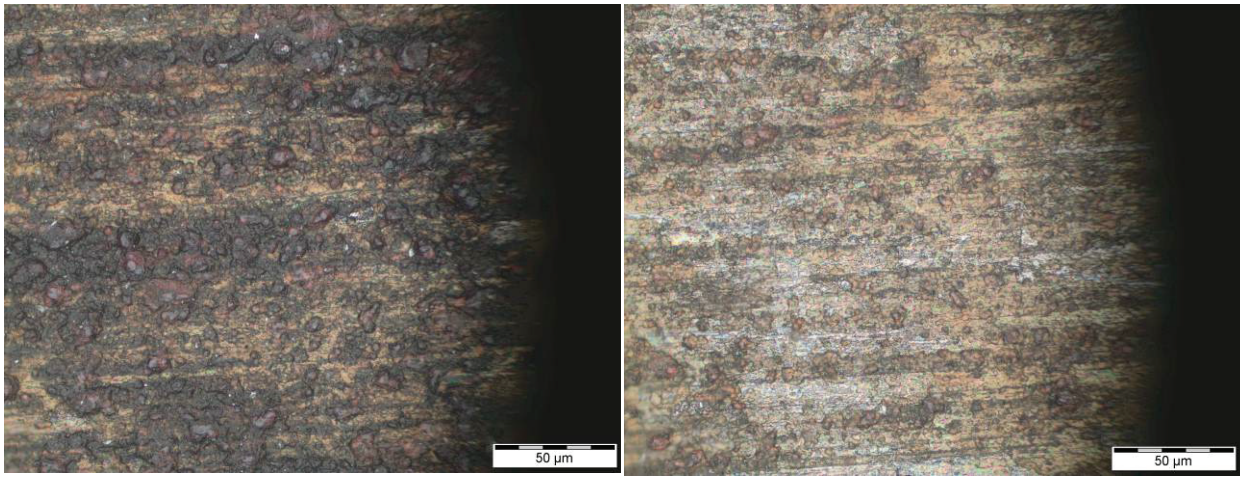

Fig. 134: Oxidized area and yellow area of A roll surface – X 500

In the oxidized and yellow areas, many cavities were created by the successive specimen rollings (Fig. 134). These cavities may be also related to the uprooting of carbides. The average size of cavities is about 10 microns in the oxidized area. These cavities exist independently of the severity of oxidation, but their size is smaller when the oxidation is lower. The cavities are then 6 µm in diameter.

An observation of a cylinder cross-section allowed us to define the size and the shape of the imprint left by a carbide uprooting. On Fig. 135, we find that carbide tearing zone (red circle) has a cylindrical shape and an approximate size of 20 microns in diameter. The cavity depth is about 15 microns.
We therefore conclude that the observed cavities of Fig. 134 correspond to areas of carbide uprooting.

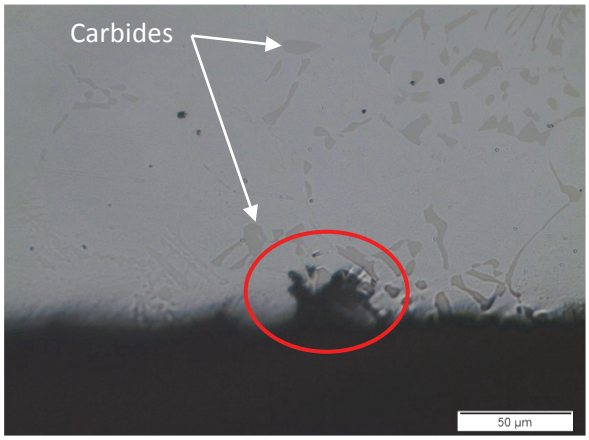

Fig. 135: Carbide uprooting on A roll

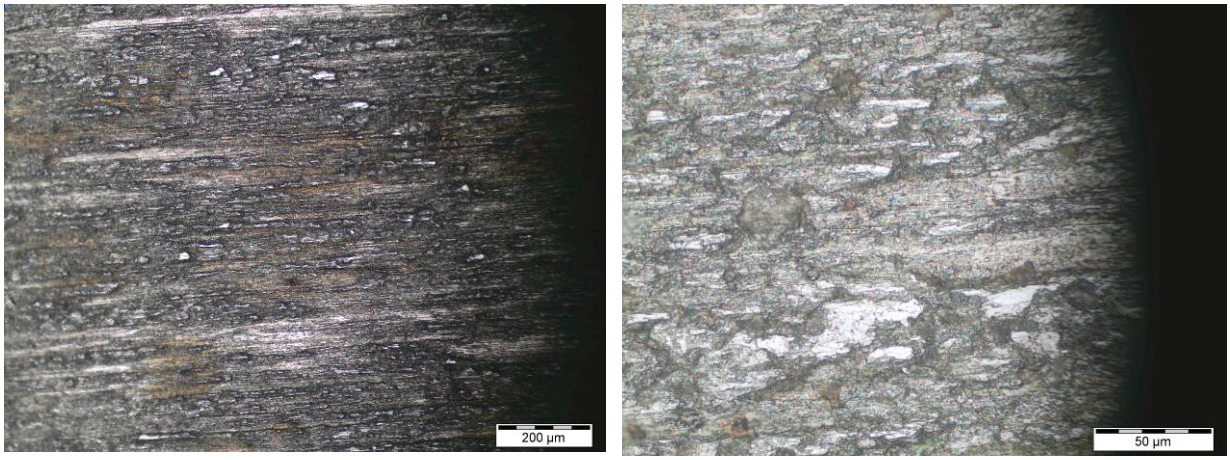

Fig. 136: Stuck particles respectively zoomed at X 100 and X 500

The distribution of white particles seems to be randomly spread over the roll surface (Fig. 136). The surface of the stuck dot zoomed in the right picture is made to be able to distinguish surface abrasion phenomenon.

A SEM analysis on the roll surface (Fig. 137) highlighted that these stuck dots corresponds to a metal particle sticking to the surface of the cylinder.

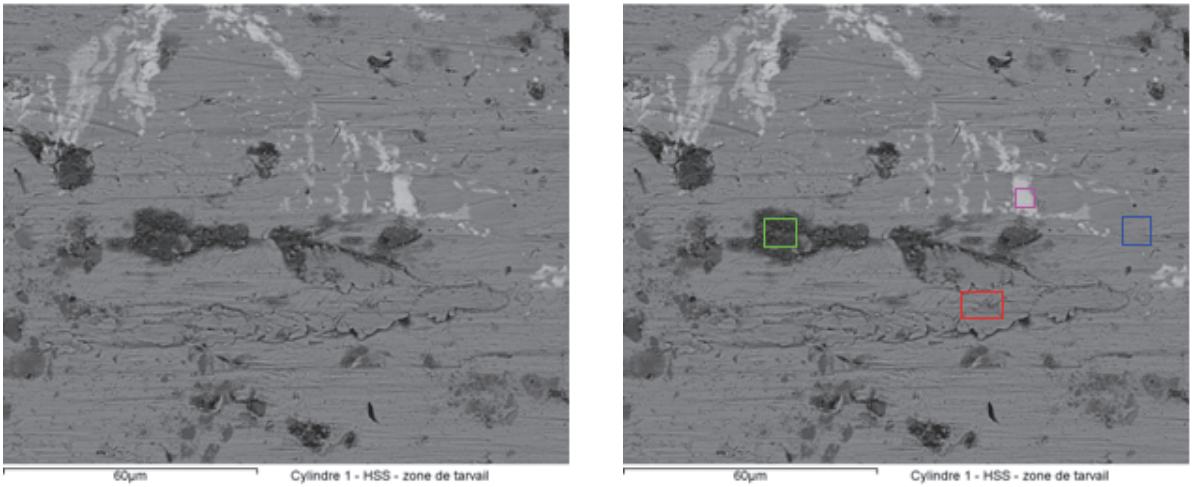

Fig. 137: SEM analysis of *A roll* surface on the stuck dots

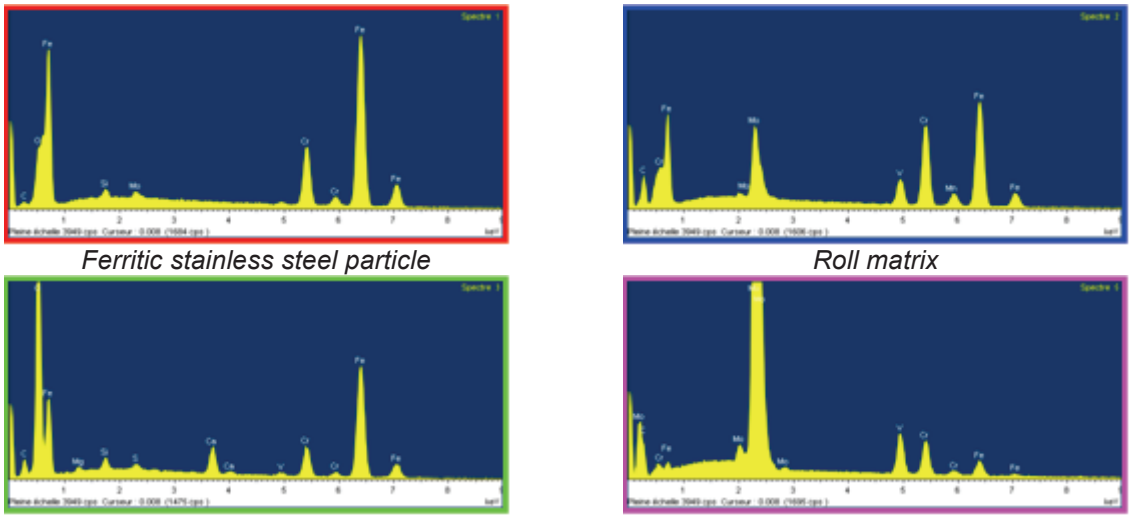

Fig. 138: EDX analysis of stuck particle

The SEM-EDX analysis (Fig. 138) confirms that the stuck particles are coming from stainless steel specimen (presence of Cr, Fe, Si) and that oxides trapped under the particle is an oxide also coming from rolled specimens (Fe, Cr).

As a result, the sticking defect was reproduced on the rolling pilot, even using rolls initially ground with grinding scratches smaller than the initial oxide layer thickness (scratches depth = 1,5 µm to be compared to transfer bar oxide thickness = 20-70 µm). It implies that having roll scratches deeper than oxide thickness is not strictly necessary to initiate sticking phenomenon.

1.3. B ROLL EXAMINATION

Note that the feature of unworn area of *A roll* and *B roll* are similar which is conform to expected results. An oxide band is located on only one side of the specimen, corresponding to the gear-motor side. This band consists of aggregates of oxides that are coming from stainless steel specimens and lined the cylinder surface. Some accumulations seem to be very important. We are still able to observe stuck dots, whose average size is approximately the same as previously, around 10 microns. Nevertheless, their density is clearly reduced to 1 particle per square millimetre.

In the band, we note that oxide is arranged in lines oriented along rolling direction (Fig. 139 - 140). These bands are approximately 200 microns wide, overlapping grinding ridges and increasing surface roughness. The dimension of these lines corresponds to the average dimensions of plateaus noticed in the beginning of this chapter and also correspond to the size of the defect noticed on industrial strips.
Out of the band, oxide has a higher covering power but also looks thinner. It looks very partially adherent and reveals cavities from carbide uprootings. These cavities have an average diameter of 10 microns but can sometimes reach higher dimensions, up to 25 microns.

This observation confirms that the initial oxides located on plateaus are transferred to roll surface and make as a partial coating on the roll.

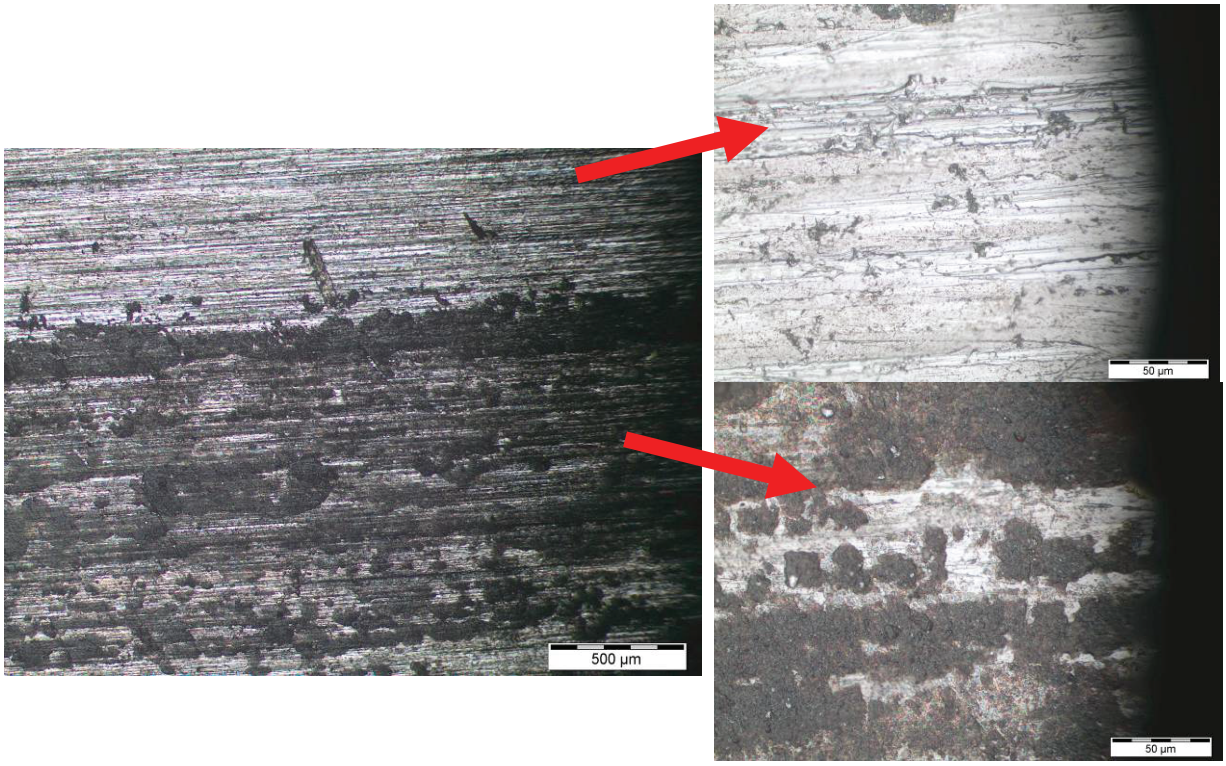

Fig. 139: Transition zone between oxidized area corresponding to specimen edge and unworn area of *B roll*

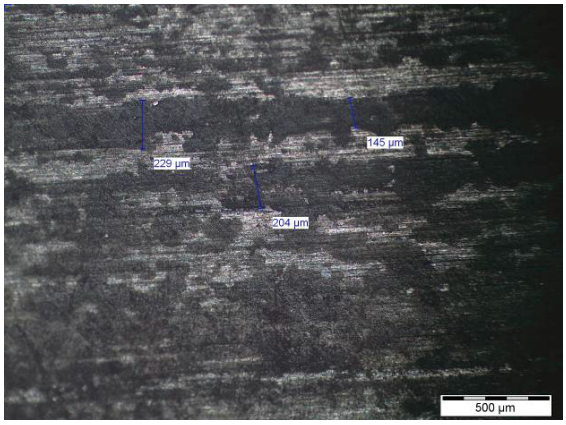

In oxide band – X 50

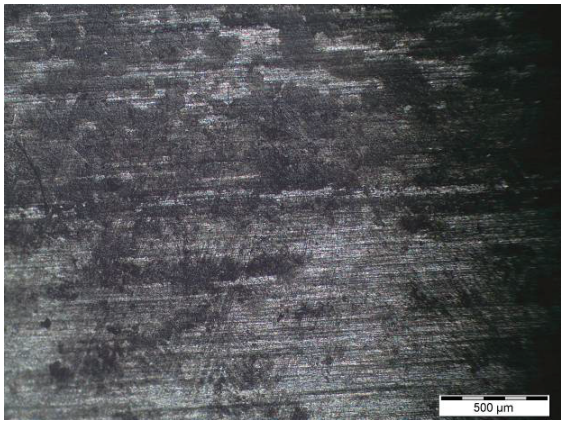

Out of oxide band – X 50

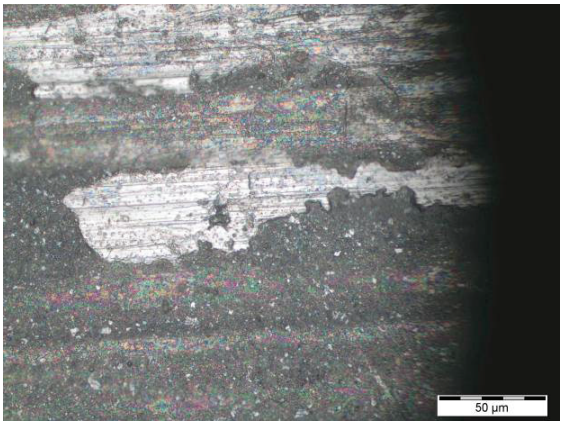

In oxide band – X 500

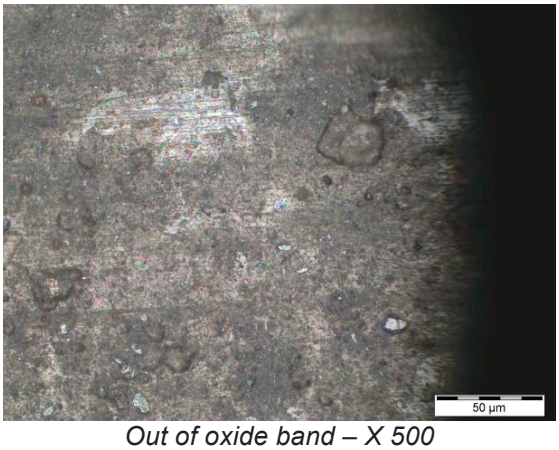

Out of oxide band – X 500

Fig. 140: Observation in the oxide band and out of it at various scales

1.4. C ROLL EXAMINATION

The roll surface is clearly different from the first two: the roll was turned (machined) and not ground which left furrows in which oxide particles initially present on B roll are deposited. Oxide fills furrows and helps to decrease surface roughness of C roll but also changed the wear of B cylinder.

It is therefore necessary to re-adjust the C roll roughness to those of other cylinders to limit oxide transfer and disconnect it for future in dry contact conditions. In future campaigns, this roll will be ground as other rolls, with the same surface characteristics.

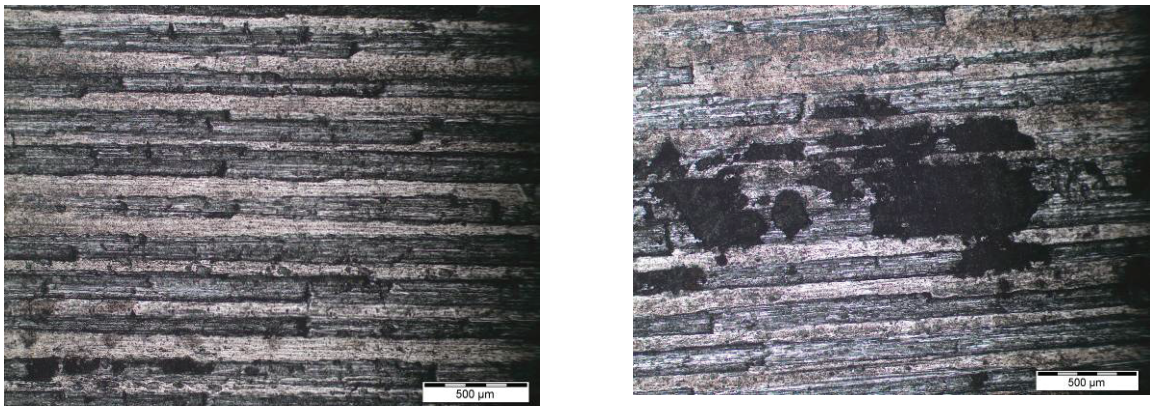

Out of worn area – X 50 *In worn area – Oxidised particles – X 50*

Fig. 141: Observation of C roll surface in and out of worn area

2. Roll wear during rolling – Roughness analysis of the roll after the rolling campaign

The roll profile was also investigated after the rolling campaign (Fig. 142). The roll surface was analysed in the worn area described earlier over a general width of 10 mm.

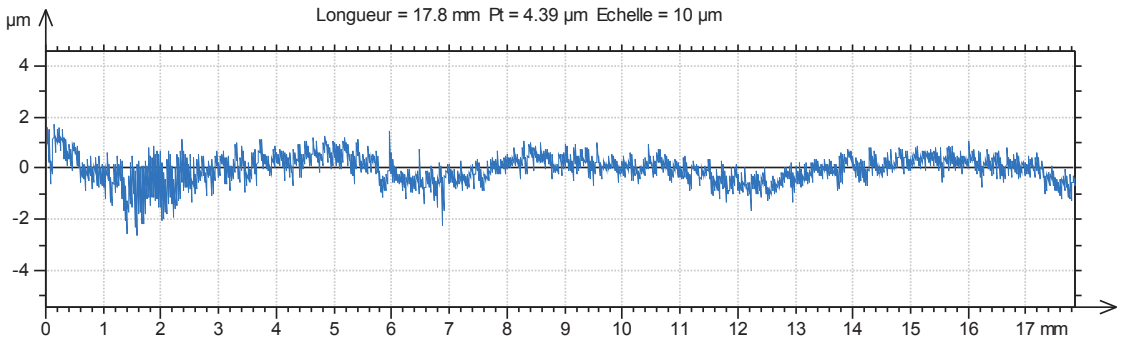

Fig. 142: Rough measured profile of roll surface along transversal direction

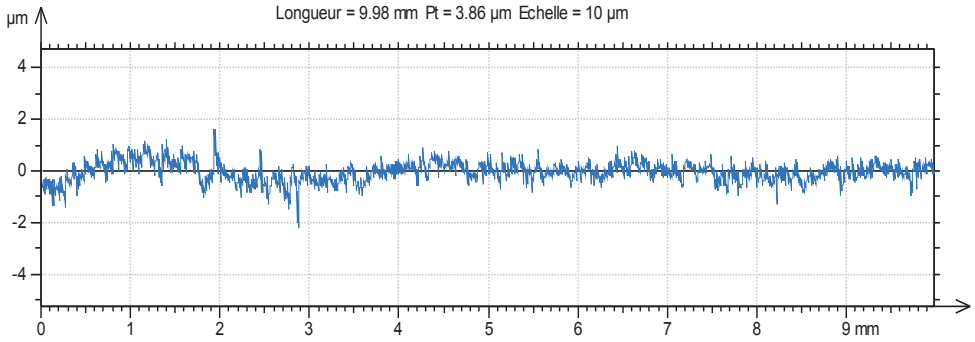

Fig. 143: Roll profile after setting of the reference line (double Gaussian filter)

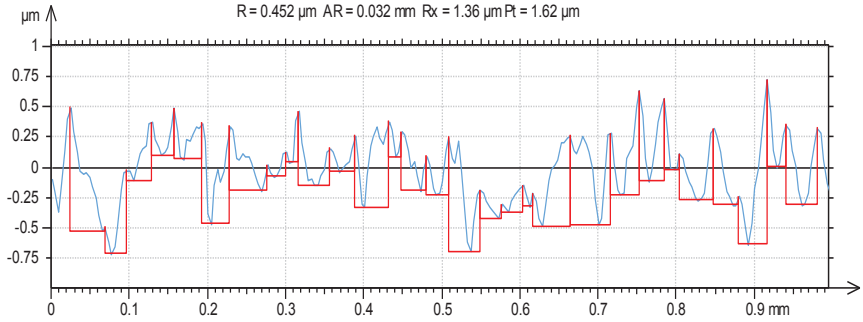

Fig. 144: Profile used for determining the roughness parameters

Tab. 27. Roughness measurements after rolling campaign

	Before test	After test	Measurements made on real rolls (chapter 2)
Pz	1,49 µm	1,62 µm	17
PSm	46,7 µm	56,7 µm	500
Pmr	28 µm	32 µm	10 - 30

Table 27 shows that strips width is quite stable (Pmr parameter) and equivalent to the measurements made on industrial rolls.
PSm value, representing the distance between two stripes increases with rolling, jumps from 46.7 to 56.7 µm. At the same time, Pz value increases with rolling from 1.49 to 1.62 µm. It results to an increase of valley size during rolling. These two values are very different from industrial configuration. Nevertheless, we succeed in reproducing the sticking defect, with a very smooth surface and very fine scratches compared to specimen oxide layer thickness.

Moreover, arithmetic roughness after rolling campaign is around 0.243 µm which is lower than the 1 µm roughness suggested by Jin and al. [JIN00] to initiate sticking phenomenon. With this analysis, we confirm that a high roll surface roughness is not strictly necessary to initiate sticking phenomenon.

D/ Conclusion on roll scratches as initiation sites for sticking phenomenon

- Reproduction of sticking phenomenon:

In this paragraph, roll examinations show that sticking defect was reproduced on the rolling pilot. Particles of ferritic stainless steel coming from specimens were clearly identified on roll, separated from it by oxide layer coming from the specimen.

This phenomenon can occur at two scales: a macroscopic scale, where particles of some millimetres can be distinguished and a microscopic scale, where particles around 10 microns in diameter can be found even in oxidized areas of the cylinder.

-Initiation of sticking phenomenon:

Cross sections of roll and roll surface examination allow us to identify the presence of cavities at the roll surface that are deeper than grinding scratches. These cavities were assimilated to carbides uprooting due to the rolling of successive specimens. Particles dimensions found in our study are similar to particles found by Lee and al. [LEE98], around 15 µm on two discs lab test (Fig. 146).

Nevertheless, our study showed that stuck stainless particles have dimensions (around 10 µm) more than two times higher than carbides cavities. As a result, localisation of stuck particles cannot be directly associated to carbides uprooting, nor grinding ridges presence, which is in contradiction with Jin mechanism [JIN00].

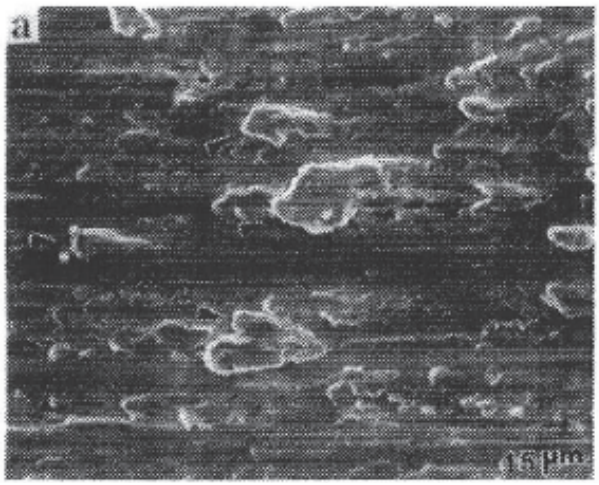

Fig. 146. Initiation of sticking on SUS 430 J1L after 7 revolutions on two discs test (HiCr roll) [LEE98]

Moreover, roll surface examination highlights that, after the rolling campaign, the roll surface is still smooth to be under Jin requirements. Rolling induces a increase in valley depth and width, but these dimensions are too small to induce direct metal/metal contact because oxide thickness of the specimen is more than 10 times thicker.

- Scale layer effect:

Jin and al. [JIN00] explain that sticking phenomenon occurs only when there is a direct contact between roll metal and stainless steel product. Jin and al. show that if a roll has an arithmetic roughness of 1 µm and if scale layer thickness is superior to 3 µm there is no sticking.

This configuration is realised in our case because arithmetic roll roughness is of 0.243 µm and specimen oxide thickness is over than 20 µm. Nevertheless, we noticed that sticking occur even in this configuration.

As a result, oxide layer as the only one barrier against direct metal-metal contact is not sufficient to explain sticking initiation via grinding scratches.

Considering, observations of transversal cut of specimens, **we highlighted that metal/metal contact is possible between rolls and specimen only on plateaus and essentially because of a low adherence of oxide layer during scale layer deformation into the roll bite**.

Presence of a **continuous comb structure at scale/metal interface will be useful to improve the adherence of outer part of the scale** and so, decrease the probability of direct metal/metal contact.

Conclusion and outlooks

The evolution of engines (new fuels, new engine technologies…) induces a modification in combustion parameters and major consequences results in an increase in exhaust gas temperature. As a result, design of new grades with higher corrosion and creep resistance is needed. A new grade is defined by changing the rate of definite chemical elements known for their impact on corrosion and mechanical resistance. Chromium is known for increasing drastically the corrosion resistance. In ferritic stainless steel, its rate varies from 11 to 22 %. The Molybdenum added to the Chromium confers also a higher corrosion resistance.

As these high alloyed steels have different behaviors compared to the standard ferritic grade 430, their design induces new challenges in their production. New defects occur in the production of hot rolled flat products on the grades containing more than 17% Chromium. These defects are characterized by a constellation of stuck particles on the sheet surface which cannot be removed during the final cold rolling sequences.
The presence of these defects induces two major problems:

- the product does not meet standard esthetics requirements for the high quality market,
- corrosion preferentially appears on the incrusted particle area leading to a decrease in product life.

The origin of these defects is linked to the sticking of the hot rolled product on working cylinders of finishing mill. High chemical affinity between the product, which contains at least 17% Cr, and the cylinder, which approximately contains 6% Cr results in sticking phenomenon that can only occur when there is a direct metal-metal contact between the two antagonists. Due to the high temperature of the product during rolling (between 950°C and 1070°C), an oxide layer (already present before entering the finishing mill) grows on the product surface and tends to prevent direct metal-metal contact, so decreases the sticking phenomenon.

In the first chapter of this work, a survey allows us to compare different effects of rolling parameters on sticking phenomenon through results based on disc-on-disc tribometers. These studies proposed a formation mechanism of the defect and, to understand the initiation of sticking phenomenon, Jin and al. [JIN00] exposed that a defect on roll surface is able to fracture oxide layer and generate metal/metal contact between roll and rolled product. Industrial notifications based on rolled product surface examination and process/quality statistics highlighted that the hypothesis base on the fact that a roll surface defect could be at the origin of the defect is called into question because:

- defect dimensions seem to be imposed by roll defect
- scale used in these trials is not the same as the oxide layer in the industrial process (chemical composition and structure)
- scratches dimensions used to demonstrate sticking initiation in literature doesn't seem comparable to scratches that we can found on industrial rolls.

In order to confirm this hypothesis, roll surface examinations on industrial rolls after a ferritic rolling campaign are exposed in chapter 2. Analyze performed in this chapter allow us to define the main topographical patterns of HSS and ICDP rolls and define three roughness parameters that will be used to describe roll scratches dimensions.
After analyzing several dozens of roll surface replicas, maximal and average dimensions of roll scratches were identified on HSS rolls (which are more prone to generate scratches than ICDP rolls). These dimensions are smaller than dimensions used in literature studies and also smaller than oxide thickness determined on the industrial transfer bar. As a result, the hypothesis of roll scratch to be the initiation site of sticking phenomenon is called into question.

In order to investigate the initiation of sticking according to process conditions, a new testing device has been designed. The specificity of this pilot compared to conventional tribometers is its possibility to use specimens from a real slab, with the industrial scale layer. It also enables the use of industrial ground rolls. So, the tribological test involves cylinders machined from real work rolls and tests are performed on specimens machined from industrial slabs in order to respect the physicochemical properties of the contact.

In chapter 4, a design of experiments has been carried out to study the effect of temperature and reduction ratio on sticking phenomenon. We noticed the evolution of friction coefficient has not a monotonic trend but is mainly influenced by modification of scale layer behaviour. At low reduction, friction coefficient increases with temperature and it is linked with a contact area increase. At higher reduction, friction is reduced for high temperatures and it is linked to the loss of external part of oxide layer, rich in iron oxides that might act as a solid powder lubricant.

Moreover, contact conditions supposed to prevent sticking by Jin and al. have lead to sticking defect when reproduced on the pilot. As a result, the hypothesis of roll scratch to be at the origin of sticking phenomenon is not a strict condition. Our observations highlight the very specific behaviour of transfer bar scale layer: the scale is particularly not adherent and observing it into transversal direction helped us to identify plateaus where sticking is generated. Finally, we noticed that a specific form of scale-metal interface having a comb form could be useful to increase scale adherence.

A better understanding of the generation of this comb form and the link between scale adherence and its morphology would help us to generate an adherent scale onto the rolled product and so, decrease sticking phenomenon. As an example, the composition of the ferritic stainless grade could be optimised to limit surface defect.

Based on an industrial point of view, this work pointed out the major effects of temperature and reduction ratio on the sticking phenomenon. But other rolling parameters have to be investigated in order to define optimised rolling standards:
- what is the effect of the rolling speed on sticking ?
- regarding lubrication:
    - what kind of lubricant ?
    - where and when is it better to lubricate ?

- concerning roll surfaces:
    - which roughness reduces sticking ?
    - which roll grade would be the most appropriate to avoid surface defect ?
    - could roll coating eliminate metal transfer from the slab ?

Working on a new roll grade or specific coatings to protect roll surface from direct metal-metal contact (with ferritic stainless steel) will be a new challenge that could succeed in suppressing definitely this defect.

References

[AKS01] M. Aksoy, O. Yilmaz, MH. Korkut. “The effect of strong carbide forming elements on the adhesive wear resistance of ferritic stainless steels”. *Wear* n° 249, pp. 639-646, 2001.

[AKS09] M Aksoy et al. “The effect of Nb on the adhesive wear resistance of ferritic stainless steels”. *Proceedings of Inst. Mech. E*, vol 223, Part J1J : Engineering tribology, pp. 39-49, 2009.

[APE00] Aperam Internet site, www.aperam.com

[ASM95] ASME B46.1. Surface Texture: Surface Roughness. New York: Waviness, and Lay, American Society of Mechanical Engineers. 1995.

[BAM06] G. Bamba , Y. Wouters , A. Galerie , F. Charlot , A. Dellali. “Thermal oxidation kinetics and oxide scale adhesion of Fe–15Cr alloys as a function of their silicon content”, *Acta Materialia*, n°54, pp. 3917–3922, 2006.

[BAR80] Baroux and al. “Structure et propriétés des aciers inoxydables ferritiques stabilisés », CRU external report n° 67.775, 1980.

[BAY02] N. Bay, Review on Methods of Testing Friction in Metal Forming, Euromech 435, Friction and Wear in Metal Forming, Valenciennes, 18-20 juin 2002.

[BOG78] W.E. Boggs, D.E. Sonon. “*Method for improving the surface quality of stainless steels and other chromium-bearing iron alloys*”, US Patent 4,078,949, 1978.

[CAL09a] E. Calmels. « Influence of grinding on the slab reheating at the hot strip mill of ArcelorMittal Châtelet (K45 and K44 grades)”, NT 2446, Aperam Internal report, 2009.

[CAL09b] E. Calmels. “Impact of the descaling operation at the slab furnace exit (grades FT90) : Descaling conditions optimisation”, NT 2237, Aperam Internal report, 2009.

[CAL10] E. Calmels. “Tribological trials « simulating » the roll bite of the 1st stand of the finishing mill for stainless steels”, NT 2802, Aperam Internal report, 2010.

[CHA84] Chamont. “Le Titane comme élément de microalliage en forte teneur dans les aciers – Etude bibliographique », IRSID Technical report RI 961, 1984.

[CHA92] H Chaudansson, J. Metivier. « Oxydation des cylindres de laminage », Aperam Internal report, RI 92/344, 1992.

[CHE84] Chemelle, Henriet. “Mise en solution et précipitation des carbonitrures de titane et de niobium dans les aciers inoxydables ferritiques stabilises”, CRU Internal report n° 148.84, 1984.

[DAO08] Daouben E., Dubois A., Dubar M., Dubar L., Deltombe R., Truong dinh N., Lazzarotto L., Effects of lubricant and lubrication parameters on friction during hot steel forging. International Journal of Material Forming, 1, pp. 1223-1226, ISSN 1960-6206, 2008.

[DEM81] P. Demont, H. Tran Nguyen, JF. Sacadura. « Influence de l'oxydation et de la rugosité sur les caractéristiques radiatives des aciers inoxydables », *Journal de Physique*, colloque C1, Tome 42, pp 161-171, 1981.

[DOD13] K. Dohda, Challenges in Sustainable Forming Processes. Internal seminar, TEMPO Lab, UVHC. 2013.

[DUB00] A. Dubois, L. Dubar, M. Dubar, J. Oudin, Caractérisation du frottement outil-pièce en mise en forme à l'ambiante des aciers. Mec. Ind., vol. 1, 639-649.2000.

[EFR85] B Efron and RJ Tibshirani. *An Introduction to the Bootstrap.* New York: Chapman and Hall. 1985.

[EKA05] S. EKAMBI-POKOSSI, *Caractérisation et identification multi-échelle de la signature peinture*, Thèse de doctorat, Ecole Centrale de Lyon, 2005.

[EUR93] EUR 15178N. The development of methods for the characterisation of roughness in three dimensions", Stout, Sullivan, Dong, Mainsah, Luo, Mathia, Zahouani, Commission of the European Communities, EUR 15178 EN. 1993.

[FUJ64] C.T. Fujii, R.A. Meussner. "The mechanism of the high temperature oxidation of iron-chromium alloys in water vapour", *Journal of the electrochemical society*, vol. 111, n°11, 1964.

[GAT87] Gates, Jago. *Materials Sciences Technology*, N°3, pp. 450 – 454, 1987.

[GON05] S.Gonzales, D.Vil. « Comportement de la nuance ferritique FS30 au train à bandes : synthèse des résultats R&D 2004 », NT 1019, Aperam Internal report, 2005.

[GUI90] I. Guillot. *Oxydation et phénomènes de frottement à chaud sur les aciers inoxydables ferritiques : Influence des éléments mineurs (Ti, Nb, Mo)*, Thèse de doctorat, Université technologique de Compiègne, 1990.

[HA08a] DJ. Ha, CY. Son, JW. Park, JS. Lee, YD. Lee, S. Lee. "Effects of high temperature hardness and oxidation on sticking phenomena occuring during hot rolling of two 430 J1L ferritic stainless steels " *Materials science and engineering A*, n°492, pp. 49-59, 2008.

[HA08b] DJ. Ha, HK. Sung, S. Lee, JS. Lee, YD. Lee. "Analysis and prevention of sticking occurring during hot rolling of ferritic stainless steel". *Materials science and Engineering A*, doi:10.1016/j.msea.2008.11.062, 2008.

[HA09] DJ. Ha, YJ. Kim, JS. Lee, S. Lee. "Effects of alloying elements on sticking behaviour occurring during hot rolling of modified ferritic STS 430J1L stainless steels", *Metallurgical and materials transactions A*, vol 40A, pp. 1080-1089, 2009.

[HAL92] P Hall. *The Bootstrap and the Edgeworth expansion*. , New York: Springer-Verlag. 1992.

[HER09] A. HERMANT, D. VIL, E. CALMELS. **"**Examens de défauts sur produits RDE de FD82 – pailles A, R et lignage – filière Gueugnon"**,** Aperam Expertise Report RE 2466, 2009.

[HER37] P. Hervé. *Mesure de l'émissivité thermique*, Techniques de l'ingénieur R 2737.

[HUN07] A.M. Huntz, A. Reckmann, C. Haut, C. Sévérac, M. Herbst, F.C.T Resende, A.C.S. Sabioni. "Oxidation of AISI 304 and AISI 439 stainless steels", *Materials Science and Engineering A*, n° 447, pp. 266 – 276, 2007.

[ISO96] ISO 11562: 1996. Geometrical Product Specifications (GPS) – Surface Texture: Profile Method -- Metrological Characteristics of Phase Correct Filters (International Organization for Standardization, Geneva,). 1996.

[ISO11] ISO 12781-1:2011 Geometrical Product Specifications (GPS) - Flatness - Part 1: Vocabulary and parameters of flatness. 2011.

[ISO12] ISO 25178-2: 2012. Geometrical product specifications (GPS) - Surface texture: Areal - Part 2: Terms, definitions and surface texture parameters. 2012.

[ISS12] J. Issartel. *Comportement des aciers inoxydables ferritiques stabilisés lors des étapes de recuit et décapage*, Thèse de doctorat, INP Grenoble, 2012.

[ISS12b] J. Issartel, S. Martoia, F. Charlot, V. Parry, G. Parry, R. Estevez, Y. Wouters. "High temperature behavior of the metal/oxide interface of ferritic stainless steels", *Corrosion Science*, n° 59, pp. 148–156, 2012.

[ISSF1] La solution ferritique, Propriétés, avantages, applications. ISSF, http://www.worldstainless.org/Files/issf/non-image-files/PDF/ISSF_The_Ferritic_Solution_ French.pdf

[JIA97] S. Jianian, Z. Longjiang, L. Tiefan. "High temperature oxidation of Fe-Cr alloys in wet oxygen" *Oxidation of metals*, vol. 48, n°3/4, 1997.

[JIN98] W. Jin, JY. Choi, YY. Lee. "Effect of roll and rolling temperatures on sticking behavior of ferritic stainless steels". *ISIJ International*, vol 38, N°7, pp. 739-743, 1998.

[JIN00] W. Jin, J.Y. Choi, Y.Y Lee. "Nucleation and growth process of sticking particles in ferritic stainless steel", *ISIJ International*, vol.40, n°8, pp. 789-793, 2000.

[JIN02] W. Jin, D. Piereder, J.G. Lenard. "A study of the coefficient of friction during hot rolling of

a ferritic stainless steel", *Lubrication Engineering* n° 58, pp. 29–37, 2002.

[JIN08] D. Jin Ha, C.Y Son, J. Wook Park, J. Seog Lee, Y. Deuk Lee, S. Lee. "Effects of high-temperature hardness and oxidation on sticking phenomena occurring during hot rolling of two 430J1L ferritic stainless steels", *Materials Science and Engineering A, n°* 492, pp. 49–59, 2008.

[JOO07] O Joos, C Boher, C Vergne, C Gaspard, T Nylen, F Rezaï-Aria, "Assessment of oxide scale influence on wear damage of HSM work rolls", *Wear*, n°263, pp.198-206, 2007.

[KAN01] YJ. KANG, JC. OH, HC. LEE, S. LEE. "Effects of C and Cr additions on the wear resistance and surface roughness of cast HSS rolls", *Metallurgical and materials transactions A*, 32A, Oct 2001, pp. 2515-2525.

[KAT92] O. Kato, H. Yamamoto, M. Ataka, K. Nakajima. Mechanisms of surface deterioration of roll for hot strip rolling, ISIJ International, vol 32, n°11, pp. 1216-1220, 1992.

[LAI09] J. Laigo, F. Chassagne. "Bibliographic review on the influence of stabilizing elements on microstructure and mechanical behaviour of ferritic stainless steels", Aperam Technical Report NT 2477, 2009.

[LEE98] S. Lee, D. Suh, S. Oh, W. Jin. "Sticking mechanism during hot rolling of two stainless steels", *Metallurgical and materials transactions A*, vol 29A, pp. 696-702, 1998.

[LER10] A. Leroy, G. Moreas. "Workroll in the roughing mill – Rollscope", CRM report, June 2010.

[LIU06] J.X. Liu, D.X. Jian, W. Shizhong, Y.J. Zhang, L. Rui. Investigation on wear behaviors of high-vanadium high-speed steel compared with high-chromium cast iron under rolling contact condition, *Materials Science and Engineering A* 434, pp. 63-70, 2006.

[LIU09] J.X. Liu, Y.J. Zhang, J.T Han. "Test research on sticking mechanism during hot rolling of SUS 430 ferritic stainless steel", *International Journal of Minerals, Metallurgy and Materials*, vol 17, N°5, pp. 573 – 578, 2009.

[LIU10] J.X. Liu, Y.J. Zhang, J.T. Han. "Test research on sticking mechanism during hot rolling of SUS 430 ferritic stainless steel", *International Journal of Minerals, Metallurgy and Materials*, vol 17, n°5, pp. 573-578, 2010.

[LNE10] JM. Boulet. *Synthèse des mesures des propriété rhéologiques et thermiques sur les nouvelles nuances, Mesures LNE*, Document interne confidentiel APERAM, 2010.

[MAL09a] J.P. Malchrowicz, E. Calmels. "Influence du meulage sur l'oxydation du K45 », CRE 2433, Aperam Internal report, 2009.

[MAL09b] J.P. Malchrowicz, E. Calmels. "Influence du meulage sur l'oxydation du K44", CRE 2444,

Aperam Internal report, 2009.

[MAR12] "*Fiches techniques Comet 70, Sirius, Aurora"*, J. MARICHAL KETIN & CIE, SA des fonderies, http://www.mkb.be/index2.html, 2012.

[MAR13] "*Fiche technique ICDP*", J. MARICHAL KETIN & CIE, SA des fonderies, http://www.mkb.be/index2.html, 2012.

[MIT11] J.-D. Mithieux, L. Peguet, F. Chassagne et P.-O. Santacreu, « Les aciers inoxydables ferritiques : une large palette de propriétés d'usage », Revue de Métallurgie 108, 3–7, 2011.

[PEL05] M. Pellizzari, A. Molinari, G. Straffelini. Tribological behaviour of hot rolling rolls, *Wear* 239, pp. 1281-1289, 2005.

[PIC04] B. Picqué. *Experimental study and numerical simulation of iron oxide scale mechanical behaviour in hot rolling*, PhD Ecole des Mines de Paris, 2004.

[SAN92] Y. SANO, T.HATTORI, M.HAGA. "Characteristics of high-carbon high speed steel rolls for hot strip mill", *ISIJ international*, Vol 32, pp. 1194 – 1201, 1992.

[SCH84] J.A. Schey, Tribology in Metalworking – Friction Lubrication and Wear, American Society for Metals, 1984.

[SEL10] M.P Sello, W.E Stumpf. "Laves phase embrittlement of the ferritic stainless steel type AISI 441", *Materials Science and Engineering A*, doi:10.1016/j.msea.2010.04.058, 2008.

[SON07] C.Y Son, C.K. Kim, DJ. Ha, S. Lee, J.S. Lee, K.T. Kim, Y.D. Lee. "Mechanisms of sticking phenomenon occuring during hot rolling of two ferritic stainless steels", *Metallurgical and materials transactions A*, vol 38A, pp.2776-2787, 2007.

[TOS04] F. TOSCAN. *Optimisation conjointe de l'adhérence des couches d'oxydes et des cinétiques d'oxydation thermique sur aciers inoxydables* , Thèse de doctorat, INP Grenoble, 2004.

[VIL08a] D. Vil. "Incrustations d'oxydes sur coils blancs – nuance K41 (FT90) », RE 2090, Aperam Internal report, 2008.

[VIL08b] D. Vil. "Incrustations d'oxydes en rive sur FD91 (K44) », RE 2136, Aperam Internal report, 2008.

[WEI97] D. Wei, A.C. Bovik, B.L. Evans. Generalized Coiflets: a new family of orthonormal wavelets, Record of *the thrity-first Asilomar Conference on Signals, Systems & Computers*, Nov. 1997, vol. 2, pp. 1259 – 1268, 1997.

[WHI13] DJ. Whitehouse, *Handbook of surface and nanometrology*, pp. 107 – 109.

[YUA00] YB Yuan, TV Vorburger,JF Song, TB Renegar. A Simplified Realization for the Gaussian Filter in Surface Metrology. Proceedings of X. International Colloquium on Surfaces. Aachen: Shaker Verlag GmbH, pp.133-144. 2000.

[ZHA12] C. Zhang, Z. Liu, Y. Xu, G. Wang. "The sticking behavior of an ultra purified ferritic stainless steel during hot strip rolling", *Journal of Materials Processing Technology*, n° 212, pp. 2183– 2192, 2012.

[ZHU10] Q Zhu, HT Zhu, AK Tieu, M Reid, LC Zhang."In-situ investigation of oxidation behaviour in high speed steel roll material under dry and humid atmospheres", *Corrosion science,* n°52, pp.2707-2715, 2010.

[ZHU11] Q. Zhu, HT Zhu, AK Tieu, C Kong, "Three dimensional microstructure study of oxide scale formed on a high speed steel by means of SEM, FIB and TEM", *Corrosion science*, n°53, pp.3603-3611, 2011.

[ZIE07] K.H. Ziehenberger, M. Windhager. "State of the art work rolls for Hot Rolling flat products", *Proceedings of CONAC 2007 – 3rd Steel Industry Conference and Exposition*, Centro Convex, Monterrey, N.L., México, 11th to 14th November, 2007.

APPENDIX 1 – HSS microstructure – Size of precipitates

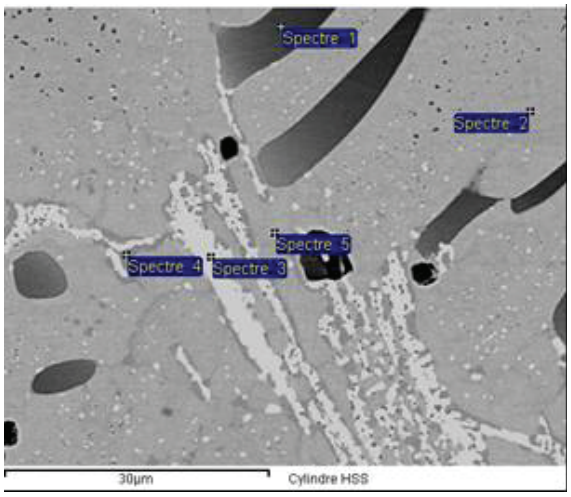

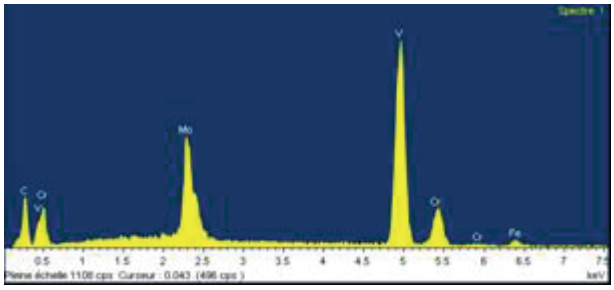

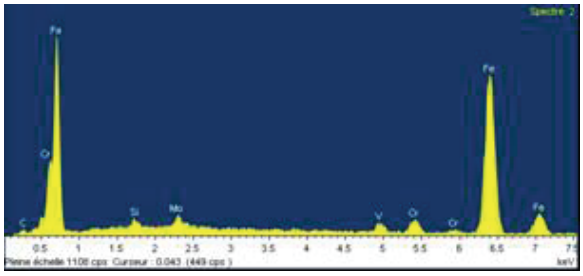

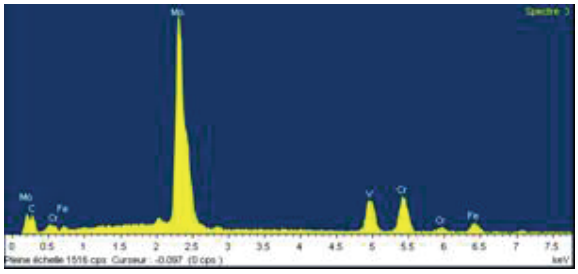

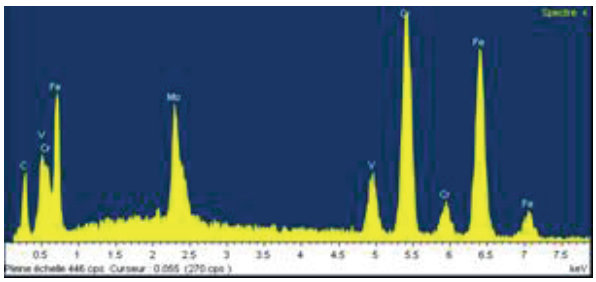

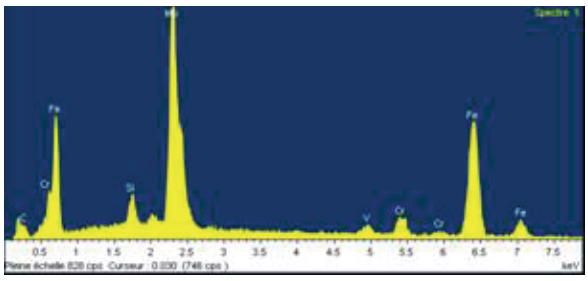

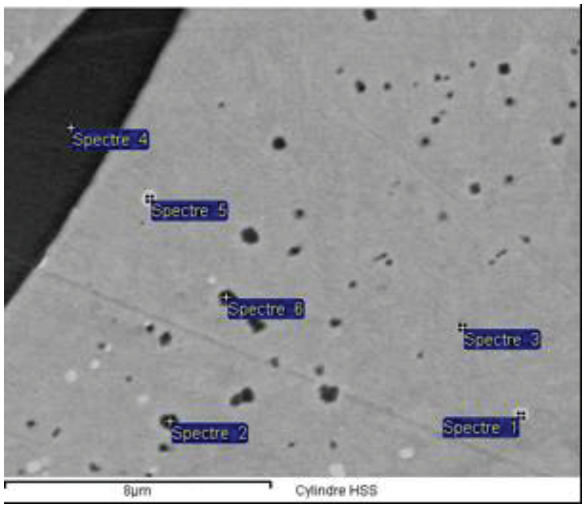

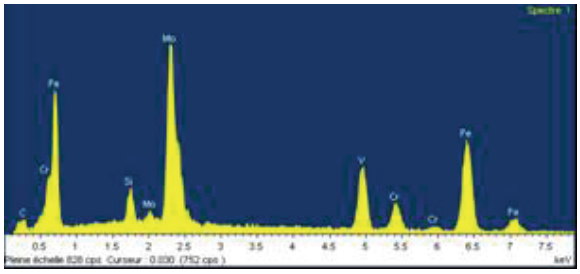

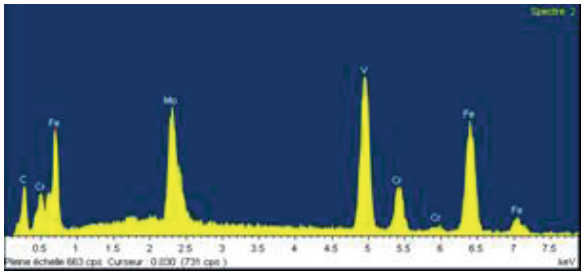

APPENDIX 2 – ROUGHNESS PARAMETERS

3D roughness parameters			
Symbol	Units	Name of parameter	Standard
Amplitude Parameters			
S_q	µm	Root mean square height	ISO 25178
S_{sk}	-	Skewness	ISO 25178
S_{ku}	-	Kurtosis	ISO 25178
S_p	µm	Maximum peak height	ISO 25178
S_v	µm	Maximum pit height	ISO 25178
S_z	µm	Maximum height	ISO 25178
S_a	µm	Arithmetic mean height	ISO 25178
S_t	µm	Total height	EUR 15178N
Spatial Parameters (ISO 25178)			
S_{al}	mm	Auto-correlation length	ISO 25178
S_{tr}	-	Texture-aspect ratio	ISO 25178
S_{td}	°	Texture direction	ISO 25178
S_{al}	mm	Fastest decay autocorrelation length	ISO 25178
Hybrid Parameters (ISO 25178)			
S_{dq}	-	Root mean square gradient	ISO 25178
S_{dr}	%	Developed interfacial area ratio	ISO 25178
S_{ds}	1/mm²	Density of summits	EUR 15178N
S_{sc}	1/mm	Arithmetic mean summit curvature	EUR 15178N
S_{fd}	-	Fractal dimension of the surface	EUR 15178N
Functional Parameters			
S_k	µm	Core roughness depth	EUR 15178N
S_pk	µm	Reduced summit height	EUR 15178N
S_{vk}	µm	Reduced valley depth	EUR 15178N
S_{r1}	%	Upper bearing area	EUR 15178N
S_{r2}	%	Lower bearing area	EUR 15178N
S_{pq}	-	Plateau root mean square roughness	EUR 15178N
S_{vq}	-	Valley root mean square roughness	EUR 15178N
S_{mq}	-	Material ratio at plateau-to-valley transition	EUR 15178N
S_{mr}	%	Areal material ratio	ISO 25178
S_{mc}	µm	Inverse areal material ratio	ISO 25178
S_{xp}	µm	Extreme peak height	ISO 25178
S_{dc}	µm	Areal height difference	ISO 25178
Volume Functional Parameters			
V_m	mm³/mm²	Material volume	ISO 25178

V_v	mm^3/mm^2	Void volume	ISO 25178
V_{mp}	mm^3/mm^2	Peak material volume	ISO 25178
V_{mc}	mm^3/mm^2	Core material volume	ISO 25178
V_{vc}	mm^3/mm^2	Core void volume	ISO 25178
V_{vv}	mm^3/mm^2	Pit void volume	ISO 25178
Functional Indices			
S_{bi}	-	Surface bearing index	EUR 15178N
S_{ci}	-	Core fluid retention index	EUR 15178N
S_{vi}	-	Valley fluid retention index	EUR 15178N
Feature Parameters			
S_{pd}	$1/mm^2$	Density of peaks	ISO 25178
S_{pc}	1/mm	Arithmetic mean peak curvature	ISO 25178
S_{10z}	µm	Ten point height	ISO 25178
S_{5p}	µm	Five point peak height	ISO 25178
S_{5v}	µm	Five point pit height	ISO 25178
S_{da}	mm^2	Mean dale area	ISO 25178
S_{ha}	mm^2	Mean hill area	ISO 25178
S_{dv}	mm^3	Mean dale volume	ISO 25178
S_{hv}	mm^3	Mean hill volume	ISO 25178
Other 3D Parameters (From Mountain™ Software)			
S_{mean}	µm	Mean height in absolute	No Standard
S_{dar}	mm^2	Developed area	No Standard
S_{par}	mm^2	Projected area	No Standard
-	μm^3	Mean volume of islands	No Standard
-	µm	Mean height of islands	No Standard
-	μm^2	Mean surface of islands	No Standard

Résumé

Le laminage à chaud de l'acier inoxydable est une étape du procédé de fabrication agissant significativement sur la qualité de surface des produits. Les nuances ferritiques stabilisées sont largement utilisées dans les applications automobiles et de décoration mais sont concernées par le phénomène de collage à chaud. Ces nuances, ayant des résistances élevées en corrosion sèche et en fluage, sont riches en éléments tels que le Cr, le Nb ou le Ti, limitant aussi l'oxydation des brames lors du laminage. Or, l'oxydation maitrisée de la brame permet de protéger la surface du métal de tout contact direct avec les cylindres de laminage.

Afin de comprendre l'initiation du collage, une première campagne d'étude sur la topographie et la dégradation de l'état de surface des cylindres a été réalisée. Il a été mis en évidence que l'initiation du collage ne serait pas du à des rayures d'usure en surface des cylindres et dont la profondeur serait supérieure à la couche d'oxyde, car la probabilité que la profondeur d'une rayure de cylindre soit plus importante que la couche d'oxyde est très faible.

Ensuite, un banc d'essai reproduisant les conditions tribologiques de l'emprise du laminoir a été conçu afin de mieux appréhender les mécanismes à l'origine du collage. Etant donné l'importance de l'état de surface des brames et des cylindres, ce banc d'essai a permis de travailler sur des échantillons pris en production, permettant d'étudier la surface oxydée des tôles. Cette deuxième campagne d'étude a mis en évidence l'importance des oxydes de silicium sur l'adhérence partielle de la couche d'oxyde, ainsi que la relative hétérogénéité en épaisseur et en composition chimique.

Mots clés: Laminage à chaud, acier inoxydable, collage, cylindre, rugosité, topographie, oxydation.

Abstract

Hot rolling of stainless steel is one of the most important steps in manufacturing process regarding surface quality of the product. Stabilised ferritic stainless steels are widely used in automotive and cosmetic appliances but are also concerned by sticking phenomenon. These grades, having high dry corrosion and creep resistance, are enriched in specific chemical elements such as Cr, Nb or Ti, limiting also slab oxidation during hot rolling. Nevertheless, the mastered oxidation of slab surface is a way to protect metal surface from direct contact with rolls.

In order to better understand initiation of sticking, a first campaign was based on topography and rolls surface state wear analysis. This study revealed that sticking initiation is not due to the presence of roll scratches which depth is higher than oxide layer thickness. Indeed, the probability that roll scratches are deeper than oxide layer thickness is very low.

In a second time, a pilot was designed, reproducing tribological conditions of a roll bite, to better understand mechanisms that initiate sticking. Keeping in mind the importance of rolls and slab surface state, this pilot is able to use specimen taking from industrial products, having the original oxide layer surface. This second study highlighted the major role of silicium oxides on scale adherence and the high heterogeneity of this scale layer in thickness and in chemical composition.

Keywords: Hot rolling, stainless steel, sticking, rolls, roughness, topography, dry corrosion.